Search for long-lived, massive particles in events with a displaced vertex and a displaced muon using sqrt{s} = 13 TeV pp-collisions with the ATLAS detector

Search for long-lived, massive particles in events with a displaced vertex and a displaced muon using $\sqrt{s} = 13$ TeV pp-collisions with the ATLAS detector

A DISSERTATION PRESENTED
BY
KARRI FOLAN DIPETRILLO
TO
THE DEPARTMENT OF PHYSICS

IN PARTIAL FULFILLMENT OF THE REQUIREMENTS
FOR THE DEGREE OF
DOCTOR OF PHILOSOPHY
IN THE SUBJECT OF
PHYSICS

HARVARD UNIVERSITY
CAMBRIDGE, MASSACHUSETTS
APRIL 2019

Thesis advisor: Professor Melissa Franklin   Karri Folan DiPetrillo

Search for long-lived, massive particles in events with a displaced vertex and a displaced muon using $\sqrt{s} = 13$ TeV pp-collisions with the ATLAS detector

Abstract

A search for long-lived particles giving rise to displaced decays with at least one muon is presented. The analysis selects events that pass a muon or missing transverse energy trigger and contain a displaced muon and a displaced vertex with at least three tracks and a vertex visible invariant mass of at least 20 GeV. A data sample of $\sqrt{s} = 13$ TeV proton–proton collisions collected by the ATLAS detector between 2016 and 2018, corresponding to a total integrated luminosity of 136 fb^{-1}, is used for this search. The analysis employs dedicated reconstruction techniques that significantly increase the sensitivity to displaced decays. Background estimates for Standard Model processes and instrumental effects are extracted entirely from data. The observed event yields are compatible with those expected from background processes. Results are presented as limits at 95% confidence level on the model-independent cross section for processes beyond the Standard Model, and interpreted as exclusion limits on scenarios with pair-production of long-lived stop squarks that decay via a small R-parity violating coupling to a quark and a muon. Stop squarks with a lifetime of 0.1 ns in these scenarios are excluded for masses up to 1.7 TeV.

To my mom.

Acknowledgments

This PhD took 20% of my life, cost me a leg, and possibly an arm. Just kidding. A little.

I've been looking forward to graduating for a long time. When I first showed up at Harvard I felt underprepared and overwhelmed. I never would have imagined feeling as grown up and ready to do physics as I do now. I owe so much to so many people who have donated their time and supported me along the way. The entire ATLAS collaboration has been especially kind, and without their hard work none of this would have been possible. Thank you everyone.

Melissa: Thank you for being the advisor I needed and more. Thank you for pushing me to ask the right questions, and being prepared to answer everyone else's. Thank you for always telling me what I needed to hear, whether I wanted to hear it or not. Thank you for challenging my ideas about physics and the world. Thank you for always giving me a chance, and for taking such wonderful care of me. Thank you for giving me so many amazing opportunities, and thank you showing me that doing physics and being happy should always be synonymous. You're an inspiration, and it's been an honor to work with you.

Larry: We made an incredible team, and we pulled off impossible feats. I really do believe we're the best ATLAS has ever had. Working with you has been more enjoyable and rewarding than I could ever have imagined, and I can't begin to explain how grateful I feel for having you as a friend. Thank you for showing me that there is a place for big ideas in particle physics. Your love of physics and embrace of challenges is one of the reasons I want to stay in this field. Thank you for always answering my questions, and for always putting up with my nonsense. Thank you for making every day of work

exciting and always sharing in a good laugh. This analysis (and my PhD) would be a dumpster fire if it weren't for you.

Alex: Thank you for being there at the beginning and the end of my time at CERN. When I first showed up at CERN, you helped me grow from a grad student with no knowledge about particle physics or ATLAS to a grad student who was actually useful. Throughout the years, watching you work and approach questions has taught me so much about how to solve problems and how to do an analysis. Thank you for helping me reach the finish line. Thank you for the head tilts and the laughs, thank you for your care, and thank you for always sharing your optimism.

Tony: Thank you for being an amazing DQ partner in crime. Thank you for showing me how to play detective, and for always going above and beyond what was asked of you. Your care for the detector and the data inspired me to be a better student. Thank you for the many chats about physics, life, and good drink. This last year of graduate school was much less fun without you.

Ann: Even though we technically never worked together, it sometimes feels like we worked together the most. Thank you for being an excellent co-worker, roommate, and friend. Thank you for always asking the questions no one else thought to ask. Thank you for your patience at home, and thank you for challenging me to be better, both at physics and in life.

Masahiro, John, and João: Thank you for taking the time to share your expertise, and thank you for always answering my questions. Your feedback and support have been incredibly helpful over the years.

Georgi: Thank you for a wonderful experience teaching physics 16 and for being such a supportive committee member. Thank you for your feedback over the years.

Roxanne: Thank you for agreeing to be on my committee. Your feedback and questions have been extraordinarily helpful, especially in writing this thesis, and I'm looking forward to seeing more of you at Fermilab.

Tiesheng, Philipp, Christoph, and Zhen: Thank you for trusting me with the MDTs, and thank you for your patience whenever I made a mistake. I learned so much about detectors and how to keep an experiment running from you. Thank you for always being excellent, and always challenging me to be better. Thank you for making Muon Operations one of the most enjoyable experiences I've had at CERN.

Paolo: Thank you for sharing your knowledge of detectors with me. Thank you most of all for your wit and your patience, and making sure that there was never a dull moment in the lab.

The SUSY Displaced Vertex team: Simone and Laura, thank you for being the physicists I aspire to be. Thank you for your questions and suggestions when designing this analysis, and thank you for all of your support. Hide, this analysis would be nothing without your hard work and expertise. Thank you for taking the time to pay attention to details, ask questions, and provide incredibly helpful feedback. Christian, thank you for donating so much of your time to DV+muon. There is no way we would have finished this in time if it weren't for you. Rebecca, Jennifer, Margaret, Emily, and Filip, thank you for making this analysis group so fun. It was a pleasure to learn and grow with all of you.

Zach, Till, Iacopo, and Federico: You've all made the SUSY group an exciting place to learn about physics. Your feedback has helped me to grow as a physicist, and think beyond the scope of my own analysis. Thank you so much for all of your support and encouragement.

To the DV+muon Ed board: Thank you for the many hours spent carefully reviewing this analysis.

problem sets and advisors, and thank you for always welcoming me back at Harvard.

To my fellow Harvard ATLAS grad students: Thank you for making the Harvard ATLAS group a second family. Tomo, Emma, thank you for being wonderful role models, and exemplifying what it means to be a supportive older grad student. Sun, thank you for ditching me in data quality, and thank you for breaking my leg. Neither experience was pleasant, but both made me stronger. Stephen, thank you for your impressions, and thank you Julia for the adventures. Brendon, Gabe, and Anne the Younger, thank you for bring a new perspective to this old student.

To the Harvard summer students, especially Madeline and Sarah: It was such a pleasure to work with you. Thank you for brightening up summers at CERN with your questions and your fun. You make the future of physics exciting.

To my family, especially my mom: Thank you for giving me every opportunity I could have dreamed of and more. Thank you for somehow always being proud of me, and also inspiring me to be better. Without your support none of this would have been possible.

Kuleen: You've been my source of strength, optimism, sanity, and everything else that is good for so many years. Thank you for never doubting my intelligence, my work ethic, or my aspirations. Thank you for always putting up with my feisty personality, especially when it required infinite amounts of patience. Thank you for your many treks across the Atlantic, and always supporting me.

Contents

List of figures

List of tables

List of Acronyms

CERN   the European Organization for Nuclear Research

LHC   Large Hadron Collider

ATLAS   A Toroidal LHC Apparatus

CMS   Compact Muon Solenoid

RF   Radiofrequency

PS   Proton Synchotron

SPS   Super Proton Synchotron

ID   Inner Detector

ECAL   Electromagnetic Calorimeter

HCAL   Hadronic Calorimeter

MS   Muon Spectrometer

IBL   Insertable B-Layer

SCT   Silicon Microstrip Tracker

TRT   Transition Radiation Tracker

LAr   Liquid Argon

FCAL   Forward Calorimeter

MDT   Monitored Drift Tubes

CSC   Cathode Strip Chambers

RPC   Resistive Plate Chambers

TGC   Thin Gap Chambers

sMDT   small Monitored Drift Tubes

L1   Level 1

HLT   High Level Trigger

CTP   Central Trigger Processor

L1Calo   Level 1 Calorimeter Trigger

L1Muon   Level 1 Muon Trigger

ASIC   application-specific integrated circuit

FPGA   field-programmable gate array

RoI   Region of Interest

JVT   Jet Vertex Tagger

JVF   Jet Vertex Fraction

MC   Monte Carlo simulation

SM   Standard Model

BSM   Beyond the Standard Model

SUSY   Supersymmetry

MSSM   Minimal Supersymmetric Standard Model

LSP   Lightest Supersymmetric Particle

AMSB   anomaly-mediated Supersymmetry breaking

GMSB   Gauge Mediated Supersymmetry Breaking

QED   Quantum Electro-Dynamics

QCD   Quantum Chromodynamics

PDF   Parton Distribution Function

SR   Signal Region

VR   Validation Region

CR   Control Region

LEP   Large Electron–Positron Collider

PV   primary vertex

DV   displaced vertex

Part I

Introduction

1

Introduction

Particle physics is concerned with the smallest, most irreducible pieces of matter, fundamental particles, and the interactions which govern these particles. The Standard Model (SM) of particle physics, is the best known description of these particles.

Thus far, the Standard Model has successfully described all known particles and their interactions, withstanding decades of scrutiny. However, there are many reasons why the Standard Model is likely to be an incomplete picture of the universe. For example, the Standard Model does not provide an explanation for the hierarchy puzzle, a candidate for dark matter, or a quantum description of gravity. Searches for evidence of physics Beyond the Standard Model (BSM) have been performed in many experimental setups. However, some of the most stringent constraints come from searches for new particles at high energy colliders.

The Large Hadron Collider (LHC) at the European Organization for Nuclear Research (CERN) is a 27 km particle accelerator located on the border of Geneva, Switzerland and France. The accelerator uses superconducting magnetics to circulate two counter-rotating bunches of protons, which are brought to collide at four points along the ring. Particle detectors, such as the A Toroidal LHC Apparatus (ATLAS) and Compact Muon Solenoid (CMS) experiments, are positioned around these points of collision to measure and identify outgoing particles from collisions.

If two particles collide with sufficient energy, new and heavier particles can be created. The LHC is the highest energy proton collider in the world, and is currently the only way to study some of the heaviest particles of the Standard Model, including the Higgs boson and top quark. One of the major goals of the ATLAS and CMS experiments is to discover a new particle which is not predicted by the Standard Model, and provides new insight about the nature of the universe.

Unfortunately, ATLAS and CMS have found no signs of new physics thus far. Run 2 of data taking has just finished, and LHC is not scheduled to take data again until 2021. Run 3 will bring a only modest increase in the center of mass energy of collisions, and take several years to double the size of the ATLAS and CMS datasets. When designing searches for new particles, it is essential to consider models that result in more challenging final states, and reevaluate commonly made assumptions. One of the most interesting parameters to consider is the lifetime of any new BSM particle.

A particle's lifetime is considered *prompt* if on average the distance between the particle's production and its decay position is smaller than, or comparable to, the spatial resolution of the detector. A particle is *long-lived* if the particle decays after traveling a distance significantly larger than the spatial resolution of the detector. In these cases, the decay is considered *displaced*. If the particle decay occurs

at an even longer length scale, such that it is possible to reconstruct the trajectory of the particle, or the particle escapes the detector, it is considered *meta-stable* or *stable*.

Most searches for new physics at the LHC assume that a new particle decays almost immediately, or is invisible and escapes the detector. However, there are already several particles in the Standard Model that break this assumption, and several BSM theories that predict new particles with lifetimes that can result in displaced decays.

In particular, Supersymmetry (SUSY) is an appealing extension of the Standard Model, which could result in new long-lived particles if R-parity is violated. In models which violate R-parity, the lightest SUSY particle can only decay via diagrams which violate lepton or baryon number. In the model considered by this thesis, the Supersymmetric partner of the top quark, the stop $\tilde{t}$, is the lightest SUSY particle, and decays semi-leptonically via a small lepton number violating coupling to a muon and a jet. The stop particle is long-lived due to the small R-parity coupling, and results in displaced decays inside the ATLAS detector. This model is interesting from a theory perspective because a stop with a mass close to the weak scale is crucial for SUSY to provide a solution to the hierarchy puzzle.

This thesis uses 136 fb^{-1} of pp-collisions collected by the ATLAS experiment between 2016 and 2018. Events with at least one displaced muon and at least one displaced vertex in the ATLAS Inner Detector are selected. The expected background contribution from cosmic muons, muons from heavy-flavor decays, and instrumental effects are predicted from data. Observed yields in data are in good agreement with the background prediction, and exclusion limits are set on R-parity violating decays of the Supersymmetric partner of the top quark.

Chapter 2 provides some helpful formulas for describing long-lived particles. Chapter 3 motivates

4

searches for long-lived particles at the LHC, with an emphasis on R-parity violating Supersymmetric models. An outline of the Standard Model is given, as well as a discussion of some of the benefits of Supersymmetry. This is followed by a more in-depth discussion of R-parity violation, and the simplified model considered by this thesis. Previous constraints on the model are also discussed.

Chapter 4 summarizes the LHC design and performance during Run 2, as well as how the delivered luminosity is measured. Chapter 5 provides an overview of the ATLAS detector design. Emphasis is given to the Inner Detector and Muon Spectrometer, which are of particular importance for this thesis. Chapter 6 describes the reconstruction of charged particle tracks, secondary vertices, muons, and calorimeter clusters, all of which are used in the analysis. The ATLAS trigger, which is used to select events for the analysis is described in Chapter 7. The dataset used in the analysis, as well as the simulation of R-parity violating signal events is described in Chapter 8.

Events with a displaced muon and displaced vertex are selected using a dedicated muon trigger, as well as a missing transverse energy trigger, as described in Chapter 9. The data-driven method used to predict background contributions is described in Chapter 10. Chapter 11 describes uncertainties on the number of signal events which are expected to pass the event selection.

Results are presented in Chapter 12, as well as the exclusion limits set on R-parity violating Super-symmetric scenarios. Chapter 13 provides the conclusion.

The analysis presented in this thesis is described in an abbreviated form by the ATLAS Collaboration as a conference note [1]. More detail can be found in an Internal ATLAS note [2], from which parts of this thesis are adapted.

Part II

Theory and Motivation

2

Long-lived Particle Basics

This chapter provides some helpful information and formulas related to long-lived particles. It includes a discussion of how to compute a particle's lifetime, mean decay length, and the probability for an individual particle to decay at a particular distance.

2.1 PARTICLE WIDTH AND LIFETIME

A particle's lifetime is inversely proportional to its total decay rate Γ, or *width*,

$$\tau = \frac{1}{\Gamma_{\text{Total}}}. \tag{2.1}$$

A particle's width is the probability per unit time that the particle will decay. Particles often decay

via several different channels. The *partial decay width* for a given decay mode can be thought of as the probability per unit time that a particle will decay via that particular channel. In the case a particle can decay via several modes, the particle's total width can be computed as

$$\Gamma_{\text{Total}} = \sum_{i=1}^{n} \Gamma_i.$$ (2.2)

For a given process, the partial decay width can be calculated using Fermi's golden rule [3]

$$\Gamma_i = \frac{1}{2m_X} \int d\Pi_f |\text{M}(m_X \rightarrow \{p_f\})|^2.$$ (2.3)

The mass of the particle is given by m_X, M is the *matrix element* for the particle's decay into the decay products $\{p_f\}$, and $d\Pi_f$ is the allowed Lorentz-invariant phase space for the decay. The above formulas use $\hbar = c = 1$.

The matrix element quantifies the transformation from the initial particle to its decay products, and can be computed for a given process using Feynman rules. Generally, the matrix element includes terms for the initial particle, any intermediate particles in the process, as well as the outgoing particles. Couplings which describe the strength of the interactions between particles also contribute to the matrix element.

Stable particles have infinitely narrow widths, while particles with very short lifetimes have wider widths and will appear as resonances around their nominal mass.

In the Standard Model, particles have lifetimes which span several orders of magnitudes. Figure 2.1 shows the lifetime and mass of several Standard Model particles. Shaded regions roughly indicate

which particles are considered prompt, and which are considered stable to a general purpose detector (assuming particles are moving at the speed of light, $\beta = 1$).
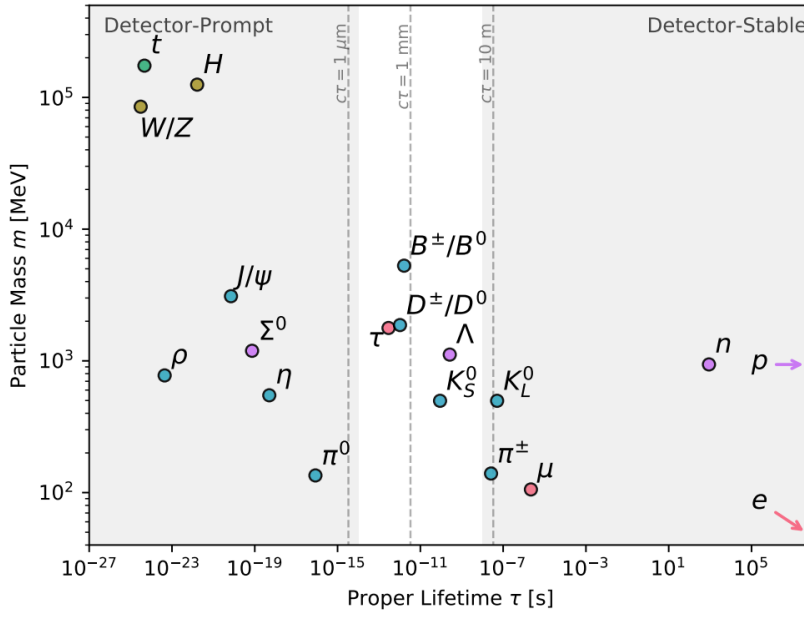
Figure 2.1: A selection of SM particles are shown as a function of their mass and proper lifetime. Shaded regions roughly represent the detector-prompt and detector-stable regions of lifetime space, for a particle with $\beta = 1$ [3].

From equations 2.3 and 2.1, a particle can obtain a long-lifetime if there is limited phase-space available for the decay or if there is a small matrix element. A decay process can have a small matrix element for a variety of reasons, including decays which involve small couplings, as well as a decay which proceeds via highly virtual intermediate particles.

2.2 Mean Decay Length

At the LHC, a particle's lifetime can be inferred by measuring the three-dimensional distance between the point at which it was produced, and the point at which it decays. This quantity is known as the decay length, ΔL. A particle's mean decay length is defined as

$$\langle \Delta L \rangle = \frac{v}{c}\gamma\tau = \beta\gamma\tau \tag{2.4}$$

where $\beta\gamma$ is the ratio of the particle's momentum to its mass $\frac{p}{m}$, and τ is the particle's lifetime in its rest frame.

Particles at the LHC are produced with a large range of momenta. Reconstructible particles have momenta which range from ≈ 1 GeV to momenta as high as ≈ 1 TeV. Table 2.1 shows the average decay length for several Standard Model particles produced at the LHC. Electrically charged and electrically neutral particles are shown separately. Particles with longer $\langle \Delta L \rangle$ are shown first.

The first group of particles look stable to a general purpose tracking detector (i.e have mean decay lengths greater than approximately 1 meter). If these stable, or meta-stable particles are are electrically charged, it is possible to reconstruct their trajectory as a track. The middle group of particles decay within the detector, a measurable distance away from the point at which they were produced. The last group of particles decay so quickly that it is only possible to detect their decay products.

In ATLAS, the decay length can be measured directly by reconstructing a displaced vertex (DV) at the position where long-lived particle decayed. Reconstructing a displaced vertex involves reconstruct-

Table 2.1: Particle lifetime, mass, and average decay length (if the particle's momentum $p = 1$ GeV and $= 100$ GeV).

Charged Particle	Lifetime [s]	$\langle \Delta L \rangle$ at 1 GeV	$\langle \Delta L \rangle$ at 100 GeV
$e^{\pm}$	∞	∞	∞
$p^{\pm}$	∞	∞	∞
$\mu^{\pm}$	$2.2 \cdot 10^{-06}$	6.2 km	620 km
$\pi^{\pm}$	$2.6 \cdot 10^{-08}$	56 m	5.6 km
$K^{\pm}$	$1.2 \cdot 10^{-08}$	7.5 m	750 m
$\Sigma^{\pm}, \Xi^{\pm}, \Omega^{\pm}$	$\sim 1.2 \cdot 10^{-10}$	~ 3 cm	~ 3 m
$D^{\pm}$	$1.0 \cdot 10^{-12}$	170 μm	17 mm
$B^{\pm}$	$1.6 \cdot 10^{-12}$	93 μm	9.3 mm
τ	$2.9 \cdot 10^{-13}$	49 μm	4.9 mm
W	$3 \cdot 10^{-25}$	$\ll$ nm	$\ll$ nm
t	$5 \cdot 10^{-25}$	$\ll$ nm	$\ll$ nm

Neutral Particle	Lifetime [s]	$\langle \Delta L \rangle$ at 1 GeV	$\langle \Delta L \rangle$ at 100 GeV
γ	∞	∞	∞
ν	∞	∞	∞
n	881	$2.8 \cdot 10^{8}$ km	$2.8 \cdot 10^{10}$ km
K_L	$5.116 \cdot 10^{-08}$	31 m	3.1 km
$\Lambda^0, \Sigma^0, \Xi^0$	$\sim 2.2 \cdot 10^{-10}$	~ 7 cm	~ 7 m
K_S	$9.0 \cdot 10^{-11}$	5.4 cm	5.4 m
B^0	$1.5 \cdot 10^{-12}$	86 μm	8.6 mm
D^0	$4.1 \cdot 10^{-13}$	65 μm	6.5 mm
π^0	$8.5 \cdot 10^{-17}$	0.19 μm	19 μm
Z	$3 \cdot 10^{-25}$	$\ll$ nm	$\ll$ nm
H	$1.56 \cdot 10^{-22}$	$\ll$ nm	$\ll$ nm

ing the trajectories of a particle's decay products. These decay products will form a vertex at the point where their trajectories intersect, which directly corresponds to the point in space where the long-lived particle decayed. The distance between the displaced vertex and the point where the long-lived particle was produced, indicated by a primary vertex (PV), is equal to the decay length.

The decay length can also be inferred by measuring the *impact parameter* of the decay products. If the decay products have electric charge, their trajectories may be reconstructed as tracks. The impact parameter of a track is then defined as the distance of closest approach of the track to the primary vertex.

Figure 2.2 shows a schematic of a long-lived particle decaying to several charged daughter particles. The primary vertex is where the long-lived particle is produced, and the displaced vertex is where the long-lived particle decays. The distance between the primary vertex and displaced vertex is the decay length, whereas the impact parameter for a single displaced track is shown.

2.3 Exponential Decay

The probability a particle survives for a time t before it decays is described by an exponential. At the LHC, particles are rarely produced at rest, and the most interesting quantity to measure is the distance traveled by the particle inside the detector before it decays. For a particle with a given $\beta\gamma$, the probability a particle survives for a distance L is given by,

$$P(L) = e^{-L/(\beta\gamma\tau)}, \qquad\qquad (2.5)$$
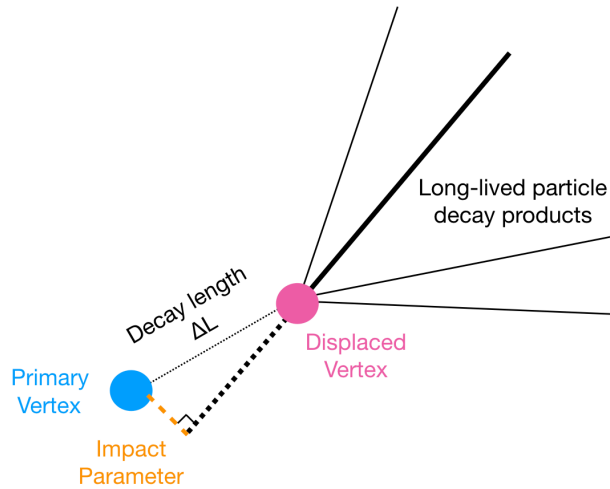
Figure 2.2: A Schematic of a long-lived particle decay is shown. The long-lived particle is produced at the primary vertex (blue), and decays at the location of a displaced vertex (pink), which can be reconstructed from the electrically charged daughter particles (solid black lines). The three dimensional decay length ΔL (dotted black line) of the long-lived particle is indicated, as well as the impact parameter (orange) of one of the daughter particles produced in the decay (thick solid black line).

Where τ is the particle's mean lifetime as measured in the particle's rest-frame.

Figure 2.3 shows some example distributions of the probability that a particle decays at a particular decay length L, for a particle with a mean proper lifetime of $\tau = 1$ ns and several possible values of $\beta\gamma$. These distributions are shown for L up to 10 m, the typical scale of a general purpose detector.

For particles with the same momentum, $\beta\gamma$ is smaller for particles with larger masses. Particles with larger $\beta\gamma$, or longer lifetimes, will have larger mean decay lengths than particles with less boost, or shorter lifetimes.

Typical LHC experiments look for evidence of a long-lived particle decay inside a single sub-detector. Because the decay position of long-lived particles are described by an exponential, the sensitivity of any search depends on the sub-detector volume and position. For detectors of a fixed volume, the sensitiv-
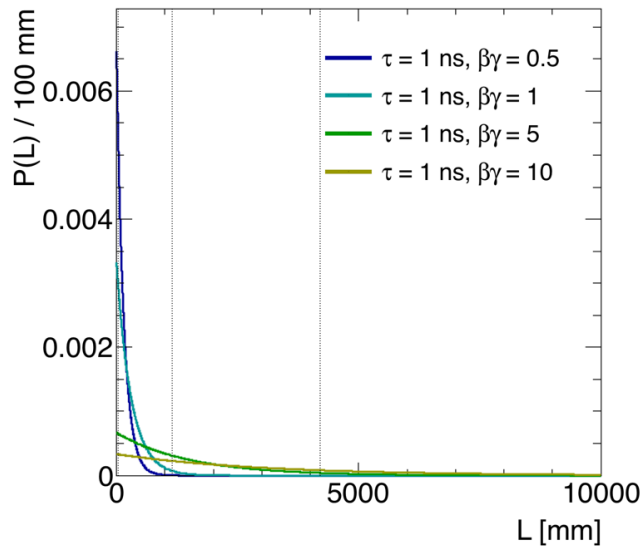
Figure 2.3: Decay length distributions for a long-lived particle with $\tau = 1$ ns. Decay length distributions are shown for several possible values of $\beta\gamma$. Vertical dotted lines indicate useful dimensions of a general purpose detector. The vertical dotted line at 1.1 m indicates the typical separation between the tracking detector and calorimeter, and the vertical dotted line at 4.2 m indicates the typical separation between the calorimeter and muon spectrometer. The figure extends to 10 m, the usual outer edge of a muon spectrometer.

ity improves as the distance to the primary vertex is decreased. For detectors with a fixed position, the

sensitivity improves as the volume is increased.

3

Theory

The Standard Model of particle physics describes the dynamics of all known particles, under three of the four known forces. Developed in the 1970s, the Standard Model has been immensely successful at predicting a wide array of phenomena, and survived many high-precision tests. However, the Standard Model is likely incomplete, especially at energies higher than those probed by current particle accelerators.

Supersymmetry is one possible extension of the Standard Model. SUSY posits a new symmetry between fermions and bosons, and may help resolve the hierarchy puzzle [4]. Supersymmetric models which violate R-parity are of particular interest to this thesis, and would result in a rich phenomenology to explore at the LHC. This section explores the theoretical motivation for R-parity violating SUSY, as well as the relevant constraints from experiments.

This section also discusses the simplified model considered by the search described in Part IV. In this model, the Supersymmetric partner of the top quark, the stop squark $\tilde{t}$, is predicted to be long-lived. The stop squark decays via a small, but non-zero, R-parity violating coupling to a muon and a hadronic jet. Such long-lived particle decays would result in a displaced vertex signature.

3.1 The Standard Model

The Standard Model of particle physics is described in the framework of quantum field theory. The dynamics of the theory are described by a Lagrangian. Each particle is represented as a field, and the construction of the theory proceeds by postulating a set of symmetries, and by writing down the most general renormalizable Lagrangian for the particle content that satisfy those symmetries.

The Standard Model must be invariant under any choice of reference frame. As a result, the Standard Model is symmetric under translations, rotations, and boosts (also known as the Poincaré symmetry). The Standard Model must also be gauge invariant. The local $SU(3) \times SU(2) \times U(1)$ gauge symmetry defines the Standard Model. Each gauge invariant symmetry is roughly responsible for one of the three forces described by the Standard Model.

Particles in the Standard Model can be divided into two categories: fermions and bosons. Fermions are particles with half-integer spin, while bosons have integer spin. Fermions consist of two types of particles, quarks and leptons, which both have spin-$\frac{1}{2}$, and obey Fermi–Dirac statistics. Particles with spin-1 are known as gauge bosons, and act as force carriers on the fermions. In the Standard Model there is only one example of a boson with spin-0, the Higgs boson. The Higgs boson provides

a mechanism that gives mass to other particles in the Standard Model. Figure 3.1 depicts all known Standard Model particles.
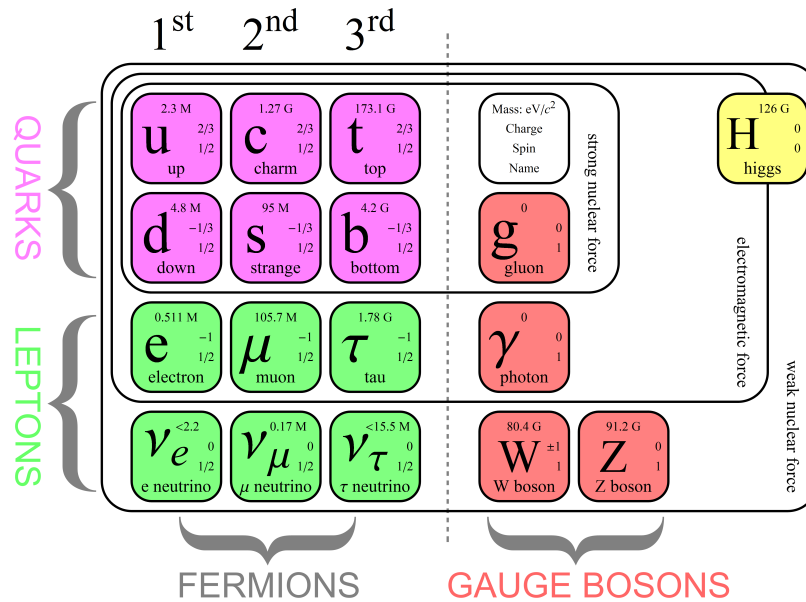
Figure 3.1: Standard Model particles [5].

This section first describes the particle content of the Standard Model, including fermions, force carrying particles, and the Higgs boson. One feature of the Standard Model which is important for this thesis is the hierarchy puzzle and its relationship to the Higgs mass. This section ends with a discussion on the conservation laws which are obeyed in the Standard Model. More information about the Standard Model can be found in References [6, 7].

3.1.1 Leptons

There are three generations of electrically charged leptons in the Standard Model: electrons (e), muons (μ), and taus (τ). These three generations are ordered by mass, and the different generations correspond to mass eigenstates. Each charged lepton has negative electromagnetic charge, and has an anti-particle with positive electromagnetic charge. Charged leptons interact under the electromagnetic and weak forces.

There are also three generations of neutral leptons, or neutrinos. For neutrinos, the flavor eigenstates do not correspond to mass eigenstates. As a result, as neutrinos propagate through space, they oscillate between flavor states. Neutrinos are not electromagnetically charged, and only interact weakly, making neutrinos notoriously difficult to detect.

3.1.2 Quarks

There are three generations of quarks, and just like the charged leptons, the generations of quarks are ordered by mass. Quarks are electrically charged and interact weakly like leptons, but they also interact under the strong force.

The three generations of quarks come in pairs of *up*-type and *down*-type quarks. Up-type quarks have electric charge $+\frac{2}{3}q_e$, and down-type quarks have electric charge $-\frac{1}{3}q_e$, where q_e is the charge of an electron. There are six flavors of quarks: up, down, strange, charm, bottom, and top. Quarks also have color charge, which means that they interact via the strong force. Individual quarks have color charge of red, green, or blue, and anti-quarks can be anti-red, anti-green, or anti-blue.

Bare quarks are not observed in nature due to *color-confinement*, which is discussed more in Section 3.1.3. As a result of color-confinement, stable Standard Model particles must not have color charge. In nature, quarks form color-neutral composite particles, known as *hadrons*. States which consist of two quarks are referred to as *mesons*, and states with three quarks are referred to as *baryons*. Mesons consist of a quark and an anti-quark with opposite color charges. Baryons consist of three quarks with different color charges forming a neutral color state.

3.1.3   GAUGE BOSONS AND FORCES

Forces in the Standard Model are mediated by bosons with spin-1. Force mediators act on fermions which are charged under the corresponding force's quantum numbers. Forces are generated by requiring the Standard Model Lagrangian be invariant under various local gauge transformations, or symmetries.

The total symmetry group of the Standard Model is

$$SU_C(3) \times SU_L(2) \times U_Y(1), \tag{3.1}$$

where C stands for color, the charge of the strong force, L stands for left, because the weak force is left-handed, and Y stands for *hypercharge*, the quantum number or charge of the electroweak force. Electromagnetism and the weak force are two low-energy manifestations of the more fundamental electroweak force. The process of electroweak symmetry breaking describes how the the electroweak forces is spontaneously broken into the separate electromagnetic and weak forces.

The electromagnetic force is mediated by the photon (γ), and affects particles with electric charge. The electromagnetic force is described by Quantum Electro-Dynamics (QED). Because the photon is massless the electromagnetic force is long-range.

The electroweak bosons, the $W^\pm$ and Z bosons, mediate the weak force, which affect all fermions. The W boson interacts with left-handed particles (which have spin oriented opposite to their direction of motion) and right-handed anti-particles. The Z boson interacts with both left-handed and right-handed particles. The W boson has a mass of 80.4 GeV and the Z boson has a mass of 90.2 GeV, making the weak force short-range. Because W bosons carry electric charge, they couple to the photon.

The strong force arises from the $SU_C(3)$ symmetry, and is described by Quantum Chromodynamics (QCD). Gluons (g), which are massless like the photon, mediate the strong force, The strong force affects quarks which carry color charge. Gluons also have color charge, and which means that they couple to one another. Gluons are a combination of one color and an anti-color (eg. red–antiblue), resulting in an eightfold multiplicity of gluons. As a result of gluon color charge, the strength of the color force, or the strong coupling constant, increases with increasing distance.

The strong coupling constant α_s evolves as a function of energy, or scale μ, as

$$\alpha_s(\mu) = \frac{12\pi}{(32 - 2n_f)\ln\frac{\mu^2}{\Lambda_{\text{QCD}}^2}}, \tag{3.2}$$

where n_f is the number of active quarks at the scale μ, and Λ_{QCD} is an experimentally determined cutoff scale (usually ≈ 0.2 GeV).

The evolution of the strong coupling constant results in two key features

20

- Color-confinement: Stable particles must have neutral color charge because the coupling constant increases with distance. Consider a quark–antiquark pair in a meson. As the separation between the two quarks is increased, increasing amounts of energy are required to continue to separate the two quarks. Eventually, it is more energetically favorable to produce a second quark-antiquark pair than to continue to separate the original quarks. The initial hadron then becomes two hadrons with neutral color charge, instead of producing two particles with color charge.

- Asymptotic freedom: The coupling constant of the strong force also decreases at very small distances. Inside a hadron, quarks approach a state where they can move without resistance from the strong force.

At high energies, when the coupling constant is small, perturbation theory can be used to make QCD predictions. However, as the coupling coupling becomes larger processes are non-perturbative. The energy which separates the two regimes is referred to as Λ_{QCD}. When calculating a cross section for a LHC process, the calculation is separated into its perturbative and non-perturbative processes. For example, the production of high energy quarks and gluons is described by perturbative QCD. However the process by which quarks and gluon form colorless composite particles, *hadronization*, is non-perturbative.

At the LHC, when high energy quarks and gluons are produced in collisions, they radiate additional colored particles in a process called *fragmentation* or *parton showering*. This process continues until particles' energies reach $\approx$ 1 GeV. The resulting spray of particles then hadronize to form colorless composite particles. This resulting spray of particles is called a *jet*. ATLAS detects jets rather than individual quarks and gluons.

3.1.4 Higgs boson

The Higgs boson is unique in that it is the only spin-0 particle in the Standard Model. The Higgs boson gives mass to all fundamental particles besides the photon and gluon (and possibly neutrinos). The charged leptons and quarks obtain mass through Yukawa couplings to the Higgs. The W and Z bosons obtain mass through the process of electroweak symmetry breaking.

The Higgs boson mass is a free parameter in the Standard model, which means that there aren't any symmetries or dynamics in the Standard Model that lead to a particular mass. Presumably, gravity provides a fundamental mass scale, the Planck scale $M_P \sim 10^{19}$, though the details of gravity are not understood. However, the Higgs boson mass has been experimentally measured to be 124.97 ± 0.24 GeV [8]. The large ratio of the gravitational scale to the observed Higgs mass is referred to as the *hierarchy puzzle*.

The hierarchy puzzle strongly suggests that there is a new physics which is not far beyond the weak scale. The puzzle of the Higgs mass is interesting for collider experiments at the TeV scale. If Supersymmetry is relevant to the hierarchy puzzle, new particles should be within reach of these experiments.

3.1.5 Conservation Laws

In the Standard Model, all particles will decay to lighter particles, unless the decay is prohibited by a conservation law. A more detailed discussion of Standard Model conservation laws and tests of these laws can be found in Reference [9].

Every symmetry observed in the Standard Model corresponds to a conservation law. Conservation

laws which are a result of a symmetry are absolute, and include the following:

- Translations in time $\rightarrow$ conservation of energy

- Translations in space $\rightarrow$ conservation of momentum

- Rotations in space $\rightarrow$ conservation of angular momentum

- Lorentz invariance $\rightarrow$ conservation of combined charge conjugation, parity, and time reversal (CPT)

There are also some quantum numbers that are conserved in all Standard model processes observed so far. These quantum numbers include baryon number, B, and lepton number L. However, there are reasons to believe that these interactions are not governed by exact conservation laws.

Lepton number is defined as the number of leptons minus number of anti-leptons. At high energies where neutrino masses are irrelevant, this rule can also be applied to each flavor of lepton. As a consequence, the electron, the lightest charged lepton is stable. Second and third generation charged leptons decay via the weak force to lighter leptons. For example, the muon decays via a W boson to an electron and two neutrinos, conserving lepton number

$$\mu^+ \rightarrow e^+ + \nu_e^+ + \bar{\nu}_\mu. \tag{3.3}$$

In contrast, neutrinoless double-beta decay, and decays such as $\mu^- \rightarrow e^- + \gamma$ are prohibited by lepton number conservation.

Baryon number is equivalent to assigning a quark $B = \frac{1}{3}$. Consequently, baryons have $B = 1$, anti-baryons have $B = -1$, and mesons have $B = 0$. As a result, the lightest SM baryon, the proton is

stable. However, other baryons are allowed to decay. For example, the neutron can decay to a proton, electron, and electron neutrino

$$n \rightarrow p^+ + e^- + \bar{\nu}_e. \qquad (3.4)$$

3.2   SUPERSYMMETRY

Supersymmetry is an extension of the Standard Model first posited in the 1970s. In addition to the normal symmetries of special relativity (translations, rotations, and boosts), SUSY adds another symmetry between fermions and bosons. This new symmetry changes a particle's spin by $\frac{1}{2}$, turning fermions into bosons, and bosons into fermions.

Building a theory with this new symmetry implies the existence of new particles, and Supersymmetry roughly doubles the particle content of the Standard Model. Supersymmetric partners of Standard Model particles are referred to as *superpartners*. The superpartners of fermions are called *sfermions*, and their names are constructed by adding an *s*, for scalar, to the beginning of the name of the Standard Model particle. For example, the *selectron* is the superpartner of the electron. The superpartners of Standard Model bosons all have names which end with *-ino*. For example, the superpartner of the gluon is the *gluino*. A Standard Model particle and its superpartner form a *supermultiplet*.

Superpartners have the same quantum numbers as their SM partners, except for spin. From experiment, it is clear that if Supersymmetry exists, it is a broken symmetry. Superpartners with the same mass as their Standard Model partners, i.e. a selectron with the same mass as an electron, would have

been observed a long time ago. If Supersymmetry exists, superpartners are likely to have higher masses than their SM partners. Often, SUSY-breaking terms are added to the Lagrangian of Supersymmetric models, but the mechanism by which SUSY is broken is left unspecified.

This section discusses the particle content and interactions of the Minimal Supersymmetric Standard Model (MSSM), the simplest self-consistent Supersymmetric extension of the Standard Model. It also defines R-parity, and discusses likely mass spectra of superpartners. A more detailed discussion of Supersymmetry can be found in Reference [4].

3.2.1 PARTICLE CONTENT

The Minimal Supersymmetric Model is the simplest self-consistent Supersymmetric extension of the Standard Model. In the MSSM all Standard Model particles receive a superpartner. The only exception to this rule is the Higgs boson. There must be two Higgs supermultiplets in order for all Standard Model fermions and their superpartners to receive non-zero Yukawa couplings. The particle content of the MSSM is described below.

In the MSSM, each Standard Model charged fermion gets two spin-0 partners. *Sleptons* are superpartners of leptons, and are denoted by $\tilde{l}$. Superpartners of the left-handed and right-handed parts of the leptons are called left- and right-handed sleptons, and are denoted $\tilde{l}_L$ and $\tilde{l}_R$. These left-handed and right-handed sleptons mix to form two mass eigenstates $\tilde{l}_1$ and $\tilde{l}_2$, where $\tilde{l}_1$ is the lighter mass eigenstate. *Squarks* are the superpartners of quarks, and they are denoted by $\tilde{q}_R$ and $\tilde{q}_L$. Squarks also mix to form two mass eigenstates $\tilde{q}_1$ and $\tilde{q}_2$, where $\tilde{q}_1$ is lighter. Each left-handed neutrino, ν_L is associated with a single spin-0 *sneutrino*, denoted by $\tilde{\nu}_L$.

The Higgs sector of the MSSM contains two Higgs doublets. One doublet couples to up-type quarks and the other doublet couples to down-type quarks and charged leptons. After electroweak symmetry breaking, there are five Standard Model Higgs bosons: A, H, H^+, H^-, and h. The lightest neutral Higgs boson h, is usually assumed to be the Higgs boson which was discovered at the LHC. The potentially undiscovered Higgs bosons include the CP-even H, which is usually taken to be heavier than h, the CP-odd A, and the scalar charged states $H^\pm$.

The supersymmetric partners of the Higgs doublets are referred to as *higgsinos*. The higgsinos mix with the superpartners of the electroweak gauge bosons, the electroweakinos, resulting in mass eigenstates referred to as neutralinos and charginos. Neutralinos are electrically neutral while charginos are electrically charged. The MSSM contains four neutralinos, $\tilde{\chi}_1^0$, $\tilde{\chi}_2^0$, $\tilde{\chi}_3^0$, $\tilde{\chi}_4^0$ ordered by mass, and two charginos, $\tilde{\chi}_1^\pm$ and $\tilde{\chi}_2^\pm$, also ordered by mass.

The particle content of the MSSM is summarized in Table 3.1. Note that mixing between electroweak gauginos is ignored for simplicity.

Table 3.1: Minimal Supersymmetric Standard Model particle content. Mixing between electroweak gauginos is ignored for simplicity.

Spin-1	Spin-1/2	Spin-0
gluons g	gluinos $\tilde{g}$	
photons γ	photino $\tilde{\gamma}$	
$W^\pm$	Winos $\tilde{W}_{1,2}^\pm$	$H^\pm$
Z	Zinos $\tilde{Z}_{1,2}$	H
	higgsino $\tilde{h}^0$	h^0, A
	leptons l	sleptons $\tilde{l}$
	quarks q	squarks $\tilde{q}$

3.2.2 Interactions

The MSSM adds many new possible interactions between Standard Model particles and SUSY particles, most of which are not relevant for this thesis. A general rule is that any Standard Model vertex can have two interacting particles replaced with their superpartners. At colliders, the interactions which are most interesting for the production and decay of superpartners involve couplings of Standard Model gauge bosons to MSSM particles, and the couplings of MSSM gauginos to (scalar, fermion) pairs.

Interactions of the MSSM gauginos are shown in Figure 3.2. Gauginos couple to (squark, quark), (slepton, lepton), and (Higgs, higgsino) pairs. Note that as one might expect, winos only couple to left-handed squarks and sleptons, and that the gluino does not couple to (lepton, slepton) and (Higgs, higgsino) pairs.
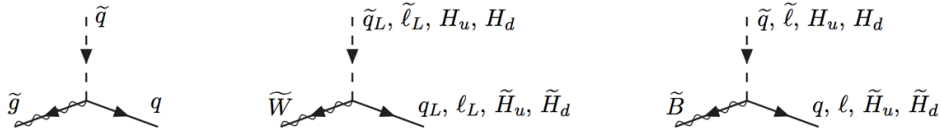
Figure 3.2: MSSM gaugino couplings to (scalar, fermion) pairs [4].

In addition to these interactions, there are several terms that could appear in the MSSM Lagrangian that violate baryon number, B, and lepton number, L. These terms are

27

$$W_{\Delta L, B=1} = \frac{1}{2}\lambda_{ijk}L_iL_jE_k^c + \lambda'_{ijk}L_iQ_jD_k^c + \frac{1}{2}\lambda''_{ijk}U_i^cD_j^cD_k^c + \mu_iH_uL_i. \qquad (3.5)$$

The symbols i,j,k are generational indices, and a summation over generational indices and gauge indices is implied. Lepton and charged lepton supermultiplets are given by L and E. Similarly, Q, U, and D represent quark, up-type quark, and down-type quark supermultiplets. The Higgs multiplet is denoted by H. Terms with λ, λ' and μ couplings violate lepton number, while the λ'' term violates baryon number.

Baryon number and lepton number are both conserved in Standard Model interactions, apart from small non-perturbative effects [10, 11]. Often, these couplings are excluded from the MSSM in order to preserve these conservations laws. Rather than simply setting these couplings to zero, a new $U(1)$ symmetry is imposed in order to obtain a conserved quantity, R-parity. R-parity is defined as

$$R\text{-parity} = (-1)^{2s}(-1)^{3B+L}. \qquad (3.6)$$

Where s is spin, B is baryon number, L is lepton number. All Standard Model particles have R-parity $= +1$, whether fundamental or composite. This is trivial to see because any Standard Model particles with lepton or baryon number have spin-$\frac{1}{2}$, and all Standard Model bosons have B, $L = 0$. In contrast, supersymmetric particles have R-parity $= -1$. The conservation of R-parity results in a conservation of the number of SUSY particles minus the number of anti-SUSY particles.

There are several important consequences of R-parity conservation. The first consequence is that the Lightest Supersymmetric Particle (LSP) is stable. If the LSP is electrically neutral it is a candidate

for dark matter. The second consequence is that a SUSY particle must always decay to an odd number of other SUSY particles. Eventually the SUSY particle must decay to an odd number of LSPs, though usually the final state will just contain a single LSP. Finally, at colliders, SUSY particles are always produced in pairs.

Figure 3.3 shows the production cross sections for a variety of SUSY particles at the LHC, assuming R-parity is conserved. Strongly interacting particles have higher production cross sections than particles that are color-neutral. Gluinos have the highest cross sections, followed by squarks, electroweakinos, and sleptons. Cross sections also rapidly decrease with particle mass. Depending on their mass, some SUSY particles may be accessible at the LHC, while others may not be accessible.
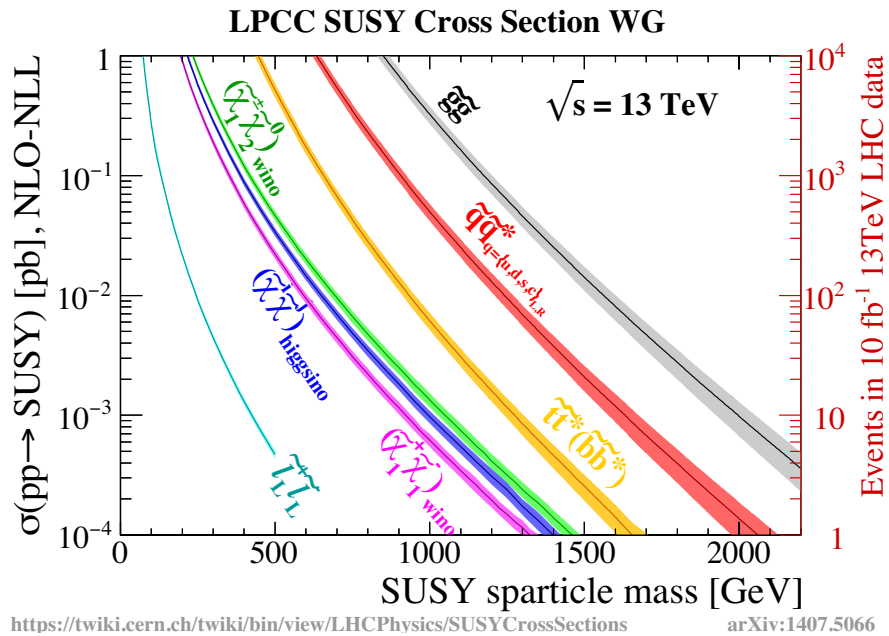
Figure 3.3: MSSM production cross sections at $\sqrt{s} = 13$ TeV, shown as a function of SUSY particle mass. In some cases, the gluino, sbottom, and stops are decoupled from the rest of the particle spectrum [12].

In contrast, when R-parity is not conserved, the lightest SUSY particle is not stable, and can decay to Standard Model particles. R-parity violation results in a rich phenomenology, which can include long-lived particles. The consequences of R-parity violating Supersymmetry are discussed in more detail in Section 3.3.

3.2.3   Mass spectra

As mentioned above, Supersymmetry is not an exact symmetry. SUSY must be a broken symmetry in order to explain why SUSY particles do not have the same masses as their Standard Model partners. There are several proposed mechanisms for Supersymmetry-breaking, and these mechanisms can inform predictions about particle mass spectra. Other common features of SUSY models are driven by phenomenological constraints, or to provide solutions to unexplained phenomena such as dark matter. Some common features of MSSM particle mass spectra are described below, and extra attention is given to scenarios which could result in long-lived particle signatures.

The most common assumption in SUSY models considered at the LHC is that the lightest neutralino is the lightest SUSY particle. In these models, the lightest neutralino only interacts with other particles via weak and gravitational interactions, making an attractive dark matter candidate. There are a variety of predictions about the mixings of electroweak gauginos that make up the lightest neutralino.

One of the more interesting scenarios occurs in anomaly-mediated Supersymmetry breaking (AMSB) models [13]. The mass spectra of gauginos are constrained such that the LSP, the lightest neutralino, is the mostly wino, and the lightest chargino is only slightly heavier. This small mass difference between

the lightest neutralino and lightest chargino, is predicted to be approximately 160 MeV. The chargino would have a lifetime on the order of picoseconds to nanoseconds, resulting in a disappearing track signature at the LHC.

There are two exceptions to the assumption that the lightest neutralino is the LSP. The first exception, is that if R-parity is violated, the LSP is no longer stable and would not make a good candidate for dark matter. If this is the case, the LSP need not be electromagnetically-neutral or color-neutral. The second scenario occurs in Gauge Mediated Supersymmetry Breaking (GMSB) models [14]. In these models the Supersymmetric partner of the graviton, the gravitino, is the LSP. The next-to-lightest SUSY particle has a small coupling to the gravitino, and the coupling strength is set by the scale of SUSY breaking. These small couplings could make the next-to-lightest SUSY particle long-lived, and depending on the scale of SUSY breaking, the gravitino could make an attractive dark matter candidate.

In general, the gluino will be much heavier than the lighter neutralinos and charginos. Regardless of the SUSY breaking mechanism, the gluino's mass is expected to be larger than other SUSY particles because of the quantum corrections it receives from other particles. The gluino is strongly interacting, a color octet, and couples to all squark-quark pairs. As a result, the gluino receives more quantum corrections than other SUSY particles, especially the electroweakinos.

Another common feature of SUSY models is that the first and second generation squarks are nearly mass degenerate, and heavier than sleptons. Again, this feature is due to radiative corrections to the squark masses. The lightest stop and sbottom are likely to be the lightest squarks. This feature is useful from a phenomenological perspective. In order to provide a solution to the hierarchy puzzle, the stop

mass must be on the order of 1 TeV.

There are other models which do not follow the general prescriptions listed above. For example, the gluino could be kinematically accessible at the LHC, while the squarks have masses that are several orders of magnitude larger than the gluino. These models are referred to as Split SUSY models [15, 16], and would result in gluinos which have long-lifetimes because their decays proceed via highly virtual squarks. Split-SUSY models could evade several experimental constraints, but would not provide an attractive solution to the hierarchy puzzle.

3.3 R-parity Violation

This section provides further discussion on R-parity violation, with a particular emphasis on the R-parity violating couplings presented in equation 3.5. More information regarding R-parity violating Supersymmetry can be found in these review articles [17, 18].

Altogether, there are 3 bilinear (μ_i) couplings, and 45 trilinear (λ) couplings. The trilinear couplings are the focus of this thesis. Figure 3.4 shows some basic tree-level diagrams associated with these couplings. The λ and λ' interactions violate lepton number, while λ'' interactions violate baryon number. Sometimes the λ_{ijk}, λ'_{ijk} and λ''_{ijk} couplings are referred to as the LLE, LQD, and UDD couplings, respectively, because of how the generational indices refer to the associated supermultiplets. For example, a non-zero λ'_{231} coupling couples a second generation lepton supermultiplet to a third generation quark supermultiplet and a first generation down quark supermultiplet. This coupling would allow a stop squark to decay to a muon and a down quark.
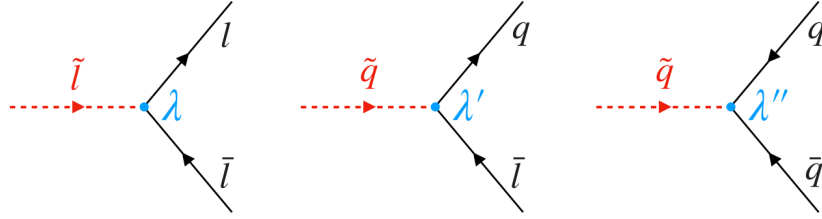
Figure 3.4: Some basic tree-level diagrams associated with trilinear R-parity violating couplings. λ and λ' interactions violate lepton number, while λ'' interactions violate baryon number. SUSY particles are indicated with tildes, and arrows indicate the flow of lepton or baryon number.

Due to gauge invariance, there is antisymmetry of the λ_{ijk} couplings with respect to the first two generational indices,

$$\lambda_{ijk} = -\lambda_{jik}, \tag{3.7}$$

and of λ''_{ijk} with respect to the second two generational indices

$$\lambda''_{ijk} = -\lambda''_{ikj}. \tag{3.8}$$

This results in 9 λ_{ijk} and 27 λ'_{ijk} couplings which violate lepton number, and 9 λ''_{ijk} couplings which violate baryon number.

The strength of these couplings is not usually predicted by SUSY models, and constraints must be obtained from experiment. At colliders, searches are usually interpreted in terms of a model with a particular lightest SUSY particle, and consider a single non-zero R-parity violating coupling. The LSP

can then decay via this R-parity coupling to Standard Model particles. Depending on the strength of these couplings, the lifetime of the lightest SUSY particle could be meta-stable, long-lived, or prompt. The simplified model considered by this thesis is discussed in the next section.

3.4 Simplified Model

Complete Supersymmetry models are incredibly complex, and depend on a large number of parameters. The MSSM, with R-parity conservation, has 120 free parameters that determine the masses and interactions of SUSY particles. The picture becomes even more complicated when allowing for R-parity violation. For searches at the LHC, which target particular signatures and only consider a few particles, many of these parameters aren't relevant. Instead it makes sense to focus on a subset of new particles, and the interactions between them, in a *simplified model*.

Simplified models are defined by an effective Lagrangian which describes the interactions of a small number of particles. Usually a simplified model focuses on a single Feynman diagram, which describes the production of SUSY particles and their subsequent decays. By using a simplified model instead of the full theory, it is easy to tune the masses of the particles considered, as well as their branching ratios or lifetimes.

This thesis considers the simplified model shown in Figure 3.5. This model begins with the production of a stop ($\tilde{t}$) and its antiparticle (also $\tilde{t}$). In this model, the stop is the lightest SUSY particle, and the only way it can decay is via R-parity violating couplings to Standard Model particles. This model targets nonzero values of the λ'_{23k} coupling. All other R-parity violating couplings are assumed to be

exactly zero. As a result, the stop decays via the λ'_{23k} coupling into a muon and a quark (of generation k) with a 100% branching ratio.
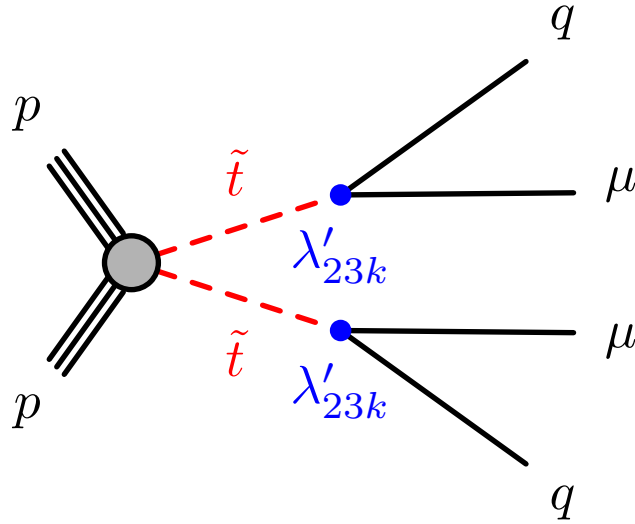
Figure 3.5: Diagram showing production of a stop and its antiparticle (both denoted by $\tilde{t}$). The stop decays into a muon and a quark via the R-parity violating coupling λ'_{23k}. If λ'_{23k} is sufficiently small, the $\tilde{t}$ will obtain a lifetime long enough to result in displaced decays at the LHC.

There are several experimental constraints on the strength of λ'_{ijk} couplings, especially for light-flavors. These constraints include measurements of the Cabibbo–Kobayashi–Maskawa matrix, constraints on neutrinoless double-beta decay, and B-physics results, as described in Section 3.5. Many of these constraints imply that any non-zero λ' coupling must be small. Because the stop particle must decay via a small λ'_{23k}, this could result in stop particle with a long-lifetime. In this model, the lifetime of the stop depends on the size of the λ' coupling as follows [19]

$$\tau(\tilde{t}) \quad = \quad \frac{16\pi}{m(\tilde{t}) \left[\lambda'_{23k} \cos\theta_t\right]^2} \tag{3.9}$$

$$\approx \quad \left(\frac{1 \text{ TeV}}{m(\tilde{t})}\right) \left(\frac{10^{-7}}{\lambda'_{23k}}\right)^2 \left(\frac{0.06}{\cos^2\theta_t}\right) \times 10^{-3} \text{ ns}, \tag{3.10}$$

where θ_t is the mixing angle between the left- and right-handed stops ($\tilde{t}_R$ and $\tilde{t}_L$). In this thesis, it is assumed that the analysis is only sensitive to $\tilde{t}_1$, the lighter stop mass eigenstate.

Depending on the size of the λ'_{23k}, there are three distinct scenarios to consider at the LHC. Because stop squarks are produced by strong interactions through quark–antiquark ($q\bar{q}$) annihilation or gluon–gluon fusion, the cross section of stop-quark pair production is largely decoupled from the choice of SUSY parameters. However, the lifetime of the stop will increase as the size of λ'_{23k} decreases.

1. For couplings larger than approximately 10^{-8}, the stop particle will decay promptly. This signature could be targeted by searching for prompt leptons and jets.

2. As the λ'_{23k} decreases in size, the stop particles obtain longer lifetimes, and stop particles begin to decay inside the detector. If these decays occur in the tracking detector it will be possible to reconstruct displaced vertices, displaced muons, and displaced jets.

3. The λ'_{23k} coupling is less than approximately 10^{-10}, and results in a stop particle which looks stable to a general purpose detector. It is unlikely that the stop would be truly stable because of phenomenological constraints. Because the stop has color charge, if the stop were truly stable it would form heavy isotopes which have not been observed. The stop would decay as shown in Figure 3.5, but the decay would nearly always occur outside the detector. This signature could be targeted in a number of ways, and some of these strategies are discussed in following sections.

It is important to note that the stop particle carries color charge. If the stop's lifetime is longer than the hadronization timescale of QCD, the stop particle will hadronize with Standard Model particles,

forming a color-neutral state known as an R-hadron. Stop R-hadrons can form meson-like or baryon-like states, and may have non-zero electric charge. R-hadrons can interact with the ATLAS detector, even changing electric charge. If the stop particle is electrically charged and has a sufficiently long decay length (longer than ~ 1 m), it may be possible to directly detect the stop particle. For shorter decay lengths the stop can only be detected indirectly from its decay products.

This simplified model is very different from those used in vast majority of searches for stop particles at the LHC. Most searches for the stop assume that R-parity is conserved, and that the LSP is the lightest neutralino. Regardless of their differences, both types of models would provide a solution to the hierarchy puzzle.

There are several other proposed BSM scenarios that could result in long-lived particle decays to at least one muon and a hadronic jet. These scenarios include long-lived lepto-quarks [20], long-lived BSM particles appearing in decays of Higgs bosons [21, 22], scenarios with right-handed neutrinos with Majorana masses below the electroweak scale [23] and R-parity violating scenarios with a long-lived electroweakino LSP decaying via a virtual smuon and a λ'_{2jk} coupling [24].

3.5 Previous Constraints

This section discusses constraints on R-parity violating λ' couplings, with an emphasis on constraints which are most relevant for the simplified model introduced in Section 3.4.

Many constraints on R-parity violating couplings can be obtained from low-energy measurements, phenomenological observations, and high-energy precision measurements. This section discusses constraints on λ' couplings obtained from experiments other than those located at the LHC. Many of these constraints are not applicable to a single non-zero R-parity coupling, but are applied to the product of two non-zero couplings. The most stringent constraint on the coupling relevant for this analysis, λ'_{23k}, comes from measurements of the Z boson partial width at the Large Electron–Positron Collider (LEP).

Rapid proton decay is one of the most cited concerns regarding models which violate R-parity. If both lepton number and baryon number couplings are unsuppressed, the proton would have a dangerously short lifetime. Figure 3.6 shows an example of a tree-level Feynman diagram for proton decay via R-parity violating couplings. In this diagram, two quarks from the proton produce a virtual strange squark, via a λ'' coupling which violates baryon number. The virtual squark then decays to a lepton and an up-type quark via a λ' coupling, which violates lepton number. The quark hadronizes with the proton's other up-type quark to form a pion.

For this particular decay mode, the proton partial width can be approximated as [4]

$$\Gamma_{p^+ \to e^+ \pi^0} \sim m_{\text{proton}}^5 \sum_{i=2,3} |\lambda'_{11i} \lambda''_{11i}|^2 / m_{\tilde{d}_i}^4, \tag{3.11}$$

where m_{proton} is the mass of the proton, and $m_{\tilde{d}_i}$ is the mass of the virtual squark. For a virtual
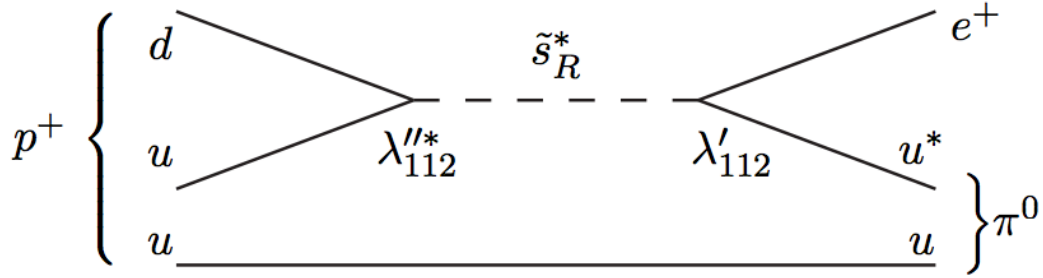
Figure 3.6: Example proton decay, $p^+ \to e^+ + \pi^0$, mediated by a virtual strange squark and R-parity violating couplings. Lepton number is violated by $\Delta L = 1$ and baryon number by $\Delta B = 1$ [4].

squark mass of 1 TeV, and R-parity violating couplings which are of order unity, the proton lifetime would be $\approx 10^{-13}$ seconds. This prediction is in stark contrast to observation. The most stringent limits on the proton lifetime is greater than 10^{34} years, set by Super-Kamiokande [25].

Of course there are other diagrams, and other combinations of R-parity violating couplings, which could lead to proton decay. Final states generally include one lepton and one hadron, where the lepton may be an electron, muon, or neutrino, and hadrons are usually kaons and pions. The dominant final state depends on which components of λ' and λ'' are largest.

From equation 3.11, it is clear that constraints from the lifetime of the proton are applied to the combination of λ' and λ'', and not to the individual couplings. The most stringent constraints are applied to $|\lambda'_{imk}\lambda''_{11k}|$, where $i = 1, 2, 3$ and $m = 1, 2$, because these couplings can result in proton decay at tree-level. The index k can be any down-type squark. Other flavor indices will lead to proton decay, but at the one-loop level, resulting in weaker constraints.

For a 1 TeV squark, conservative bounds from the proton lifetime exclude $\lambda' \cdot \lambda'' > 10^{-11}$ [26]. This exclusion includes couplings which involve third generation up-type quarks, such as the simplified model considered in this thesis. Note however, that the simplified model used in this analysis assumes any baryon number violating couplings are zero, which means that the individual limit on λ'_{23k} from proton decay is negligible.

There are a variety of other constraints which can be applied to λ' couplings. Many of these constraints come from measurements of the Cabibbo-Kobayashi-Maskawa matrix, B-physics measurements, and neutrinoless double-beta decay. These processes often require two non-zero R-parity couplings, and also set exclusions on the product of the relevant couplings.

One phenomenological concern related to non-zero λ' couplings is that lepton number violation is deeply tied to baryogenesis. Certain values of non-zero R-parity couplings could produce exactly the right amount of lepton number violation for baryogenesis, but other values could easily erase correct amount. Most constraints on λ' from baryogenesis use models which assume the lightest SUSY particle is a neutralino. These constraints cannot be directly applied to the simplified model considered in this analysis, which considers a stop as the LSP.

Another concern for the simplified model considered by this thesis, is that if the lightest SUSY particle has color charge and a very long-lifetime, it could form new hadrons (eg. $(\tilde{t}ud)^+$ or $(\tilde{t}dd)^0$). This would result in heavy isotopes of hydrogen, which have not been observed. This lack of observation means that if the stop is the LSP it cannot be stable. Because this thesis is most concerned with stop particles which have decay lengths of the scale of the ATLAS detector, an LSP with color charge would not produce the unobserved stable heavy isotopes.

R-parity violating λ' couplings can also lead to $Zf\bar{f}$ vertex corrections. These corrections affect the Z boson partial width for decays to leptons. The dominant Feynman diagrams which contribute to the $\Gamma_{Z\to\mu\bar{\mu}}$ partial width are shown in Figure 3.7.
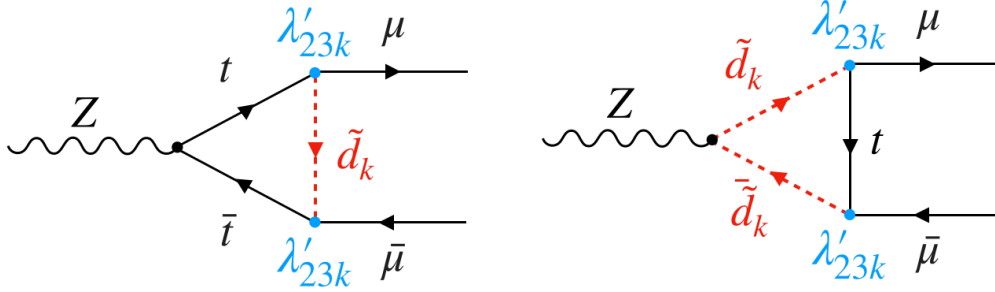
Figure 3.7: R-parity violating contributions to the leptonic Z decay width.

For the coupling considered by this analysis, λ'_{23k}. the strongest constraints come from partial width measurements of the Z boson at LEP, which exclude $\lambda'_{23k} > 0.45$, assuming the existence of a squark of mass 100 GeV. This constraint is obtained from a fit to about 200 measurements from four LEP experiments. Measurements include the cross sections of $Z \to q\bar{q}$, cross sections of $Z \to l\bar{l}$, as well as leptonic forward-backward asymmetries at different center-of-mass energies.

3.5.2 Constraints from Large Hadron Collider searches

The ATLAS and CMS collaborations have performed several searches for a stop squark which decays via R-parity violating couplings. These results are summarized in Figure 3.8. This section focuses on searches which target $\tilde{t} \to \mu + j$ decays.

41
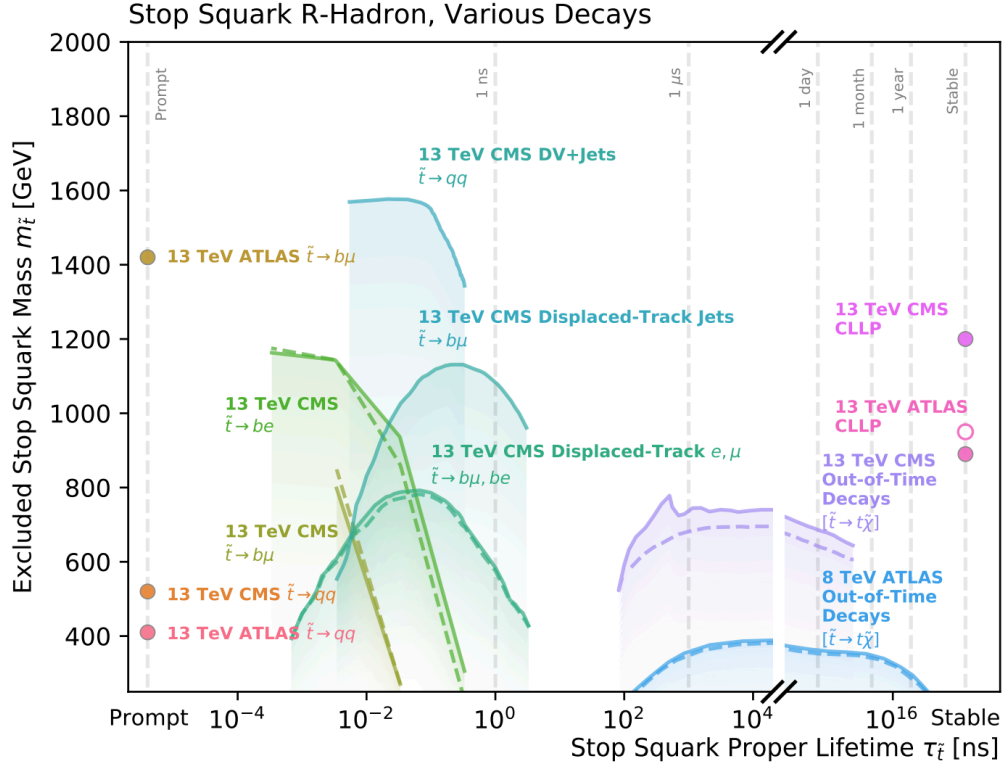
Figure 3.8: Limits on a long-lived stop squark decaying via R-parity violating couplings, as a function of the stop mass v. lifetime. When available, dashed lines and open circles denote the expected limits while solid lines and closed circles represent the observed limits. Labels indicate the long-lived particle signatures considered by each search. If no long-lived particle signature is listed, the search assumes the stop particle decays promptly [3] .

In the prompt lifetime regime, both the the ATLAS and CMS collaborations perform searches for prompt decays of the stop via λ'_{ijk} couplings [27, 28]. ATLAS sets the most stringent limits with a search that excludes stops with masses below 1.4 TeV, using 36 fb^{-1} of $\sqrt{s} = 13$ TeV data. The equivalent CMS search for prompt stop decays was reinterpreted in terms of long-lived scenarios, and excludes stops with masses below approximately 500 GeV, with lifetime $\tau(\tilde{t}) = 10^{-2}$ ns. The sensitivity of prompt searches to long-lived stop decays decreases as a function of stop lifetime, because

prompt searches apply impact parameter requirements to leptons, in order to ensure the lepton was produced at the primary vertex.

There are two CMS searches which place exclusion limits on long-lived stop squarks decaying to a muon and a hadronic jet. The first search selects events with displaced jets, by selecting jets with tracks that have large impact parameters, or jets that have no tracks at all. Figure 3.8 shows limits from a version of this search that uses 2.6 fb^{-1} of $\sqrt{s} = 13$ TeV of pp-collisions collected by the CMS experiment. CMS has since updated this search with 36 fb^{-1} of data. Updated exclusion limits are shown in Figure 3.9, and stop masses below 1.4 TeV have been excluded for a stop mean proper lifetime of 0.1 ns [29–31].

The second search from the CMS experiment targets long-lived $\tilde{t} \rightarrow b + l$ decays by selecting events with displaced leptons. This search selects events with an electron and a muon that both have transverse impact parameter values between 200 μm and 10 cm. These displaced leptons are not required to be associated to any displaced vertex, and no hadronic activity is required in the event selection. For simplicity, this search assumes lepton universality in the stop squark decay vertex, so that the branching fraction to any lepton flavor is equal to one third. This result uses 2.6 fb^{-1} of pp-collisions at $\sqrt{s} = 13$ TeV. For a stop squark with a mean proper decay length of $c\tau(\tilde{t}) = 2$ cm, masses below 870 GeV are excluded at the 95% confidence level.

Searches for semi-leptonic decays of long-lived particles have also been performed by the ATLAS collaboration [32, 33]. The most competitive search uses 20.8 fb^{-1} of $\sqrt{s} = 8$ TeV pp-collisions, which were collected during Run 1 of the LHC, and is a refinement of similar searches which use smaller data samples.
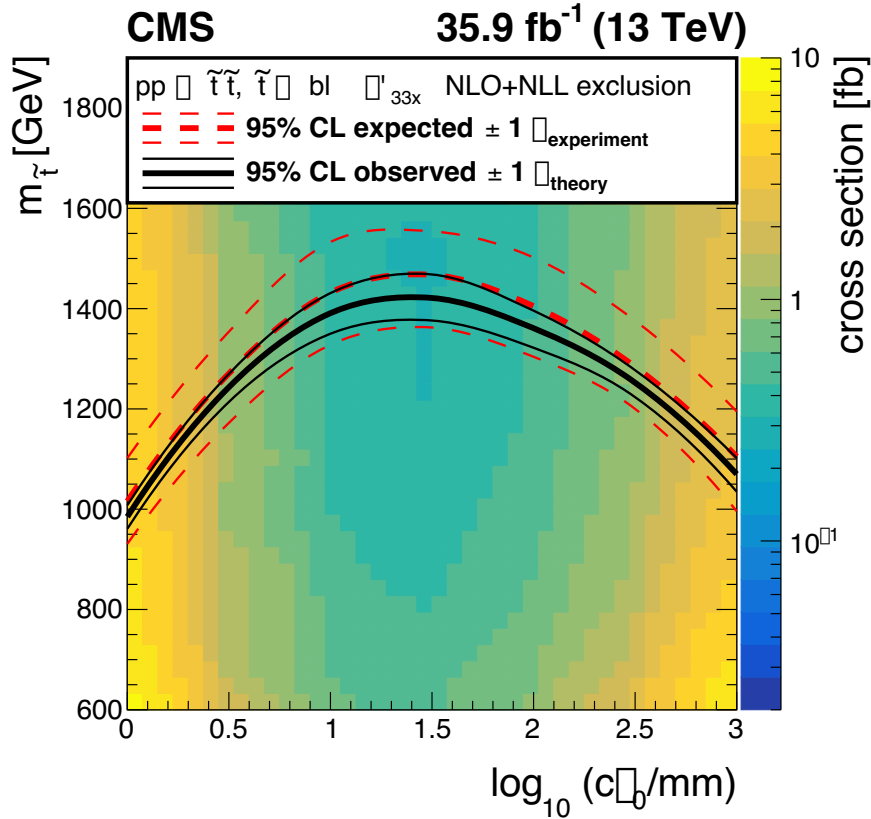
Figure 3.9: 95% CL limits on $\tilde{t} \to b + l$ from a CMS search for displaced jets. A 100% branching fraction for $\tilde{t} \to b + l$ is assumed. Stop masses and lifetimes below the solid black line have been excluded [31].

This ATLAS search has several signal regions, including final states with at least one muon, at least one electron, multiple jets, or missing transverse energy. Events are required to contain at least one multi-track displaced vertex in $r_{DV} < 300$ mm, and $|z_{DV}| < 300$ mm. Displaced vertices are required to have at least five associated tracks, which may be electrons, muons, or hadrons, and a mass of $m_{DV} > 10$ GeV.

This ATLAS displaced vertex search is not interpreted in terms of the $\tilde{t} \to \mu + q$ simplified model.

Instead this search is interpreted in terms of the simplified model shown in Figure 3.10. The process

begins with the production of a squark and anti-squark pair. Squarks decay to a quark and a neutralino.

In this model, the neutralino is the LSP. The neutralino decays via a non-zero λ' coupling to a muon,

or a muon neutrino, and two quarks.
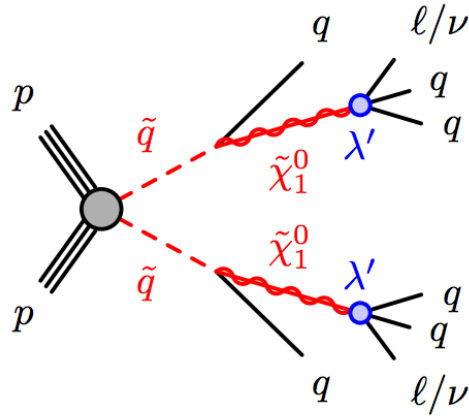
Figure 3.10: Feynman diagram for the process studied by the search in [33]. This model begins with squark and anti-squark pair production. Squarks decay to a quark and a neutralino. In this model, the neutralino is the LSP. The neutralino decays via a non-zero λ' coupling to a charged lepton, or a neutrino, and two quarks.

Upper limits on the production cross section for two squarks, and long-lived neutralinos from the

ATLAS displaced vertex search are shown in Figure 3.11. Note that these exclusions do not directly

translate to the $\tilde{t} \rightarrow \mu + q$ simplified model considered in this thesis.

Both ATLAS and CMS have performed searches sensitive to meta-stable stop squarks (with life-

times $\tau(\tilde{t})$ greater than ~ 10 ns) using a variety of signatures to select events. This includes searches

for strongly interacting long-lived particles which are stopped by the detector material, and decay in

a subsequent bunch crossing [34, 35]. Other signatures include searches for massive charged particles,

45
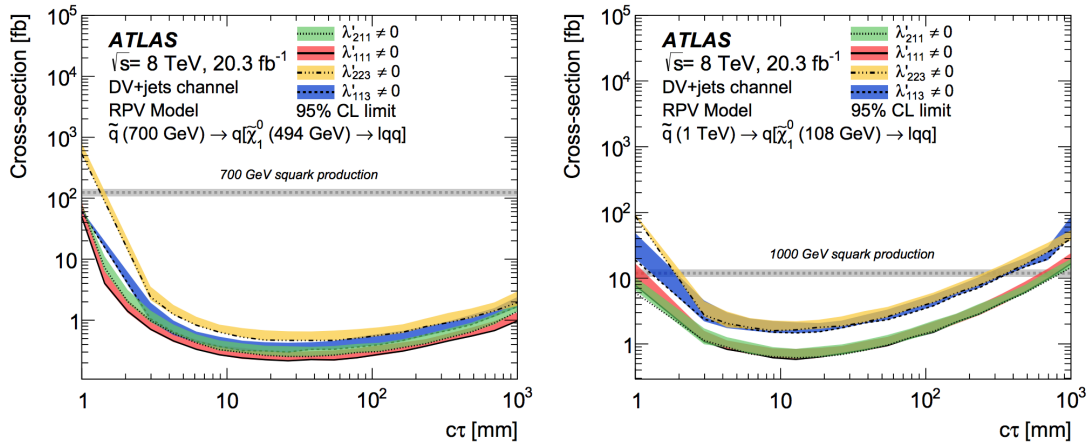
Figure 3.11: ATLAS 95% CL upper limits on di-squark production and long-lived neutralinos in R-parity violating scenarios. Results are obtained from a signal region which requires a displaced vertex and multiple jets. The squark and neutralino masses are (left) 700 GeV and 494 GeV or (right) 1 TeV and 108 GeV [33].

which result in tracks that are either highly ionizing or slowly moving [36, 37]

Part III

The Experiment

4

Large Hadron Collider

The Large Hadron Collider (LHC) is a circular collider located on the border of Switzerland and France. The LHC is 27 km in circumference, and designed to accelerate two beams of protons to an energy of 7 TeV. Proton beams are brought to collide head-on, at four points along the ring, producing collisions at a center-of-mass energy, $\sqrt{s}$ of 14 TeV, and a peak instantaneous luminosity of 1.0×10^{34} cm^{2}s$^-$1. Between 2015 and 2018, referred to as Run 2 of the LHC, the LHC provided pp-collisions at $\sqrt{s} = 13$ TeV. The peak instantaneous luminosity was 2.1×10^{34} cm^{2}s$^-$1, and the LHC delivered 156 fb^{-1} of integrated luminosity to the ATLAS detector.

This chapter discusses how particle colliders are used to study fundamental interactions. Some basic information about particle accelerators is introduced in Section 4.1, and Section 4.2 discusses specifics of the LHC design. Operating parameters during Run 2 of the LHC are described in Section 4.3,

and a discussion of the luminosity measurement is provided in Section 4.4. More information about particle accelerators and colliders are discussed in References [9, 38], and more details about the LHC can be found in References [39, 40].

4.1 Accelerator Basics

Accelerators are used to accelerate particles to ultra-relativistic speeds and produce collisions at high energies. New heavy particles can be produced from high-energy collisions, as long as the energy of the interaction is greater than the rest mass of new hypothetical particle (allowed by $E = mc^2$). Accelerators can also be used as a microscope to probe small structures. The spatial resolution of the accelerator increases with particle energy according to the De Broglie relation $\lambda = \hbar/p$, where λ is the De Broglie wavelength, which indicates the length scale, $\hbar$ is the Planck constant, and p is the incoming particle momentum. In both cases, outgoing particles produced in these high energy collisions are studied in detectors.

Collisions are either produced by colliding a single beam with a fixed-target, or colliding two beams head-on. For the same beam energy, producing collisions with head-on beams results in center of mass energies twice that of a fixed-target experiment, and typically results in higher luminosities. In a fixed-target experiment it is also possible to produce a secondary beam of particles that may be stable or unstable, charged or neutral, whereas head-on collisions usually involve only stable charged particles (electrons, protons, or their anti-particles).

There are two general accelerator designs for producing head-on collisions. Linear colliders consist

of two identical halves. Each half accelerates a beam in a straight line, and collisions are produced at the center of the accelerator, where the two beams meet. Circular accelerators bend beams in two counter-rotating circles, collide the beams at fixed points along the circle. In circular colliders, the beam can be reused, usually resulting in larger integrated luminosity than at linear colliders.

The simplest way to accelerate particles is using a constant electric field. If the electric field is aligned in the particle's direction of motion, this method can accelerate particles up to a few MeV, but is limited by the highest voltage that can be applied. In order to achieve the high energies of interest to particle physicists, electric fields can be alternated, as is done in Radiofrequency (RF)-cavities [41].

The fields in RF-cavities are made to alternate such that when a particle passes through a single cavity, and before it arrives at the next cavity, the electric fields are reversed. Reversing the electric fields ensures particles can only pass through the device in a single direction. Particles with slightly different energies, arriving earlier or later, will be accelerated or decelerated so that they stay close to the energy of the ideal particle. In this way, the particle beam is sorted into discrete packets called *bunches*. The spacing in time between bunches (25 ns at the LHC) is set by constraints of the detector, because the detector must be able to resolve individual bunches.

In a circular collider, magnets are used to circulate the beam at a constant radius. The force, $\vec{f}$ a particle with charge q and velocity, $\vec{v}$, experiences in a magnetic field, $\vec{B}$, is given by

$$\vec{f} = q\vec{v} \times \vec{B}. \tag{4.1}$$

Dipole magnets are used to create a magnetic field perpendicular to the velocity $\vec{v}$, while quadrupole

magnets are used to focus the beam. The radius of circle is then

$$R = \frac{p}{q \cdot B},$$ (4.2)

where R is the radius of the accelerator. p is the momentum perpendicular to the dipole magnetic field with strength B. If B is expressed in Tesla, and $q = q_e$, as it does for protons and electrons, equation 4.2 can be reduced to solve for the energy of the beam in GeV as a function of the magnetic field strength and size of the accelerator.

$$E_{\text{beam}} = 0.3B \cdot R.$$ (4.3)

In Run 2 of the LHC, beams reach a maximum energy of 6.5 TeV. Given a radius of 27 km, this means magnets that can produce a field of ≈ 7.5 T are required. Fields this strong can only be produced by superconducting magnets operated at low temperatures. In iron, magnetic fields saturate at strengths between 1.6 and 2.2 T.

Synchrotron radiation, the energy lost by relativistic charged particles due to acceleration, is another challenge for circular colliders. The energy loss due to the acceleration required to bend particles in a circular path is proportional to γ^4. Electrons have smaller mass than protons, which means that for the same energy electrons have a much larger γ. For circular colliders that accelerate electrons, synchrotron radiation is one of the major limiting considerations. In linear colliders, there is negligible loss of energy due to synchrotron radiation in comparison to circular colliders.

There are other considerations which come into play when deciding between colliding electrons and protons. Electrons are fundamental particles, while protons are composite particles. At the energies produced in LHC, collisions occur between the constituents of the proton, quarks and gluons (using the de Broglie relation 1 TeV $\rightarrow 1.25 \times 10^{-18}$ m, whereas the size of a proton is $\approx 10^{-15}$ m).

Because collisions occur between quarks and gluons, multiple production mechanisms are available at colliders which use protons. The fraction of proton momentum carried by these constituents isn't known *a priori*, but must be measured, as Parton Distribution Function (PDF)s, which model the probability of finding a quark or gluon with a given momentum. These parton interactions produce collisions at a variety of energies, and the precise energy of any given collision is unknown. Interactions besides the hard scatter of interest often occur, and in rare cases, multiple partons from the same proton can produce two hard scatter collisions. The only quantity which is known, is the total momentum in the plane transverse to the beam, which must be zero.

Another option is to collide protons with anti-protons. Anti-protons are harder to produce than protons, and generally limit the amount of integrated luminosity. However, there are several advantages to using anti-protons. Collisions with anti-protons result in different production mechanisms than a proton-proton collider, and protons and anti-protons can circulate in the same beam.

At electron colliders, the energy of the collision is known, and momentum is balanced in the longitudinal plane. Because electrons are fundamental particles, there is no ambiguity in production mechanism of new particles. In general, electron colliders provide a much cleaner environment than hadron colliders.

Another concern in accelerator design is the amount of data required to study interesting physics

processes. For a given process, the number of predicted events in a dataset can be computed as

$$N_{\text{events}} = L_{\text{int}} \times \sigma_{\text{process}}, \tag{4.4}$$

where L_{int} is the integrated luminosity of the dataset, and σ_{process} is the cross section for the interesting physics process in question.

Cross sections have dimensions of area, and are sometimes quoted in *barn* (*b*), where

$$1\,\text{b} = 10^{-24}\,\text{cm}^2. \tag{4.5}$$

The integrated luminosity, is the integral of the instantaneous luminosity, L, with respect to time.

$$L_{\text{int}} = \int L dt \tag{4.6}$$

Cross sections for different physics processes can vary over many orders of magnitude. For example, the total inelastic cross section at $\sqrt{s} = 13$ TeV is measured to be $\sigma_{\text{inel}} = (79.5 \pm 1.8)$ mb [42]. The cross section for $t\bar{t}$ production, a relatively common Standard Model process, is predicted to be $\sigma_{t\bar{t}} = 831.76$ pb. In contrast, the cross section for pair-production of a 1.5 TeV stop squark, the process studied in this thesis, is predicted to be $\sigma_{\tilde{t}\tilde{t}} = 2.57 \times 10^{-4}$ pb. In the dataset considered by this analysis, which has an integrated luminosity of 136 fb^{-1}, this would correspond to nearly 35 predicted stop-antistop events.

Obtaining the integrated luminosity necessary to study a given processes is a question of optimizing

the instantaneous luminosity, because it is very difficult to increase the amount of time an accelerator can produce collisions in a given year.

The instantaneous luminosity is the number of collisions that can be produced in a detector per cm^2 and per second, and can be computed as

$$L = \frac{N_b^2 \, n_b \, f_{\text{rev}} \, \gamma}{4\pi \, \sigma_x \sigma_y} \, F = \frac{N_b^2 \, n_b \, f_{\text{ref}} \, \gamma}{4\pi \, \sqrt{\epsilon_x \epsilon_y \beta_x \beta_y}} \, F. \tag{4.7}$$

The instantaneous luminosity is proportional to N_b^2, the number of protons per bunch ($\approx 10^{11}$ at the LHC), as well as n_b, the number of bunches in each beam (≈ 2500), and f_{rev}, the frequency of revolution, or the number of times the beam circulates in one second (≈ 1 kHz). The instantaneous luminosity is inversely proportional to the root mean square, or rms, of the beam width in the x and y directions, σ_x and σ_y. The emittance is denoted by ϵ, while β describes the transverse displacement of particles in the beam. The beta function changes as a function of position along the beam, and is referred to as $\beta*$ at the collision point. The term F is a reduction factor due to the geometry of the beam crossing.

The instantaneous luminosity can be increased by increasing the number of bunches in the beam, increasing the number of protons per bunch, or reducing the rms spread of the particles in x and y directions at the interaction point. This step is referred to as *squeezing* the beam, and achieved with focusing quadrupole magnets.

During the course of a run, proton beams circulate and produce collisions. The number of protons per bunch, N_b, decreases due to beam losses, not due to collisions, producing a falling instantaneous

luminosity. Runs continue for approximately ten hours at a time. The downtime between runs is usually a few hours, with extra breaks for scheduled and unscheduled maintenance for accelerator complex and detectors. There are also extended stops of several months each year, to upgrade detectors and the accelerator. In general, there are roughly ten weeks of data taking per year.

In Run 2 of the LHC, the peak instantaneous luminosity observed in ATLAS was $2.1 \times 10^{34}\,\mathrm{cm^2 s^{-1}}$, roughly twice the design instantaneous luminosity. One consequence of the high instantaneous luminosity at the LHC is *pile-up*, in which multiple collisions occur during the same bunch crossing, referred to as *in-time* pile-up. Pile-up can also be *out-of-time*, for detectors which are read out over intervals longer than the time between bunch crossings. For these detectors, it is important to associate signals to the correct beam-crossing.

Two important quantities are used to describe the amount of pile-up in a dataset. The first quantity is the number of primary vertices per event, NPV. The second is the average number of inelastic interactions per bunch crossing, $\langle \mu \rangle$, and can be computed as

$$\langle \mu \rangle = \frac{L \cdot \sigma_{\mathrm{inelastic}}}{N_{\mathrm{bunch}} \cdot f_{\mathrm{LHC}}}. \tag{4.8}$$

The mean $\langle \mu \rangle$ of the full ATLAS Run 2 dataset is approximately 33 interactions per bunch crossing, and the peak $\langle \mu \rangle$ is approximately 70 interactions per bunch crossing. There are many challenges for the ATLAS experiment due to pile-up. In overcoming these challenges, it is vital to identify the correct primary vertex that produced an interaction of interest. With this information, it is possible to try to ignore other activity in the same bunch crossing, mainly jets from pile-up interactions, and only use

particles associated with the interesting primary vertex.

4.2 Large Hadron Collider Design

The LHC injection chain begins with a bottle of hydrogen gas located before Linac 2. An electric field is used to strip the hydrogen atoms of their electrons, producing protons. Linac 2 accelerates these protons to 50 MeV, using a series of RF-cavities. Protons are then transferred to the Proton Synchrotron Booster. The Proton Synchrotron Booster consists of four stacked synchrotron rings, and accelerates protons from 50 MeV to 1.4 GeV. Protons are then injected into the Proton Synchotron (PS). The Proton Synchrotron consists of 277 iron electromagnets arranged along a circular beam path with a circumference of 628 meters, and accelerates the protons up to 25 GeV. The 25 GeV protons are then injected into the Super Proton Synchrotron (SPS). The SPS is 7 kilometers in circumference, and accelerates protons to 450 GeV with conventional magnets.

The SPS then injects these protons into the LHC, which accelerates protons to 6.5 TeV. This process is achieved with eight RF cavities, which increase the energy of the beam, and over 8000 superconducting magnets, which bend the beam in a circle.

The LHC's RF cavities increase the energy of the beam from 450 GeV after injection to 6.5 TeV for collisions, more than 14 times their injection energy. This process is referred to as *ramping*. The LHC radiofrequency cavities oscillate at a frequency of 400 MHz. Each cavity can reach a maximum voltage of 2 megavolts (MV), corresponding to 16 MV in total, with an acceleration gradient of 5 MV/m. Each time a proton circulates through the LHC it receives 16 MeV of energy. The maximum

energy is achieved in around 20 minutes, and corresponds to the bunches having passed through the RF cavities more than 10 million times. The RF cavities also compensate for the 7 keV of energy lost due to synchrotron radiation per beam per revolution.

The Large Hadron Collider contains over 8000 niobium and titanium (NbTi) superconducting magnets. These magnets are cooled to 1.9 K by liquid helium, which requires extensive cryogenics. Of the 8000 superconducting magnets, 1232 are the main bending dipoles, and the remaining magnets consist of quadrupoles, sextapoles, octopoles, and single bore dipoles. These magnets are used in focusing the beams, squeezing the beams before collisions, correcting trajectories, and damping oscillations in beam position. As the energy of the beam is increased, the current in the magnets is increased in order to keep the beam at fixed radius (following equation 4.2).

The tunnel has a diameter of 3.7 m, which makes it difficult to install two separate proton rings. To save space, the LHC circulates both proton beams within the same cryostat, with separate magnetic fields and vacuum pipes for each beam. A cross section of an LHC dipole is shown in Figure 4.1

The LHC beam is divided into 3654 bunches, each separated by 25 ns or ≈ 9.6 m. The maximum allowed number of filled bunches in the LHC is 2808 and the maximum number of filled bunches in Run 2 was 2556. Bunches are injected from the SPS to the LHC in *bunch trains*. It is necessary to leave empty bunches between trains, due to the fill patterns of the previous accelerators, and in order to leave space to safely dump the beam.

LHC DIPOLE : STANDARD CROSS-SECTION

- ALIGNMENT TARGET
- MAIN QUADRIPOLE BUS-BARS
- HEAT EXCHANGER PIPE
- SUPERINSULATION
- SUPERCONDUCTING COILS
- BEAM PIPE
- VACUUM VESSEL
- BEAM SCREEN
- AUXILIARY BUS-BARS
- SHRINKING CYLINDER / HE I-VESSEL
- THERMAL SHIELD (55 to 75K)
- NON-MAGNETIC COLLARS
- IRON YOKE (COLD MASS, 1.9K)
- DIPOLE BUS-BARS
- SUPPORT POST
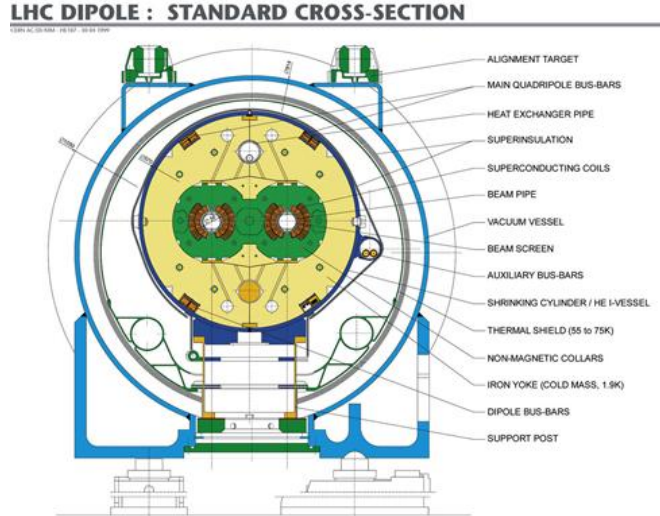
Figure 4.1: A cross section of an LHC dipole magnet [43].

4.3 RUN 2 OPERATING PARAMETERS

Table 4.1 shows the relevant operating parameters during Run 2. After a long shutdown, in 2015, the energy of the beam was increased from 4 TeV to 6.5 TeV, and bunch spacing was decreased from 50 ns to 25 ns. Increasing the energy in the beam required months of *training* dipole magnets. A magnet is trained by increasing the current in the magnet until it quenches, and repeating the process over and over again until the maximum desired current is achieved. Reducing the spacing between bunches required overcoming electron-cloud and space-charge challenges, in which negatively charged electrons liberated from the accelerator walls are attracted to the positively-charged proton beam. The electron cloud was reduced by an intense period of *scrubbing*. In order to improve the surface of the beam pipe, the LHC circulated intense beams, containing many bunches, but at low energies. Due to the many challenges in commissioning, only 3.2 fb^{-1} of data were collected in 2015.

58

Table 4.1: LHC parameters during Run 2, by year [44].

Parameter	Design	2015	2016	2017	2018
Energy	7.0	6.5	6.5	6.5	6.5
Number of bunches	2808	2244	2220	1868-2556	2556
Bunches per train	288	144	96	144-128	144
Energy per beam [MJ]	362	280	280	315	312
$\beta*$ [cm]	55	80	40	30-40	25-30
Protons per bunch [10^{11}]	1.15	1.2	1.25	1.25	1.1
Emittance [μm]	3.75	2.6-3.5	1.8-2	1.8-2.2	1.8-2.2
Peak luminosity [10^{34}cm^{2}s^{-1}]	1.0	<0.6	1.5	2	2.1
Half Crossing Angle [μrad]	142.5	185	140-185	120-150	130-150

The years 2016-2018 were production years for the LHC. Each year, the LHC performance was improved, and surpassed several design parameters. The peak instantaneous luminosity was more than twice design values, due to reductions in $\beta*$, increases in the number of protons per bunch, and the number of bunches per beam.

The LHC performed so well that the ATLAS and CMS experiments had to use *luminosity leveling* in order to cope with the rate of collisions. Luminosity leveling consists of adjusting the beam crossing angle, and separating the beams to reduce the effective cross section. In ATLAS, the computing power available for the software-based High Level Trigger, which is described in Chapter 7, was the limiting factor in coping with instantaneous luminosity.

Figure 4.2 shows the integrated luminosity accumulated over time. Between 2015 and 2018, the LHC delivered 156 fb^{-1} of *pp*-collisions to the ATLAS detector. ATLAS recorded 147 fb^{-1} of data, and 139 fb^{-1} are certified to have good data quality. This analysis makes use of 136 fb^{-1} collected between 2016 and 2018.
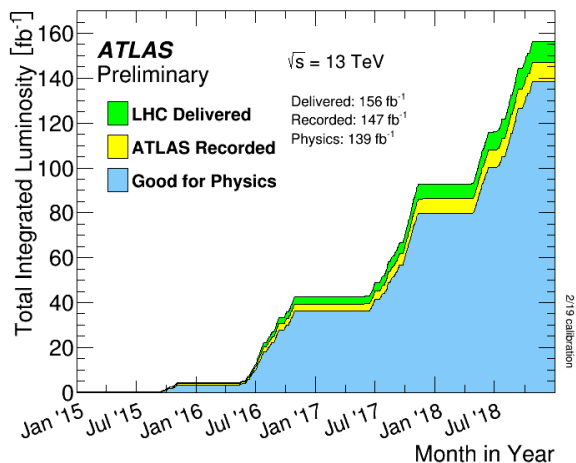
Figure 4.2: Cumulative luminosity versus time delivered to ATLAS (green), total integrated luminosity recorded by ATLAS (yellow), and certified to be good quality data (blue) during stable beams for pp collisions at 13 TeV centre-of-mass energy in 2015-2018 [45].

Figure 4.3 show the luminosity-weighted distribution of the mean number of interactions per bunch crossings for data collected between 2015 and 2018. The mean number of interactions per crossing is computed from equation 4.8. The integrated luminosity is computed from a preliminary luminosity calibration for 2018, based on methods discussed in Section 4.4. The average $\langle\mu\rangle$ is 33.7 interactions per bunch crossing, and the peak $\langle\mu\rangle$ is approximately 70 interactions per bunch crossing.

4.4   Measuring Luminosity

The ATLAS detector measures the instantaneous and integrated luminosity delivered by the LHC in a two step process, using methods similar used to those described in Reference [46].

First, dedicated sub-detectors measure the number of pp inelastic collisions that occur while the

60
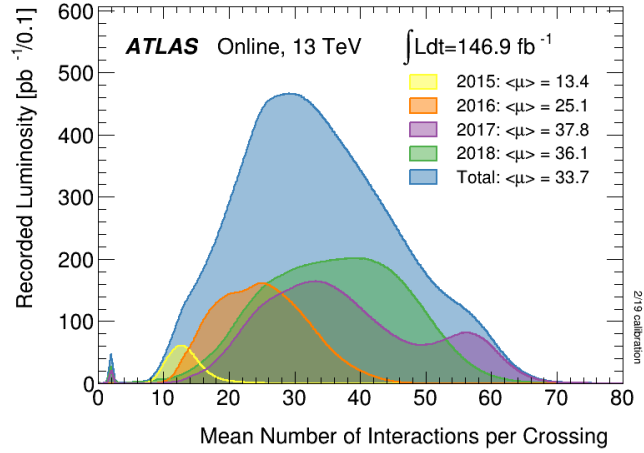
Figure 4.3: Mean number of interactions per bunch crossing for $\sqrt{s} = 13$ TeV pp-collision data collected between 2015-2018. All data recorded by ATLAS is shown, and data collected during different calendar years are indicated by different colors. For each year, the mean $\langle \mu \rangle$ is provided in the legend [45].

LHC is running. These measurements are performed online during data taking, and offline during the reconstruction step. Online luminosity measurements ensure the ATLAS detector is efficiently collecting data (to adjust the trigger menu, and choose an appropriate luminosity leveling scheme) and ensure that the ATLAS sub-detectors are protected from challenges that could arise during high instantaneous luminosity. Offline measurements are important for the most accurate determination of the size of the dataset.

The second step calibrates the observed rate of pp-collisions, as measured in the first step, to a luminosity measurement. This step is performed with dedicated *van der Meer* scans [47]. During a van der Meer scan, the beams begin by producing collisions head on. Then, one of the LHC beams is moved in discrete steps the x direction, until the hit rate drops to zero. This is designed to measure the profile of the beam. The same process is repeated in the y direction in discrete steps.

5

The ATLAS Detector

The ATLAS experiment is a general purpose detector with nearly 4π steradian coverage in solid angle. ATLAS was designed to study LHC proton-proton collisions at $\sqrt{s} = 14$ TeV. A schematic of the ATLAS detector is shown in Figure 5.1.

Like most general purpose detectors, ATLAS is composed of three concentric cylindrical sub-detectors which surround the pp-interaction point: the Inner Detector followed by the Calorimeter and Muon Spectrometer. Most detectors are separated into *barrel* and *end-cap* regions. The barrel consists of detector layers positioned along concentric cylinders which surround the beam line. The end-cap consists of detectors positioned along disks perpendicular to the beam line, placed at either end of the barrel.

The Inner Detector is designed for the reconstruction of charged particle trajectories. The Inner De-

tector sits inside a 2 Tesla solenoidal magnetic field, which bends the paths of these particles, enabling a measurement of their charge and momenta. The Inner Detector is surrounded by the Calorimeter, which is used to measure the energy of particles, using separate detector technologies for electromagnetic and hadronic showers. The Calorimeter is surrounded by the Muon Spectrometer. The Muon Spectrometer is used for tracking and triggering on muons, as well as measuring their momenta, in a magnetic field produced by air-core toroids. Additional detectors are used monitor the beam position and measure the luminosity, and are discussed elsewhere [48, 49].
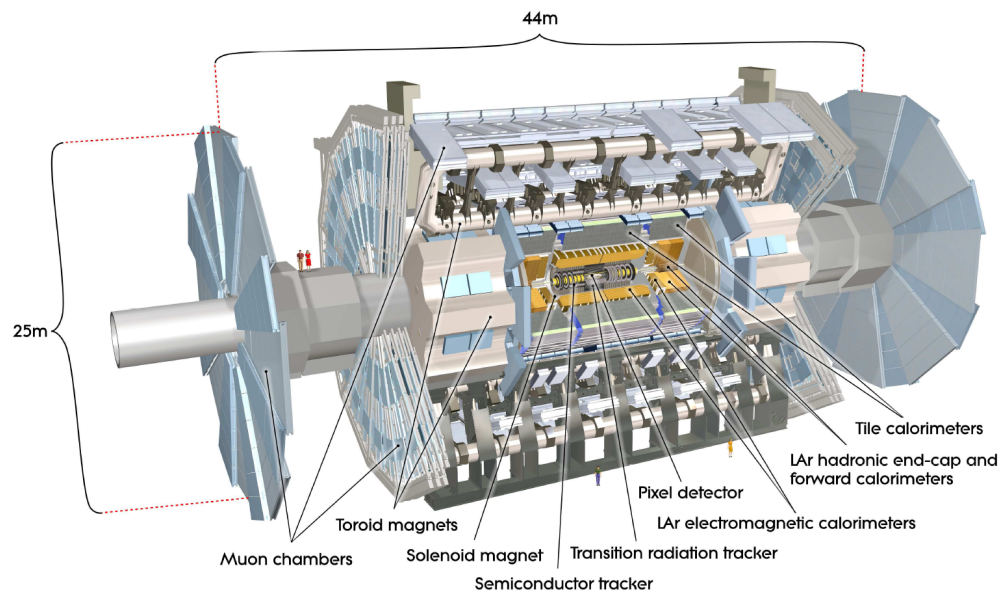
Figure 5.1: A diagram of the full ATLAS detector. ATLAS is 44 m long in the z-direction, and 25 m long in diameter. [50]

The ATLAS coordinate system is described in Section 5.1. The motivations for the ATLAS detector design are discussed in Section 5.2, and the rest of this chapter discusses the details of the detector which are most relevant for this analysis. A description of the Inner Detector can be found in Section 5.5.

63

Section 5.6 describes the Electromagnetic and Hadronic Calorimeters, and Section 5.7 describes the Muon Spectrometer. More details about the ATLAS detector can be found in Reference [50].

5.1 COORDINATE SYSTEM

The ATLAS detector uses a Cartesian right-handed coordinate system, as shown in Figure 5.2. The nominal pp-interaction point defines the origin of the detector. The beam direction defines the z-axis, and the x-y plane is transverse to the beam direction. The positive x-axis points from the origin of the detector to the center of the LHC ring, while the positive y-axis points upwards. The positive z-axis points along the counter clockwise direction of the beam. The side of the detector in positive z is referred to as the A-side, and the side in negative z is the C-side.
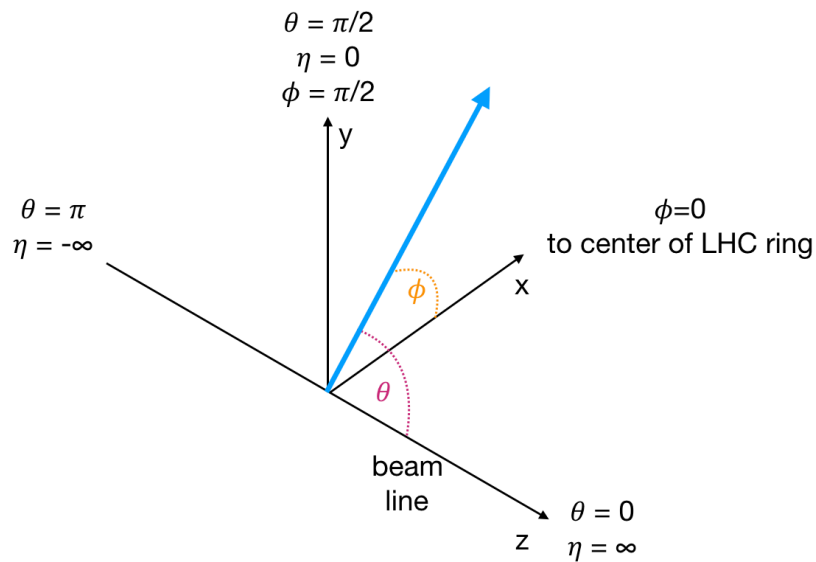
Figure 5.2: ATLAS coordinate system. The x, y, and z-axes are shown, as well as geometric angles θ, η, and ϕ.

The azimuthal angle, ϕ, is measured around the beam axis, such that $\phi = 0$ along the positive x-axis, and ϕ is positive for positive y. The polar angle, θ, is measured with respect to the beam axis. The radial distance measured from the origin, in the x-y plane is defined as R, and the longitudinal distance is defined as z. This thesis aims for consistency, but sometimes R is also denoted as r or R_{xy}.

The following variables are used to characterize the kinematics of particles produced in LHC collisions. Because the initial momentum of the colliding partons in the z direction is not known, it is useful to use variables which are invariant under boosts in the z direction. For example, differences in rapidity are invariant to these boosts. The rapidity, Y, is defined as

$$Y = \frac{1}{2}\ln\frac{E + p_z}{E - p_z},$$
(5.1)

where E is the particle's energy, and p_z is the particle's momentum in the z-direction. If the approximation that a particle is massless ($m \ll p_{\mathrm{T}}$), the rapidity can be approximated by the pseudorapity, which is defined as

$$\eta = -\ln\tan(\theta/2).$$
(5.2)

The pseudorapidity is equal to zero for a particle which travels perpendicular to the beam line, and $\eta = \pm\infty$ along the z-axis.

Pseudorapidity is often used instead of rapidity because it is a purely geometric variable which does not depend on a particle's mass. The pseudorapidty is also used instead of θ because differences in η are Lorentz invariant in the massless approximation.

The proximity between two particles is often denoted by the distance ΔR, where ΔR is defined in pseudorapidity-azimuthal space as $\Delta R = \sqrt{\Delta\eta^2 + \Delta\phi^2}$. When the massless approximation is not appropriate ΔR may be defined in rapidity-azimuthal space as $\Delta R = \sqrt{\Delta Y^2 + \Delta\phi^2}$.

The energy and momentum of particles are frequently projected onto the x-y, or transverse, plane. The transverse plane is used because in this plane, the initial transverse energy and momenta of the colliding partons are close to zero. A particle's transverse momentum is referred to as p_T, and its transverse energy as E_T, where $E_\mathrm{T} = E\sin(\theta)$. The negative sum of momentum in the in the transverse plane indicates the presence of undetected particles and is referred to as the missing transverse momentum, or missing transverse energy, and defined as $\vec{E_\mathrm{T}^{\mathrm{miss}}} = -\sum_{\mathrm{particles}} \vec{E_\mathrm{T}}$, with magnitude $E_\mathrm{T}^{\mathrm{miss}}$.

Particles are most frequently represented by their $(p_\mathrm{T}, \eta, \phi)$, because these three variables are all Lorentz invariant under boosts in the z-direction (in the massless approximation).

5.2   Physics Motivations

The ATLAS detector was designed with a wide range of physics goals in mind. In particular, much of the design was devoted to the discovery of the Higgs boson, with additional considerations made for studying electroweak symmetry breaking, vector boson scattering, and searches for BSM particles.

Before the discovery of the Higgs boson, its mass was expected to be ~ 100 GeV, but was not explicitly known. Direct searches at LEP have excluded Higgs masses below 114 GeV, while indirect constraints indicated a mass above $160 - 170$ GeV was disfavored. Because the production and decay mechanisms of the Higgs vary depending on the mass of the particle, all channels would need to be

considered at the LHC. Important channels at the LHC include $h \rightarrow WW \rightarrow l\nu l\nu, h \rightarrow ZZ \rightarrow 4l$ and $h \rightarrow \gamma\gamma$. Higgs decays which probe its direct couplings to fermions most often involve decays to two b-jets or two taus, and both of these channels require excellent secondary vertex identification.

Studying vector boson fusion and vector boson scattering processes were also essential to understanding electroweak symmetry breaking. Both processes are characterized by two well-separated jets at high rapidity, requiring calorimetry placed in harsh radiation environments.

In addition, physicists also wanted to search for possible new phenomena, including searches for high mass resonances and evidence of Supersymmetry. Searches for new heavy gauge bosons would involve decays to leptons with p_T as high as several TeV. Finally, searches for R-parity conserving Supersymmetry would result in large amounts of $E_\mathrm{T}^\mathrm{miss}$, requiring a calorimetry with nearly full coverage in solid angle.

There are also many challenges associated with designing a detector at a hadron collider. For pp-collisions at $\sqrt{s} = 14$ TeV (the design energy), the cross section for inelastic pp-interactions was predicted to be 80 mb. Given the design instantaneous luminosity of the LHC and the bunch cross spacing, each bunch crossing contains multiple pp-collisions. Any interaction of interest will be accompanied by other, less interesting inelastic interactions, or pile-up interactions, and it is important to identify which interaction is the one of interest. Another challenge for the detector is that multi-jet production cross sections dominate over rare processes associated with Higgs decays or searches for BSM physics.

The most commonly produced particle at the LHC are pions, which have a mass of 0.14 GeV, and mean transverse momentum of approximately 0.8 GeV. In single bunch crossing, a generic detector

is expected to see more than 2000 of these pions, many of which are produced in pile-up interactions. In order to measure the $E_{\mathrm{T}}^{\mathrm{miss}}$ for the collision of interest, it is necessary to measure the energy carried away by these pions.

These goals and challenges translate to the following requirements for detector design.

- Radiation hard detector elements and electronics

- High granularity

- Large acceptance in pseudorapidity and almost full coverage in ϕ

- Charged particle momentum resolution and reconstruction efficiency

- Ability to reconstruct secondary vertices from b-jets and τ-leptons

- Calorimetry for electron and photon identification and energy measurement

- Calorimetry for jet and missing transverse energy measurement

- Muon identification and resolution over a wide range of momenta

At the LHC, general purpose detectors are generally designed to have full coverage out to pseudorapidity $|\eta| < 5$, with an emphasis on placing precise detectors in the range $|\eta| < 2.5$. This strategy is motivated by the rapidity distributions of particles produced at the LHC, as well as harsh radiation conditions at larger values of pseudorapidity. Generally, particles are produced with a uniform distribution in rapidity, with a kinematic edge at Y_{max}, which is can be roughly estimated as [51]

$$Y_{\mathrm{max}}(M) \sim \ln(\sqrt{s}/M). \tag{5.3}$$

Emphasis is placed on precision tracking and lepton identification for pseudorapidities less than $|\eta| = 2.5$, because heavy particles are preferentially produced with central rapidity. Consider a hy-

pothetical new boson with mass $M = 1$ TeV which decays to leptons, produced in $\sqrt{s} = 13$ TeV pp-collisions. These new bosons will be produced with $Y_{\mathrm{max}} \sim 2.5$.

At larger values of pseudorapidity, general purpose detectors and front-end electronics face rate limitations and harsh radiation conditions. For $2.5 < |\eta| < 5$, emphasis is placed on calorimetry which is designed to measure the transverse energy of the many pions produced in pile-up interactions, as well as tagging jets from vector boson fusion processes. These calorimeters must be radiation hard, but can have coarser granularity than the central calorimeter. Tracking and lepton identification is unnecessary in this region of rapidity.

Another concern in measuring the $E_{\mathrm{T}}^{\mathrm{miss}}$ in an event, is that the detector has sufficient granularity to measure the position and momentum of every particle produced. General purpose detectors are usually designed with many distinct detection elements. These elements have roughly uniform size in pseudorapidity and azimuthal angle, because particle production is roughly uniform in both variables. This means each element has an equal probability of being struck by an incident particle.

Suppose each element has a size of $\delta\eta = \delta\phi/2\pi = 0.1$. If the detector extends up to $|\eta| = 5$ and has full coverage in ϕ, this results in 6300 individual detector elements. If there are over 2000 pions produced in a single bunch crossing, the odds that any one tower is occupied by a particle is $\sim 30\%$.

The spatial granularity required by an individual detector technology depends on the type of particle that is being detected, and the the time to read out the detector. Detectors which are read out over several bunch crossings require higher spatial granularity, because these detectors must resolve particles produced in multiple bunch crossings.

At the LHC, general purpose detectors are designed to identify and measure all Standard Model particles which are produced in pp-collisions. There are several strategies for identifying Standard Model particles, depending on whether the particle is prompt, long-lived, or stable. Depending on the detector technology, the smallest resolvable distance is between tens of micrometers to tens of millimeters. As a result, particles are considered prompt if their mean decay length is shorter than about ten micrometers. In contrast, particles are treated as stable or meta-stable if their mean decay length is greater than about one meter, which is the typical length of a sub-detector.

Referring back to the Standard Model mean decay lengths presented in Table 2.1, this means particles which decay promptly include heavy electroweak bosons, as well as the top quark and neutral pion. Prompt particles and their decays cannot be directly detected, but it is possible to study their decay products and glean information about the originally produced particle.

Particles with average decay lengths greater than micrometers but smaller than meters include b-hadrons, c-hadrons, K^0_S, and tau leptons. These particles are not detected directly, but are also inferred from their decay products. One important feature of identifying such Standard Model long-lived particles includes reconstructing their decay products as displaced tracks, which sometimes form a displaced vertex.

Truly stable Standard Model particles include the photon, electron, proton, and neutrinos. At the LHC, particles which can be treated as meta-stable include neutrons, muons, charged pions, and kaons. A general purpose detector will need to be able to be able to distinguish between all stable and

meta-stable Standard Model particles.

This process of particle identification requires the use of multiple detector technologies. Moving radially outwards from the point of collisions through the detector, a particle usually passes through four distinct layers. Each layer has a different purpose, and together they can be used to identify stable particles.

The Inner Detector is designed to detect electrically charged particles. The Inner Detector (ID) is usually surrounded by a solenoid magnetic field, so that the charged particle's paths are bent, providing information for a momentum measurement. The most commonly detected particles in the ID include charged leptons (electrons and muons) and hadrons (protons, pions, kaons). The ID is also necessary for identifying secondary vertices from long-lived Standard Model particles.

After passing through the Inner Detector, particles then enter the Calorimeter, which usually consists of two different technologies. First is the Electromagnetic Calorimeter (ECAL), which absorbs and measures the energy from electromagnetically interacting particles (electrons and photons). The ECAL must fully contain electromagnetic showers, and this usually requires at least 20 radiation lengths, X_0 of absorbing material. The ECAL is surrounded by the Hadronic Calorimeter (HCAL), which in turn absorbs and measures the energy from hadronically interacting particles, including hadronic jets. Hadronic showers are usually contained in 9 nuclear absorption lengths, λ_0.

Muons and neutrinos are the only stable Standard Model particles which should escape the HCAL. The final system is the Muon Spectrometer. Also a tracking detector, the Muon Spectrometer of ATLAS sits in a toroidal magnetic field, and is designed to reconstruct the paths of muons and measure their momentum. Neutrinos are the only Standard Model particle which should escape the entire

ATLAS detector without interacting, and their momentum can be estimated as E_T^miss.

Figure 5.3 shows a mock-up of Standard Model particle signatures in ATLAS. Note that the ATLAS detector was not designed with searches for new long-lived particles in mind. The design of the detector assumes stable Standard Model particles are produced at the pp-interaction point. Generally, this means that identifying highly displaced tracks, leptons, or jets is more challenging.
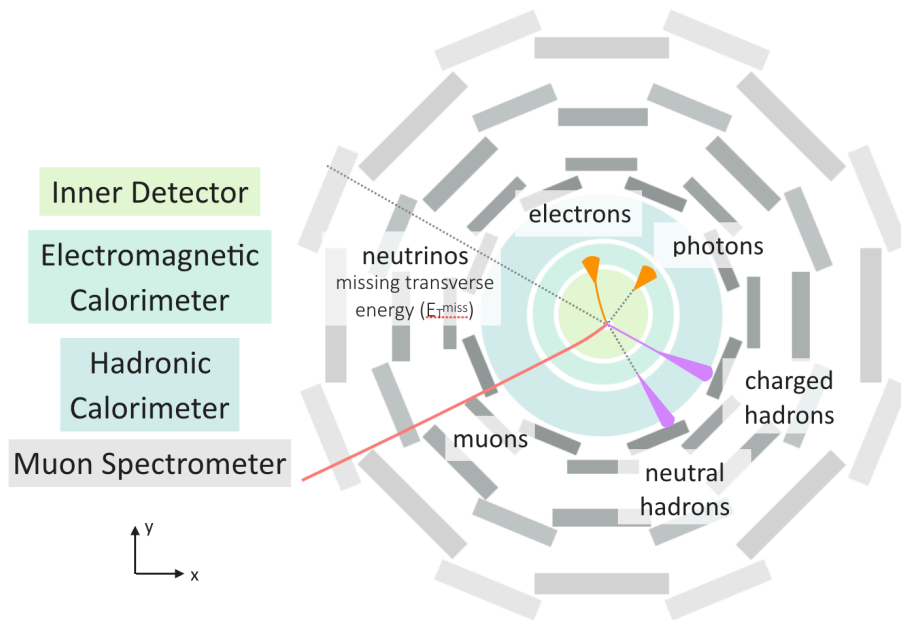
Figure 5.3: A schematic of Standard Model particle identification in ATLAS. A mock-up of the ATLAS detector and four key sub-detectors is shown in the transverse plane. Detectors are not drawn to scale. The detector signatures for stable Standard Model particles are shown.

5.4 Helpful Formulas

This thesis is mostly concerned with reconstructing the trajectories of charged particles, particularly muons and pions, as tracks. This section provides a few formulas which are helpful for understanding

how precisely a general purpose detector is able to measure these particles given certain parameters of the detector. More detail can be found in References [9, 52]

5.4.1 TRACK RECONSTRUCTION

A particle with unit charge in a constant magnetic field follows the trajectory of a helix. The magnetic field in ATLAS is constant in the z-direction. A charged particle with transverse momentum, p_T results in a track with the following radius of curvature in the transverse plane

$$p_T = 0.3 \, B \, R, \tag{5.4}$$

where p_T is measured in GeV, B is the magnetic field strength in Tesla, and R is measured in meters.

A track's sagitta, s, is used to measure the radius of curvature, and infer the particle's transverse momentum

$$s \approx \frac{L^2}{8R} = \frac{0.3 \, BL^2}{8p_T}. \tag{5.5}$$

where L is the path length of the track in meters. Figure 5.4 shows a schematic of a track's sagitta and radius of curvature.

Table 5.1 provides a few radii and sagitta for tracks with different transverse momenta, assuming a magnetic field strength and track length consistent with the ATLAS Inner Detector. Particles with larger momenta will produce tracks with smaller sagitta. For example, particles with $p_T = 1$ TeV, in ATLAS will result in nearly straight tracks, with sagitta of 75 micron.
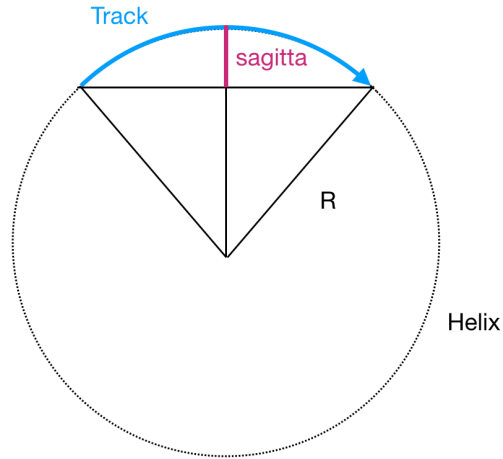
Figure 5.4: Schematic of a track and its sagitta, as viewed in the transverse plane. The track is shown in blue, and follows the path of a helix. The radius of curvature, R is indicated in black, and the sagitta is shown in pink

Table 5.1: Radius of curvature and sagitta for tracks with different transverse momenta in a 2 Tesla magnetic field, assuming a track length of 1 m

p_T	Radius of curvature [m]	Sagitta [mm]
1 GeV	1.67	75
10 GeV	16.7	7.5
100 GeV	167	0.75
1 TeV	1670	0.075

5.4.2 MULTIPLE-SCATTERING

Charged particles which pass through detector material undergo several small-angle scatters, or *multiple-scattering*. Multiple scattering affects the measurement of a particle's trajectory, and can degrade resolution of the momentum and impact parameter measurements. The angle of deflection due to multiple-scattering follows a Gaussian distribution, where the rms spread of the deflection is given by

$$\theta_0 = \frac{13.4\text{MeV}/c}{\beta p} q \sqrt{\frac{d}{X_0}}. \tag{5.6}$$

The thickness of the detector is given by d and the radiation length of the material used is given by X_0. Multiple scattering limits the precision with which we can measure a particle's momentum and impact parameters, because the charged particle's trajectory will deviate from a helix. For this reason, it is important to minimize the amount of material used in detectors.

5.4.3 Momentum resolution

The precision of the sagitta measurement, σ_s, is related to the number of position measurements made along the charged particle's trajectory, the resolution of each point measurement, as well as effects from multiple scattering. Combining all of these effects, the resolution of transverse momentum measurement for a particle with unit electric charge is given by the Gluckstern formula

$$\frac{\sigma_{p_\text{T}}}{p_\text{T}} = \left(\frac{p_\text{T}}{0.3} \frac{\sigma_\text{point}}{BL^2} \right) \sqrt{\frac{720}{N+4}} \oplus \left(\frac{\sigma_{p_\text{T}}}{p_\text{T}} \right)_{MS}. \tag{5.7}$$

The track p_T is measured in GeV. The uncertainty on an individual point measurement in meters is given by σ_point. The magnetic field strength in Tesla is B, and L is track length in meters. This formula assumes N, the number of point measurements is large. The magnetic field strength and long path length are dominating terms in the measurement precision in comparison to the number of measurements. The multiple scattering contribution to the momentum resolution is given by

$$\left(\frac{\sigma_{p_{\mathrm{T}}}}{p_{\mathrm{T}}}\right)_{MS} = \frac{0.0136}{0.3\,\beta\,BL}\sqrt{\frac{(N-1)x/\sin\theta}{X_0}}\sqrt{C_N}, \tag{5.8}$$

where L is the length of the tracker, and $\frac{(x/\sin\theta)}{X_0}$ is the total material thickness traversed by a particle, in units of the radiation length. C_N is a combinatoric factor which depends on the number of point measurements. For three measurements $C_N = 2.5$, while for an infinite number of measurements $C_N = 1.33$.

5.4.4 Impact parameter resolution

Another important component of detector design is the need to identify decays of heavy leptons and quarks, which are displaced from the interaction point. Tau leptons, b-hadrons, and c-hadrons all have lifetimes of approximately $\tau \sim 1$ ps. Depending on the momenta of these particles produced at the LHC, these particles decay with length scales on the order of tens of microns to millimeters, according to equation 2.4. In order to reconstruct secondary vertices from the decay products of these particles, an impact parameter resolution of 10 to 20 μm is required.

The resolution of the impact parameter in the transverse plane, d_0, is given by

$$\sigma_{d_0} \approx \frac{\sigma_{\mathrm{point}}}{\sqrt{N}}\sqrt{1 + \frac{12(N-1)}{(N+1)}\left(\frac{r}{L}\right)^2} \oplus \theta_0\,r_{pv}\sqrt{\frac{N(2N-1)}{6(N-1)^2}}. \tag{5.9}$$

The first term results from the extrapolation of the track from the tracker to the primary vertex. The impact parameter resolution is roughly proportional to the ratio of the extrapolation distance r to the tracker length L. The extrapolation distance is defined as the distance between the first measurement

76

and the impact parameter. As a result, it is important to make the first measurement close to the interaction point, in order to reduce the position error from extrapolating. The challenge with placing a silicon detector close to the point is the increasing radiation dose, which scales with $1/R$. The impact parameter resolution is also linearly dependent on the point resolution.

The second term is due to multiple scattering. This term is approximated by extrapolating from the first point measurement to the primary vertex, and assuming the slope of this extrapolation is smeared by multiple scattering. The distance from the first point measurement to the primary vertex in the transverse plane is given by r_{pv}.

For a pixel detector with four layers as in ATLAS, at radii between 3.3 cm and 12.3 cm, and with a point resolution of about 10 μm, the first term in equation 5.9 yields $\sigma_{d_0} \approx 12.5$ μm. For the same geometry, and a radiation length thickness of $0.03\ X_0$, the resolution due to multiple scattering is approximately 90 μm GeV$/p$.

5.4.5 Detector requirements

Given the physics motivations discussed in Section 5.2 the desired performance of the ATLAS detector is summarized in Table 5.2.

5.5 Inner Detector

The Inner Detector is a tracking detector, which is designed to reconstruct the trajectories of charged particles. The ID is surrounded by a superconducting solenoid, which produces a 2 Tesla magnetic field, uniform in the z-direction. A charged particle's trajectory bends in the azimuthal coordinate,

77

Table 5.2: General performance goals of the ATLAS detector. Note that for the muon spectrometer, the performance is independent of that of the tracking detector. Units for p_{T} and E are in GeV.

Detector Component	Required Resolution
Tracking	
Momentum resolution	$\sigma_{p_{\mathrm{T}}}/p_{\mathrm{T}} = 0.05\% \, p_{\mathrm{T}} \oplus 1\%$
Impact parameter	10 to 20 μm for $\lvert d_0 \rvert < 30$ mm
EM Calorimetery	$\sigma_E/E = 10\%/\sqrt{E} \oplus 0.7\%$
Hadronic Calorimetery (jets)	
Barrel+End-caps ($\lvert \eta \rvert < 3.2$)	$\sigma_E/E = 50\%/\sqrt{E} \oplus 3\%$
Forward ($3.1 < \lvert \eta \rvert < 4.9$)	$\sigma_E/E = 100\%/\sqrt{E} \oplus 10\%$
Muon spectrometer	$\sigma_{p_{\mathrm{T}}}/p_{\mathrm{T}} = 10\%$ at $p_{\mathrm{T}} = 1$ TeV

allowing for the determination of the particle's charge and momentum, as described above.

There are three sub-detector technologies used in the ATLAS Inner Detector arranged in concentric cylinders around the beam line. From the pp-interaction point outwards, particles first pass through the Pixel detector, then the Silicon Microstrip Tracker (SCT), followed by the Transition Radiation Tracker (TRT). The Pixel detector and the SCT both use a semi-conducting silicon technology while the Transition Radiation tracker consists of drift tubes. Each of the three sub-detectors is divided into a barrel region, consisting of cylindrical layers around the beam line, and an end-cap region, consisting of disks placed at fixed z. This geometry increases the detector coverage in η without a large increase in detector surface area, and minimizes the amount of material traversed by particles at large pseudo-rapidity.

The Inner Detector is of particular importance for this thesis, which aims to reconstruct displaced tracks and secondary vertices from massive long-lived BSM particles. The radial positions of the Pixel and SCT layers determine the size of the fiducial volume in which displaced vertices can be recon-

structed, as well as the precision of the impact parameter measurement for a given track. Figure 5.5 shows the layout of the ATLAS Inner Detector. The Pixel and SCT detectors are located in $|\eta| < 2.5$, and the TRT provides coverage up to $|\eta| = 2.0$.
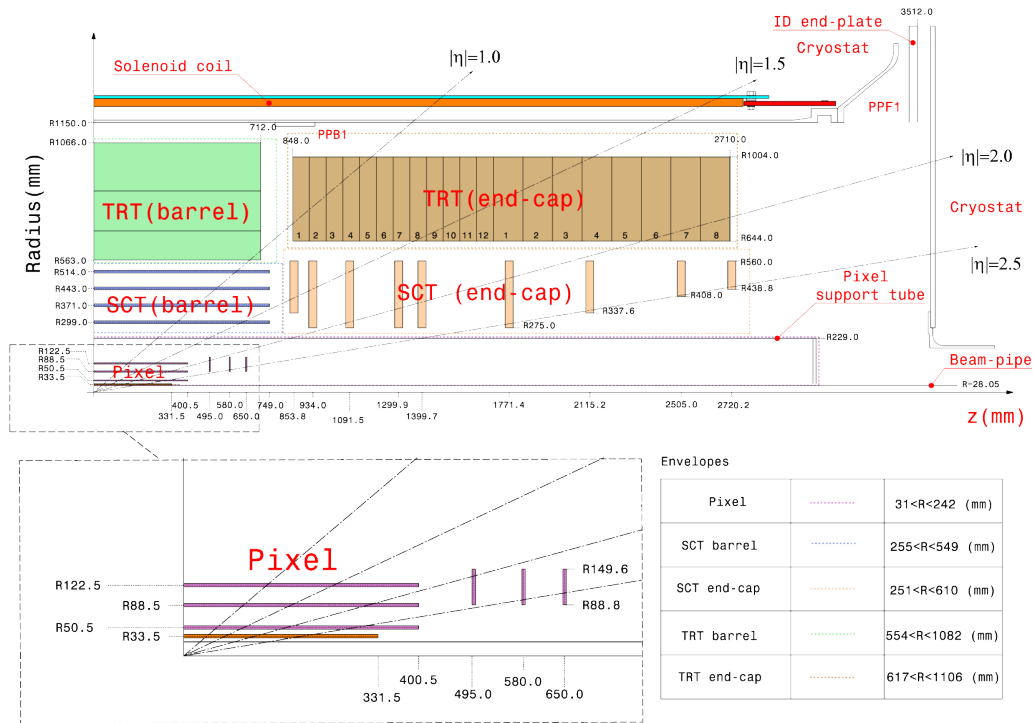
Figure 5.5: A quadrant of the ATLAS Inner Detector for Run 2, as seen in the R-z plane [53]. The top panel shows the entire Inner Detector, and the bottom-left panel shows a magnified view of the Pixel detector region. Lines are drawn to indicate various values of η.

5.5.1 PIXEL

The Pixel detector is the first sub-detector traversed by particles produced in ATLAS. The Pixel detector is a semiconductor-based tracker, and the most basic unit of the detector is a rectangular

pixel. Pixels provide a precise three-dimensional measurement, and the detector is particularly useful for impact parameter measurements and reconstructing secondary vertices from long-lived particles.

A schematic of an ATLAS Pixel module is shown in Figure 5.6. In ATLAS, hybrid pixels are used, where the sensing detector elements are individually bump bonded to readout electronics. Sensors are 250 μm thick, and use oxygenated n-type bulk. Readout pixels consist of n^+-implants on one side of the sensor with a p-n junction on the other side.
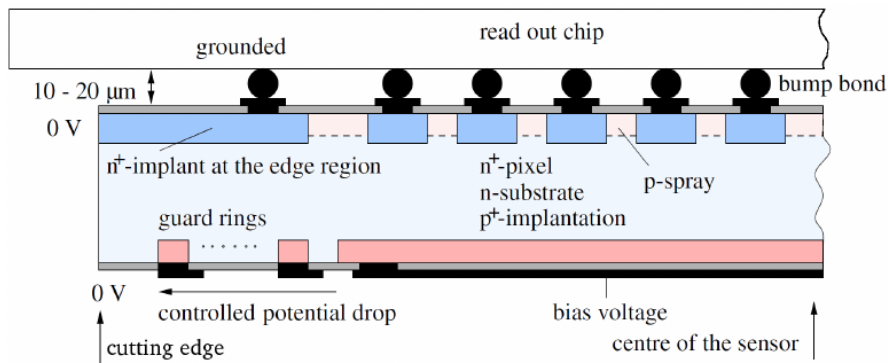
Figure 5.6: The cross section of a Pixel module is shown, which is not to scale. The sensor consists of an n-type bulk which is shown in light blue. The sensor has n^+-pixel implantations located on the top of the sensor in darker blue, and a p-n junction on the back side (where the light blue and pink meet). Connections between pixel sensors and the readout electronics are made by bump bonds (black) [54].

There are four concentric cylindrical layers of pixels in the barrel. These four layers surround the beam pipe, which is located at a radius of 24.3 mm. The Insertable B-Layer (IBL) is the inner-most layer of the Pixel barrel, and is located at a radius of 33 mm [55]. The IBL was installed before the start of Run 2, and is surrounded by the three layers of the original Pixel detector from Run 1. The second layer of the Pixel detector is the B-Layer, or Layer-0, which is located at a radius of 88.5 mm. The IBL and B-Layer are named for their vital role in identifying signatures from the decays of b-hadrons. The

third and fourth layers of the Pixel detector are known as Layer-1 and Layer-2, and are located at radii

of 88.5 mm, and 122.5 mm, respectively. The end-cap of the Pixel detector consists of three disks,

which are located at distances of 495, 580 and 650 mm from the interaction point in the z-direction.

The original Pixel detector consists of 80.4 million readout channels spread over 1744 Pixel modules. Each module consists of 16 silicon sensors with individual readout electronics. Each pixel sensor

consists of 47232 pixels, and pixels have a size of $50 \times 400 \ \mu\mathrm{m}^2$. Individual pixels in the barrel have

intrinsic accuracies of 10 μm in the $R\phi$-direction (the track bending direction) and 115 μm in the z-

direction (the non-bending direction). In the end-cap disks, individual pixels have intrinsic accuracies

of 10 μm in the $R\phi$-direction and 115 μm in R.

The IBL consists of 12 million pixels. The IBL is composed of fourteen identical units in ϕ, referred

to as staves. Each stave is composed of twelve planar silicon sensor models. The IBL also has 3D

modules located at the ends of the staves, with pseudorapidity $|\eta| > 2.5$, which are not used in

reconstruction. The size of IBL pixels in the planar modules is $50 \times 200 \ \mu\mathrm{m}^2$, which results in a

spatial resolution of 10 μm in the $R\phi$-direction, and 60 μm in the z-direction. As a result of the

smaller sized pixels used in the IBL, approximately 90% of the sensor area consists of active detecting

material. In comparison, roughly 70% of the original Pixel detector sensors consist of active detecting

material.

The IBL was installed for several reasons before the start of Run 2, around a new narrower and

smaller beam pipe than was used in Run 1. The smaller, and thinner beam pipe used in Run 2 re-

duces the amount of material traversed by particles before the first position measurement by the Pixel

detector. The smaller beam pipe allows the IBL to be positioned closer to the pp-interaction point,

reducing the extrapolation from the first hit measurement to the impact parameter of a track. The IBL also benefits from smaller sized pixels than the original three layers of the Pixel detector. Collectively, the thinner beam pipe, smaller pixel size, and closer measurement all improve the impact parameter resolution of tracks by a factor of two with respect to Run 1. The IBL also acts as shielding for the B-Layer. This shielding is important because the B-Layer would have died from radiation damage before the end of Run 3.

5.5.2   Silicon Microstrip Tracker

The SCT is a silicon strip detector, which is arranged in four cylindrical layers in the barrel, and nine layers of disks in the end-cap. Each layer is designed to make a three-dimensional point measurement of a track. The entire SCT provides at least four such point measurements per incident charged particle in $|\eta| < 2.5$. Strips are used instead of pixels at larger radii in order to reduce costs and the total number of readout channels.

Individual strip sensors contain 768 readout strips, separated by a 80 μm pitch. The area of a sensor is 6.36×6.40 cm^2. Pairs of sensors are wired bonded together, forming long strips with a length of 12.8 cm. Two of these pairs of sensors are then glued together, back-to-back, but at a 40 mrad angle with respect to each other, enabling a three-dimensional hit position measurement. These four sensors, and readout electronics, form a module. A schematic of an SCT module is shown in Figure 5.7

In the barrel, one set of strips runs parallel to the beam direction, and in the end-cap region one set of strips runs radially. The back-to-back sensor arrangement in SCT modules produces a hit position measurement with 17 μm resolution in the bending $R\phi$-direction. In the barrel, the resolution is
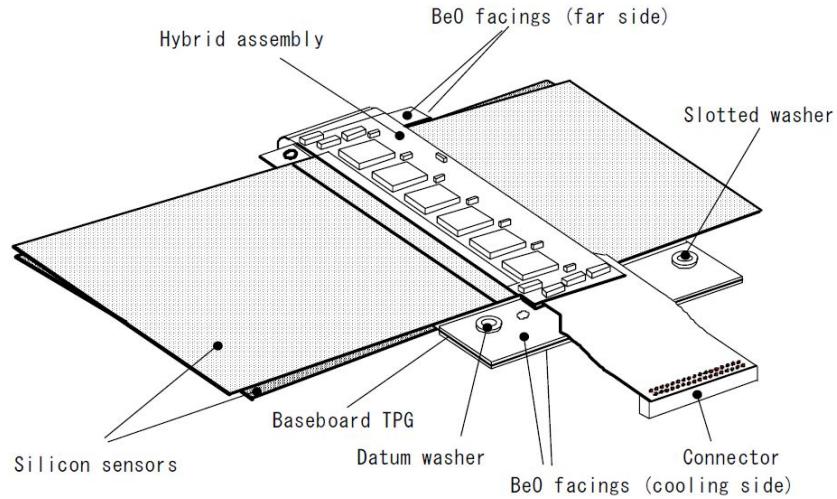
Figure 5.7: A schematic of SCT module design. Two silicon sensors (gray) are wire bonded together, and two of these pairs glued back-to-back at an angle to each other [56].

580 μm in the z-direction, and in the end-cap the resolution is 580 μm in the R-direction.

There are approximately 6.3 million readout channels in the entire SCT detector. The four cylindrical layers of the SCT barrel are placed 299, 371, 443 and 514 mm away from the interaction point in the radial direction. The end-cap disks are placed at a distance ranging from 934 to 2720 mm from the interaction point along the beam direction.

5.5.3 TRANSITION RADIATION TRACKER

The Transition Radiation Tracker consists of straw drift tubes with 4 mm diameter, and has coverage extending up to $|\eta| = 2.0$. The detector is designed to provide improved transverse momentum

resolution with reduced costs in comparison to using a tracker which consists entirely of silicon. The TRT roughly doubles the length of the track measured in the radial direction (from $L = 0.5$ m to $L = 1.1$ m) corresponding to a factor of four improvement in the p_T resolution. The TRT also reduces the density of material in the tracker with respect to a fully silicon tracker, and increases number of measurements per track (the TRT provides ≈ 35 measurements per track, while the silicon detectors provide 7-8 measurements).

Straw tube walls are made from Kapton and aluminum, and a gold-plated tungsten wire runs through the center of of each tube. The straw wall is the cathode, which is held at 1530 V, while the wire is the anode, resulting gain of 2.5×10^4. The gas inside the tubes is a mix of 70% xenon, 27% carbon dioxide, and 3% oxygen.

The barrel of the TRT consists of 73 layers of 144 cm long straws, while 160 layers of 37 cm long straws are used in the end-caps. In the barrel, straws point parallel to the direction of the beam, and are placed at fixed ϕ. The wires are divided into two halves at $\eta = 0$. In the end-cap, straws are also placed at fixed ϕ, and straws point in the radial direction.

The straws have a position accuracy of 130 μm in the $R\phi$-direction. The position resolution in $R\phi$ is related to the accuracy to which the drift time can be calibrated. The straws provide no intrinsic η information, except that hits are positioned at the center of the straws. This corresponds to a resolution of approximately 42 cm in the z-direction in the barrel, and approximately 10 cm in the R-direction for the end-cap.

The maximum drift time for electrons produced by ionizing particles is 48 ns. This means that charge must be integrated over several bunch crossings. This effect results in higher occupancy than

the Pixel and SCT detectors, and makes pattern recognition more difficult. During Run 2, the TRT was at nearly full occupancy for highest instantaneous luminosities delivered by the LHC, reducing the efficiency of reconstructing a track from an incident particle.

5.6 Calorimeter

The ATLAS Calorimeter is separated into an Electromagnetic Calorimeter and a Hadronic Calorimeter. The Electromagnetic Calorimeter is designed to accurately detect and measure the energy of electrons and photons. The Hadronic Calorimeter is designed to absorb and measure the energy from hadronic showers.

Both the Electromagnetic and Hadronic Calorimeters are constructed from alternating layers of absorbers and active material. The absorbing layers produce showers from incident particles, and the active layers measure the energy of the resulting shower. This design is referred to as a sampling calorimeter, because the entire energy of the incident particle is not measured. Some of the energy is lost to the absorbers.

The ATLAS Calorimeter benefits from impressive absorption power, segmentation, and granularity. The ECAL varies between 24 and 27 radiation lengths deep, depending on the pseudorapidity. The combined depth of the ECAL and HCAL is greater than 10 interaction lengths. The central Calorimeter has seven sampling layers (if a presampling layer located before the solenoid is counted), the end-cap has eight, and the Forward Calorimeter has three.

5.6.1 Electromagnetic Calorimeter

The ECAL consists of two half barrels and two end-caps. The half barrels are separated by a small gap (4 mm) at $z = 0$. The barrel module covers $1250 < R < 2050$ mm and $|z| < 3100$ mm. The end-caps are divided into two coaxial wheels. An outer wheel covers the region $1.375 < |\eta| < 2.5$ and an inner wheel covers the region $2.5 < |\eta| < 3.2$. The ECAL uses liquid argon as the active layer, and lead plates as the absorbing layer, and is referred to as the Liquid Argon (LAr) Calorimeter. The lead plates are folded into an accordion geometry, designed to provide full coverage and symmetry in ϕ.

Table 5.3 contains details of the Electromagnetic Calorimeter geometry, including the locations of the detector in R and z, the coverage in pseudorapidity, as well as the segmentation of each layer. Over the region devoted to precision physics ($|\eta| < 2.5$), the ECAL is segmented in three layers in depth. For the end-cap inner wheel, which covers ($2.5 < |\eta| < 3.2$), the ECAL is segmented in two sections in depth and has a coarser granularity.

A small active layer referred to as the presampler is located before the solenoid. It is designed to correct for the energy lost by electrons and photons upstream of the Calorimeter. The first layer of the ECAL is 4 radiation lengths (X_0) thick, and only a fraction of the shower is deposited there. The first layer has fine segmentation in η, which provides a position measurement for photons, which is necessary because unconverted photons do not produce a track in the ID. This segmentation also helps to discriminate between neutral pions which decay to two photons ($\pi^0 \rightarrow \gamma\gamma$) and single photons. The second layer is approximately 16 radiation lengths in thickness, which is designed to contain the

vast majority of the electromagnetic shower. The energy deposited in the third layer helps to separate electromagnetic showers from hadronic showers. It also provides an estimate of energy which leaks out of the Electromagnetic Calorimeter.

The nominal operating voltage of the ECAL is 2000 V. Copper electrodes are placed at a distance of 2.1 mm from the absorbers, resulting in an average electron drift time of approximately 450 ns. Signals from multiple electrodes are summed, forming a cell. The signal shape from a cell is sampled five times, every 25 ns.

The energy resolution of the Electromagnetic Calorimeter is

$$\frac{\sigma(E)}{E} = \frac{10\%}{\sqrt{E}} \oplus 0.7\%, \tag{5.10}$$

where E is the energy of the cluster, $\sigma(E)$ is the resolution of the cluster, and $\oplus$ represents a sum in quadrature. The constant noise is around 250 MeV per cluster.

5.6.2 HADRONIC CALORIMETER

The Hadronic Calorimeter consists of several different detector technologies. Each detector is best suited to the energy resolution required as well as the radiation environment. Table 5.4 summarizes the granularity of each detector technology.

The barrel of the Hadronic Calorimeter, the Tile Calorimeter, consists of alternating tiles of steel as the absorber and tiles of plastic scintillating as the active material, and covers the range $|\eta| < 1.7$. Hadronic showers are generated in the steel tiles. The scintillating tiles produce a light signal that is

Table 5.3: Granularity and segmentation of the ATLAS Electromagnetic Calorimeter [50]

Layer	Granularity ($\delta\eta \times \delta\phi$)	Radiation lengths [X_0]
Presampler	0.025×0.1	—
Barrel		
Layer 1	$(0.025/8 \times 0.1) - (0.025 \times 0.025)$	≈ 4
Layer 2	$(0.025 \times 0.025) - (0.075 \times 0.025)$	≈ 17
Layer 3	0.05×0.0245	$\approx 1 - 10$
Endcap		
Layer 1 ($|\eta| < 2.5$)	$(0.025/8 - 0.025) \times (0.025 - 0.1)$	≈ 4
Layer 1 ($2.5 < |\eta|$)	0.1×0.1	≈ 25
Layer 2 ($|\eta| < 2.5$)	$(0.025 - 0.1) \times (0.050 - 0.1)$	≈ 26
Layer 2 ($2.5 < |\eta|$)	0.1×0.1	$\approx 3 - 11$
Layer 3 ($|\eta| < 2.5$)	0.05×0.025	$\approx 5 - 15$

proportional to the number of minimum ionizing particles produced in the shower. The light from the shower is transmitted to two photomultipliers on either side of the tile via wavelength shifting optical fibers. The Tile Calorimeter extends from an inner radius of 2.28 m to an outer radius of 4.25 m.

The Hadronic Calorimeter end-cap uses liquid argon as the active material and copper absorber, and covers the range $1.5 < |\eta| < 3.2$. The end-cap extends from $|z| \approx 4300$ mm to $|z| \approx 6100$ mm. For the nominal high voltage of 1800 V, the typical drift time for electrons is 430 ns.

The Forward Calorimeter (FCAL) is located at $3.1 < |\eta| < 4.9$, approximately 4.7 m from the interaction point in the z-direction. The FCAL is designed to provide a coarse energy measurement in a harsh radiation environment. The detector consists of liquid argon as the active material and copper and tungsten as the absorber. The gaps of liquid argon are smaller than those of the ECAL, in order to prevent the build up of ions and to produce a faster signal.

Table 5.4: Granularity and segmentation of the ATLAS Hadronic Calorimeter [50].

Detector	Granularity ($\delta\eta \times \delta\phi$)	Interactions lengths [λ]
Tile Calorimeter ($|\eta| < 1.0$)		
Layer 1	$(0.1 \times 2\pi/64)$	1.5
Layer 2	$(0.1 \times 2\pi/64)$	4.1
Layer 3	$(0.2 \times 2\pi/64)$	1.8
$(0.8 < |\eta| < 1.7)$		
Layer 1	$(0.1 \times 2\pi/64)$	1.5
Layer 2	$(0.1 \times 2\pi/64)$	2.6
Layer 3	$(0.2 \times 2\pi/64)$	3.3
LAr Endcap	$(0.1 \times 0.1) - (0.2 \times 0.2)$	≈ 10
Forward Cal		
Layer 1	(0.1×0.1)	2.66
Layer 2	$\sim (0.2 \times 0.2)$	3.68
Layer 3	$\sim (0.2 \times 0.2)$	3.60

The energy resolution for a single pion passing through the entire ATLAS Calorimeter in the barrel is

$$\frac{\sigma(E)}{E} = \frac{55\%}{\sqrt{E}} \oplus 2.3\% \oplus \frac{3.2\text{GeV}}{E}. \tag{5.11}$$

5.7 Muon Spectrometer

The Muon Spectrometer consists of four gaseous sub-detectors in a toroidal magnetic field. The Muon Spectrometer (MS) surrounds the Calorimeter, and is the outermost layer of the ATLAS detector. The Muon Spectrometer is designed to provide an independent measurement of the momentum of charged particles with $|\eta| < 2.7$ and trigger on charged particles up to $|\eta| < 2.4$. The layout of

the ATLAS Muon Spectrometer is shown in Figure 5.8.
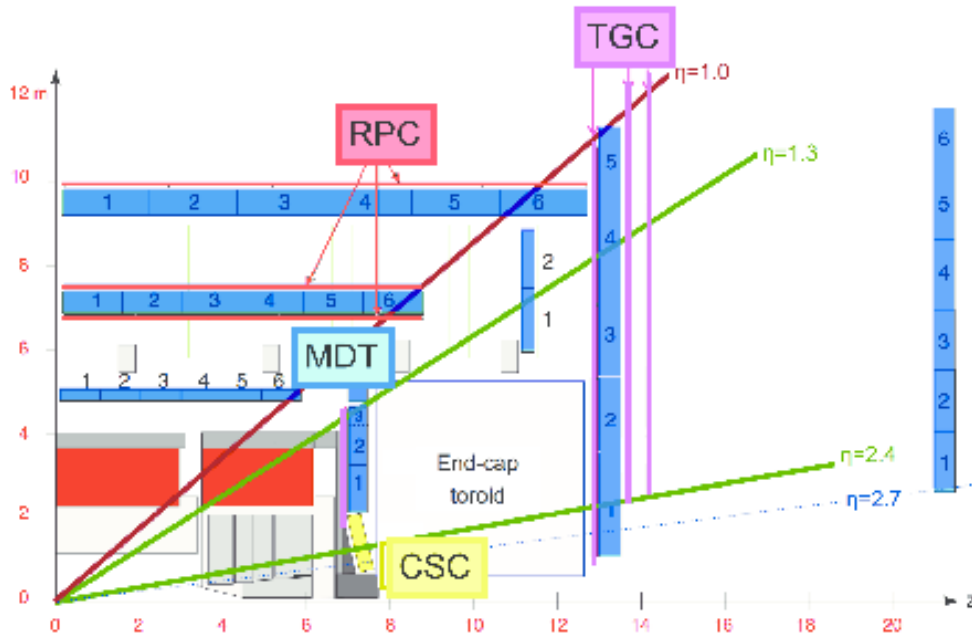
Figure 5.8: The ATLAS Muon Spectrometer is shown in the R-z plane. Four detector technologies are used. The Monitored Drift Tubes (blue) and Cathode Strip Chambers (yellow) provide precision tracking capabilities, and the Thin Gap Chambers (purple) and Resistive Plate Chambers (red) provide triggering capabilities. The end-cap toroid sits between the Inner and Middle station of the end-cap, and the barrel toroid sits between the Inner and Outer stations of the barrel [57].

The ATLAS Calorimeter is designed to stop all neutral hadrons, photons, and charged particles produced at the pp-interaction point, except for muons with momentum greater than approximately 3 GeV and neutrinos [58]. Because neutrinos are not expected to interact with the detector, muons should be the only high energy Standard Model particle which can produce a track in the Muon Spectrometer.

However, there are a variety of background sources which can produce tracks or hits in the Muon Spectrometer. For example, some hadronic or electromagnetic showers may not be fully contained in

the Calorimeter and *punch-through* to the Muon Spectrometer, producing tracks which are consistent with a jet. Calorimeter showers also produce low-energy neutrons and photons, which might reach the Muon Spectrometer as *cavern background*, producing hits which are not correlated with a track. Cosmic muons are another source of background, which produce tracks that do not point back to the pp-interaction point, and may also be out of time with respect to the collision.

The air-core toroid in the Muon Spectrometer provides a magnetic field with an average strength between $0.5 - 1$ Tesla. The toroid consists of eight coils in the barrel and eight coils in each end-cap, resulting in an eight-fold symmetry in ϕ. This magnet configuration provides a field which is mostly orthogonal to the muon trajectories. As a result of the magnetic field configuration, muons bend in η and have constant ϕ. Therefore, η is the precision coordinate.

In the barrel, chambers are arranged in three cylindrical layers around the beam axis. In the transition and end-cap regions, chambers are positioned in planes perpendicular to the beam. The three layers are referred to as the Inner, Middle, and Outer stations, indicating their relative proximity to the pp-interaction point. The chambers extend from the end of the Calorimeters, about 5 meters away from the beam line, to about 10 meters in the radial direction. In the end-cap, chambers extend from around 7 m to 20 m in $\pm z$.

The bending power of the toroid is characterized by the field integral $\int B \, dL$, where B is the magnetic field component which is normal to muon direction, and the integral is computed along an infinite-momentum muon's trajectory through the Muon Spectrometer. The barrel toroid provides 1.5 to 5.5 Tm of bending power in the pseudorapidity range $0 < |\eta| < 1.4$, and the end-cap toroids approximately 1 to 7.5 Tm in the region $1.6 < |\eta| < 2.7$. The bending power is lower in the

transition regions where the two magnets overlap ($1.4 < |\eta| < 1.6$).

The choice of air-core magnets minimizes the degradation of momentum resolution due to multiple scattering. Because the MS is capable of making a standalone muon momentum measurement, only the material muons encounter after exiting the Calorimeter contributes to the multiple scattering term in the momentum resolution. In the barrel, the cumulative amount of material traversed by a muon is about $1.3\ X_0$. Multiple scattering effects dominate the momentum resolution between 30 GeV and 200 GeV. In the end-caps, there is an increased amount of material, because the toroid has a heavier mechanical structure. Reconstructed tracks in the Muon Spectrometer may also be combined with a track in the Inner Detector, to further improve momentum resolution. More information about the momentum resolution of muons in ATLAS can be found in Section 6.3.

The Monitored Drift Tubes (MDT) and Cathode Strip Chambers (CSC) are used as precision tracking chambers. These precision chambers require multiple bunch crossings to collect charge produced from incident ionizing particles. As a result, separate detectors are used to provide triggering capabilities. Trigger chambers have a fast time response in order to provide bunch-crossing identification. Trigger chambers provide a coarse η measurement which is used to define p_{T}-thresholds in the trigger, and also measure the muon's azimuthal coordinate. Resistive Plate Chambers (RPC) are used to trigger in the barrel and Thin Gap Chambers (TGC) are used in the end-cap.

The Muon Spectrometer is of particular importance for this analysis, which selects displaced muons. Features of reconstructed muons, particularly features which result from the geometry of the MS are essential for rejecting muons from background sources.

One challenge for this analysis is the creation of low energy protons and neutrons produced be-

tween the first and section stations of the MS from interactions with the end-cap toroid. These lower energy protons and neutrons creates muon tracks with hits in only two stations, and do not necessarily point back to the pp-interaction point.

Another feature which is important for this analysis is the lack of detector coverage in the Muon Spectrometer near $\eta = 0$. These gaps in coverage extend from $\eta = 0$ up to $|\eta| = 0.04$ and $|\eta| = 0.08$, in order to leaves space for detector services to exit the detector. Another region of the Muon Spectrometer with a lack of coverage is the *feet* of the detector, where ATLAS is held up by supports, resulting in a lack of space for chambers.

5.7.1 Monitored Drift Tubes

In the barrel, MDT chambers are placed at a radial distance of 5, 7.5 and 10 m from the interaction point. Chambers are rectangular, and the drift tubes point perpendicular to the beam direction in order to make a precise η measurement. In the end-cap, chambers are placed on four wheels. The three main wheels are placed 7, 13, and 21 m away from the interaction point in $\pm z$. An additional, smaller wheel is placed on top of the end-cap toroid at a distance of 11 m from the interaction point. End-cap chambers are trapezoidal, and drift tubes are placed at fixed ϕ.

The most basic unit of the MDT is a drift tube which is approximately 3 cm in diameter. The drift gas consists of 90% argon with 10% carbon dioxide, and tubes are operated at a pressure of 3 bar. A tungsten-rhenium wire runs through the center of each tube, and is held at a potential of approximately 3 kV. Incident muons ionize the gas in the tube. The electric field is strong enough to produce an avalanche near the wire. The resulting electrons are collected along the wire, producing

a signal current. Tubes have a maximal drift time of approximately 700 ns, and the measured drift time is used to determine the distance from the center of the wire that the incident muon traversed the tube.

A schematic of a MDT chamber is shown in Figure 5.9. Chambers consist of two separated *multilayers*, where each multilayer consists of three *layers* of tubes. An exception is made for chambers in the Inner station of the MS, which have four layers of tubes per multilayer. The additional layers of tubes for Inner station chambers are included because interaction rates are higher in these regions, and the MDT hit efficiency decreases at higher rates. In the end-cap, MDT chambers extend up to up to $|\eta| = 2.7$, except for in the Inner station, where MDT chambers extend to $|\eta| = 2.0$. Background hit rates are too high for MDT chambers in the Inner station of the end-cap for $2.0 < |\eta| < 2.7$.
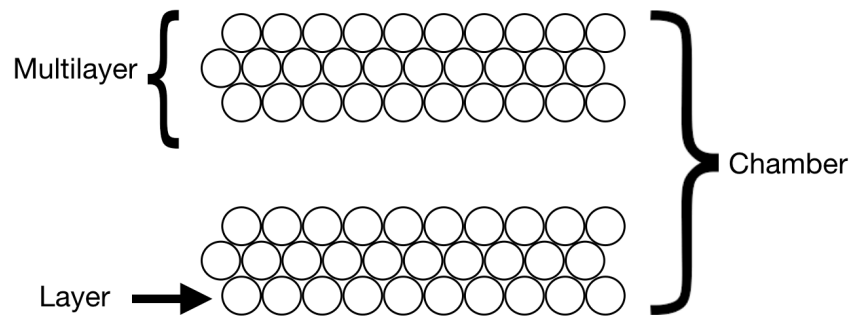
Figure 5.9: Schematic of an MDT chamber. Each chamber consists of two multilayers, and each multilayer consists of 3 or 4 layers of tubes.

Figure 5.10 shows an example of how a barrel MDT chamber is positioned in ATLAS. The η coordinate of the muon can be determined from the radius obtained from the drift time measurement.

94

The position resolution of a single tube is approximately $60 - 80$ μm in η, allowing for momentum resolution of $\sim 10\%$ for muons with $p_{\mathrm{T}} = 1$ TeV, and charge identification up to $p_{\mathrm{T}} = 3$ TeV. The position resolution of an MDT hit depends on the drift time measurement and alignment of the chamber. The MDT do not provide a position measurement in ϕ, except that hits are positioned at the center of the tube. This results in a position resolution of ≈ 0.11 radians in the ϕ-direction.
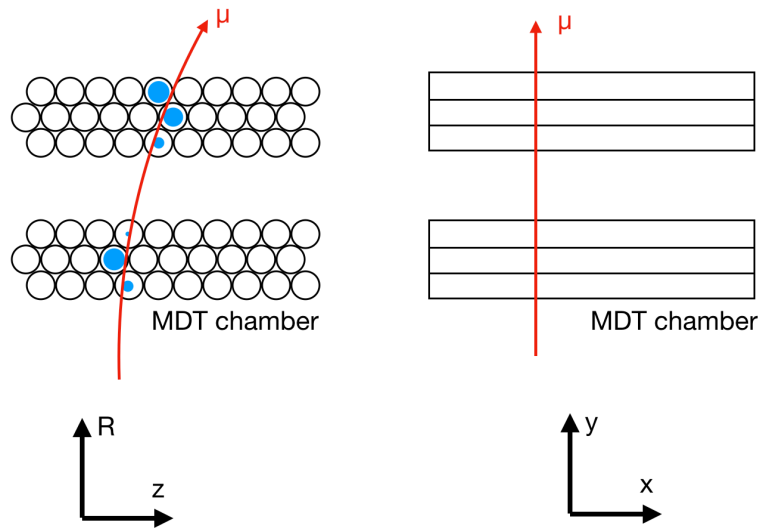
Figure 5.10: Views of an example barrel MDT chamber and incident muon in the R-z plane (left) and the x-y plane on the right. In the Muon Spectrometer, muons bend in η, and are straight in ϕ. MDT tubes measure the radius at which the incident muon traversed the tube. These radii are shown with blue circles. These radii are used to measure the η coordinate of the muon, while the ϕ measurement is taken to be the center of the tube.

The MDT are divided into 16 sectors in ϕ. Sectors in ϕ alternate between large and small rectangular chambers. The eight large chambers sit between the coils of the toroid, while the eight small chambers sit inside or along the toroid coils. In the barrel, alternating radial displacement between sectors allows for chamber overlaps and full coverage in ϕ. In the end-caps, alternating displacement

in z allows for chamber overlap.

The alignment of tubes with respect to each other is achieved using an optical laser alignment system. The alignment corrects for changes in tube position due to temperature, gravitational sag, and even the toroid turning on and off. The alignment of an entire chamber position is performed with data collected while the Toroid is off, resulting in straight tracks. Chambers are aligned with a precision ranging from 30 to 60 μm.

SMALL MDT CHAMBERS

In 2017, twelve new small Monitored Drift Tubes (sMDT) chambers were installed in the ATLAS detector. These sMDT chambers have tubes with a diameter of 1.5 cm, half the size of regular MDT chambers. These chambers have shorter charge collection times (by a factor of ≈ 4) and higher rate capabilities (by a factor of ≈ 8). These twelve new chambers were installed in ϕ sectors 12 and 14, where there is a limited amount of space for regular MDT chambers, in order to improve muon acceptance. Figure 5.11 shows the location of these sMDT chambers.

5.7.2   CATHODE STRIP CHAMBERS

CSC are installed in the Inner station of the Muon Spectrometer end-cap, at pseudorapidities of $2 < |\eta| < 2.7$. This region experiences the highest hit rate in all of the Muon Spectrometer. MDT chambers can only sustain hit rates of approximately 300 kHz per tube, or roughly 500 Hz/cm^2 without suffering drastic losses in efficiency. This region in pseudorapidity exceeds the hit rate capabilities for the MDT. In contrast, the CSC can sustain hit rates as high as on the order of 100 kHz/cm^2,
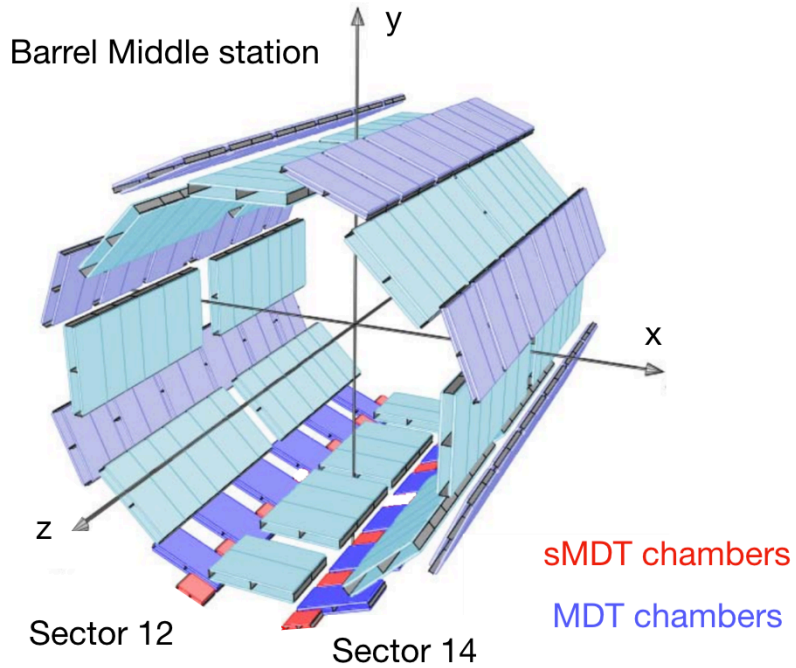
Figure 5.11: Locations of new sMDT chambers in ATLAS are shown. Chambers were installed in 2017, in the Middle station of the barrel. The new sMDT chambers are shown in red, while MDT chambers are shown in blue.

which is sufficient to survive in this region.

Cathode Strip Chambers are multi-wire proportional chambers which use a gaseous mixture of 80% argon and 20% carbon dioxide. Wires are held at a voltage of 1900 V, and point in the radial direction. Wires are sandwiched between two planes of strip cathodes. One plane consists of strips that point in ϕ and provide the precision η measurement. The second plane consists of strips that run parallel to the wires and provide a measurement of the azimuthal coordinate.

The wire signals are not read out, and the position of the incident particle can be obtained by mea-

suring a cluster position. The cluster position is obtained from measuring the relative amount of charge deposited on neighboring strips. Individual strip widths are 1.519 mm for large chambers and 1.602 mm for small chambers. The strip pitch is 5.31 mm for large chambers and 5.56 mm for small chambers, for the plane which provides the η measurement. This configuration corresponds to a position resolution of 60 μm in R. The CSC resolution in ϕ is approximately 5 mm. The spacing between the two cathode planes is 5 mm, which results in a maximum electron drift time of 40 ns.

The CSC are segmented into large and small chambers in ϕ. Each chamber consists of four layers, and produces four independent measurements of η and ϕ per incident particle. CSC chambers are positioned at an angle, such that muons from pp-interaction point will traverse the chambers at a perpendicular angle.

5.7.3 RESISTIVE PLATE CHAMBERS

RPC are used in the barrel in order to trigger on muons and provide a ϕ position measurement. The RPC have a fast drift time, of approximately 5 nanoseconds. After accounting for time spread due to the signal propagation and electronics, the timing resolution is between 15 and 25 ns, allowing the RPC to identify which bunch crossing produced the incident muon with greater than 99% probability.

The most basic unit of the RPC consists of two parallel resistive plates, which are separated from each other by 2 mm. Chambers are filled with $C_2H_2F_4$, and a voltage of 9.8 kV is applied between the two plates. The small gas gap and applied voltage results in an electric field of $4 - 5$ kV/mm, and produces a quick signal. Both sides of the chamber have readout strips. One side of the chamber has

strips that run in the z-direction, while the other side has strips that run in ϕ, measuring the azimuthal and precision coordinates respectively. Strips have a width of $25-35$ mm.

Each RPC chamber consists of two detector layers, and each chamber therefore makes two ϕ measurements and two η measurements. The RPC have the same sixteen-fold symmetry in ϕ as the MDT. RPC chambers are positioned on either side of the MDT chambers in the Middle station of the Muon Spectrometer barrel. A third set of chambers is located in the Outer station. In the Outer station, RPC are positioned outside of the MDT in the large sectors, while in the small sectors the RPC are positioned inside the MDT.

The RPC faced many operational challenges in Run 2. Several chambers experienced severe gas leaks, leading to reduced efficiency in various regions of the detectors. In addition, RPC chambers occasionally experience electronic noise, which leads to high, unsustainable, trigger rates. These chambers are occasionally excluded from data taking, reducing the trigger efficiency.

5.7.4 THIN GAP CHAMBERS

The TGC are multi-wire proportional chambers which measure the muon ϕ coordinate and provide triggering capabilities in the end-cap. Like the RPC, the TGC have a fast time response, and coarser spatial resolution than precision chambers.

The TGC principle of operation is similar to that of the CSC. The precision coordinate, η, is determined from the anode wires, while the ϕ measurement is made using cathode strips. Wires and strips run perpendicular to each other. The distance between the wires is 1.8 mm, and the distance from the wire to the cathode is 1.4 mm. The TGC use a gas mixture which contains 55% CO_2 and 45%

n-C_5H_{12}. Anode wires are kept at a nominal potential of 2.9 kV. Individual TGC chambers are made up of multiple gas gaps.

Unlike the other detectors in the MS, the TGC have 12-fold symmetry in ϕ. There are four layers of TGC chambers positioned at different locations in z (as shown in Figure 5.8). One layer is placed before the MDT and CSC chambers that make up the Inner station of the end-cap. This Inner station layer does not have full coverage in ϕ. The other three layers are located near the Middle station of the Muon Spectrometer end-cap. One of these layers is located behind the MDT, and the other two are located afterwards.

6

Reconstruction

Event reconstruction is the process which converts electronic detector signals into measurements of particles produced in the collision. Reconstruction is usually a multi-stage process, first using detector signals to identify hits or form intermediate objects such as tracks and clusters. This process culminates in finding particle-like signatures, which enable the measurement of physical properties of the incident particles, such as their charge, momenta, or energy. Particle identification takes the reconstructed objects in an event and works to combine and classify these objects into physics objects such as electrons, muons, or jets.

This section focuses on aspects of reconstruction and particle identification which are of particular interest for this analysis. The first sections focus on *standard* reconstruction algorithms, which are used by all ATLAS analyses. The process of reconstructing Inner Detector tracks is described in

Section 6.1, and the process of identifying primary vertices is described in Section 6.2. Muon reconstruction, which uses information from both the Inner Detector and Muon Spectrometer, is described in Section 6.3. The process of reconstructing topological clusters in the Calorimeter is described in Section 6.4, as well as how those clusters can be used to compute the event's missing transverse energy.

Note that this analysis makes use of *non-standard* reconstruction algorithms. The standard ATLAS Inner Detector tracking algorithms are designed to reconstruct the trajectories of primary particles, and only reconstruct tracks with small impact parameters ($|d_0| < 10$ mm). An additional pass of tracking targeting large displacement is made to retain efficiency for tracks produced in long-lived particle decays, which is described in Section 6.5.1. These non-standard reconstruction algorithms also involve the reconstruction of displaced vertices, which is described in Section 6.5.2.

The additional pass of tracking and secondary vertex reconstruction are both computationally intensive. In order to save computing time, the non-standard reconstruction methods used in this analysis are only applied to a subset of the ATLAS Run 2 dataset. This subset of data is selected using a few triggers of interest and making loose object selections, for several ATLAS long-lived particle searches. The process of selecting which events are reconstructed is described in Section 8.1.1.

This section does not discuss the reconstruction of jets, electrons, photons, and taus. Nor does it discuss the algorithms used to identify jets containing *b*-hadrons. These processes are described elsewhere [59–62]. However, it is important to note that the analysis presented in this thesis does reconstruct these physics objects. Though no explicit requirements are made on jets or electrons, an overlap removal procedure is performed in order to avoid double counting of muons which are reconstructed as two different close-by objects. More information about these other physics objects which are used

in the analysis and the overlap removal procedure is provided in Section 9.3.

6.1 Inner Detector Track Reconstruction

The process of converting Inner Detector hits into the trajectories of charged particles is a complex task. At the LHC, this task is complicated by a high density of charged particles, resulting from the multiple pp-collisions that occur per event. Each event contains thousands of particles, which produce tens of thousands of hits in the tracking detector. These hits must be combined to produce a coherent picture of what occurred during the event. The hits produced by a single charged particle must be reconstructed as a track, which represents its trajectory through the detector.

The complexity of this task is demonstrated in Figure 6.1, which shows an event display from the first data-tacking run with stable beam collisions in Run 2. The main image shows an x-y view of the Inner Detector, zoomed in on the silicon layers. The trajectories of particles are bent in ϕ by the solenoidal magnetic field, which points in the z-direction. The bottom right image shows the R-z view of the event, where it is clear that there are multiple pp-collisions. This event has 17 reconstructed primary vertices, roughly half than average number of primary vertices per event in Run 2.

As discussed in Section 5.4, the trajectory of a charged particle in a solenoidal magnetic field is reconstructed as a helical track. In ATLAS, charged particles must have transverse momentum greater than ≈ 0.3 MeV to form a track. Otherwise the particle's radius of curvature will be so small that the particle will produce loops at small radii, never reaching the outer layers of the tracker.

Tracks are defined by their charge, as well as their momentum and position measured at any given
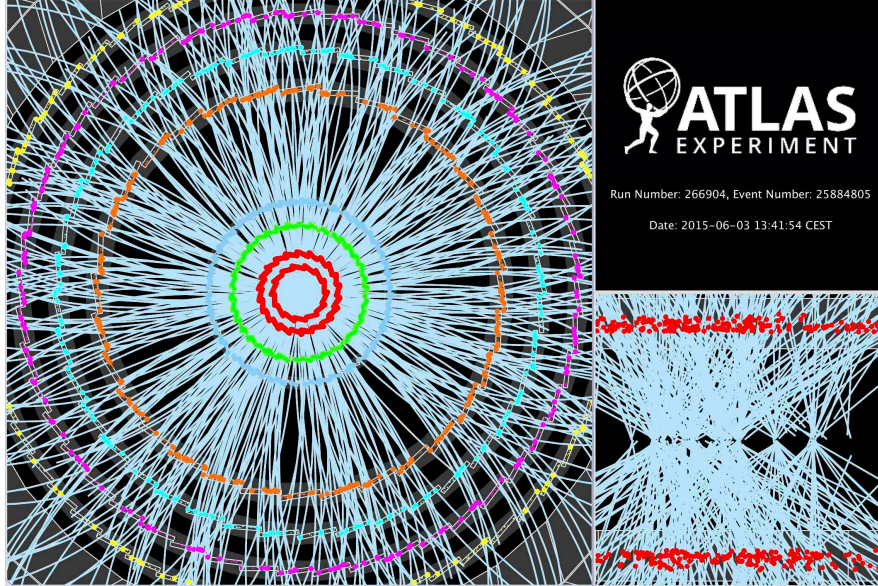
Figure 6.1: Display of a proton-proton collision event recorded by ATLAS on 3 June 2015, with the first LHC stable beams at a collision energy of $\sqrt{s} = 13$ TeV. The main view shows the Inner Detector in the x-y plane. Tracks reconstructed by the Inner Detector are shown as light blue lines, and hits in the layers of the silicon tracking detector are shown as colored filled circles. The four inner layers are part of the Pixel detector and the four outer layers are part of the SCT. The view in the bottom right shows the R-z view of the same event, and is zoomed in to show hits from the IBL only [63].

point along the track. In ATLAS, the track's position and momentum are expressed at the distance of closest approach with respect to the beam-spot, unless otherwise specified. A track's transverse impact parameter, d_0, and longitudinal impact parameter, z_0, represent the radial and longitudinal distances from the distance of closest approach to the beam spot. A track's position and momentum may be computed at any other point, given knowledge of the magnetic field and the detector material, by a process called *track extrapolation*.

Standard ATLAS track reconstruction is optimized for particles which originate at the pp-interaction point, or *primary particles*. There is sensitivity to secondary particles from specific topologies, most

notably the decays of *b*-hadrons, but these algorithms target particles with small impact parameters, or d_0 on the order of a few millimeters. Strict requirements of $|d_0| < 10$ mm and $|z_0| < 250$ mm are placed on reconstructed tracks in order to reconstruct primary particles with high efficiency and reasonable computation time.

This strategy is not ideal for searches which aim to detect the decay products of long-lived particles (with lifetimes of approximately $0.1 < \tau < 10$ ns), which decay with significant displacement from the primary vertex. In order to retain sensitivity to highly displaced tracks ($|d_0| < 300$ mm and $|z_0| < 1500$ mm), an additional pass of tracking is used in this analysis. This section focuses on the standard ATLAS tracking procedure. The dedicated tracking algorithm for long-lived particle searches is described in Section 6.5.1.

The majority of tracks from promptly decaying particles are reconstructed by the *inside-out* algorithm. In this algorithm, seed tracks are first formed in the silicon detectors, and then extrapolated to the Transition Radiation Tracker. A second pass of tracking is referred to as an *outside-in* algorithm because tracks are seeded in the TRT, and then extrapolated to the silicon detectors. This outside-in algorithm is designed to recover tracks that were not reconstructed due to detector inefficiency, or because the tracks originated from particles that decayed inside the silicon detector volumes. This thesis emphasizes the first algorithm because the non-standard tracking algorithm used by the analysis, is based on the *inside-out* algorithm.

The first step in finding Inner Detector tracks is to take information from the silicon detectors and convert it to three-dimensional spatial information, or *space-points*. For the Pixel detector this step is easy, because individual hits form clusters which immediately provide two-dimensional information

in $\phi \times z$, and the Pixel layer's location provides R (in the cylindrical layers). For the SCT, space-point formation requires hits from two adjacent layers of strips. The two layers of strips are positioned at an angle with respect to each other, and with the beam-spot as a constraint, can be used to find three-dimensional spatial information. An example of an SCT space-point is shown in Figure 6.2.
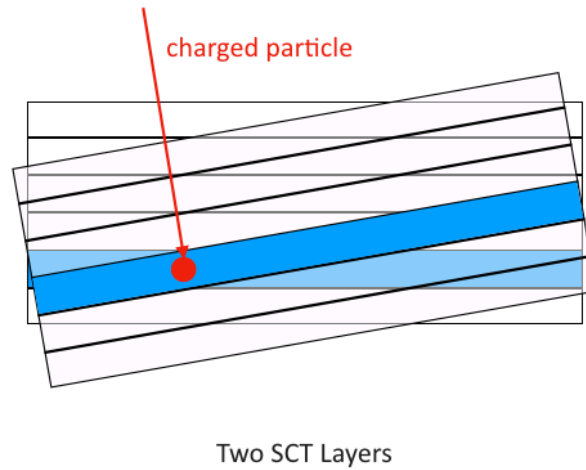
Figure 6.2: Three dimensional space-point information from the SCT. In the SCT two layers of strips are used to form clusters. Strips which have hits are shown in blue, and the angle between these two strips is used to find three dimensional information.

These silicon space-points are used to seed track reconstruction. Track seeds, shown in Figure 6.3, are formed by matching combinations of three space-points from the silicon detectors to pre-built templates. These templates correspond to tracks that are consistent with a given momentum and transverse impact parameter. Track seeds are used to define wide *roads*. Roads define a range in η and ϕ, in which the algorithm looks to add hits, in order to extend the length of the track, as shown in Figure 6.3.

Once seeds and roads have been formed, space-points are no longer used in the track reconstruction process. From this point on, the original detector hits are used to fit tracks. The reason for using the detector hits instead of space-points is that some hits may not be associated to space-points.

The process of extending the track length to all layers of silicon detectors is performed using a Kalman Filter algorithm [64]. The Kalman Filter algorithm alternates between fitting the track, and identifying which hits should be added to the track. The algorithm first uses the hits associated to the current track to estimate the track's parameters and uncertainties. This estimate is used to make a prediction about where the next hit along the length of the track will be located. If a potential hit is identified, and is consistent with the original prediction, the hit is added to the track. The track's parameters are updated, and another prediction is made about the next hit location. This process continues iteratively until the end of the track is reached (i.e. there are no more available layers in the silicon detector). Once the end of the track is reached, a final refit of the track parameters is performed with a detailed detector geometry, in order to fully account for effects from multiple scattering, resulting in a *track candidate*. An example of a track candidate is shown in Figure 6.3.

At this stage, hits can belong to several track candidates. Several track candidates are incomplete, and other track candidates are reconstructed from hits associated to multiple particles. In order to resolve the ambiguity between track candidates, candidates are ranked according to a scoring procedure. This score incorporates the track quality of fit (χ^2/N_{DoF}), the number of associated hits (in order to favor fully reconstructed tracks), and weights hits according to their precision (Pixel clusters are favored over SCT hits). Penalties are also applied to tracks which traverse an active layer of material that is missing a hit (referred to as a track *hole*). Hits that are shared between track candidates are generally
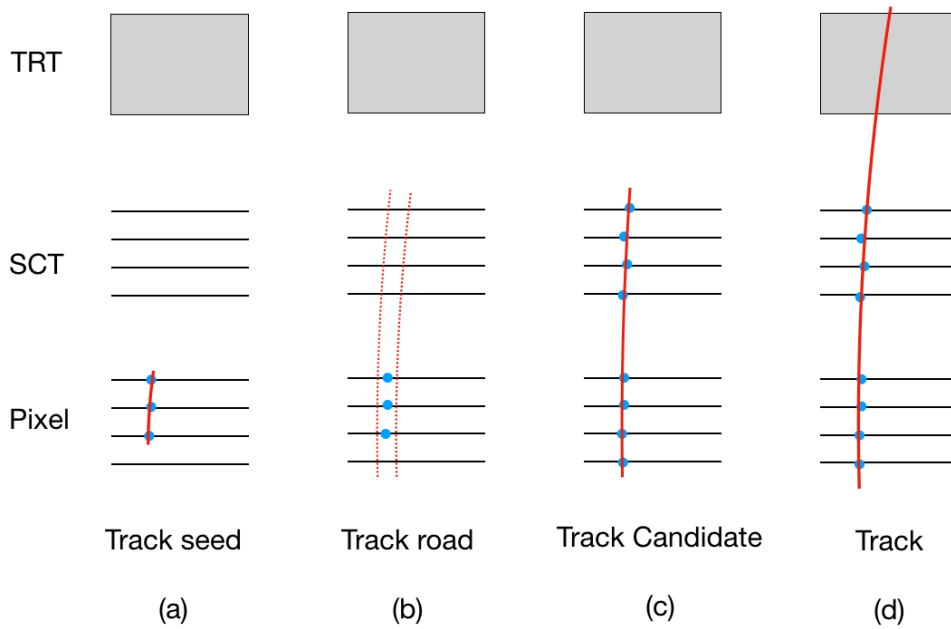
Figure 6.3: A cartoon of steps in track reconstruction. Four layers of the Pixel detector, four layers of the SCT, and the TRT are shown. (a) Track seeds are formed from the combination of three space-points in the silicon detectors. (b) Track seeds are used to construct roads, and roads are used to search for hits which can be used to extend the length of the track to other layers. (c) The Kalman Filter is used to find track candidates, which consist of silicon hits. (d) Tracks are formed from a track candidate and its TRT-extension.

given to the candidate with a higher score, and refits of the new track candidates are performed. This process is repeated until no hits are shared between track candidates. Finally, track candidates with a score below a certain threshold are discarded.

The final step in the inside-out algorithm is to extrapolate tracks into the TRT. The silicon track candidate is used to define a road, and within the road a search is made for TRT hits. If TRT hits located inside the road are found, they are added to the silicon track candidate as a TRT-*extension*. A full refit of the track is performed to obtain the final track parameters. If the combined track has a higher score than the silicon track candidate, the parameters from the combined track are used. If the

silicon track has a higher rank than the full track, the silicon track parameters are used instead.

The *outside-in* algorithm is then run on any remaining hits which are not already associated to tracks. The outside-in algorithm first forms track candidates from TRT hits. In a subsequent step, hits in the Pixel and SCT are checked for compatibility with the candidate.

ATLAS has two pre-defined track selections: `Loose` and `Tight`. The `Loose` selection aims to select tracks with high efficiency, at the cost of reconstructing *fake* tracks, which are reconstructed from an accidental combination of hits. The `Tight` selection is optimized to reject fake tracks, at the cost of reduced tracking efficiency. The `Loose` quality requirements are summarized in Table 6.1, and the `Tight` selection is defined in Table 6.2

Table 6.1: `Loose` track quality requirements

$$p_\mathrm{T} > 500\ \mathrm{MeV}$$
$$|\eta| < 2.5$$
$$N_{Si} \geq 7\ \text{(Number of silicon hits i.e. Pixel + SCT, including dead sensors)}$$
$$N_{mod}^{\mathrm{sh}} \leq 1\ \text{(Number of shared silicon hits: i.e. hits assigned to multiple tracks)}$$
$$N_{Si}^{\mathrm{hole}} \leq 2\ \text{(Number of silicon holes, i.e. missing hits in the Pixel detector and the SCT)}$$
$$N_{Pix}^{\mathrm{hole}} \leq 1\ \text{(Number of Pixel holes, i.e. missing hits in the Pixel detector)}$$

Table 6.2: `Tight` track quality requirements

$$\text{In addition to the Loose quality requirements}$$
$$N_{Si} \geq 9,\ (\text{if } |\eta| < 1.65)$$
$$N_{Si} \geq 11,\ (\text{if } |\eta| > 1.65)$$
$$\text{At least one hit on one of the two innermost Pixel layers}$$
$$N_{Pix}^{\mathrm{hole}} = 0$$

The efficiency for reconstructing a track as a function of its transverse momentum p_T and pseudo-

rapidity η is shown in Figure 6.4. The efficiency of reconstructing an Inner Detector track is defined as the fraction of particles with $p_T > 500$ MeV and $|\eta| < 2.5$ which are matched to a reconstructed track in simulation.
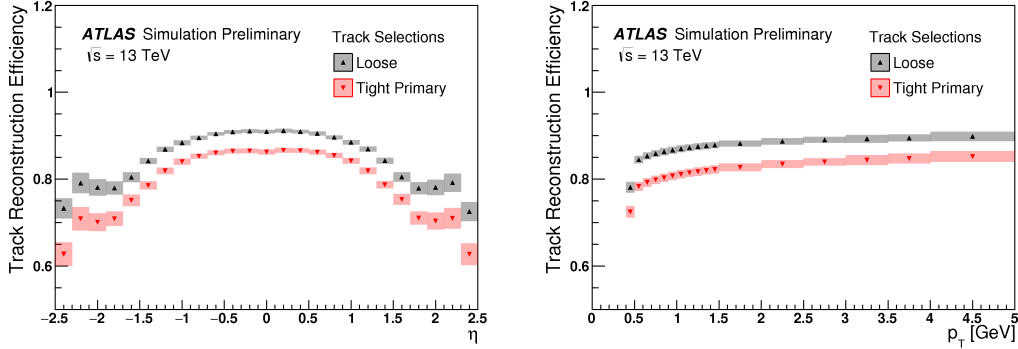
Figure 6.4: Inner Detector track reconstruction efficiency as a function of η (left) and p_T (right). The efficiency is shown for two selections of tracks, and is computed from simulation [65].

Tracks with $p_T > 500$ MeV and $|\eta| < 2.5$ are within the geometrical acceptance of the Inner Detector. However, the efficiency for reconstructing a track decreases with decreasing transverse momentum, due to the increased probability of multiple scattering. Tracking efficiency is also reduced as a function of increasing η. Tracks with large η traverse a higher density of material, also increasing the probability of multiple scattering. The `Loose` selection has a tracking efficiency between 73% and 91%, while the `Tight` selection has an efficiency between 63% and 86%.

Figure 6.5 shows the average number of reconstructed tracks as a function of $\langle\mu\rangle_{\text{bunch}}$, the average number of interactions per bunch crossing. The number of tracks which are reconstructed from genuine charged particles should be proportional to the number of pile-up interactions. Any deviation above linearity in Figure 6.5 is due to fake tracks, which are reconstructed from an accidental combina-

tion of hits, and do not correspond to a real charged particle. The `Loose` track selection has non-linear

behavior for $\langle\mu\rangle_{\mathrm{bunch}} > 30$, while the `Tight` selection is linear for all $\langle\mu\rangle_{\mathrm{bunch}}$.
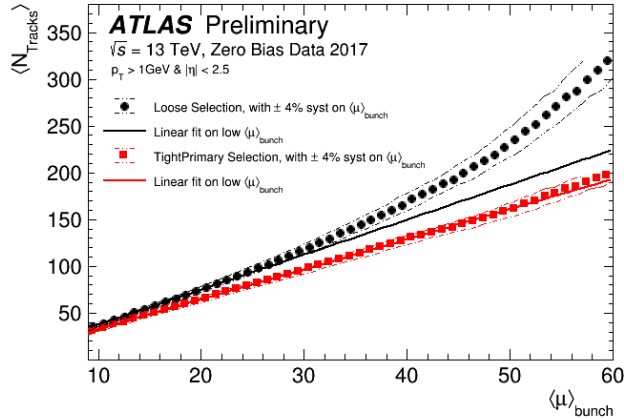
Figure 6.5: Average number of charged particle tracks that pass a preselection of $p_\mathrm{T} > 1$ GeV and $|\eta| < 2.5$ reconstructed per event in the ATLAS Inner Detector as a function of $\langle\mu\rangle_{\mathrm{bunch}}$, for the `Loose` and `Tight` track selections. $\langle\mu\rangle_{\mathrm{bunch}}$ is the estimated mean number of inelastic interactions per bunch crossing, averaged over all colliding bunches. The solid lines show a linear fit to the data in the region $9 < \langle\mu\rangle_{\mathrm{bunch}} < 16$, and extended to higher $\langle\mu\rangle_{\mathrm{bunch}}$. The $\pm4\%$ systematic variation on $\langle\mu\rangle_{\mathrm{bunch}}$ represents a preliminary estimate of the impact of present uncertainties associated with the luminosity measurement [66].

6.2   Primary Vertex Reconstruction

In the dataset used in this analysis, there are an average of 33 pp-interactions per event. These interactions are reconstructed as primary vertices. Reconstructing primary vertices is essential for identifying which physics objects were produced at a primary vertex of interest, and which physics objects were produced at a pile-up primary vertex. The process of reconstructing primary vertices is separated into two steps, vertex finding and vertex fitting. More information regarding the details of primary vertex reconstruction can be found in Reference [67].

The process of finding the position of a primary vertex begins with selecting Inner Detector tracks that satisfy the `Tight` quality requirement. The longitudinal location of the vertex is estimated by computing the global maximum of the longitudinal impact parameter z_0 of all selected Inner Detector tracks. The impact parameter z_0 is computed with respect to the center of the beam spot in the z-direction.

In the second step of vertex finding, an iterative procedure is used to refine the vertex position. Tracks which are close by the z_0 maximum are used to seed vertex reconstruction. Each input track is assigned a weight, reflecting its compatibility with the primary vertex. The vertex position is recalculated using the weighted tracks, and track weights are recomputed. This procedure is repeated until the vertex location no longer changes.

Once a primary vertex is found, tracks which are incompatible with the primary vertex by seven standard deviations are removed from the primary vertex. These discarded tracks are used to search for another primary vertex seed. This process is repeated until all tracks have been reconstructed into primary vertices or no additional vertices can be found.

Once all vertices have been found, vertices are additionally required to have at least two tracks and $|z_{\mathrm{PV}}| < 200$ mm. For events which have multiple primary vertices, the vertex with largest $\Sigma(p_{\mathrm{T}}^{trk})^2$ is selected as the primary vertex, and the other vertices are treated as pile-up vertices.

The positions of reconstructed vertices can in turn be used to determine the size, position, and shape of the beam spot. The transverse size of the beam spot is determined by the focusing of LHC beams, while the longitudinal size of the beam spot is determined by the bunch length and by the angle at which the two proton beams cross. Typical Run 2 sizes of the beam spot are of about 15 μm

in the transverse direction, and 45 mm in the longitudinal direction. During the course of Run 2, the position of the beam spot moved by as much as 0.1 mm in the transverse direction, and ~ 40 mm in the longitudinal direction, due to various adjustments of LHC parameters.

6.3   Muon Reconstruction

The reconstruction and identification of muons is based on information from the Inner Detector, Calorimeter, and Muon Spectrometer. This section focuses on the algorithms performed in the Muon Spectrometer, and the process of combining information from all three sub-detectors. More information regarding the details of muon reconstruction and performance can be found in Reference [68].

There are many challenges associated with reconstructing tracks in the Muon Spectrometer. The magnetic field produced by the Toroid is non-uniform, so there is no simple way to model the trajectory of charged particles. In contrast, in the Inner Detector, the magnetic field is of uniform strength in the z-direction, and tracks can be easily described as helices. An additional challenge for pattern recognition in the MS is that there are stark differences between the η and ϕ information available from the four muon sub-detectors (as described in Section 5.7). The MDT only provides precision η information, and a rough ϕ measurement is obtained from the position of the tube. Furthermore, MDT chambers are physically separated from the RPC and TGC chambers which provide ϕ measurements.

Generally, there are four major steps in muon reconstruction. The first step converts raw detector signals to a position measurement. The second step uses the position measurements within an indi-

vidual chamber to reconstruct a short track, referred to as a *segment*. Then, segments from multiple chambers are used to reconstruct a *Muon Spectrometer track*. Finally, the MS track is combined with an Inner Detector track to form a *combined muon*, in a process which also accounts for energy lost in the Calorimeter. Figure 6.6 shows an illustration of the last three major steps.
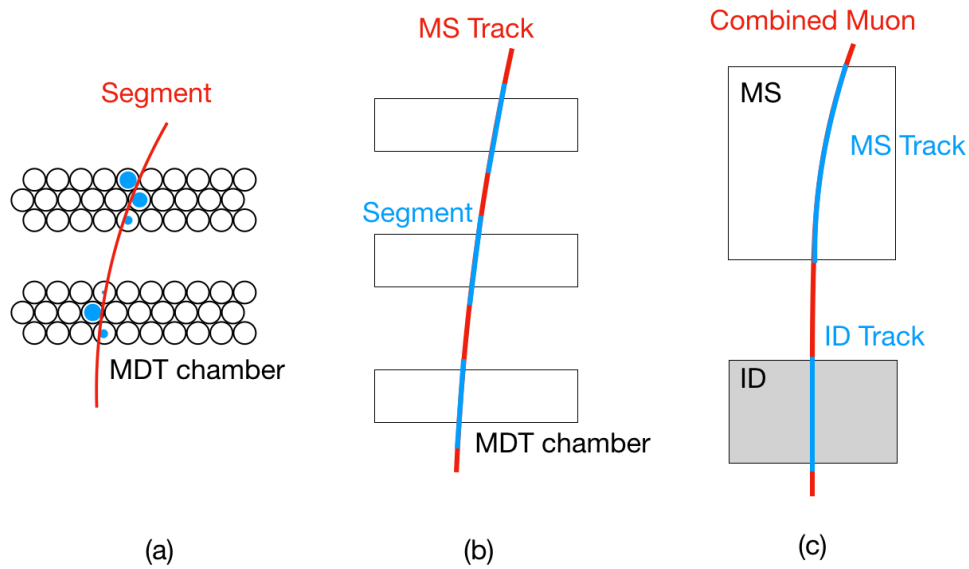
Figure 6.6: A cartoon with steps of muon reconstruction. Each sketch is drawn in the *R-z* plane. Trigger chambers are ignored for simplicity, and figures are not to scale. In (a), a segment, shown in red, is reconstructed using the position measurements, in blue, from an individual MDT chamber. In (b), segments from multiple chambers, shown in blue, are used to reconstruct a Muon Spectrometer track, shown in red. In (c), the Muon Spectrometer track, in blue, is combined with an Inner Detector track, also in blue, to form a combined muon, shown in red.

6.3.1   Hit calibration

The first step in muon reconstruction is to take the detector signal, as measured by an MDT tube, and convert it to a radial measurement, or *drift circle*. Figure 6.7 shows an example of a muon travers-

ing a single MDT tube. The radius R_{min} is defined as the smallest distance between the muon's trajectory and the wire, and defines the radius of the drift circle. As the muon traverses the tube, the muon ionizes the gas and produces primary electrons. The primary electrons drift towards the anode, and eventually form an avalanche of secondary electrons near the wire. The induced signal propagates through the wire to the end of the tube, where it reaches the readout electronics.
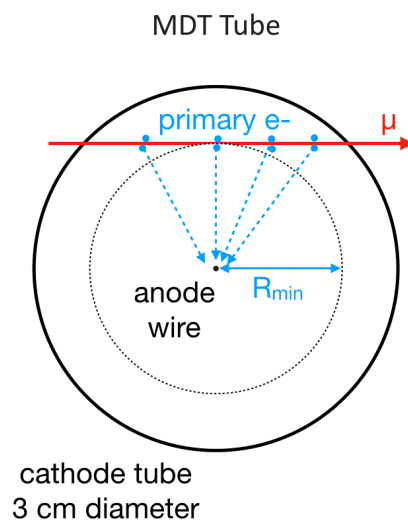
MDT Tube

Figure 6.7: Cross section of an MDT tube, shown in black, with a traversing muon, shown in red. The muon frees primary electrons, shown in blue, as the muon traverses the tube. The primary electrons subsequently drift towards the anode wire, eventually forming an avalanche near the wire. The induced signal propagates through the wire to the end of the tube, where it reaches readout electronics, and the timing information is used to measure the radius of the drift circle, R_{min}.

The readout electronics send the signal through an amplifier, shaper, and discriminator. The signal is then sent through an analog to digital converter, which saves a time measurement. This time measurement has several contributions. These contributions include the time of flight for the particle to reach the tube, the time for the signal to propagate through the tube, the time delay due to cabling and

electronics, and the *drift time*. The drift time is the time between primary ionization, and the arrival of the electrons at the wire. The drift time can be used to make a measurement of $R_{\min}$.

In order to obtain the drift time, a timing offset, t_0, is subtracted from the hit time measurement. This timing offset is measured for each individual tube, using fits to the spectrum of hit measurements for hits associated with muons. An example hit time spectrum is shown in Figure 6.8, which shows the t_0 offset and $t_{\max}$ (known as the maximum drift time) of the distribution. Qualitatively, muons with hit times close to t_0 traverse the tube near the central wire, while muons with hit times close to $(t_0 + t_{\max})$ traverse the tube close to the tube wall. The $t_{\max}$ is not used in reconstruction, but is used to monitor the tube performance. Both the t_0 and $t_{\max}$ are sensitive to a variety of parameters, including the gas composition, tube environment, and electronics.
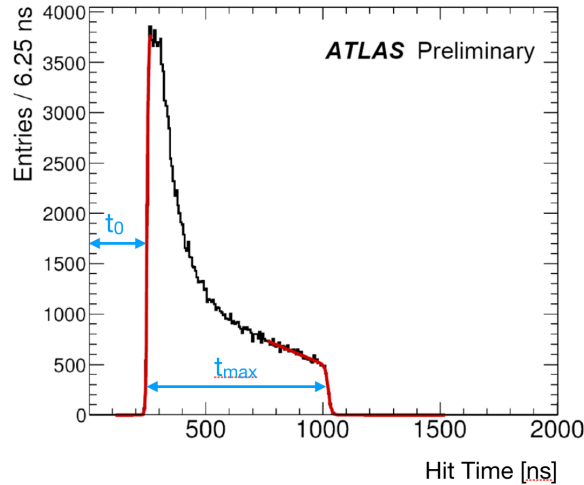
Figure 6.8: An example distribution of MDT hit time measurements. The hit time has been converted to nanoseconds, and only hits which are associated to muons are included. The t_0 and $t_{\max}$ are shown in blue, and fits used to obtain the t_0 and $t_{\max}$ are shown in red [69].

After the t_0 has been subtracted, the hit time is equivalent to the drift time. A radius-time relation-

ship, or *rt-relation*, can be used to convert the drift time into the final position measurement, a drift circle with radius R_{min}. Figure 6.9 shows an example rt-relation of a single MDT tube. There is a non-linear relationship between R_{min} and the drift time, due to the electric field inside the tube, which scales inversely with the radius of the tube. The rt-relation is roughly estimated from simulation, but is calibrated with data in order to account for changing environmental conditions.
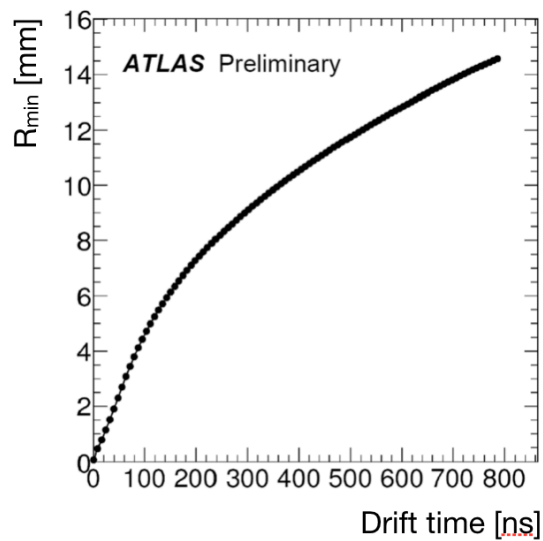
Figure 6.9: An example radius-time relation for a single MDT tube. The x-axis shows the drift time in nanoseconds (the drift time is obtained from calibrated hits), and the y-axis shows the drift circle radius, or R_{min} [69].

6.3.2   Muon Segments

Sets of Muon Spectrometer hits are then reconstructed as short tracks within individual stations of the Muon Spectrometer. These short tracks are known as segments. Segment reconstruction is seeded by using a Hough Transform [70] pattern matching algorithm. The Hough Transform searches for

patterns of hits that could belong to the same muon. Patterns are made in the R-z plane, called η patterns, from MDT hits, and patterns are also made in the x-y plane, called ϕ patterns, from trigger chamber hits. These patterns are combined, and the hits associated to patterns are used to seed segment reconstruction.

Segments are reconstructed by fitting lines which are tangent to the drift circles found in each layer of the MDT chamber. At least three MDT hits per chamber are required to make a segment. The search algorithm includes a loose requirement on the compatibility of the track with the beam-spot.

6.3.3   Muon Tracks

In the next step of muon reconstruction, several segments from the different stations of the Muon Spectrometer are used to form a track. A high-quality segment in the Middle station of the Muon Spectrometer is used to seed MS track reconstruction, and form a *road* in η and ϕ. This road is used to identify segments located in the Inner and Outer stations, which also have positions and directions consistent with the segment from the Middle station. During the matching process, a preference given to segments with high-quality. When there are no remaining segments in the Middle station, segments in the Inner and Outer stations are used to seed track formation.

An overlap removal process is then performed to resolve ambiguity between tracks which share segments. Generally, segments are not allowed to belong to two track candidates. The only exception is that two track candidates can share two segments in the Inner and Middle station if there are no shared hits in the Outer station segments. Each track is required to have at least two segments, except in the transition region between the barrel and end-cap, where only one segment is required.

After overlap removal has been performed, track candidates are refined by removing and adding hits. Hits with a large contribution to the track candidate's χ^2 are removed, and the track candidate is refit after removing those hits. Hits can also be added to the candidate if they are consistent with the track, and the candidate is again refit after adding those hits.

The final track parameters are extracted by fitting a helix to all hits on track. The fit function is modified by parameters that allow the muon to change its momentum and direction in regions of dense material. The five track parameters, η, ϕ, transverse impact parameter d_0, longitudinal impact parameter z_0, and track curvature q/p are computed for three locations: at the entrance to the Muon Spectrometer, at the origin of the detector, and at the primary vertex of the event. In order to extrapolate the muon's trajectory to the origin or the primary vertex, the energy loss in the Calorimeter is taken into account. This energy loss is calculated using a function parametrized by the muon's position and momentum.

6.3.4 COMBINED MUONS

The final step of muon reconstruction is to form combined muons from well matched Muon Spectrometer and Inner Detector tracks. A Muon Spectrometer track is extrapolated inwards to the Inner Detector, in order to define a road. A search for matching Inner Detector tracks is performed inside the road. The Inner Detector track which has the most consistent position and direction is selected to seed a combined muon. Combined muons are then reconstructed by forming a full refit of the hits from the Inner Detector and Muon Spectrometer tracks. Individual hits may be added or removed in order to improve the combined muon's quality of fit.

ATLAS has several pre-defined muon selections to identify muons. These selections apply different quality requirements in order to ensure the muon is well reconstructed. These definitions are designed with several goals in mind. For example, the Medium muon selection maximizes the efficiency for reconstructing prompt muons from $Z \to \mu\mu$ decays, while retaining reasonable momentum resolution. The Tight muon selection minimizes the probability to select a muon which was reconstructed from the decay in flight of a pion or kaon. The High-p_T muon selection requires hits in all three Muon Spectrometer stations, in order to ensure a precise momentum measurement for muons with $p_\mathrm{T} > 200$ GeV.

This analysis makes use of combined muons, which may include Inner Detector tracks reconstructed by the standard ATLAS tracking algorithm or by the non-standard Inner Detector tracking discussed in Section 6.5.1. A modified version of the Medium definition is used in this analysis, where modifications are designed to ensure good identification efficiency of displaced tracks. The Medium muon selection requirements are summarized in Table 6.3, and described in more detail below.

Table 6.3: Medium muon quality requirements ($|\eta| < 2.5$)

At least two precision layers (if $|\eta| > 0.1$)
At least one precision layer, and no precision layer holes (if $|\eta| < 0.1$)
$\sigma(q/p) < 7$
$N_{SCT} \geq 5$
$N_{Pix} \geq 1$
$N_{Pix}^{hole} + N_{SCT}^{hole} < 3$

Medium muons are required to have at least three precision hits in at least two Muon Spectrometer stations. An exception is made for muons with $|\eta| < 0.1$, where there is reduced detector coverage,

and only one station is required to have at least three hits. The number of stations with at least three hits is referred to as the *number of precision layers*. A muon has a *precision layer hole* if one station of the Muon Spectrometer has fewer than three hits, and that station is sandwiched by two stations which have at least three hits. Muons with $|\eta| < 0.1$ are additionally required to have no precision layer holes. Figure 6.10 shows the average number of precision layers per `Medium` muon in 2016 data as a function of muon η and ϕ. The number of precision layers per muon is extremely sensitive to detector geometry and data quality issues.
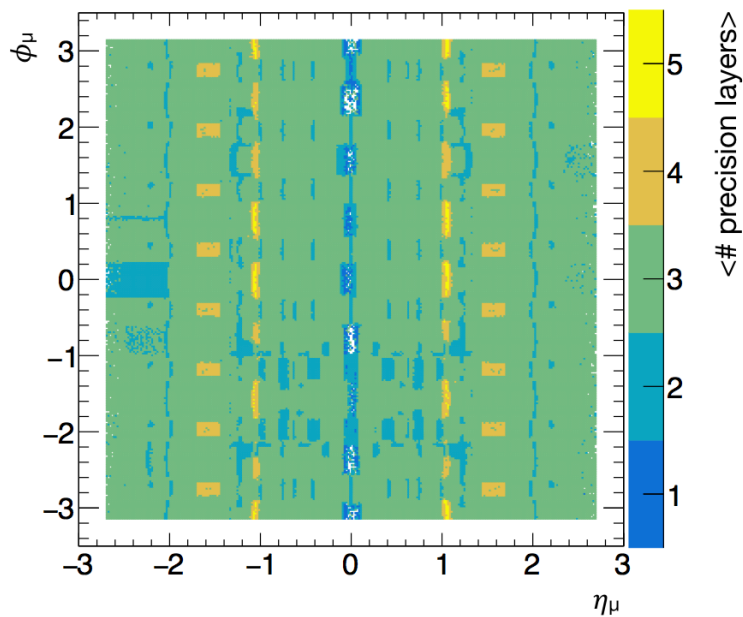
Figure 6.10: The average number of precision layers per muon is shown as a function of muon η and ϕ. Data are from 2016, and muons are required to pass a `Medium` selection.

A requirement is also made on the consistency of the momentum and charge measurements made in the Inner Detector and Muon Spectrometer. This requirement is applied to a quantity known as

the q/p-*significance*. The q/p-significance, $\sigma(q/p)$, is defined as

$$\sigma(q/p) = \frac{|q/p_{\mathrm{ID}} - q/p_{\mathrm{MS}}|}{\sqrt{\sigma(q/p_{\mathrm{ID}})^2 + \sigma(q/p_{\mathrm{MS}})^2}}. \tag{6.1}$$

The numerator consists of the absolute difference between the charge-to-momentum ratio measured in the ID and in the MS. The ratio of this difference is taken with respect to to the square root of the sum of squared uncertainties on the charge-to-momentum ratio in each sub-detector. The `Medium` muon selection requires $\sigma(q/p) < 7$ in order to reject muons which are reconstructed from the decays in flight of hadrons. When a pion or kaon decays to a muon inside the detector, the muon is reconstructed with a kinked topology, and the momentum measured by the ID and MS may not be compatible.

Requirements are also placed on the number of hits in the Inner Detector which are associated to the combined muon. Combined muons are required to have least five SCT hits, and at least one Pixel hit. These requirements are adjusted for this analysis in order to select muons which are produced from long-lived particle decays which occur beyond the last layer of the Pixel.

The efficiency for reconstructing a `Medium` muon is shown in Figure 6.11. The efficiency is shown as a function of the muon transverse momentum, and as a function of the muon pseudorapidity. The efficiency is measured by selecting $Z \to \mu^+\mu^-$ events in data and simulation, and performing a *tag and probe* analysis. A muon which passes a tight selection is considered the tag, while an Inner Detector track matched to a Calorimeter deposit is considered the probe. The efficiency is defined as the ratio between the number of probes which also pass the `Medium` selection to the total number of probes.

The efficiency of reconstructing a `Medium` muon is between 98% and 99%, except for muons located in $|\eta| < 0.1$, where the efficiency is approximately 85% due to reduced detector coverage.
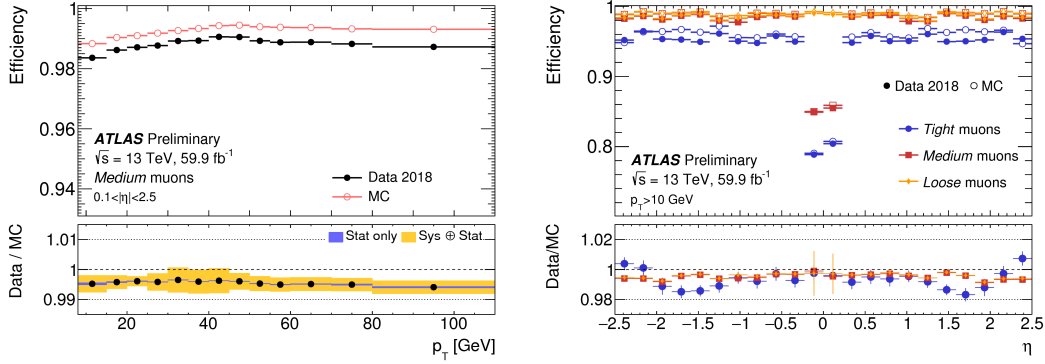
Figure 6.11: The efficiency for reconstructing a `Medium` muon as measured in $Z \to \mu\mu$ events. Efficiency is shown as a function of the muon p_T (left) and η (right). Open circles show the prediction by the detector simulation, while filled circles correspond to the measurement in 59.9 fb^{-1} of pp-collisions from 2018. The bottom panels show the ratio between expected and observed efficiencies [69].

The efficiency for reconstructing a muon in simulation is slightly higher than the efficiency observed in data. The efficiency is lower in data because the Monte Carlo simulation does not account for data quality related issues, such as chambers excluded from data taking, and slightly underestimates the effects of pile-up on detector efficiency. Corrections are applied to the simulation in order to ensure the muon reconstruction efficiency matches that of the data.

Figure 6.12 shows the momentum resolution for Muon Spectrometer tracks, predicted from simulation. For muons with high momentum ($p_T > 200$ GeV), the p_T resolution is limited by the detector precision, including the resolution of individual MDT tubes, and the alignment of MDT chambers. For muons with moderate momentum ($20 < p_T < 200$ GeV), the p_T resolution is limited by multiple scattering due to material in the Muon Spectrometer. For muons with lower momen-

tum ($p_T < 20$ GeV), the p_T resolution is limited by fluctuations in the energy loss of muons, due to material in front of the Muon Spectrometer.

Figure 6.12 also shows the momentum resolution for Muon Spectrometer and Inner Detector tracks, as well a for combined muons. The momentum resolution was obtained by comparing two muons reconstructed from a single cosmic event, using the tracks reconstructed in the the upper and lower halves of the detector. For muons with transverse momentum less than 50 GeV, the Inner Detector momentum measurement dominates. For muons with momentum in the range $50 < p_T < 100$ GeV, both the Muon Spectrometer and the Inner Detector contribute to the momentum measurement and uncertainty. For muons with $p_T > 100$ GeV, the momentum measurement is dominated by the Muon Spectrometer measurement [58].
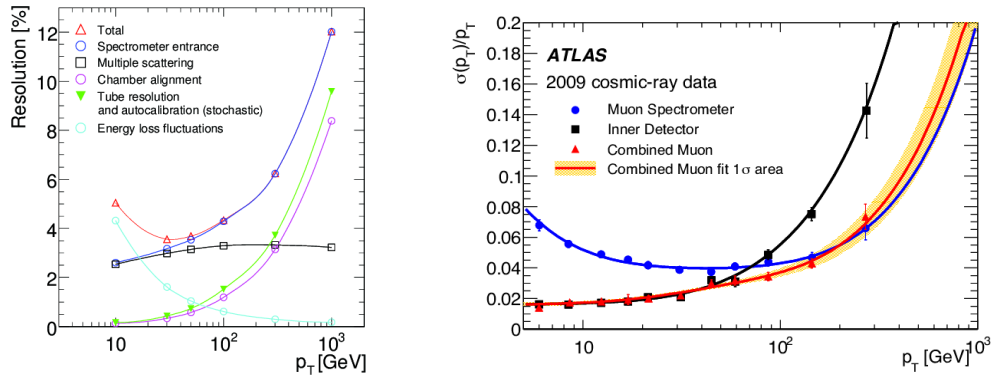
Figure 6.12: Left: Momentum resolution for muon spectrometer tracks. MS tracks are required to have segments in three stations of the Muon Spectrometer. The momentum resolution is predicted in simulation, and the different components which contribution to the resolution are indicated separately [71]. Right: Momentum resolution for MS tracks, ID tracks, and combined muons [72].

6.4 CLUSTER-BASED E_T^{MISS}

The missing transverse energy, E_T^{miss}, used in this thesis is calculated from *topological clusters* reconstructed in the Calorimeter. In ATLAS, this E_T^{miss} definition is known as `LocHadTopo`.

The magnitude, E_T^{miss}, of the missing transverse energy in an event is computed as

$$E_T^{\text{miss}} = \sqrt{(E_X^{\text{miss}})^2 + (E_Y^{\text{miss}})^2},$$ (6.2)

where E_X^{miss} and E_Y^{miss} are computed by summing over the energy and location of all topological clusters as

$$
\begin{aligned}
E_X^{\text{miss}} &= - \sum_{i=1}^{N_{\text{clusters}}} E \sin\theta \cos\phi \\
E_Y^{\text{miss}} &= - \sum_{i=1}^{N_{\text{clusters}}} E \sin\theta \sin\phi.
\end{aligned}
$$ (6.3)

This section begins with description of how topological clusters are reconstructed in the Calorimeter. This section also includes a discussion of why this cluster-based E_T^{miss} definition is useful for the analysis even though the simplified model of interest contains no final state particles which are expected to be undetected (neutinos or neutralinos).

6.4.1 Topological clusters

Topological clusters are reconstructed from neighboring Calorimeter cells using a three-dimensional clustering algorithm. Individual topological clusters can represent the full shower from a single particle, a fractional shower, or the merged response of several particles, depending on the incident particle type and energy, as well as spatial separations between particles. These clusters are used by ATLAS to reconstruct electrons, photons, and hadronic jets. The algorithm is based on the methods described in Reference [73].

In the first step, *proto-clusters* are reconstructed as follows:

1. Any cell with $|E_{\text{cell}}| > 4\sigma_{\text{noise}}$ seeds the cluster.

2. Cells with $|E_{\text{cell}}| > 2\sigma_{\text{noise}}$ that are contiguous to the cluster are added to the cluster until no such cells remain.

3. An additional layer of all contiguous cells is added to the cluster, regardless of cell energy.

Both the energy of the cell, and the expected level of noise, σ_{noise}, are measured on the electromagnetic scale. This means the energy of the cell is calibrated to reproduce the signal due to a single electron. This calibration was obtained using test beam data [74–76]

The algorithm also accepts cells with negative energies. Cells with negative energy arise from fluctuations in pile-up and electronic noise. Including cells with negative energies improves noise suppression (resulting in local cancellations of upward and downward fluctuations), and reduces a bias in the reconstructed energy from requiring $E_{\text{cell}} > 0$.

In a second step, proto-clusters with two or more local maxima are split in order to account for two or more particles injecting energy into the Calorimeter in close spatial proximity. Proto-clusters

are split in three-dimensions, and cells which are shared between clusters contribute a fraction of their energy with each cluster. The fraction of energy contributed is determined by the cell's proximity to each cluster, as well as the cluster relative energy. After the splitting step, proto-clusters are used as topological clusters in further steps of reconstruction.

Topological clusters are assigned a mass of zero. Their energy is calculated as the sum of the energies of its constituent cells. The η and ϕ position of each cluster is calculated as the energy-weighted average of the η and ϕ of their constituent cells.

The expected level of noise in each cell, is estimated on a cell-by-cell basis for both the LAr and Tile Calorimeters, using data collected with random triggers. The noise in a cell is defined as the sum in quadrature of electronic noise, as well as the effect of pile-up on the baseline cell energy distribution,

$$\sigma_{\text{noise}} = \sqrt{(\sigma_{\text{noise}}^{\text{electronic}})^2 + (\sigma_{\text{noise}}^{\text{pile-up}})^2}. \tag{6.4}$$

Here, $\sigma_{\text{noise}}^{\text{electronic}}$, is the electronic noise, and $\sigma_{\text{noise}}^{\text{pile-up}}$ is due to pile-up. In Run 2, the effects of pile-up dominated over the electronic noise, and $\sigma_{\text{noise}} \approx \sigma_{\text{noise}}^{\text{pile-up}}$.

6.4.2 $E_{\text{T}}^{\text{MISS}}$

Once all topological clusters have been reconstructed, they must be calibrated to the appropriate scale. For the $E_{\text{T}}^{\text{miss}}$ definition used in this analysis, topological clusters are calibrated to the *hadronic scale*. This means calorimeter clusters are calibrated to reproduce the Calorimeter's energy response due to hadrons. The hadronic calibration is derived using Monte Carlo simulation (MC) simulation

127

of single pions. Both charged and neutral pions of a wide range of energies are considered. Corrections are made in order to account for out-of-cluster energy loss, as well as dead material. This calibration was verified in data with single isolated charged hadrons using isolated ID tracks with well-measured momentum [77].

After calibration, topological clusters which have positive energy are used to compute the cluster-based E_T^{miss}, defined by equation 6.2. This cluster-based E_T^{miss} definition is useful for the analysis because it is similar to the E_T^{miss} definition used in the E_T^{miss} trigger, as discussed in Chapter 7.

This analysis uses an E_T^{miss} trigger to select events with high momentum muons. High momentum muons deposit only a small fraction of their energy in the Calorimeter. Events with high momentum muons will have a large cluster-based E_T^{miss}, unless these muons have momentum vectors which cancel in the transverse plane. The correlation between cluster-based E_T^{miss} and the vector sum of muon momenta, $\Sigma \vec{p_T}(\mu)$, is shown in Figure 6.13, for simulated signal events. Because events with large $\Sigma \vec{p_T}(\mu)$, also have large cluster-based E_T^{miss}, these events fire the E_T^{miss} trigger with high efficiency.

6.5   NON-STANDARD RECONSTRUCTION

This analysis makes uses of several non-standard reconstruction methods in order to improve sensitivity to long-lived particle decays. The standard tracking reconstruction places strict limits on the impact parameters of tracks, reducing the efficiency of reconstructing displaced charged particles. In order to improve the efficiency of reconstructing charged particles produced in long-lived particle decays, this analysis uses an additional pass of tracking with loosened impact parameter and hit require-
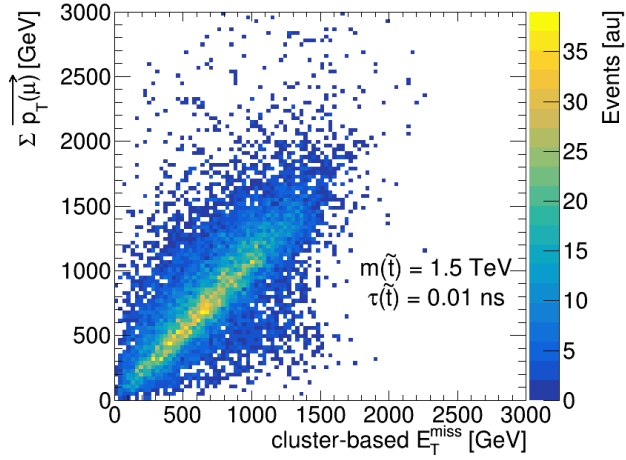
Figure 6.13: Cluster-based E_T^{miss} versus the vector sum of the muon transverse momenta from $\tilde{t} \rightarrow \mu + j$ simulated events.

ments. This additional pass of tracking is referred to as *Large Radius Tracking*, and is described in Section 6.5.1. This analysis also uses a dedicated algorithm to reconstruct displaced vertices, which is described in Section 6.5.2.

It is important to note that the displaced tracks reconstructed by the Large Radius Tracking are used in other steps of event reconstruction besides forming displaced vertices. Most importantly for this analysis, these Large Radius tracks can be used to form combined muons just like standard Inner Detector tracks. The resulting combined muons may also be included in displaced vertices.

There are several challenges associated with using the Large Radius tracking and secondary vertexing algorithms. The Large Radius tracking suffers from a large rate of fake tracks, which are reconstructed from an accidental combination of hits. Displaced vertices reconstructed from these fake tracks constitute a major background for this analysis.

Additionally, these methods are very computationally intensive, and only used by a few analyses in ATLAS. In order to reduce the impact of using this non-standard methods, this analysis uses a special data flow, described in more detail in Section 8.1.1. Features of the non-standard tracking and secondary vertexing algorithms which are specific to the analysis are discussed in Chapter 9.

6.5.1 LARGE RADIUS TRACKING

The Large Radius Tracking algorithm is used to reconstruct charged particles produced from long-lived particle decays as displaced tracks. An example sketch of how these displaced tracks compare to a standard Inner Detector track is shown in Figure 6.14. The example standard Inner Detector track is a primary particle, produced at the pp-interaction point, and traverses all eight layers of the silicon detectors. In contrast, the example Large Radius tracks have a production radius, r_{prod}, which is located beyond the last layer of the Pixel detector. These displaced tracks have impact parameters larger than $|d_0| > 10$ mm, and no hits in the Pixel detector. Without Large Radius Tracking, these displaced tracks would not be reconstructed.

Large Radius Tracking aims to reconstruct displaced vertices from long-lived particle decays that occur at radii as large as $R = 300$ mm, which roughly corresponds to the first layer of the SCT. This maximum radius was chosen in order to ensure that tracks produced from long-lived particle decays would form clusters in all four layers of the SCT. Requiring clusters in all four SCT layers is important for several reasons. In theory, it is possible to reconstruct displaced tracks with only the TRT, which would extend this maximum radius to $R = 563$ mm. However, the TRT is at nearly full occupancy in Run 2 pile-up conditions, and suffers from reduced tracking efficiency.
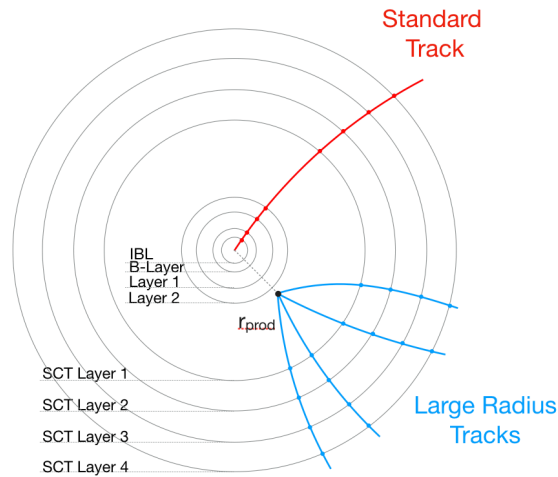
Figure 6.14: A cartoon which compares standard Inner Detector tracks to Large Radius tracks. A view of the Pixel and SCT detectors is shown in the transverse plane, with labels indicating the different layers. An example standard Inner Detector track is shown in red, and several example Large Radius tracks are shown in blue.

A second possibility would be to extend this maximal production radius from $R = 300$ mm to $R = 370$ mm, the radial position of the second SCT layer. This strategy would mean charged particles could have as few as three silicon clusters on track. This strategy would result in reduced tracking efficiency and a higher fake rate. Because the Large Radius Tracking algorithm is based on the standard inside-out algorithm, described in Section 6.1, it seeds tracks in the silicon detectors. Requiring charged particles to traverse four SCT layers increases the probability a seed will be formed. Requiring clusters in all four layers instead of just three also reduces the rate of tracks which are reconstructed from accidental combinations of hits to manageable levels. Moreover, because the position of long-lived particle decays follows an exponential distribution, extending the maximum allowed radius from $R = 300$ mm to $R = 370$ mm would not substantially improve the geometric acceptance for recon-

structing a displaced vertex.

The Large Radius Tracking algorithm is sometimes referred to as the *third pass* of tracking, because it is run after an event has been processed with the two standard ATLAS tracking algorithms. The Large Radius Tracking algorithm makes use of hits that are not associated to tracks reconstructed in the previous two tracking passes. Some parameters of the standard inside-out tracking algorithm are modified to improve efficiency to displaced tracks and to reduce contamination from fake tracks. The complete list of requirements applied in the standard ATLAS tracking algorithms and in the Large Radius Tracking algorithm are listed in Table 6.4, and the major differences between the Large Radius Tracking algorithm and the first pass of standard ATLAS tracking are summarized below.

- The allowed region used to search for hits used for seeding is extended slightly.
- The requirements on the transverse and longitudinal impact parameters are loosened.
- Some quality cuts are tuned for displaced tracks, in particular the required hit multiplicities in the Pixel, SCT, and TRT.

In Table 6.4, N_{Pix}, N_{SCT}, and N_{TRT} indicate the number of Pixel, SCT, and TRT hits associated to a track, while N_{Si} indicates the number of silicon hits ($N_{Pix} + N_{SCT}$). A hole is defined to be a layer which does not have an associated hit, which is sandwiched by two layers which have hits. Similarly, $N_{Si}^{\text{double hole}}$ is defined to be two consecutive layers which do not have associated hits on track, which are sandwiched by layers which do have associated hits. The number of silicon hits which are shared with another track or tracks is indicated by N_{Si}^{sh}, while $N_{Si}^{\text{not sh}}$ indicates the number of silicon hits which are not shared with any other track.

More information about the Large Radius Tracking can be found this ATLAS Internal Note, which details an analysis based on data collected in 2016 [78], and the Large Radius Tracking Pub Note [79],

Table 6.4: Requirements applied in the different tracking algorithms.

cut	Si-seeded	TRT-seeded	high-d_0 tracking
max d_0	10 mm	100 mm	300 mm
max z_0	250 mm	-	1500 mm
min p_{T}	500 MeV	2 GeV	900 MeV
min N_{Pix}	0	-	0
min N_{Si}	7	4	7
min N_{TRT}	9*	15	9*
min $N_{Si}^{\mathrm{not\ sh}}$	6	4	5
max N_{Si}^{sh}	1	1	2
max N_{Si}^{hole}	2	2	2
max N_{Pix}^{hole}	1	2	1
max N_{SCT}^{hole}	2	2	2
max $N_{Si}^{\mathrm{double\ hole}}$	1	1	1

*on TRT track extension

which is based on simulation. Both of these notes use events which are reconstructed with an older software release from the release used in this thesis. There are only two differences between the two releases in terms of Inner Detector tracking, which are described below.

- The first pass of tracking (inside-out) p_{T} threshold is 400 MeV in both releases. However the requirement for a track to be saved in an event is increased from $p_{\mathrm{T}} = 400$ to 500 MeV.

- The minimum p_{T} threshold for reconstructing a Large Radius track is increased from $p_{\mathrm{T}} = 500$ MeV to 900 MeV. This threshold was raised in order to reduce the rate of fake tracks which were reconstructed with low p_{T} in events with many pile-up interactions.

Figure 6.15 shows two simplified models which are used to study the performance of the Large Radius Tracking in Reference [79]. In the first model, squarks are pair produced and decay to a quark and long-lived neutralino. The neutralino decays via a small λ coupling to a pair of charged leptons (ee or $\mu\mu$) and a neutrino. The mass of the squark is set to 700 GeV, the mass of the neutralino is 500 GeV, and the lifetime of the neutralino is $\tau(\tilde{\chi}_1^0) = 0.1$ ns. In subsequent plots, this sample is

referred to as *displaced leptons*. In the second simplified model, which is inspired by Split SUSY, long-lived gluinos are pair produced and decay to two quarks and a neutralino. When the gluino decays inside the Inner Detector volume, this model results in displaced hadronic jets. For these studies, the mass of the gluino is set to 1.4 TeV, and the mass of the neutralino is 1.3 TeV. This sample is referred to as *displaced hadrons*.
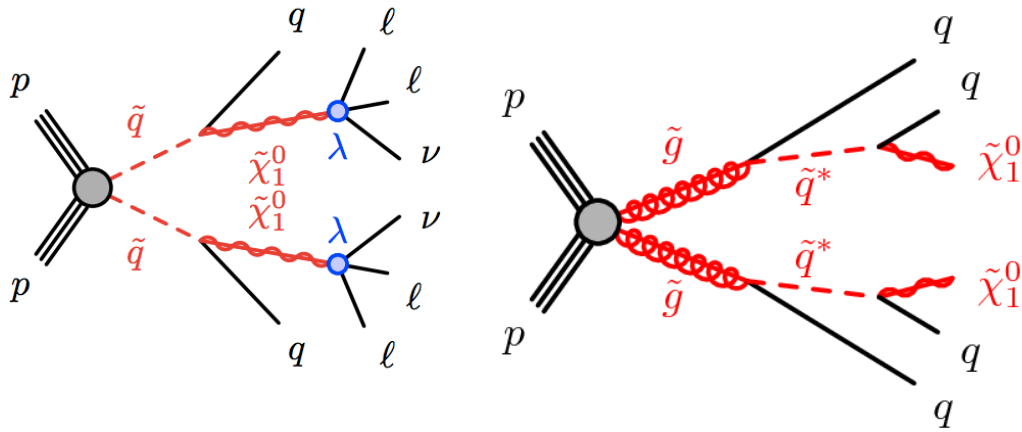
Figure 6.15: Representative simplified models used to study Large Radius Tracking efficiency. Left: Production of squarks decaying via long-lived neutralinos in R-parity violating SUSY. Right: Production of long-lived gluinos in Split-Supersymmetry [79].

Charged leptons and hadrons produced from a long-lived particle decay in these two simplified models are used to study the Large Radius Tracking performance. A fiducial selection is applied to these charged particles in order to ensure the daughter particles are within the geometric acceptance of the detector and tracking algorithm. These requirements are summarized in Table 6.5.

Figure 6.16 shows the r_{prod} and p_{T} spectra of these displaced leptons and hadrons. A particle's r_{prod}, is the radial position at which the particle was produced, and corresponds exactly to the long-lived

Table 6.5: Fiducial selections applied to truth particles to study track reconstruction efficiency.

$p_{\mathrm{T}} > 1\,\mathrm{GeV}$
$|\eta| < 2.5$
$r_{\mathrm{prod}} < 400\,\mathrm{mm}$
charge $= \pm 1$
From long-lived particle decay

particle decay position. The gluino in the long-lived Split SUSY sample has a longer lifetime than the neutralino in the R-parity violating sample. As a result, displaced hadrons are produced at larger radii than displaced leptons, on average. Due to the small mass difference between the gluino and the neutralino in the Split SUSY model, the displaced hadrons have a relatively soft p_{T} spectrum. The transverse momenta of displaced hadrons range from a few GeV to a few tens of GeV, whereas the displaced leptons have p_{T} as high as several hundred GeV.
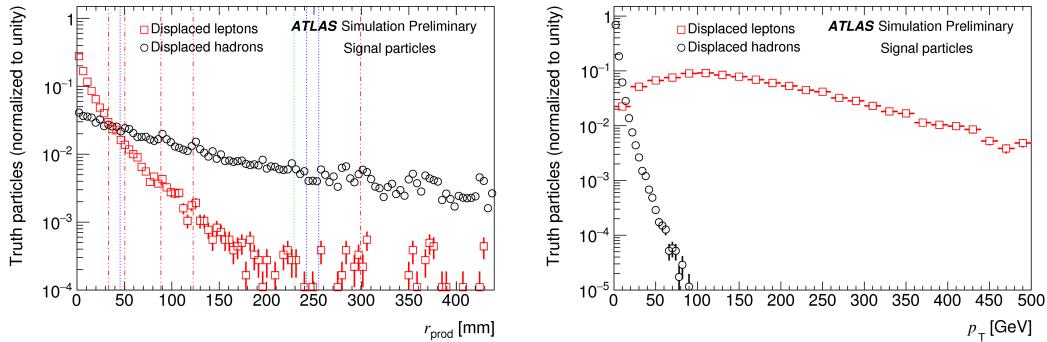
Figure 6.16: Left: The production radius r_{prod} for charged particles produced in the displaced lepton and hadron samples, normalized to unity. Blue, red, and green, dotted lines represent radial positions of material. Right: The p_{T} spectrum for charged particles in the displaced lepton and displaced hadron samples, normalized to unity [79].

Figure 6.17 shows the inclusive tracking efficiency as a function of r_{prod} for displaced leptons and

hadrons. The tracking efficiency is defined as the fraction of particles which pass the fiducial selection in Table 6.5, which are matched to a reconstructed track. The tracking efficiency is shown separately for charged particles which are reconstructed by standard ATLAS Inner Detector tracking, and charged particles which are reconstructed with Large Radius tracking. The total tracking efficiency is the sum of the standard ATLAS and Large Radius tracking efficiencies. The standard ATLAS tracking efficiency drops below 20% for displaced particles with $r_{prod} = 50$ mm, and is further reduced at larger radii. The Large Radius Tracking algorithm substantially increases the reconstruction efficiency beyond $r_{prod} = 50$ mm. Within statistical uncertainties, there is no significant difference between the efficiency for reconstructing hadrons or leptons.
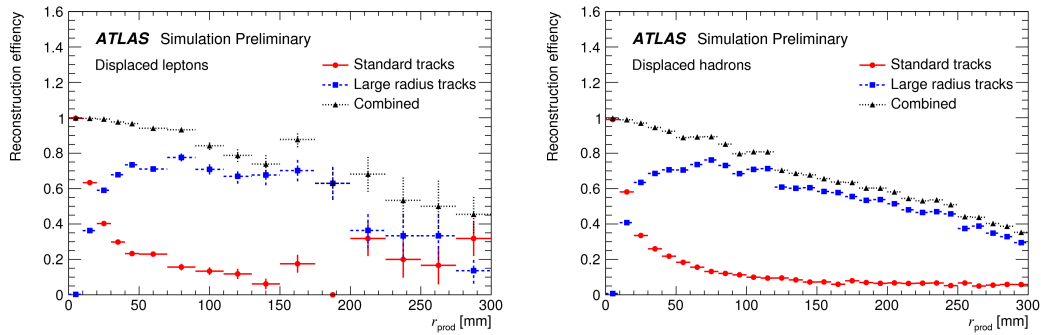
Figure 6.17: The inclusive efficiency for reconstructing a displaced charged particle as a function of its production radius r_{prod}. The efficiencies for standard ATLAS tracking and Large Radius Tracking are shown separately, in red and blue respectively. The total efficiency is shown in black [79].

Even with the addition of Large Radius tracking, the inclusive tracking efficiency remains below 100% for large r_{prod}. Part of the reason the inclusive efficiency never reaches 100% is due to the geometry of the Inner Detector. For charged particles with large impact parameters it is often not possible to produce a sufficient number of hits in the detector to satisfy Large Radius Tracking requirements.

136

In order to disentangle this effect from inefficiency due to the algorithm itself, a technical efficiency is computed. In addition to the fiducial requirements described above, charged particles are also required to be able to produce at least seven silicon hits in the detector in order to evaluate this technical efficiency. This technical efficiency is shown in Figure 6.18. The technical efficiency is 90% or higher for all production radii $r_{\mathrm{prod}} < 300$ mm.
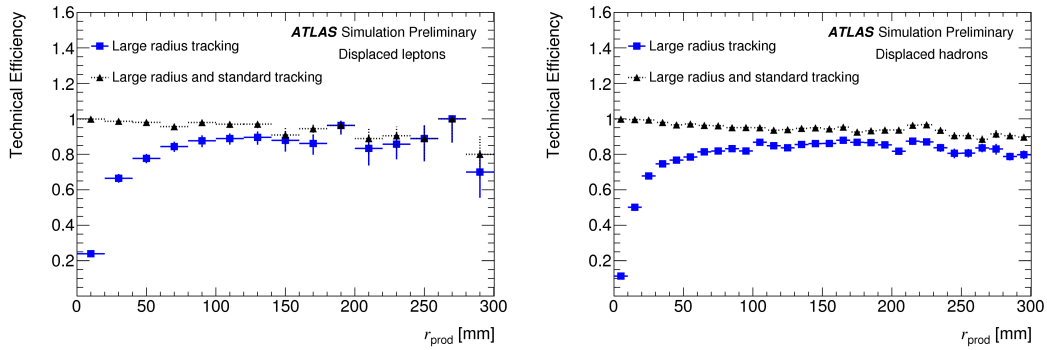
Figure 6.18: The technical efficiency for reconstructing a displaced charged particle as a function of its production radius r_{prod}. The technical efficiency for the Large Radius Tracking is shown in blue, and the total technical efficiency is shown in black [79].

In order for these reconstructed tracks to successfully be reconstructed as a secondary vertex, their tracking parameters must accurately represent the original charged particle which traversed the detector. Figure 6.19 shows the difference between the transverse impact parameter d_0 of the reconstructed track and the truth charged particle for the displaced lepton and hadron samples. The width of the residual distributions are larger for Large Radius tracks than for tracks reconstructed by standard algorithms. However, this effect is expected because Large Radius tracks are, on average, produced at larger radii than standard tracks. The larger extrapolation between the first hit and the interaction point leads to a degradation in impact parameter resolution. The displaced lepton sample has a better

impact parameter resolution than the displaced hadrons. This behavior is as expected from the shorter lifetime and higher p_T of the displaced lepton sample in comparison to the displaced hadrons sample. The shorter lifetime results in a shorter extrapolation distance, and the higher p_T results in reduced multiple scattering, which both improve impact parameter resolution.
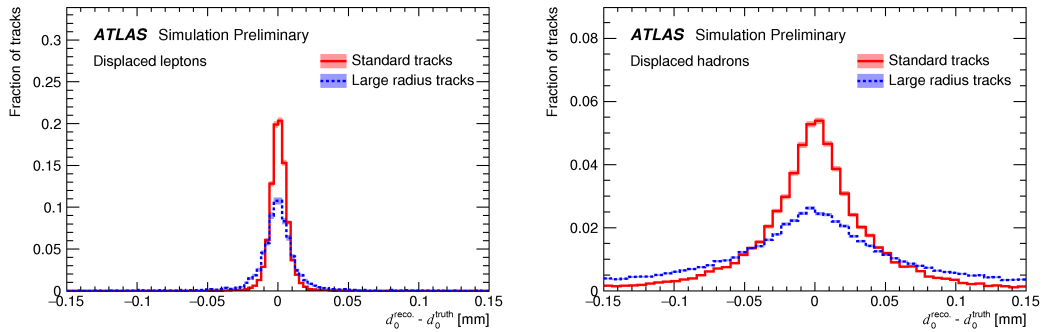
Figure 6.19: Normalized distributions of the difference between the transverse impact parameter, d_0, for the truth charged particle and the corresponding reconstructed track, for displaced leptons (left) and displaced hadrons (right). Residuals are shown separately for standard and Large Radius Tracks in red and blue, respectively [79].

Because the Large Radius Tracking algorithm requires fewer associated hits than the standard tracking requires, the Large Radius Tracking produces more tracks from an accidental combination of hits than the standard tracking. In order to study the rate of these accidentals, or fake tracks, a *fake rate* is computed. The fake rate is defined as the number of tracks which are not matched, or poorly matched to a truth charged particle, divided by the total number of reconstructed tracks. In the displaced lepton and hadron samples, the fake rate is nearly 80%. The large rate of fake tracks in events processed with Large Radius tracking is a challenge for this analysis, because these fake tracks can randomly cross and produce background secondary vertices. One important handle on these fake tracks is that they

tend to have fewer hits on track than tracks reconstructed from real charged particles.

6.5.2 Displaced Vertex Reconstruction

The displaced tracks which originate from a long-lived particle decay can be used to reconstruct a displaced vertex and identify the position at which the long-lived particle decayed. In ATLAS, there are several algorithms used to reconstruct displaced vertices. These algorithms have been used to study the position of the Inner Detector material with hadronic interactions and for other searches for long-lived particles. This section focuses on the secondary vertexing algorithm used to reconstructed displaced vertices for the analysis described in this thesis. Internally to ATLAS, this algorithm is known as `VrtSecInclusive`. A technical description of this algorithm can be found in an Internal Note [80], and the performance of this algorithm is characterized across a range of BSM theories in this Pub Note [81].

The `VrtSecInclusive` algorithm reconstructs displaced vertices in several steps. These major steps are summarized below.

1. Select tracks to be used in vertex seed formation.
2. Form vertex seeds from pairs of tracks which are compatible with a long-lived particle decay.
3. Combine all two-track vertex seeds into multi-track vertices.
4. Attach nearby unassociated tracks which are compatible with a vertex.

Once an event with a primary vertex has been selected, displaced vertex reconstruction is seeded by pairs of tracks which are roughly compatible with a long-lived particle decay. Due to the high multiplicity of tracks which are reconstructed in an event, and because the possible number of vertex seeds increases roughly with the number of tracks squared, only a small subset of tracks are used to seed vertex formation. The quality criteria used to select this subset of tracks are listed in Table 6.6. Tracks which are used to seed vertex formation are referred to as *selected tracks*.

Table 6.6: Selected track requirements

All tracks must satisfy the following requirements:
$p_{\mathrm{T}} > 1$ GeV
$\chi^2/N_{DoF} < 50$
$N_{TRT} > 0$ or $N_{Pix} \geq 2$
$N_{SCT} \geq 6$ or $N_{Pix} \geq 0$
$|d_0| > 2$ mm and $|d_0| < 300$ mm
$|z_0| < 1500$ mm
Not used in the fit of any primary vertex
Tracks with $p_T < 25$ GeV additionally required to have:
$N_{SCT} \geq 7$
if $|\eta| < 1.7$, $N_{TRT} > 20$

The selected track criteria are designed to be strict in order to reduce the contribution of fake tracks to the vertex seeding process. These criteria include requiring tracks have $p_{\mathrm{T}} > 1$ GeV, applying a loose requirement on the track χ^2/N_{DoF}, and placing several p_{T} dependent requirements on the number of hits associated to each track. Additionally, tracks may not be associated to any primary vertex in the event, and are required to have transverse impact parameter $|d_0| > 2$ mm. These displacement

requirements reduce the probability that tracks produced from Standard Model processes will form vertex seeds.

Seed vertex formation

These selected tracks are then used to form all possible two-track vertices. The position of the vertex is obtained by minimizing the vertex χ^2, which penalizes differences of the track parameters with respect to the vertex position, weighted by the covariance of the track parameters. If a vertex position is found, but the radial position of the vertex R is greater than 563 mm, the vertex is rejected. Vertices are also rejected if the vertex χ^2/N_{DoF} is greater than 5. These two-track vertices are also required to pass several requirements in order to ensure that the vertex position and tracks are consistent with a long-lived particle decay.

Tracks are required to have a hit pattern consistent with the reconstructed vertex position. Two examples of hit pattern requirements are shown in Figure 6.20. It is assumed that daughter particles from the long-lived particle fly from inner to outer radii of the detector. This requirement means that tracks are forbidden to have hits in layers with a radial position, R, which is smaller than the radial vertex position. Tracks are also required to have hits in detector layers with larger R than the vertex position. If the vertex is located nearby a Pixel detector layer, that layer is neither forbidden or required to have hits. If a vertex is formed just before a disabled module in R, that module is not required to have a hit.

Finally, several kinematic requirements are also applied to two-track vertices. The vertex pointing vector, $\vec{r} = \vec{r}(r_v, z_v, \phi_v)$, is defined as the relative position of the vertex with respect to the primary
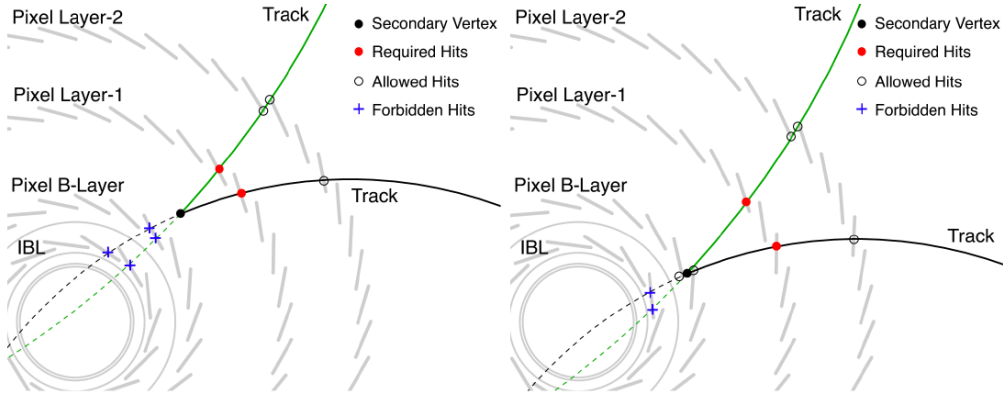
Figure 6.20: Hit pattern requirements applied to example vertex seeds formed from pairs of tracks. A transverse view of the Pixel detector is shown. Left: The vertex seed is shown in black, and is located between the B-Layer and Layer-1 of the Pixel Detector. The tracks of the vertex seed are forbidden to have hits in the IBL and B-Layer, and must have hits in Layer-2. Right: The vertex seed is located close to the B-Layer pixel sensors. The tracks of the vertex seed are forbidden to have hits in the IBL, and must have hits in Layer-1 of the Pixel, but no requirement is placed on having hits in the B-Layer [81].

vertex. Requirements are placed on the azimuthal angle between each associated track and $\vec{r}$, in order to reject seed vertices formed from randomly crossing tracks that point backwards, towards the primary vertex. The vector sum of the momenta of the two tracks, $\vec{p}^{\,\text{sum}} = \vec{p}^{\,\text{sum}}(p_\text{T}^\text{sum}, \eta^\text{sum}, \phi^\text{sum})$ is also defined. The azimuthal angle between $\vec{p}^{\,sum}$ and $\vec{r}$ must satisfy $\cos(\phi^\text{sum} - \phi_v) > -0.8$, in order to ensure that the vertex momentum does not point backwards, towards the primary vertex.

Multi-track vertex formation

Once all possible two-track vertices are formed, they are iteratively merged to form all possible n-track vertices using an incompatibility graph approach. Roughly, this means that vertex seeds which share the same tracks are merged into an n-track vertex.

At this point, one track still may be compatible with multiple vertices. The ambiguity between

tracks shared with multiple vertices is resolved by iteratively removing tracks and merging vertices. The track which is associated to the largest number of vertices is identified, and the χ^2 of that track with respect to each vertex is computed (defined as the χ^2 per track). The track is removed from vertices with the worst χ^2 per track. In addition, vertices are merged if their positions are compatible within 10σ. The value σ is defined as the uncertainty of the distance between the two vertices, and is computed as the sum in quadrature of the two covariance matrices of the vertex fits.

These steps are repeated until there are no remaining shared tracks. Finally, vertices are merged if they are within ≤ 1 mm of each other. Any merged vertices are refit.

Track Attachment

At this point, tracks which failed the selected track requirements in Table 6.6 are not associated to any vertex, even if they originated from the same long-lived particle decay. Including these unassociated tracks in the vertex can improve various kinematic properties of the vertex, including increasing the number of tracks and reconstructed invariant mass, which are both important quantities for long-lived particle analyses. In order to regain any efficiency lost by the tight selected track requirements, a track attachment procedure is performed.

These *attached tracks* are required to pass a number of requirements, summarized in Table 6.7. Any track with $p_T > 1$ GeV and a track $\chi^2/N_{DoF} < 5$ can potentially be attached to a vertex. In order to determine whether or not to attached a track to a vertex, the transverse and longitudinal impact parameter significances with respect to the target vertex is computed. If these impact parameter significances are less than 5, and if the track satisfies a hit pattern matching requirement, the track will

143

be attached to the vertex.

Table 6.7: Attached track requirements

$p_T > 1$ GeV
track $\chi^2/N_{DoF} < 5$
Modified hit pattern matching
$\|d_0\|$-significance < 5, of the track with respect to the secondary vertex
$\|z_0\|$-significance < 5, of the track with respect to the secondary vertex

Attached tracks have a modified hit pattern matching requirement with respect to selected tracks. If a vertex is located after a Pixel layer in R, a hit is required in the next layer, but no requirement is placed on hits in the inner layers. This modification is designed to accept tracks which point backwards towards the primary vertex, which sometimes occurs during the decay of a massive long-lived particle ($m \sim 1$ TeV). If a vertex is before the innermost Pixel detector layer in R, hits are required in first two layers of the Pixel detector.

Track attachment is attempted for vertices with the highest track multiplicity first. Once a track is attached to a secondary vertex, it will not be considered for attachment to any other vertex. If a track is attached to a vertex, the vertex position is refit. If the resulting vertex χ^2/N_{DoF} is greater than 20, the track will not be attached to the vertex.

At this point, one final fit of all vertices is performed, and track parameters with respect to the vertex position are re-calculated. The vertex invariant mass is calculated assuming the charged pion mass for all tracks, using the track momentum vectors at the location of the vertex.

Track cleaning

Because attached tracks are not subjected to the same quality criteria as the tracks used to seed vertices, there is an increased potential for attaching irrelevant or fake tracks to secondary vertices. One of the most concerning features of track attachment is that the distribution of attached tracks in ϕ is asymmetric. This section characterizes this asymmetry in ϕ, discusses the cause of this feature, and presents cleaning criteria which are used restore a symmetric ϕ spectrum of attached tracks.

Figure 6.21 shows properties of these attached tracks from a subset of events with displaced vertices in the 2016 dataset. There is a clear excess of attached tracks with $-0.5 < \phi < 2.5$, and with d_0 which correspond to the radial positions of Pixel sensor layers. These tracks also tend to have η which correspond to the region where the SCT end-cap and barrel overlap.
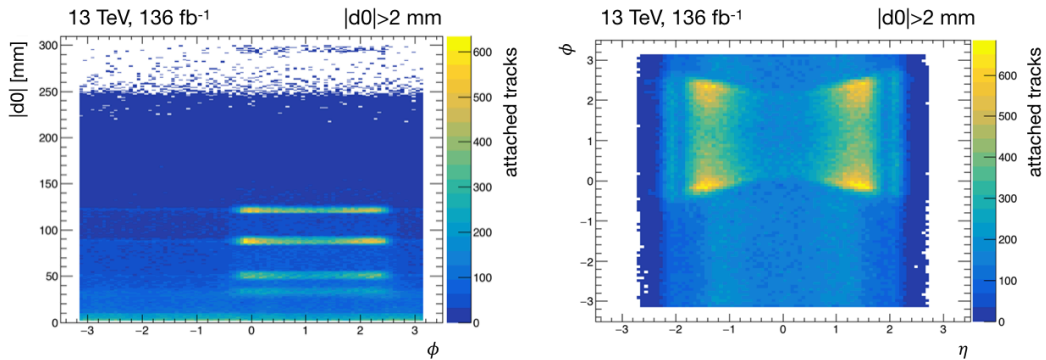
Figure 6.21: Attached tracks in 2016 data. Left: Tracks are shown as a function of the transverse impact parameter $|d_0|$ [mm] and ϕ. Right: Tracks are shown as a function of η and ϕ.

Extensive studies of these problematic tracks which have $|d_0|$ consistent with Pixel layers indicate that they are fake tracks, produced by an accidental combination of hits. These tracks have fewer

associated hits than tracks which are produced from real charged particles, and the asymmetry in ϕ increases with an increasing number of pile-up interactions. The features in track ϕ and $|d_0|$ are also observed in both data and simulation, as shown in Figure 6.22. Because these features are consistent in data and simulation, it is clear that the feature is not due to a data quality issue, but due to the track attachment algorithm itself.
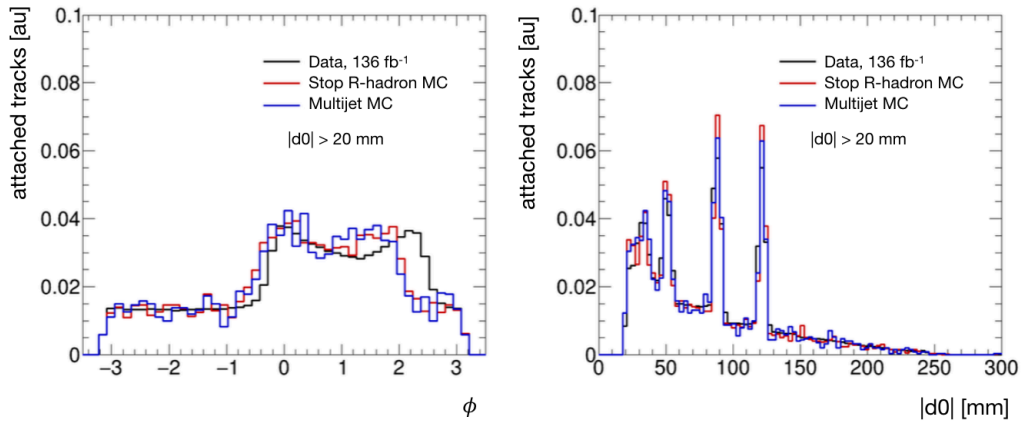
Figure 6.22: Attached tracks in data and simulation. Tracks are required to have $|d_0| > 20$ mm. Tracks in data are shown in black, while tracks from a signal sample with stop R-hadrons are shown in red, and tracks in a simulated multijet sample are shown in blue. All distributions are normalized to unity. Left: Track ϕ distribution. Right: Track $|d0|$ [mm] distribution.

The cause of this asymmetry in ϕ is related to the track extrapolation method which is used to measure the impact parameter significance of tracks with respect to secondary vertices in the attachment step. This extrapolation method is has several simplifying modifications with respect to the standard ATLAS track extrapolation method. This simplified propagator uses the origin $(x, y, z) = (0, 0, 0)$ as a reference point instead of the beam spot, uses a custom helical propagator, and a simplified version of the ATLAS magnetic field. The propagator also does not account for effects such as multiple

146

scattering, which can have a large impact on low p_T tracks (p_T of a few GeV). As a result, the track parameter uncertainties used to determine whether or not a track should be attached to a vertex are likely to be incorrect, especially in extreme scenarios, such as for a track with a trajectory nearly parallel to the beam.

The simplified extrapolation method is only used in the track attachment step, and is not used to compute the track parameters with respect to the final vertex. This method was chosen for the attachment step instead of the standard ATLAS track extrapolation in order to reduce computation time. Figure 6.23 shows the attached track ϕ distribution, for tracks with d_0 consistent with Pixel layers, after applying different requirements in the track attachment procedure. The left plot shows these distributions when using the simplified propagator, while the right plot shows these distributions when using the standard ATLAS propagator. When using the simplified propagator, it is clear that the asymmetry in ϕ is introduced when making requirements on the track impact parameter significance with respect to the vertex. No ϕ asymmetry is observed when using the standard ATLAS propagator.

Reprocessing the dataset with the standard ATLAS track extrapolator was not feasible on the timescale of this thesis. In order to benefit from analysis efficiency gains provided by track attachment, and also recover a symmetric ϕ distribution of attached tracks, a cleaning procedure is applied to remove these problematic tracks from vertices. Any attached tracks which have transverse impact parameters consistent with the the radial position of Pixel layers are removed from displaced vertices. Attached tracks with $|d_0| < 2$ mm are also removed in order to avoid the attachment of prompt track to displaced vertices. Table 6.8 summarizes the cleaning requirements applied to attached tracks.

These cleaning requirements were optimized by studying the d_0 distribution of attached tracks
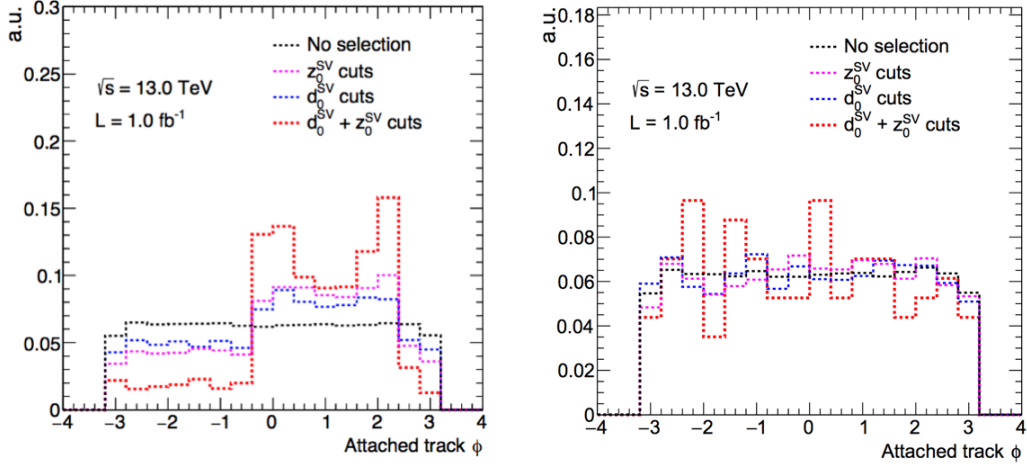
Figure 6.23: Attached track ϕ after applying different requirements in track attachment. Data correspond to $1.0\,\text{fb}^{-1}$, and only attached tracks with $|d_0|$ consistent with Pixel detector layers are shown. Tracks considered for attachment are shown in black. Tracks with $|z_0|$ significance less than 5 are shown in pink. Tracks with $|d_0|$ significance less than 5 are shown in blue, and tracks which satisfy both the transverse and longitudinal impact parameter requirements are shown in red. All distributions are normalized to unity. Left: Track attachment steps using a simplified track extrapolation method. Right: Track attachment steps using the standard ATLAS extrapolation method [82].

Table 6.8: Attached track cleaning requirements

Attached tracks are removed from vertices if
$2\,\text{mm} < |d_0|$
$26 < |d_0| < 39\,\text{mm}$
$46 < |d_0| < 56.5\,\text{mm}$
$83.5 < |d_0| < 93.5\,\text{mm}$
$117.5 < |d_0| < 128\,\text{mm}$

shown in Figure 6.24. Regions in between material were used to find a baseline, described by an exponentially falling distribution. The functional form, $C1^{C2 \cdot d_0}$ was fit to data. The constant $C1$, which describes how much the baseline moves up and down along the y-axis, was used to define a threshold. Where the distribution crosses above this threshold determines the track transverse impact parameters

which are removed in track cleaning.
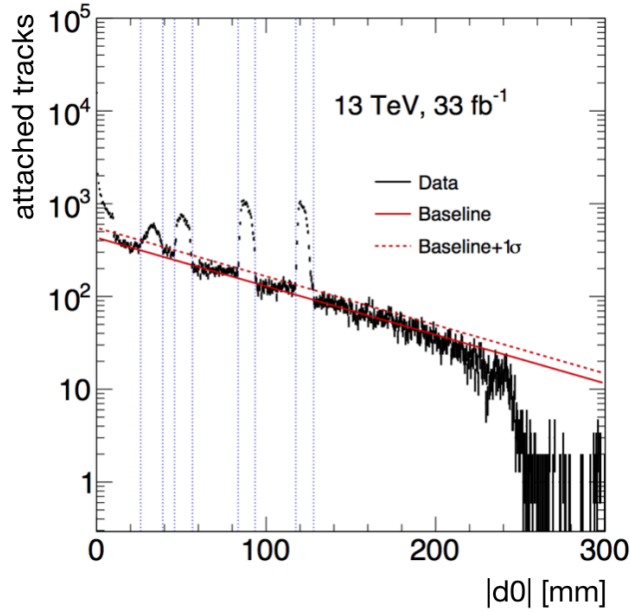
Figure 6.24: Attached track d_0 in 2016 data, shown in black. An exponentially falling distribution is fit to data and shown as a solid red line. The baseline + 1σ deviation is shown as a dotted red line. The x-axis values corresponding to where the data crosses above threshold are shown in the dotted blue lines.

Figure 6.25 show the distribution of attached tracks transverse impact parameter $|d_0|$ and ϕ, before and after track cleaning requirements are applied. The cleaning requirements reduce the effect of tracks with problematic impact parameter measurements, and also greatly reduce the ϕ asymmetry in attached tracks.

The vertex number of tracks and vertex invariant mass are recomputed after applying track cleaning requirements. Because recomputing the vertex χ^2/N_{DoF} would require access to software which is not easily accessible to analyzers, the vertex χ^2/N_{DoF} is not recomputed after cleaning. The vertex χ^2/N_{DoF} before cleaning is used instead. *Note that that all plots in this document have this track*

149
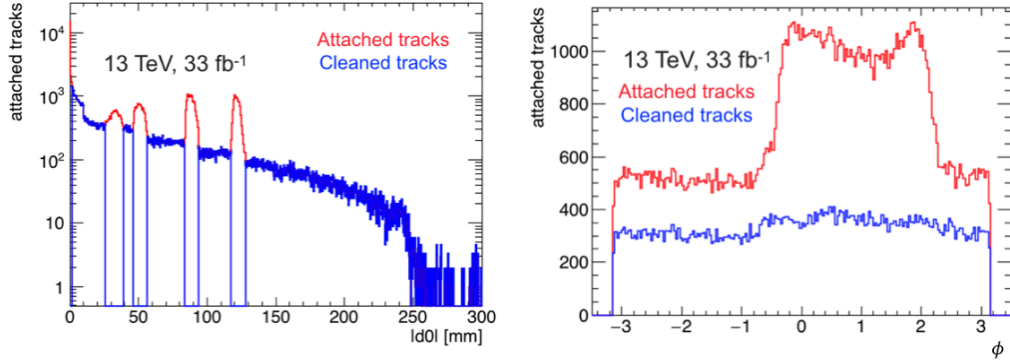
Figure 6.25: Attached tracks in 2016 data, before and after track cleaning cuts have been applied. Attached tracks before cleaning are shown in red, and attached tracks after cleaning cuts are applied are shown in blue. Left: Attached track $|d_0|$ before and after cleaning requirements are applied. Right: Attached track ϕ before and after cleaning requirements are applied.

cleaning applied apart from those presented in this section.

Displaced Vertex Performance

Three simplified models with distinct long-lived particle kinematics are used to evaluate the displaced vertex reconstruction performance. These three models are described below, and representative Feynman diagrams are shown in Figure 6.26.

- *Long-lived neutralino:* In this simplified SUSY model, gluinos are pair produced, and decay to two quarks and a neutralino. The neutralino is the lightest SUSY particle, and decays via a λ''_{112} coupling to three first and second generation quarks. The mass of the gluino is $m(\tilde{g}) = 2.4$ TeV, and the neutralino mass is varied between $m(\tilde{\chi}_1^0) = 50$ and 2350 GeV. The neutralino lifetime is $\tau(\tilde{\chi}_1^0) = 1$ ns. This model results secondary vertices with a high multiplicity of tracks.

- *Higgs portal:* In this hidden sector model, a SM Higgs boson is produced in association with a W boson, and the Higgs boson decays to a pair of BSM pseudoscalar bosons a. The a boson decays via an off-shell Higgs boson, obtaining a long-lifetime, to either a pair of bottom-quarks

or up-quarks. For these studies, the a boson has a mass $m(a) = 55$ GeV and proper lifetime $\tau(a) = 0.33$ ns. When the a decays to a pair of b-quarks, multiple secondary vertices may be reconstructed as a result of the b-quark lifetime.

- *Heavy Neutral Lepton:* In this model a Heavy Neutral Lepton, N, has small mixings with light neutrinos. The N decays to $\nu_\mu\mu^+\mu^-$, and has a mass $m(N) = 15$ GeV and lifetime $\tau(N) = 0.33$ ns. This model results in secondary vertices with lepton pairs.
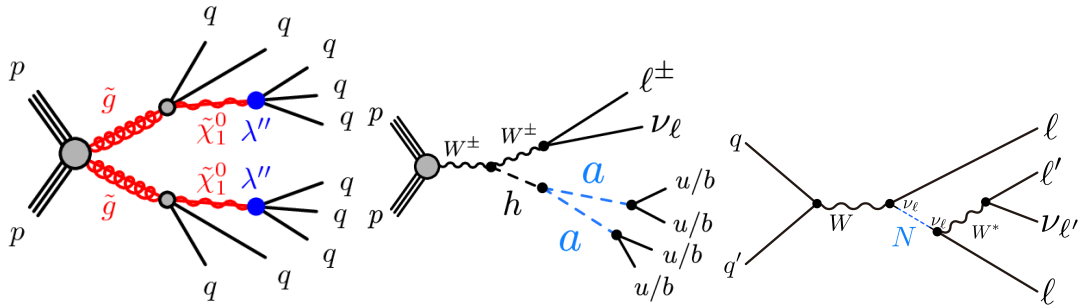
Figure 6.26: Simplified models used to study displaced vertex reconstruction performance. Left: Long-lived neutralino model. Middle: Higgs portal model. Right: Heavy Neutral Lepton

The reconstruction efficiency is defined as the rate of having a reconstructed vertex *truth matched* to an individual long-lived particle decay. Reconstructed vertices are truth matched if the majority of tracks associated to the vertex are matched to truth particles produced in the long-lived particle decay. The reconstruction efficiency is factorized into several terms, in order to separate effects from the tracking and vertexing efficiency.

The *acceptance*, A, is defined as the ratio of the number of long-lived particle decays with at least two reconstructed tracks with $p_T > 1$ GeV, to the number of long-lived particle decays with at least two charged particles with $p_T > 1$ GeV. This requirement ensures that a vertex seed can be formed by the two daughter particles, and characterizes the rate of reconstructible decays.

The *total reconstruction efficiency*, denoted ϵ^{tot}, is defined as the ratio of reconstructed, truth matched vertices, to the number of vertices which satisfy acceptance criteria. The ratio of ϵ^{tot} to the acceptance is defined as the *algorithmic efficiency*, and denoted ϵ^{alg}

The algorithmic efficiency is separated into two terms, the *seed efficiency* ϵ^{seed} and the *core efficiency* ϵ^{core}. The seed efficiency is the ratio of the number of long-lived particle decays with at least two tracks that pass the selected track criteria, to the number of long-lived particle decays in acceptance. The core efficiency is defined as the ratio of the algorithm efficiency to the seed efficiency.

The acceptance term accounts for the efficiency of reconstructing a sufficient number of tracks to form a vertex, while the seed term accounts for the selected track efficiency, and the core efficiency term probes the pure vertex reconstruction efficiency. The total vertex reconstruction efficiency is given by

$$\epsilon^{\text{tot}} = A \cdot \epsilon^{\text{alg}} = A \cdot \epsilon^{\text{seed}} \cdot \epsilon^{\text{core}}. \tag{6.5}$$

The total vertex reconstruction efficiency and each of the component terms is shown in Figure 6.27 for the three benchmark simplified models. The acceptance and efficiency is shown as a function of the long-lived particle decay position in the transverse plane, r.

The core vertex efficiency, ϵ^{core}, is nearly zero for decays which occur below $r = 2$ mm. This is an effect of the requirement that selected tracks must have $|d_0| > 2$ m. Above $r = 2$ mm, the total vertex reconstruction efficiency degrades with r. This degradation in efficiency is due to a reduction in tracking efficiency, which degrades with increasing radial displacement.

Figure 6.27 also highlights how the reconstruction efficiency increases with the number of charged
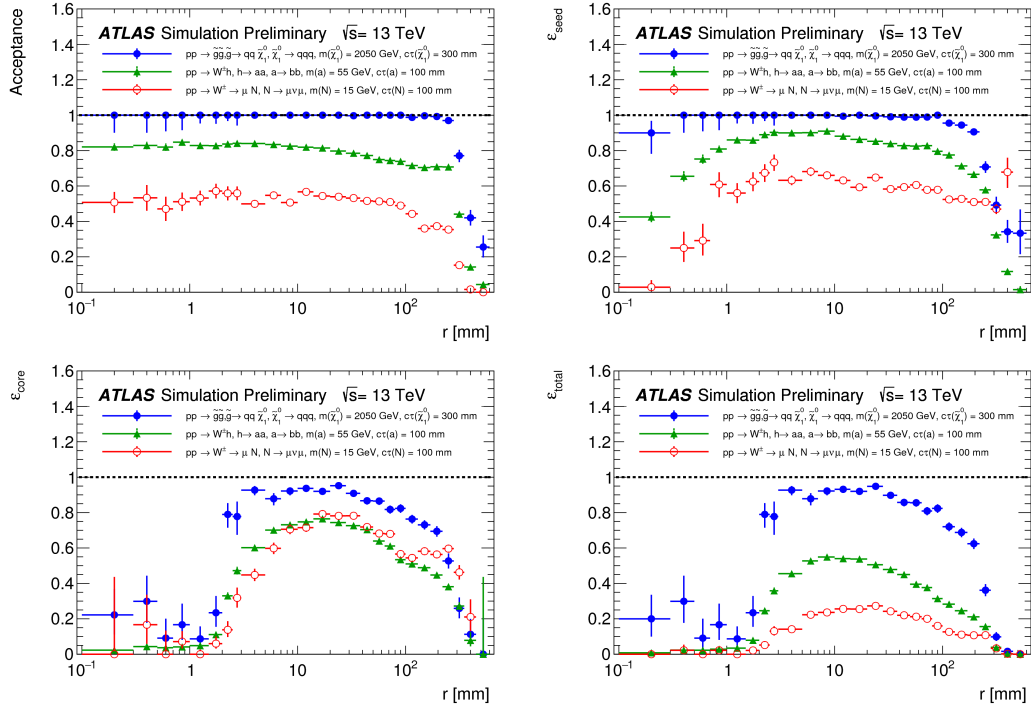
Figure 6.27: The displaced vertex acceptance (top left), seed (top right), core (bottom left), and total (bottom right) vertex reconstruction efficiency as a function of the long-lived particle decay position in the transverse plane, r. The acceptance and efficiencies are shown for the long-lived neutralino (blue), Higgs portal (green), and Heavy Neutral Lepton (red) simplified models [81].

daughter particles produced in the long-lived particle decay. If there are more charged daughter particles there is a higher probability of reconstructing a sufficient number of tracks to form a vertex. As a result, the total reconstruction efficiency is highest for the long-lived neutralino model, followed by the Higgs portal model, and then the Heavy Neutral Lepton model.

The vertex acceptance and efficiency also depends on the average number of pp-interaction per bunch crossing, $\langle \mu \rangle$. As discussed in Section 6.5.1, the Large Radius Tracking efficiency degrades as a function of $\langle \mu \rangle$. Detector hits produced from real charged particles are associated to fake tracks or

accidentals. This results in both a degradation in tracking efficiency and a degradation of the number of hits associated to tracks from real charged particles. The degradation in tracking efficiency results in a 5 to 10% degradation in the vertex acceptance between $10 < \langle \mu \rangle < 80$. The reduction in the number of hits associated to tracks results in a 5 to 20% degradation in the vertex seed efficiency between $10 < \langle \mu \rangle < 80$. The change in efficiency varies depending on the model, and models with a higher track multiplicity are more robust to the effects of pile-up. The core vertex efficiency is not affected by increasing pile-up.

Figure 6.28 shows the vertex position resolution for the long-lived neutralino model. The vertex position resolution is computed by taking difference between the reconstructed vertex position and the long-lived particle decay position, and taking the standard deviation of the resulting distribution. The position resolution is evaluated separately for differences in the radial and longitudinal directions, as σ_r and σ_z. The resolution is also measured in the ϕ direction, scaled by the radial displacement $r \times \sigma_\phi$. The position resolution improves with the number of tracks associated to the vertex. The vertex position resolution also degrades with increasing r. This effect is due to the degradation in impact parameter resolution as a function of radial track displacement.
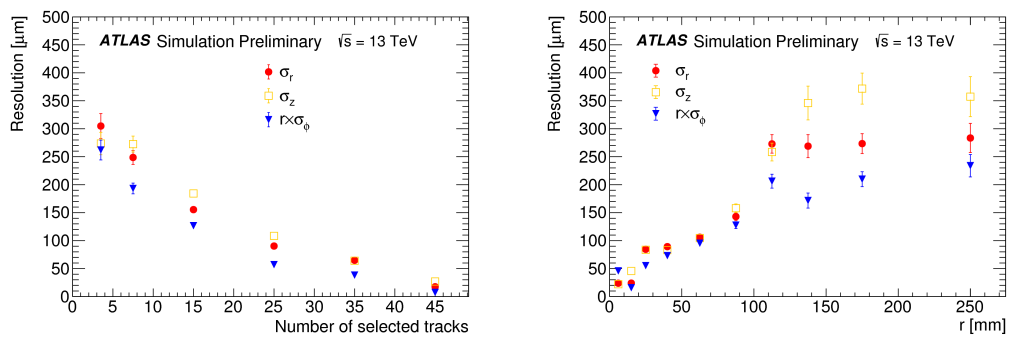
Figure 6.28: Displaced vertex position resolution as a function of the number of tracks (left) and long-lived particle decay radius, r (right). Resolutions are separately evaluated for σ_r, σ_z, and $r \times \sigma_\phi$. [81].

7

Trigger

Due to limitations in data storage, transfer rates, and computing power, only a small fraction of the collisions produced at the LHC can be recorded. Deciding which events should be saved for future analysis and which should be thrown away is the job of the trigger. The importance of the trigger cannot be overstated. If the trigger does not select an interesting event or physics process, that event is lost forever. A good trigger must balance the selection efficiency for a process of interest with strong background rejection to reduce the rate. Selections must be robust, and based on well-understood features that can separate interesting physics processes from backgrounds.

ATLAS uses a multi-stage approach to quickly decide which events are interesting. The first stage must process all of the data quickly, and is referred to as the Level 1 (L1) trigger. The L1 trigger is hardware-based, regional, and uses coarse detector information. The L1 trigger must make a decision

in 2.5 μs, and reduces the event rate from 40 MHz to 100 kHz. The second stage is referred to as the High Level Trigger (HLT). Because the HLT processes fewer events than L1, it has more time to make a decision, on average 200 ms, and can make use of higher granularity information. The HLT is software-based, and reduces the event rate to $1 - 1.5$ kHz.

Finding a trigger which can select events with displaced signatures is a challenge for nearly every long-lived particle analysis. In order to keep the rate of selected events manageable, the ATLAS trigger usually assumes all particles are produced at the pp-interaction point. For example, triggers that select events with electrons or muons typically require the leptons have impact parameters consistent with the pp-interaction point ($|d_0| < 10$ mm).

There are a few strategies which ATLAS long-lived particle searches can use to trigger on events:

1. Trigger on prompt objects in the event using standard triggers. The effectiveness of this strategy is model dependent, and in some cases can hurt sensitivity by one or two orders of magnitude.

2. Trigger on displaced jets or real E_T^{miss} using standard jet or E_T^{miss} triggers. The ATLAS jet and E_T^{miss} triggers do not explicitly associate tracks to jets or Calorimeter activity. These triggers may be used for long-lived particle decays which occur inside or before the Calorimeter detector volume. In the case of the E_T^{miss} trigger, it may also be used to trigger on long-lived particles which escape the Calorimeter volume. This strategy is most effective for signal models with heavy particles which produce jets with large transverse momentum or events with large E_T^{miss}, and is generally less effective for probing lighter long-lived particles.

3. Use a trigger in a way it was not intended. For example, a photon trigger can be used to trigger on events with displaced electrons. This strategy extends sensitivity from $|d_0| < 10$ mm to several centimeters, at the cost of increasing the momentum threshold (in 2018, this strategy would increase the p_T threshold from $p_T > 26$ to 140 GeV). The E_T^{miss} trigger can also be used to trigger on displaced muons, again trading in sensitivity to larger displacements for higher p_T thresholds.

4. Design a trigger specific to a long-lived particle signature. This process is work-intensive, and

must overcome the challenge of finding a suitable hardware-based trigger. Usually, these specialized triggers are only allocated a limited amount of bandwidth, and cannot exceed a rate of ~ 10 Hz.

This analysis uses two triggers to select events. The first trigger is specifically designed to select events with a displaced muon. The second trigger selects events with significant $E_{\mathrm{T}}^{\mathrm{miss}}$, as measured by the Calorimeter. Even though the benchmark signal model considered by this analysis does not produce particles which are invisible to the ATLAS detector, the high momentum muons only deposit a fraction of their energy in the Calorimeter, resulting is large apparent $E_{\mathrm{T}}^{\mathrm{miss}}$, and a $E_{\mathrm{T}}^{\mathrm{miss}}$ trigger.

The ATLAS trigger scheme is described in Section 7.1. The Muon Spectrometer trigger is described in Section 7.2, with an emphasis on the specific trigger used in this analysis. The $E_{\mathrm{T}}^{\mathrm{miss}}$ trigger is described in Section 7.3. A paper which uses data collected in 2015 provides more detail about the ATLAS trigger scheme and performance in $\sqrt{s} = 13$ TeV [83], including triggers not discussed in this thesis.

7.1 Trigger scheme

The LHC runs with a bunch spacing of 25 ns, corresponding to a peak *event rate*, or bunch crossing rate, of 40 MHz. Each ATLAS event contains ~ 25 MB of RAW, detector-level data. When reconstructed, the event size can be reduced to ~ 1 MB of data. If ATLAS were to save every reconstructed LHC collision, this would result in an accumulation of 40 TB of data per second, and nearly 150 petabytes per hour. It is impossible to store and process this much data, and the dataset would consist of mostly unremarkable events.

Given the size of a full ATLAS event, and the rate at which data can be transferred, it is only possible

to save data at a rate of $\sim$ 1 kHz. This means that ATLAS on average can only keep one event out of every 40,000. The ATLAS trigger is designed to quickly select which events are saved for future analysis, reducing the dataset to a manageable size using a multi-step triggering scheme. The first stage is referred to as L1 and the second as HLT. The ATLAS trigger scheme is summarized in Figure 7.1, and discussed in more detail below.
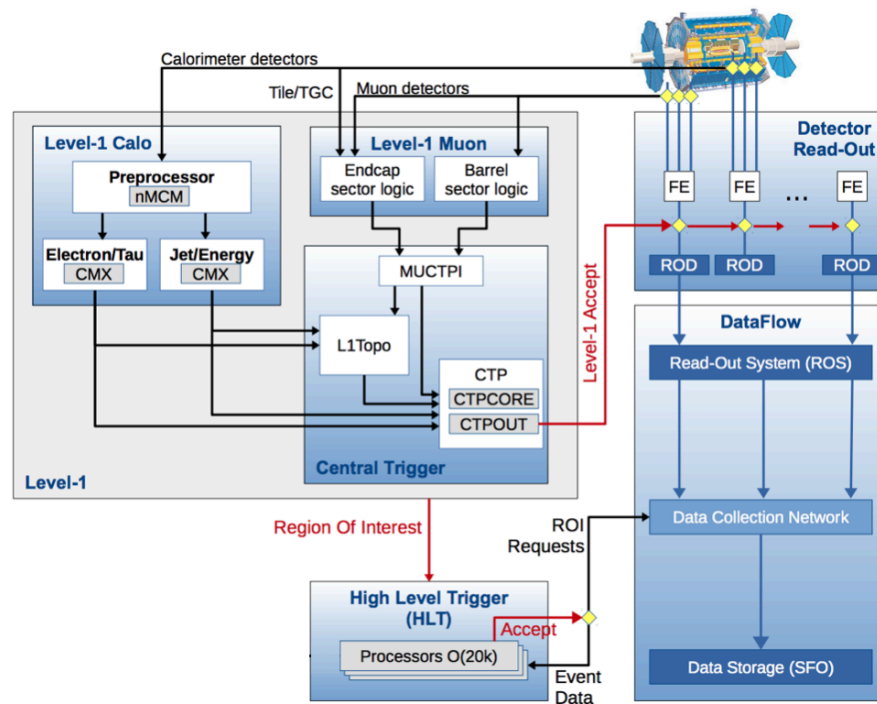
Figure 7.1: Schematic of the ATLAS trigger and data acquisition system [84]

The ATLAS *trigger menu* consists of the lists of triggers used to select which events are saved for future analysis. The menu consists of different L1 *trigger items*, HLT *trigger chains*, and their *trigger prescales*. A single L1 item can seed many HLT trigger chains, but each HLT trigger is usually seeded by

a single Lı item. A typical Lı item is L1_MU20, which is for a single muon with a momentum threshold

of 20 GeV. A typical HLT chain is HLT_mu26_ivarmedium, which selects events with a muon that

has $p_T > 26$ GeV, passes an isolation requirement, and is seeded by L1_MU20. Prescales determine the

rate at which a specific trigger item or chain should be accepted. For example, a prescale of 100 means

that 1 out of 100 events that fired the trigger are accepted.

At Lı, detectors with fast readout are used in a hardware-based trigger, which reduces the event

rate from 40 Mhz to 100 kHz. This output rate is limited by how quickly the detector can be read

out as well as how much data the HLT can process. The Lı trigger uses custom application-specific

integrated circuit (ASIC)s and field-programmable gate array (FPGA)s located near the detectors, and

must make a decision in less than 2.5 μs. This includes up to 70 ns for a particle's time of flight from

the interaction point to the detector (for the Muon Spectrometer end-caps), and roughly 1 μs needed

to transmit signals between on-detector electronics and dedicated trigger electronics in a neighboring

counting room.

The Lı trigger uses coarse detector information from the Muon Spectrometer and Calorimeter.

The Level 1 Muon Trigger (LıMuon) looks for coincidences in different layers of the RPC and TGC

that are consistent with muons produced from pp-interactions. The Calorimeter information used

for the Lı trigger is referred to as Level 1 Calorimeter Trigger (LıCalo). LıCalo uses coarse grained

information from all Calorimeter systems, and is responsible for all other triggers besides those used

for muons. This includes triggers for electrons, photons, jets, taus, event transverse energy, and E_T^{miss}.

No information from the Inner Detector is used at Lı because of the large number of channels and

long time it would take to reconstruct tracks.

About one third of events which fire a L1 trigger are selected by the Muon trigger, another third by the Electromagnetic Calorimeter trigger, and the remaining third by Hadronic Calorimeter triggers, or combined objects like a muon trigger plus an ECAL deposit. At L1, the Calorimeter and Muon triggers can flag the same event.

Figure 7.2 shows the trigger rate for several L1 items during a run taken in 2018. This run had peak luminosity of $2.0 \times 10^{34} \mathrm{cm}^{-2}\mathrm{s}^{-1}$ and a peak average number of interactions per crossing of $\langle \mu \rangle = 56$. A few representative single-object triggers are shown, which have not been prescaled. All trigger rates decay with decreasing instantaneous luminosity. Rates also increase periodically due to LHC luminosity re-optimizations. There are also dips in rate due to dead-time, as well as spikes caused by detector noise.
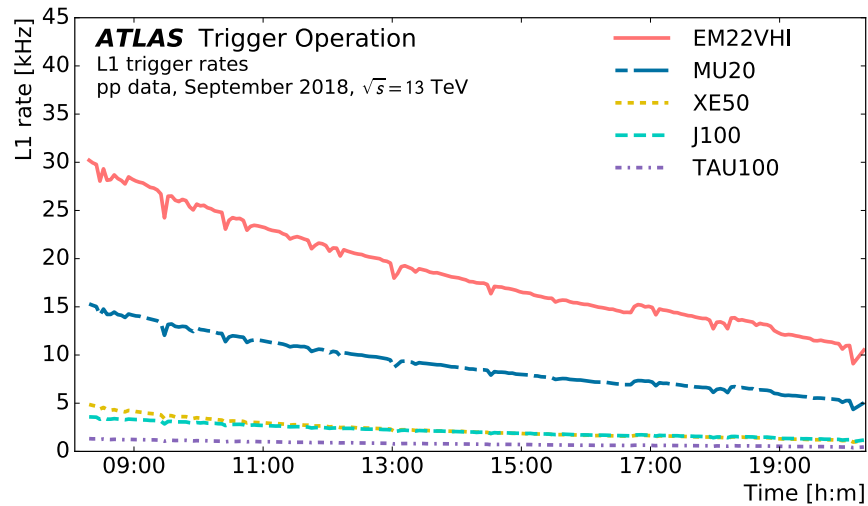
Figure 7.2: L1 Trigger rates during a run from 2018. Trigger items are based on electromagnetic clusters (EM), muon candidates (MU), jet candidates (J), missing transverse energy (XE) and tau candidates (TAU). The number in the trigger name denotes the trigger threshold in GeV. The letters following the threshold values refer to details of the selection, including variable thresholds (V), hadronic isolation (H), and electromagnetic isolation (I) [85].

If an event passes a L1 trigger, that information is sent to the Central Trigger Processor (CTP). This information includes any Region of Interest (RoI) identified by the L1Muon and L1Calo. The CTP also applies any prescales. The CTP distributes the signal that an event has been accepted at L1 to the full detector via optical cables to on-detector buffers (which hold 2.5 μs of data). When the front-end electronics receive a L1 signal the data are sent to off-detector read-out drivers in the counting room, where they are packaged and processed. Read-out drivers are detector specific, and re-package the data before sending it in a common ATLAS format to the read-out servers. Read-out drivers also have sufficient processing power to monitor the data and even perform basic calibrations. Data are then sent to read-out servers, where they await a decision from the HLT. Unlike read-out drivers, read-out servers are common to all sub-detectors.

The HLT is a software based trigger, which uses a computing farm of more than 20,000 processors to reduce the event rate to $1 - 1.5$ kHz. Any prescales applied to HLT triggers are applied before the decision is made, in order to save computing time. Many HLT algorithms use a two step process in order to reduce the time it takes to make a decision. First a rough pass at reconstruction is made inside any RoI identified by the L1 trigger. In the second stage, more complex reconstruction techniques, which are very similar to the offline reconstruction methods described in Chapter 6 and utilize the full granularity of the detector are used. The HLT is the first stage in which ID information is incorporated into the trigger.

The HLT has on average 200 ms to make a decision. It is impossible to reconstruct all of an event's ID tracks in the alloted time. In order to overcome the strict processing time constraints at HLT, Inner Detector tracks are only reconstructed inside regions of interest identified by L1. In order to reduce

CPU usage, ID track reconstruction is performed in two steps. In the first step, trigger specific pattern recognition is used to identify track seeds. In the second step, those seeds are used to reconstruct precision tracks, with methods very similar to those used in standard offline reconstruction. About 40%, 35% and 15% of the processing time at HLT is spent on Inner Detector tracking, Muon Spectrometer reconstruction, and Calorimeter reconstruction, respectively.

About 30% of events selected by the HLT are used for electron and muon triggers. About 20% of events are selected by hadronic triggers, and 15% by $E_{\mathrm{T}}^{\mathrm{miss}}$ triggers. The remaining available bandwidth is divided equally among photon, tau lepton and B-physics triggers. Figure 7.3 shows HLT trigger rates during a run from 2018 (the same run as Figure 7.2). Like the L1 rates, HLT trigger rates decay with decreasing instantaneous luminosity, and exhibit similar dips and spikes due to dead-time and detector noise.

Events selected by the HLT are saved in RAW format at the CERN Tier-0 facilities as separate data *streams*. Events used for physics analysis are saved as `physics_Main`. A subset of `physics_Main` (approximately 10 to 20 Hz) is written to an express stream, which is immediately reconstructed in order to begin important steps for calibration and data quality checks before reconstructing the full `physics_Main` dataset. There are also additional streams for calibration, monitoring, and detector performance studies. Tier-0 processes approximately one petabyte of data every day.

Events which cannot properly be processed by the HLT are saved to a *debug* stream. The most common reason events are sent to the debug stream is due to long processing times (several minutes per event). Events with many muon tracks have the longest processing times, especially those due to jets which are not fully contained in the Calorimeter.
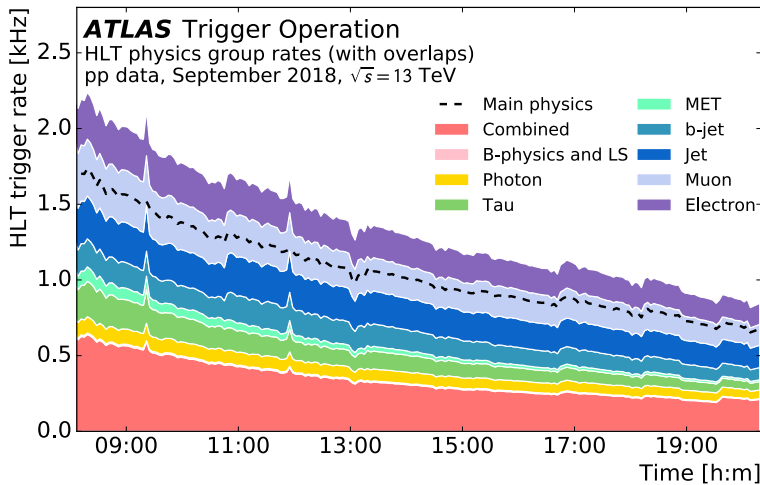
Figure 7.3: HLT Trigger rates during a run from 2018. Individual groups of triggers specific to trigger physics objects are presented. Each group contains single-object and multi-object triggers. Overlap between different groups is only accounted for in the total main physics stream rate. The combined group represents multiple triggers of different objects, as combinations of electrons, muons, taus, jets and missing transverse energy. B-physics and Light States (LS) triggers which are based on muon objects are not included here [85].

7.2 MUON SPECTROMETER TRIGGER

Many physics processes of interest at the LHC result in a final state muon. These processes include several decay modes of the Standard Model Higgs boson, the W and Z vector bosons, and many hypothetical new particles. Final state muons are expected to be produced with a wide range of momenta, necessitating a high performing muon trigger. The ATLAS muon trigger is designed to work with high efficiency and low transverse momentum thresholds in the presence of challenging backgrounds.

The L1 muon trigger works to match RPC or TGC hits to pre-defined roads. These hits must be coincident in space and time, and consistent with a muon produced at the pp-interaction point. Several triggers are defined with different momenta threshold, and are separately categorized as low-

p_T or high-p_T thresholds.

The transverse momentum of the muon candidate is estimated by comparing the muon candidate's hit pattern to the expected the hit pattern of a muon with infinite momentum, which would form a straight line. The degree of deviation in hit patterns is treated as the width of a road, and wider roads correspond to the paths of lower momentum muons. Low-p_T triggers also require fewer hit coincidences within a road than high-p_T triggers. High-p_T muons can fire the low-p_T threshold triggers, but low-p_T muons would produce hits outside a narrow road designed for a high-p_T muon. Figure 7.4 shows a schematic of typical muon tracks that would generate low-p_T and high-p_T L1 triggers in both the barrel and the end-cap.
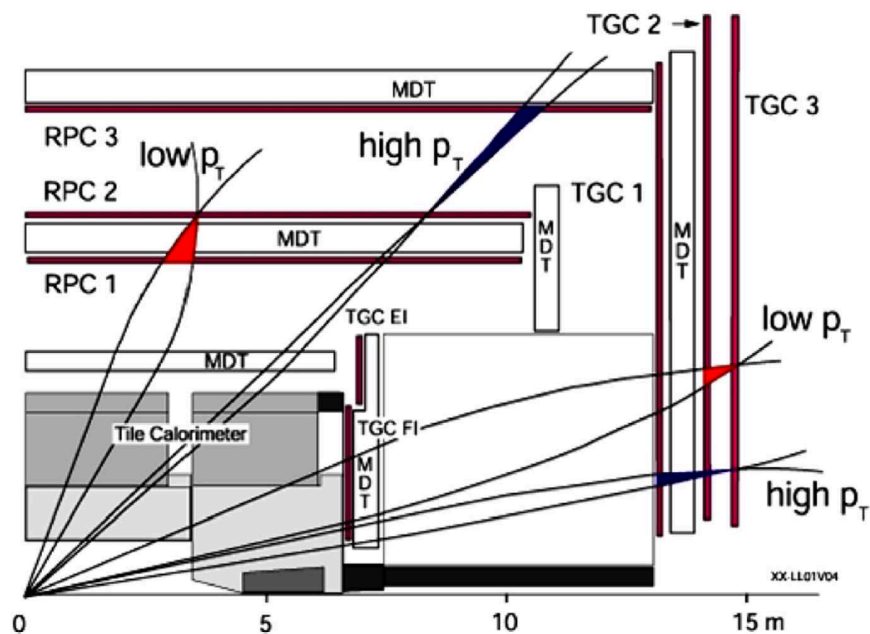
Figure 7.4: Typical muon tracks generating triggers in the Muon Spectrometer barrel and end-cap at L1 [86].

In the barrel, there are three layers of RPC chambers (RPC1, RPC2, and RPC3 in Figure 7.4). Hit coincidences are required in two of three layers (RPC1 and RPC2) in order to produce a low-p_T trigger. Hits are required in all three layers to produce a high-p_T trigger.

In the end-cap L1 hit requirements are complicated by large backgrounds from low energy protons produced in the end-cap toroid. The toroid sits between the Inner and Middle end-cap stations. Interactions with the end-cap toroid result in these low energy protons, which in turn produce hits in the Middle and Outer station of the end-cap, but not the Inner station.

In Run 1, the Inner station TGC chambers were not included as a L1 requirement. A large rate of triggers would be produced from these low energy protons. These triggers are not associated with real muons and use up valuable bandwidth. Figure 7.5 shows how without any information from the Inner station TGC chambers, it is very difficult to tell whether or not a L1 trigger is consistent with a muon produced at the pp-interaction point or from interactions in the toroid.

As a general rule, TGC hits are required in all three layers of the TGC which sandwich the Middle station of the MDT (TGC1, TGC2, and TGC3 in Figure 7.4). In some regions, exceptions are made to improve acceptance for very low-p_T muons. In Run 2, hits in the Inner station chambers (TGC EI and FI) are also required, aiming to reduce the rate of L1 coincidences from background. Adding this coincidence reduced the overall L1 muon trigger rate by $\sim 20\%$ with a 1% decrease in efficiency [88]. Unfortunately, the Inner station does not have full TGC coverage in η and ϕ, and high trigger rates are still a challenge for ATLAS.

In 2016, new RPC chambers were included in the trigger. These chambers are located in the feet region, and improved efficiency by 4% in the barrel. Figure 7.6 shows the improvement in L1 trigger
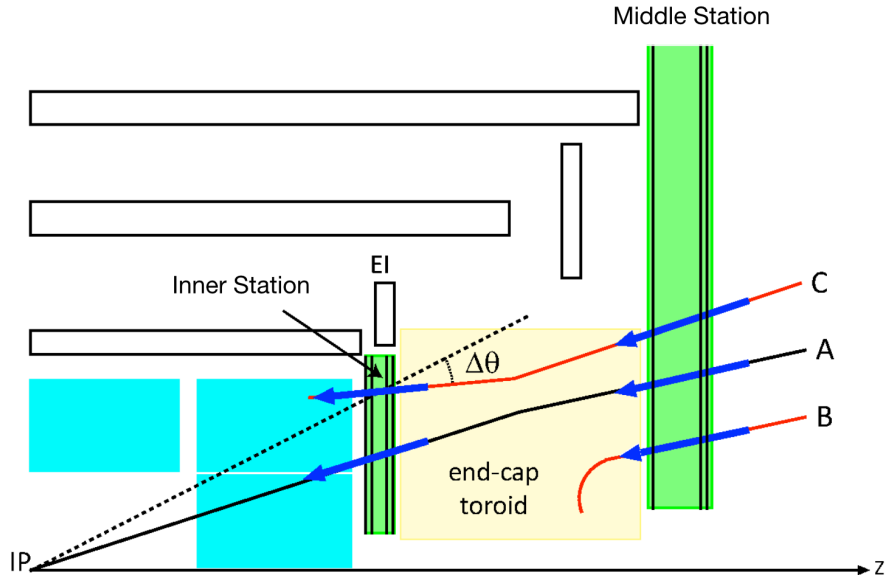
Figure 7.5: Fake L1 muon triggers produced in the Muon Spectrometer end-cap. Only the Inner and Middle stations of the end-cap are shown. Track A leaves a track in all detector regions and points towards the interaction point. Track B gives only a signal in the Big Wheel and Track C does not point towards the interaction point. Only Track A corresponds to an acceptable muon. [87].

efficiency from adding the new chambers. The change in trigger efficiency for L1_MU11 is shown for ϕ-sectors 12, and 14, which refer to the feet region. In both ϕ-sectors, adding the new chambers improves the overall efficiency, and makes the efficiency more constant as a function of η. With the new chambers, the detector coverage is $\sim 80\%$ in the barrel, and $\sim 90\%$ in the end-caps.

ATLAS has six L1 muon trigger items, three for low-p_T muons and three for high-p_T muons. The low-p_T muon items are L1MU4, L1MU6, and L1MU10 GeV. In 2015-2016, the three high-p_T muon items were L1MU11, L1MU15, and L1MU20, where L1MU11 required a 10 GeV threshold and coincidences consistent with a high-p_T muon. In 2017-2018, the three high-p_T items were L1MU11, L1MU20, and L1MU21. The last two items both applied a 20 GeV thresholds, but L1MU21 included the new RPC
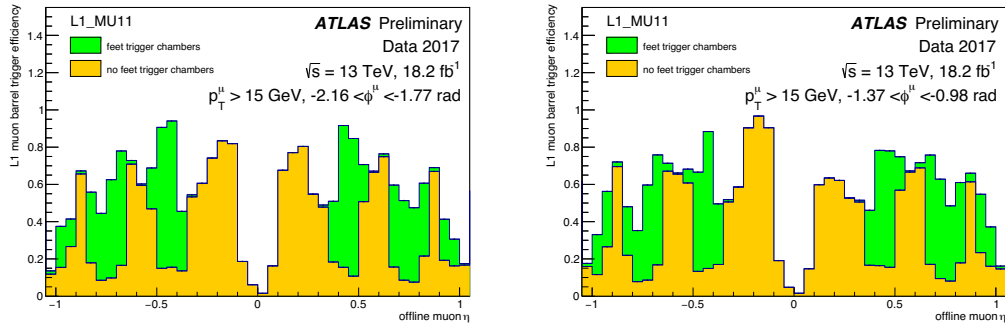
Figure 7.6: L1 trigger efficiency before and after including new RPC chambers [88]. The efficiency is computed with a subset of 2017 data, with respect to offline muon candidates which are which pass a Medium quality requirement, are isolated, and have a transverse momentum of at least 15 GeV. The trigger efficiency is shown for (left) ϕ-sector 12 and (right) ϕ-sector 14, which refer ot the feet region.

chambers in the feet while `L1MU20` did not.

The HLT receives information regarding which trigger item fired at L1, including the region of interest and p_T threshold, as well as precision measurements from the MDT and CSC. The HLT muon reconstruction is split into two steps in order to speed up processing time.

In the first step, the muon candidate from L1 is refined by including precision hits from the MDT and CSC which are inside the region of interest. Regions of interest are (0.1×0.1) in the barrel and (0.03×0.03) in the end-cap in $(\Delta\eta \times \Delta\phi)$. Precision hits and positions are used to quickly reconstruct a muon track, and the transverse momentum of the muon track is computed from a look up table.

The second step of HLT muon reconstruction is referred to as the precision stage. This step begins from the muon candidates reconstructed in the first step as seeds. Methods similar to the offline reconstruction (described in Section 6.3) are used to reconstruct segments and tracks from hits in precision

and trigger chambers. Precision muon tracks, also known as MS-only muons, are first reconstructed in the muon detectors, and are then combined with Inner Detector tracks into combined muons.

If no matching ID track is found, combined muon candidates are searched for by extrapolating ID tracks to the MS. This inside-out approach is one of the most time intensive algorithms in the HLT, and is only used if the outside-in approach fails. Additional requirements, including requiring a muon be isolated from other Inner Detector tracks, may also be applied in order to maintain a reasonable trigger rate at low transverse momentum thresholds.

The average time for the fast reconstruction step to reconstruct a MS-only candidate is $\langle t \rangle = 8.2$ ms. The average time to combine this candidate with Inner Detector information is $\langle t \rangle = 6.2$ ms. On average, the precision reconstruction step takes 239.5 ms. However, this step has a long tail which extends out to processing times on the order of seconds.

Figure 7.7 shows the muon trigger efficiency in the barrel of MS, measured using a subset of the 2018 data. The trigger efficiency is computed with respect to offline muons which pass an isolation and a Medium quality requirement. The L1 muon trigger in the barrel detector region has an efficiency of approximately 70%. Reductions in trigger efficiency at L1 are due to lack of RPC detector coverage near $\eta \approx 0$ and in the feet of the detector.

The HLT_mu26_ivarmedium trigger is seeded by the L1_MU20 trigger, and requires that a candidate satisfy a 26 GeV p_T threshold, and pass a medium isolation requirement. The HLT_mu50 trigger is also seeded by L1M_U20 at L1 and requires that a candidate satisfy a p_T threshold of 50 GeV, with no isolation or quality requirement. In ATLAS it is standard to use both HLT muon triggers. Isolation and quality requirements are made for the lower threshold trigger, in order to reduce the rate of

169
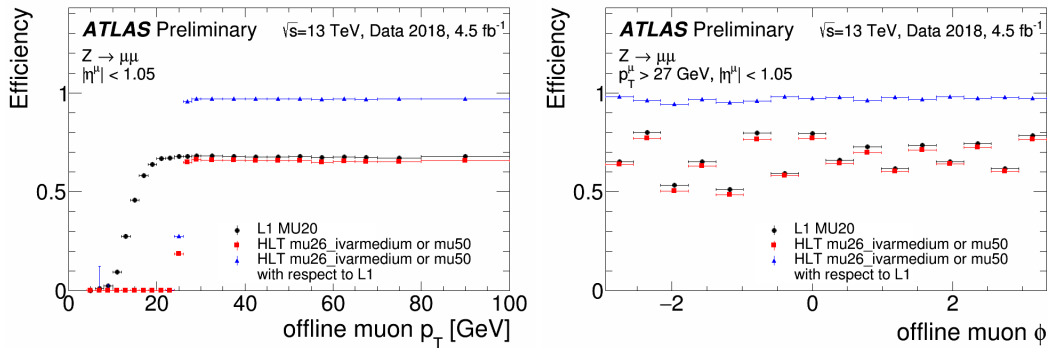
Figure 7.7: Muon Trigger efficiency at L1 and HLT for muons with $|\eta| < 1.05$, measured using $Z \to \mu\mu$ events in 2018 data. Left: efficiency versus muon p_T, Right: efficiency versus muon ϕ [89].

muons from hadron decays which fire the trigger. No such requirements need to be applied to higher momentum muons, which are produced at a lower rate. The HLT trigger efficiency is nearly 100% when computed with respect to muons which pass a L1 trigger.

Most muon triggers require combined muons, in which the ID track is strictly required to have a transverse impact parameter $|d_0| < 10$ mm. However, several long-lived particle analyses use of triggers which only require MS-only muons. Because these MS-only triggers are agnostic to Inner Detector activity, it is possible to trigger on muons produced from long-lived particles. The MS-only trigger used in this analysis is described in Section 7.2.1.

7.2.1   Muon Spectrometer Only Trigger

Muons produced in long-lived particle decays often have displacements which are too large to produce a combined muon at HLT. In order to recover efficiency that would be lost from using standard muon triggers, dedicated MS-only triggers are used in several long-lived particle analyses. However,

because these MS-only triggers are agnostic to Inner Detector activity, they suffer from a large background rate, especially in the end-caps.

In order to overcome these rate limitations, the Run 2 Muon Spectrometer only trigger is limited to the barrel ($|\eta| < 1.05$), and has a high momentum threshold which requires $p_T > 60$ GeV. This trigger is referred to as `HLT_mu60_0eta105_msonly`. This trigger is fully efficient for muon with $p_T > 62$ GeV. Muons with transverse momentum $p_T > 62$ GeV and $|\eta| < 1.05$ are considered in the trigger acceptance. Figure 7.8 shows the Muon Spectrometer only trigger efficiency as a function of muon $|d_0|$. This efficiency is measured in simulated samples, by computing the fraction of reconstructed muons in acceptance which fired the trigger.
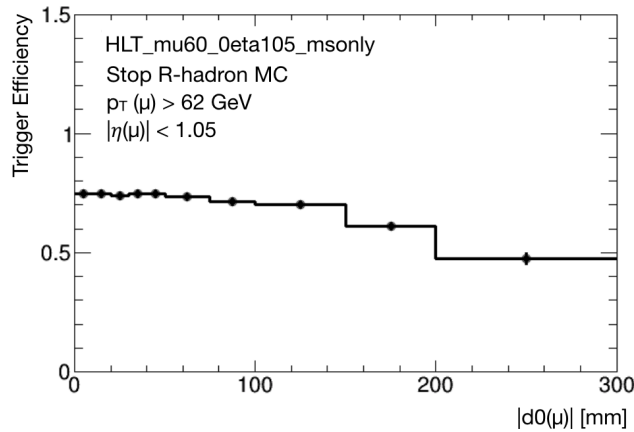
Figure 7.8: Muon Spectrometer only trigger efficiency as a function of muon transverse impact parameter $|d_0|$.

For prompt muons in acceptance, the trigger has an efficiency of approximately 75%, as measured in simulation. However, this efficiency is reduced as a function of increasing muon transverse impact parameter, and is less than 50% for muons with impact parameters $|d_0| > 200$ mm. This reduction

in efficiency is due to the Level 1 roads, which were optimized for prompt muons that point back to pp-interaction point.

7.3   Missing Transverse Energy Trigger

While offline $E_\mathrm{T}^\mathrm{miss}$ definitions usually include muons in the $E_\mathrm{T}^\mathrm{miss}$ calculation, the L1 and HLT trigger definitions do not. Only energy measurements in the Calorimeter are used in the trigger. Because muons only deposit a fraction of their energy in the Calorimeter, events with high momentum muons can also fire a $E_\mathrm{T}^\mathrm{miss}$ trigger.

In ATLAS, the $E_\mathrm{T}^\mathrm{miss}$ trigger is part of the Level 1 Calorimeter trigger. Rather than read out information from all cells individually, L1Calo sums up signals from groups of neighboring cells called *trigger towers*. The analog signals from these neighboring cells are added, digitized, calibrated, and read out as a single tower. Trigger towers have granularity (0.1×0.1) in $(\Delta\eta \times \Delta\phi)$ in the central region and (0.4×0.4) in the forward region. There are 7168 towers in total, which are split between the Electromagnetic and Hadronic Calorimeters.

The L1Calo compiles several types of trigger items. Central ($|\eta| < 3.2$) trigger towers are used for electrons and photons, taus, and jets. Trigger towers in the Forward Calorimeter ($|\eta| > 3.2$) are used for forward jet triggers. All trigger towers, (both central and forward) are used to define global triggers, for variables such as $E_\mathrm{T}^\mathrm{miss}$ and $E_\mathrm{T}^\mathrm{miss}$-significance.

The L1 $E_\mathrm{T}^\mathrm{miss}$ is computed using combinations of adjacent trigger towers in η and ϕ, which are referred to as *jet elements*. These jet elements consist of 2 adjacent towers in η and 2 adjacent towers

in ϕ, for a coverage of (0.2×0.2) in $(\Delta\eta \times \Delta\phi)$ in the central region. Electromagnetic Calorimeter towers are also combined with Hadronic Calorimeter towers with similar η and ϕ.

These jet elements are sent to a jet-energy sum processor. This processor computes the event's scalar and missing transverse energy. The E_T^{miss} is computed from the negative vector sum of $\langle E_x, E_y \rangle$ of all jet elements. If the computed E_T^{miss} is above threshold, the event passes a L1 E_T^{miss} trigger.

In order to cope with the high instantaneous luminosity delivered by the LHC in Run 2, a pedestal correction is applied to the energy measurement of each jet element. This pedestal correction is computed for each bunch. The ATLAS Liquid Argon Calorimeter signal must be integrated over 24 bunch crossings (600 ns). This long readout window means that particles produced from collisions in neighboring bunches can produce energy depositions that will contribute to the signal. Collisions which are positioned at the beginning of a bunch train have a higher on average signal than collisions produced from the end of a bunch train. The average signal amplitude is referred to as the pedestal. The pedestal is computed for each bunch, at different instantaneously luminosities, and used to correct the energy of each jet element.

Figure 7.9 shows how the pedestal correction helps to reduce the the E_T^{miss} trigger rate as a function of instantaneous luminosity. Because of this pedestal correction, ATLAS was able to keep the threshold of the lowest unprescaled L1 E_T^{miss} trigger at 50 GeV for all of Run 2. The correction is also applied to the Liquid Argon in the jet energy calibration used at HLT.

For the HLT E_T^{miss} trigger, one of the main challenges is finding a E_T^{miss} definition which is nearly consistent with the offline E_T^{miss} definition, and also robust to pile-up. Throughout the course of Run 2, many different E_T^{miss} definitions have been tested. In 2015, a cell-based approached was used
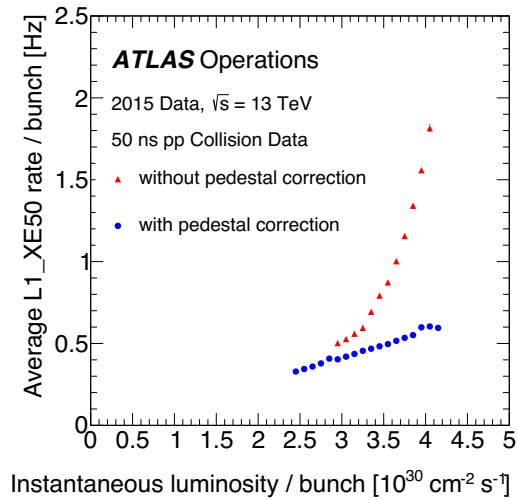
Figure 7.9: The L1 $E_\mathrm{T}^\mathrm{miss}$ trigger rate as a function of the instantaneous luminosity per bunch, for a threshold of 50 GeV. The trigger rate is shown with and without the pedestal correction. [90].

as the default $E_\mathrm{T}^\mathrm{miss}$ trigger. In 2016, a jet-based approach was used, while in 2017-2018 the default trigger used topological cluster-based algorithms with a pile-up subtraction scheme [91]. This analysis uses the the default $E_\mathrm{T}^\mathrm{miss}$ triggers for data collected between 2016-2018, with the lowest unprescaled threshold.

In 2016, the $E_\mathrm{T}^\mathrm{miss}$ trigger used the jet-based `mht` definition, where `mht` stands for missing H_T. For a given event, the missing H_T is the negative of the transverse momentum vector sum of all jets. Jets are reconstructed using the anti-k_t jet finding algorithm from topological calorimeter clusters, (which are described in 6.4.1). These jets have a radius of $\Delta R = 0.4$, as well as pile-up subtraction and jet energy scale calibration applied.

In 2017-2018, the $E_\mathrm{T}^\mathrm{miss}$ trigger used a pile-up fit, or `pufit`, algorithm. In the `pufit` method, the $E_\mathrm{T}^\mathrm{miss}$ is calculated as the negative of the transverse momentum vector sum of all calorimeter topo-

logical clusters, corrected for pile-up. The pile-up correction is performed by grouping topological clusters into coarser towers of size (0.7×0.7) in $(\Delta\eta \times \Delta\phi)$. A pile-up-dependent threshold is used to separate towers into two categories. Towers with energies below the threshold are marked as pile-up, while towers with energies above the threshold are considered to be due to the pp-interaction of interest.

A fit to below-threshold towers is performed in order to compute the event's transverse energy density due to pile-up. This fit takes tower energy resolutions and tower area in $\eta \times \phi$ into account. The fit assumes that pile-up makes no contribution to the event's E_T^{miss}, and constrains the event-wide E_T^{miss} from below-threshold towers to zero, within resolution. This fit gives the pile-up transverse energy density. This fitted pile-up transverse energy density is used to correct towers which are above-threshold.

Figure 7.10 shows the trigger cross section as a function of the mean number of interactions per bunch crossing, averaged over all bunch crossings in the LHC. Data from 2016 are used to measure the cross section of the mht based trigger, while 2017 data are used to measure the cross section of the pufit based trigger. The trigger cross section is much larger for an mht based E_T^{miss} definition. Due to rate concerns, a pufit based E_T^{miss} definition was used for 2017 and 2018 data taking.

Figure 7.11 shows the E_T^{miss} trigger efficiency at L1 and HLT as a function of the offline E_T^{miss} in $W \rightarrow \mu\nu$ events. The muon is not included in the offline E_T^{miss} definition, and treated as invisible. Events are collected with a single muon trigger. The L1 E_T^{miss} trigger reaches full efficiency by $E_T^{miss} > 180$ GeV, whereas the HLT reaches full efficiency for events with $E_T^{miss} > 200$ GeV. The pufit method has a sharper turn on curve than the mht based E_T^{miss} triggers. High efficiency was
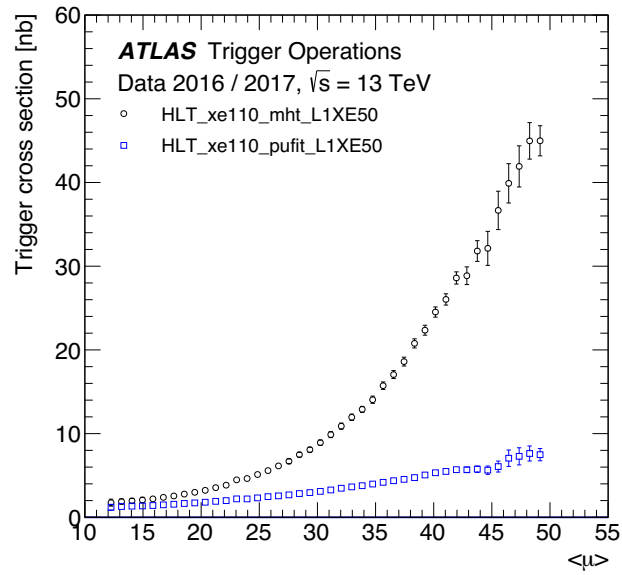
Figure 7.10: HLT E_T^{miss} trigger cross section as a function of the mean number of pp-interactions per bunch crossing. The trigger cross section is shown for both the `pufit` and `mht` E_T^{miss} definitions [91].

maintained for events with $E_T^{miss} > 200$ GeV throughout Run 2.
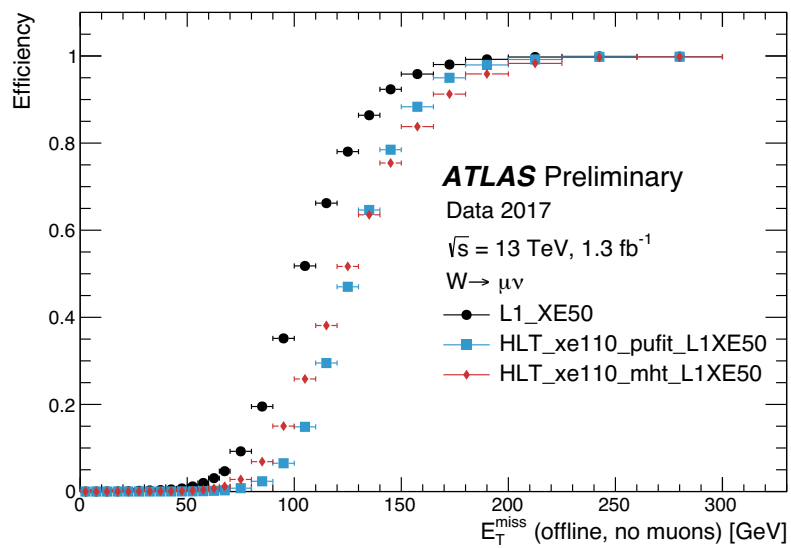
Figure 7.11: The E_T^{miss} trigger efficiency at L1 and HLT is shown as a function of offline E_T^{miss}, computed for $W \rightarrow \mu\nu$ events, where the muon is ignored. The HLT trigger efficiency is shown for both the `pufit` and `mht` definitions. [91].

8

Data and Monte Carlo Samples

This chapter describes the data and Monte Carlo samples which are used to perform the analysis described in Part IV. The dataset, and details of how the data are processed with non-standard reconstruction, is described in Section 8.1. Monte Carlo samples are generated for the benchmark signal model discussed in Chapter 3. These simulated signals are used to optimize signal region definitions and estimate the sensitivity of the analysis. The steps required to produce these samples are complicated, and described in Section 8.2. Kinematic properties of these samples are presented in Section 8.2.2.

8.1   Data

This analysis makes use of LHC pp-collision data at $\sqrt{s} = 13$ TeV collected by the ATLAS between 2016 and 2018. This dataset corresponds to an integrated luminosity of 136 fb^{-1}. The uncertainty on

the total integrated luminosity is 1.7%. The mean $\langle\mu\rangle$ is approximately 33 interactions per bunch crossing, and the peak $\langle\mu\rangle$ is approximately 70 interactions per bunch crossing.

Data are collected with a Muon Spectrometer only trigger and a missing transverse energy trigger, both of which are described in greater detail in Section 7. Non-standard reconstruction methods are used to improve sensitivity to long-lived particle decays that result in displaced tracks and displaced vertices. These reconstruction methods are computationally intensive, and require a complicated data-flow, which is described in the following section. Background processes which result in displaced muons and displaced vertices are also estimated from data.

8.1.1 DATA-FLOW

The Large Radius Tracking and secondary vertex reconstruction used in this analysis are both computationally expensive. In order to reduce the computational resources required for event reconstruction, only a subset of the the full `physics_Main` dataset is reconstructed with Large Radius Tracking and secondary vertex reconstruction.

The subset of events which are processed with non-standard reconstruction are selected with requirements designed for specific long-lived particle analyses in ATLAS. Events are selected with *filters* when standard reconstruction is run over the entire `physics_Main` event stream at Tier-0. These filters are unique to each long-lived particle analysis, and include selections with basic trigger and kinematic requirements, applied to standard physics objects. Criteria are designed to select events that are interesting for the long-lived particle analysis in mind. In total, $5-10\%$ of the full `physics_Main` dataset is selected for non-standard reconstruction.

Figure 8.1 shows the rate of events selected by long-lived particle filters for a representative 2018 run. The total rate of events selected is shown in black dots, while the rate of events selected by individual filters is indicated with a separate color. The total rate is less than the stacked histograms because the same event may be selected by multiple filters. Rates are shown as a function of *luminosity-block* and instantaneous luminosity. A *lumi-block* corresponds to roughly 60 seconds of data taking.
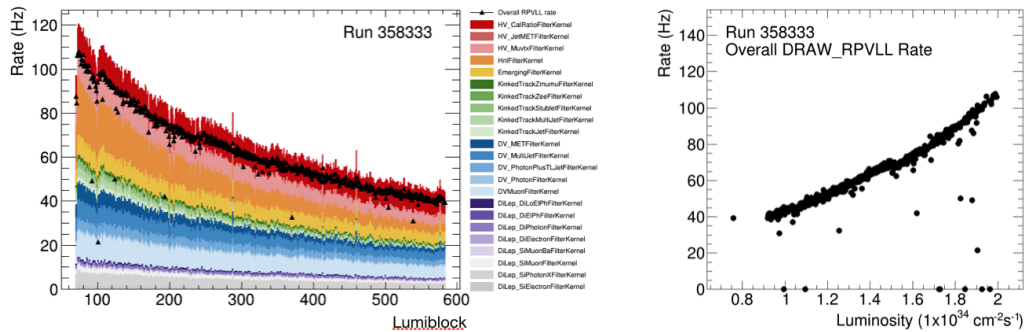
Figure 8.1: Left: The rate of events selected by long-lived particle filters for a representative 2018 run, shown as a function of lumi-block. The total rate (Overall RPVLL rate) is shown in black dots, while the rate of each filter is shown with a separate color. Right: The total rate of events selected by long-lived particle filters is shown as a function of instantaneous luminosity.

It is challenging to define a filter selection which results in good signal efficiency and allows for data-driven background estimations without exceeding rate limitations. The filtering step is not aware of the quality requirements and calibrations usually placed on physics objects in an ATLAS analysis. These quality criteria are usually defined by performance groups after filtering has already taken place. Selections placed on leptons and jets must therefore be quite loose, and are not always robust to pile-up. As a result, the rate of events saved increases exponentially with pile-up.

Events which pass a long-lived particle filter are saved in the RAW format (i.e. detector signals), as

`DRAW_RPVLL` datasets. It is necessary to save events as detector-level data because these special reconstruction methods require access to low-level information, such as Inner Detector hits. At a later time, the data are processed with non-standard reconstruction methods, and events are saved in an analysis object format.

Another challenge for long-lived particle analyses is that the standard reconstruction used in the filtering step does not always produce the same physics objects as the non-standard reconstruction. An event reconstructed with standard methods might result in a muon with a different Inner Detector track than if the event were reconstructed with Large Radius Tracking.

This analysis uses events selected by two filters. The first filter aims to select events collected by the Muon Spectrometer only trigger described in Chapter 7. The second aims to collect events which pass a missing transverse energy trigger.

The muon filter first requires events pass the `HLT_mu60_0eta105_msonly` trigger. Events are also required to contain at least one muon, which satisfies the following, year dependent, criteria.

- 2016: The event must have a least one offline muon with $p_\mathrm{T} > 60$ GeV and $|\eta| < 2.5$. If the offline muon is combined, and the ID and MS tracks have $\chi^2/N_{DoF} < 5$, the muon's Inner Detector track must also have $|d_0| > 1.5$ mm. If the ID and MS match have a $\chi^2/N_{DoF} > 5$, then no d_0 requirement is applied. No impact parameter requirements are applied if the muon is not combined. The different treatment for combined muons which have a poor χ^2/N_{DoF} match is due to the fact that filtering is performed on events without Large Radius Tracking. During the filtering step, in which nominal reconstruction is run, a very displaced signal muon could have it's Muon Spectrometer track incorrectly matched to the nearest prompt ID track. The incorrect ID track would fail a d_0 cut. To maintain signal efficiency, no d_0 requirement is applied if the χ^2/N_{DoF} indicates a poor ID-MS track match. The optimization of this requirement is described in more detail in this Internal Note [92]

- 2017 and 2018: The event must have a least one offline muon with $p_\mathrm{T} > 60$ GeV and $|\eta| < 2.5$.

No requirement is made on the muon's transverse impact parameter.

The E_T^{miss} filter for the 2016 dataset related to this search required any of the following triggers:

- `HLT_xeXX`
- `HLT_xeXX_tc_lcw`
- `HLT_xeXX_mht_L1XEYY`
- `HLT_xe110_mht_L1XE50_AND_xe70_L1XE50`
- `HLT_xeXX_topoclPS`
- `HLT_xeXX_topoclPUC`

where XX = 90, 100, 110, 120, 130 and YY = 50, 55, 60. In 2017, the E_T^{miss} filter used the following triggers in addition to those used for 2016.

- `HLT_xe110_pufit_L1XE60`
- `HLT_xe120_pufit_L1XE60`

In 2018, the E_T^{miss} filter used the following trigger in addition to those used for 2016 and 2017.

- `HLT_xe110_pufit_xe70_L1XE50`

In addition to the trigger requirement, events are also required to have cluster-based $E_T^{miss} > 180\,\mathrm{GeV}$, where the cluster-based E_T^{miss} computation is described in Section 6.4.1. This requirement is used to reduce the rate of events passing the filter.

Usually, there is only once chance to apply the filter to each run. The 2015 data were not filtered with triggers of interest to this analysis. For this reason, this analysis only uses 2016-2018 data.

Events which have passed the filters described above are reconstructed with Large Radius Tracking and secondary vertex reconstruction and saved as `DAOD_RPVLL` datasets. These `DAOD_RPVLL` datasets are then further processed into `DAOD_SUSY15` derivations. All events which pass the triggers discussed

182

above enter the `DAOD_SUSY15` derivations, but requirements are placed on the analysis level objects in those events in order to reduce the content of each event saved. For example Muon Spectrometer hits are not saved in derivations, and only Inner Detector tracks with $p_T > 1$ GeV are saved. The `DAOD_SUSY15` derivation is processed into n-tuples by analysis specific code.

8.2 Monte Carlo

This section describes how the benchmark signal is modeled in Monte Carlo simulation. In the benchmark model, stop-antistop events are produced from pp-collisions through R-parity conserving diagrams. The stop particle is long-lived and decays via an R-parity violating coupling. The stop particle has a 100% branching ratio to a muon and b-quark, but these signals are interpreted as $\tilde{t} \rightarrow \mu + j$, for reasons discussed below.

The simulation of signal processes is usually completed in the following steps.

- The energy of the colliding particles is estimated using PDF sets, discussed in Section 4.1.

- A *generator* models the hard scattering process using Matrix Elements calculations, which input information about the colliding particles and compute the resulting final states.

- In *parton showering* step, particles with color-charge probabilistically radiate gluons and quark-antiquark pairs. The resulting particles form final state hadrons.

- Additional collisions are overlaid on the event to simulate the effect of pile-up.

- Final state particles are propagated through a simulated version of the ATLAS detector, modeling interactions with material.

- In the *digitization* step, the energy deposited in the detector is converted to digital signals.

- Event reconstruction is run on those predicted detector signals, in the same way reconstruction is run on data.

For most signal models, these steps are sufficient. However for the benchmark model considered by this analysis, the process of simulating events is more complicated. Because the stop has color charge, and its lifetime is greater than the timescale for QCD hadronization, the stop particle hadronizes with Standard Model particles, forming an R-hadron.

The resulting R-hadron can interact with the detector before the R-hadron decays, which means several of the above steps need to be repeated. The propagation of the R-hadron through the detector needs to be handled before the R-hadron decays. The R-hadron decay then needs to be modeled, and the resulting particles from the decay also need to propagate through the detector. The details of simulating these signals are described below.

As described in Section 4.1, pp-collisions at $\sqrt{s} = 13$ TeV actually involve collisions between the constituents of the proton, not the protons themselves. The fraction of the proton's momentum which is carried by the constituents are described by PDF sets. PDF sets are informed from experimental measurements, and there is some variation depending on which PDF set is used. The signal samples considered here use the NNPDF2.3LO PDF set [93], which include measurements from LHC data collected by ATLAS and CMS in 2010 and 2011.

The next step is to model the hard scattering process resulting from the interaction of two of these proton constituents using a Monte Carlo generator. Generators use Matrix Elements to compute the cross section of a particular process, and also describe the probability to go from an initial state to a final state with particular kinematic properties. The generator takes each collision and produces a final state. For this analysis, MadGraph5_aMC@NLO 2.6.1 [94] is used to produce $pp \rightarrow \tilde{\tilde{t}}\tilde{\tilde{t}}$ events with up to two additional partons from initial or final state radiation, at leading order accuracy.

The resulting particles from the hard scatter process must undergo hadronization in the parton showering step. This step also includes accounting for the initial and final state radiation of additional partons. Unlike the generator step, the parton showering step is not described by perturbative QCD, but by approximations which aim to model the probability of parton splitting or gluon emission.

It is important to note that both the Matrix Element calculation in the generator step, and the parton shower process can produce events with an additional jet in the final state. In order to avoid double counting of events, a *merging* procedure is performed. This merging procedure ensures that the two leading jets are described by the Matrix Element calculation, while any additional jets may be described by the parton shower step. In the merging procedure, jet reconstruction is performed on events with an anti-k_T algorithm. The resulting jets are classified into high-p_T and low-p_T. If all high momentum jets in an event can be matched to a parton produced in the generator step, the event is kept. If not, the event is thrown out. Extra jets are only allowed if their p_T is below threshold, or if they are not the two leading jets in the event. The momentum threshold is usually ~ 10 GeV [95].

The parton showering step for the signal samples considered here is performed with PYTHIA 8.230 [96], which uses the A14 (ATLAS 2014) set of tuned parameters for the modeling of the parton shower, hadronization, and underlying event [97]. At this point, the $\tilde{t}$ is treated as a stable particle, and is not allowed to decay. PYTHIA hadronizes the $\tilde{t}$ with Standard Model particles, resulting in a stop R-hadron.

The $\tilde{t}$ may form a bound state with either one or two spectator quarks. About 90% of stop particles form meson-like states ($\tilde{t}\bar{q}$), and 10% form baryon-like states ($\tilde{t}qq$). The mass spectrum of these R-

hadrons is described by the *generic model* [98]. Figure 8.2 * shows the mass that the spectator partons contribute to the R-hadron, defined as the difference between the R-hadron mass and the $\tilde{t}$ mass. Figure 8.2 also shows the charge distributions of R-hadrons. Roughly 55% of the R-hadrons formed have nonzero electric charge, and the two R-hadrons cannot have same-sign electric charge.
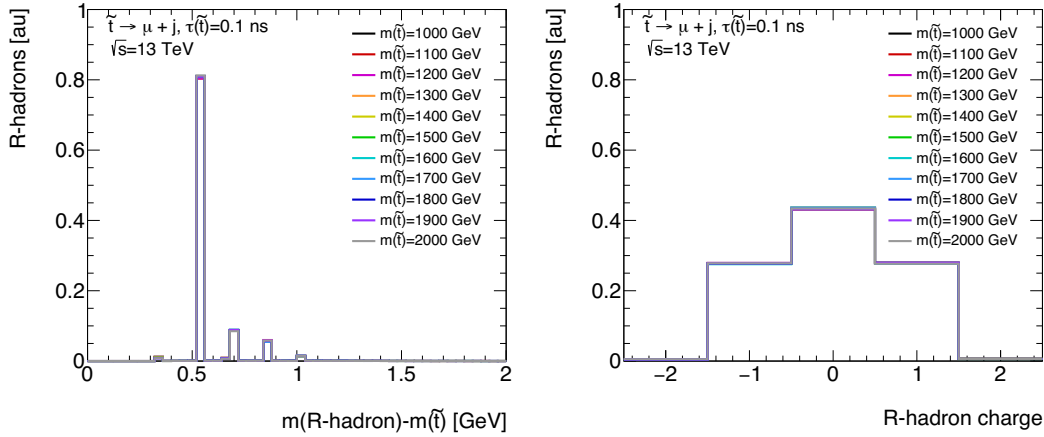
Figure 8.2: Properties of R-hadrons in Monte Carlo. Left: The difference between the $\tilde{t}$ mass and the R-hadron mass, or mass contributed to the R-hadron by spectator partons. Right: The charge distributions of stable R-hadrons.

At this stage, the events consist of final state particles from the hard interaction and showering, but does not contain particles produced in pile-up interactions, as well as effects due to activity from bunch crossings before or after the selected event. In order to model the effects of in-time and out-of time pile-up, minimum bias events are overlaid on simulated events. Minimum bias events are specifically generated for this process. These multiple interactions are simulated with soft QCD processes in PYTHIA 8.2186, which uses the A2 [99] set of tuned parameters and the MSTW2008LO PDF

---

*Note that in this thesis, [au] indicates that the one dimensional distribution has been normalized to unity. The first and last bins of one dimensional histograms also contain underflow and overflow entires unless otherwise specified

set [100].

Events are then sent to GEANT (4 v10.1.3) to simulate particles' interactions with the ATLAS detector [101]. GEANT contains a simulated version of ATLAS with information about the detector materials and their location, as well as the magnetic field. This geometry is periodically updated when upgrades to the ATLAS detector are made. Updates are also made in order to account for improvements in understanding the detector material position and chamber alignment.

Particles' trajectories in the magnetic field and detector are modeled using small steps. At each step a particle's possible interactions are considered. Possible interactions with material include energy loss and the production of new particles. These steps continue until the particle loses all of its energy, or the particle exits the detector volume. GEANT includes effects such as photon conversions, which can happen in layers of the Inner Detector.

GEANT also propagates R-hadrons through the detector using a *generic* interaction model [102–104]. In the generic interaction model model, R-hadrons have an interaction cross section of 12 mb, per spectator parton, per nucleon in the detector. The $\tilde{t}$ is assumed to have no contribution to the R-hadron's interaction with the detector. In this interaction model the content of the light-quark system in the R-hadron can be altered as it traverses the detector. If the light-quark content of the R-hadron changes during an interaction, it is possible that the total electric charge of the R-hadron also changes.

The R-hadron's lifetime is equivalent to the lifetime of the $\tilde{t}$. When the R-hadron decays, it is passed from GEANT to a second instance of PYTHIA. PYTHIA simulates the $\tilde{t}$ decay to a muon and a b-quark with branching ratio Br($\tilde{t}$) = 100% using a parton shower model, also hadronzing the $\tilde{t}$ decay products. The stable daughter particles of the R-hadron decay are handed back to GEANT in

order to simulate their interaction with the detector.

It is important to note that the $\tilde{t}$ decay and hadronization of the $\tilde{t}$ decay products, which are performed in Pythia, occur at a single step in Geant. Only stable particles from the $\tilde{t}$ decay are handed back to Geant. Any information about intermediate particles between the b-quark production and its final state decay products is lost. In simulated events, all stable particles from the stop decay are produced at the same location in the detector. As a result, effects of the b-quark lifetime, such as tertiary vertices, are not simulated. Due to the lack of tertiary vertices from the b-quark decay, these signal samples are interpreted in a $\tilde{t} \to \mu + q$ decay model, where q is a light-quark.

Once all of the event's particles have propagated through the ATLAS detector, the energy deposited into active sensors is converted into signals that resemble the actual detector response in the digitization step. These responses are usually taken from parametrized functions in ATLAS specific software, and include effects for electronic noise and dead sensors.

Once the simulated particles have been converted into detector signals, the same reconstruction software used on data can be used on the MC. Detector signals are reconstructed into particles using the same Large Radius Tracking and secondary vertex reconstruction methods described in Chapter 6. One key difference between events in data and MC is that the MC keeps original information about the generated particles. This information is referred to as *truth* information, and is often used to measure the efficiency of reconstructing individual particles or selecting signal events.

MC signal samples are prepared for $\tilde{t}$ masses varying from 1 TeV to 2 TeV, in steps of 100 GeV. Samples with lifetimes, $\tau = 0.01, 0.1,$ and 1 ns are prepared for each $\tilde{t}$ mass sampled. Table 8.1 shows the production cross sections for $pp \to \tilde{t}\tilde{\bar{t}}$ at $\sqrt{s} = 13$ TeV.

Signal cross sections are calculated to approximate next-to-next-to-leading order in the strong coupling constant, adding the re-summation of soft gluon emission at next-to-next-to-leading-logarithmic accuracy (approximate NNLO+NNLL) [105–107]. The nominal cross section and the uncertainty are derived using the PDF4LHC15_mc PDF set, following the recommendations of Ref. [108].

Table 8.1: Stop-antistop production (NNLO+NNLL) cross sections in pp-collisions at $\sqrt{s} = 13$ TeV

Stop Mass [GeV]	Cross Section [pb]
1000	$0.683 \cdot 10^{-2} \pm 11.2\%$
1100	$0.335 \cdot 10^{-2} \pm 12.12\%$
1200	$0.170 \cdot 10^{-2} \pm 13.13\%$
1300	$0.887 \cdot 10^{-3} \pm 14.21\%$
1400	$0.473 \cdot 10^{-3} \pm 15.37\%$
1500	$0.257 \cdot 10^{-3} \pm 16.63\%$
1600	$0.142 \cdot 10^{-3} \pm 17.96\%$
1700	$0.796 \cdot 10^{-4} \pm 19.4\%$
1800	$0.451 \cdot 10^{-4} \pm 20.94\%$
1900	$0.258 \cdot 10^{-4} \pm 22.6\%$
2000	$0.148 \cdot 10^{-4} \pm 24.38\%$

8.2.1 Corrections applied to simulation

The simulation may not perfectly describe data for several reasons. The material description of the detector may not be perfect, and there may be data quality issues which occur during data taking that are not modeled in MC. There may also be differences in the pile-up modeling in MC, and the distributions observed in data. In order to account for these differences, several corrections to Monte Carlo signal samples, and uncertainties on the observed efficiencies, are applied. These corrections and uncertainties are discussed in more detail in Chapter 11. Additional Monte Carlo and data samples

189

which are used to evaluate these corrections and uncertainties are the focus of this section.

The efficiency for reconstructing and selecting muons is of particular importance for this analysis. In order to account any differences in efficiency observed in data and MC, $Z \rightarrow \mu^+\mu^-$ events are compared in data and MC. In MC these events are generated using POWHEG vi r2856 [109] and PYTHIA 8.186 [110]. These events are reconstructed with standard ATLAS software. Additional uncertainties are also applied to account for differences in tracking efficiency, as discussed in Chapter 11.

The pile-up profile in MC may not match the pile-up profile observed in data. The choice of pile-up profile in MC is made before data are collected, and is based on expected LHC operating parameters. These parameters are often different than what was expected for a variety of reasons, including LHC performance, and ATLAS luminosity leveling. Separate MC *campaigns* try to anticipate the ATLAS geometry and LHC performance for each year of data taking. Later, analyzers reweight the pile-up profile of the MC to match the pile-up profile observed in data.

The simulated signal samples used in this analysis consist of three separate MC *campaigns*, referred to as MC16a, MC16d, and MC16e. MC16a is reweighted to match the pile-up profile of the 2016 dataset, while MC16d is reweighted to 2017, and MC16e is reweighted to 2018. This reweighting procedure is performed in two dimensions, in order to ensure the distributions of the number of primary vertices, as well as the mean number of interactions per bunch crossing match in data and MC.

8.2.2 R-HADRON KINEMATICS

This analysis only considers the decay products of the R-hadrons. The charge of the R-hadron, and the R-hadron's potential interaction with the detector should not have an impact on the analysis.

Kinematic properties of the R-hadron samples are shown below, for different $\tilde{t}$ masses and lifetimes. For these studies, R-hadrons are required to decay within $R_{xy} < 300$ mm and $|Z| < 300$ mm, where a displaced vertex could be reconstructed. Distributions shown in this section, and subsequent sections of this chapter are normalized to unity, to highlight shape differences in distributions rather than overall scale differences due to the stop particle mass.

Kinematic properties of the R-hadron samples are shown below, for different $\tilde{t}$ masses and lifetimes. For these studies, R-hadrons are required to decay within $R_{xy} < 300$ mm and $|z| < 300$ mm. Distributions shown in this section, and subsequent sections of this chapter are normalized to unity, to highlight shape differences in distributions rather than overall scale differences due to the stop particle mass. The highest bin also contains overflow entries, and the lowest bin contains underflow entires.

In Figure 8.3, the transverse and longitudinal R-hadron decay position is shown for three lifetimes. As expected, the decay position in R_{xy} follows an exponentially falling distribution. The z position of the R-hadron decay has some spread due to the size of the beam spot, which is roughly ± 100 mm in the z-direction. On average, R-hadron decays occur further away from the interaction point in R_{xy} and z for $\tilde{t}$ with longer lifetimes.

In Figure 8.4, the R-hadron $\beta\gamma$ and transverse momentum is shown for three different $\tilde{t}$ masses. R-hadrons with lower masses tend to be more boosted, and have larger $\beta\gamma$. R-hadrons with larger mass tend to have larger transverse momentum. Due to the nature of pair-production of heavy particles at a hadron collider, particles produced with a larger pseudorapidity tend to be more boosted and have a larger value of $\beta\gamma$.

Figure 8.5, shows the R-hadron η and ϕ for three different $\tilde{t}$ masses. There is no significant change in
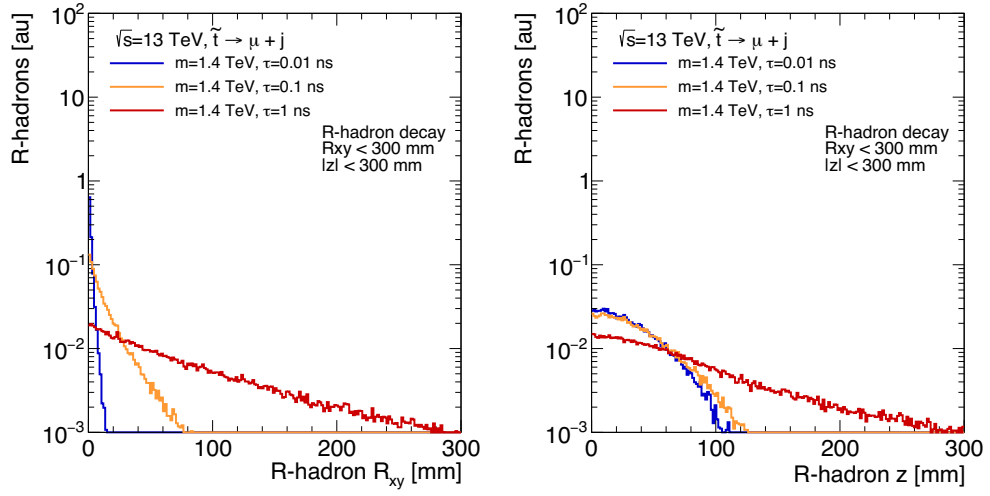
Figure 8.3: Left: R-hadron decay position in R_{xy} for different lifetimes. Right: R-hadron decay position in z for different lifetimes.
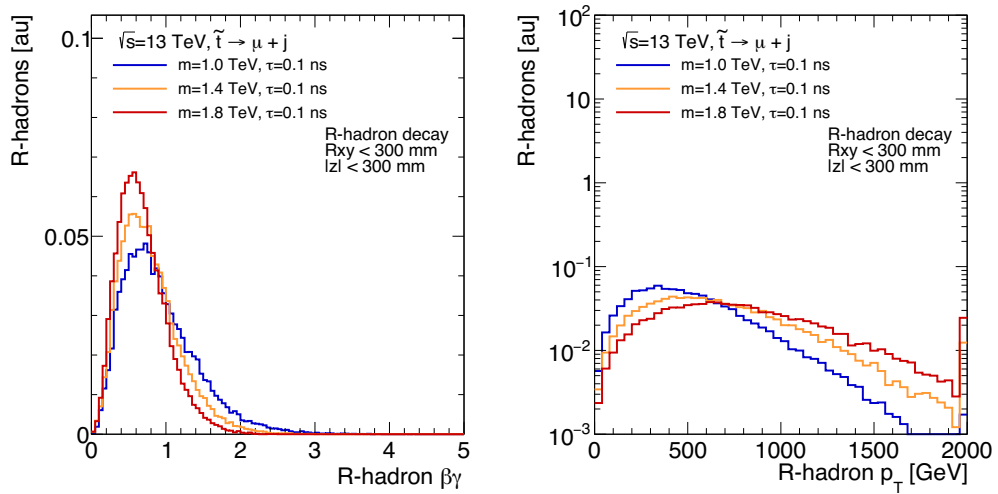
Figure 8.4: Left: R-hadron $\beta\gamma$ for different stop masses. Right: R-hadron transverse momentum for different stop masses.

the ϕ distributions for different $\tilde{t}$ masses. Distributions of R-hadrons are symmetric in ϕ as expected. Due to the kinematics of pair-produced heavy particles at a hadron collider, slight differences in the η distributions are observed for $\tilde{t}$ particles with different masses. The width of the η distribution decreases with increasing $\tilde{t}$ mass.
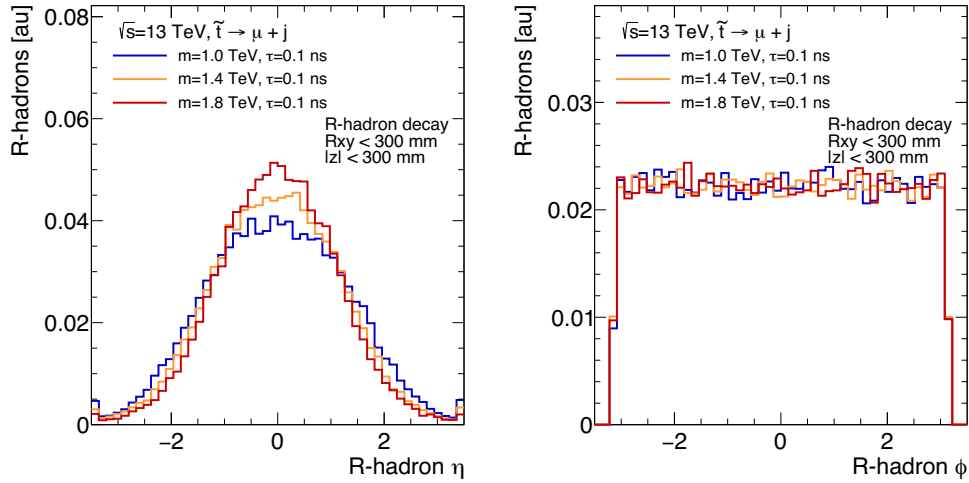
Figure 8.5: Left: R-hadron η for different $\tilde{t}$ masses. Right: R-hadron ϕ for different $\tilde{t}$ masses.

Figure 8.6, shows the number of stable daughter particles from the R-hadron decay which have electric charge $= \pm 1$ and $p_{\mathrm{T}} > 1$ GeV. The selection applied to the R-hadron decay products is intended to study the number of daughter particles which could be reconstructed as Inner Detector tracks. Stop quarks with larger mass tend to produce more reconstructible decay products. The mass which would be reconstructed from these decay products is also shown. Stop quarks with larger mass tend to have larger reconstructible mass, and the reconstructible mass is on average two thirds of the stop particle mass. Roughly one third of the stop particle decay products are electromagnetically neutral or have

transverse momentum less than 1 GeV.
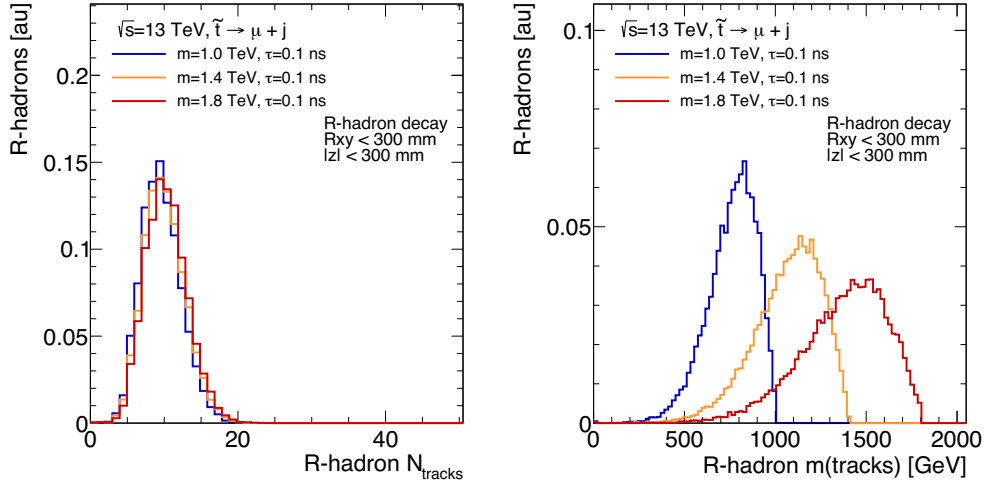
Figure 8.6: Left: Number of charge $= \pm 1$ particles with $p_T > 1$ GeV produced in the R-hadron decay, referred to as the R-hadron's number of tracks. Shown for different R-hadron masses. Right: Invariant mass of the R-hadron daughter particles with charge $= \pm 1$ and $p_T > 1$ GeV, referred to as R-hadron's track mass. This includes the momentum contribution from the muon in the decay of the $\tilde{t}$. Shown for different R-hadron masses.

8.2.3 MUON KINEMATICS

This section discusses kinematics of the muons produced in R-hadron decays, and how these kinematics depend on the stop mass and lifetime. Muons are required to be produced from R-hadrons which decay with $R_{xy} < 300$ mm and $|z| < 300$ mm.

Figure 8.7 shows the transverse impact parameter of muons produced from stop particles with different lifetimes. Stop quarks with larger lifetimes result in muons with larger impact parameters. Stop particles with $\tau(\tilde{t}) = 0.01$ ns, result in muons with impact parameters less than 20 mm, while

stop particles with $\tau(\tilde{t}) = 0.1$ ns result in muons with transverse impact parameters less than 60 mm.

Stop particles with $\tau(\tilde{t}) = 1$ ns result in muons with impact parameters as large as 300 mm. Figure 8.7

also shows the muon transverse momentum for different $\tilde{t}$ masses. Stop quarks with larger masses

result in higher p_{T} muons.
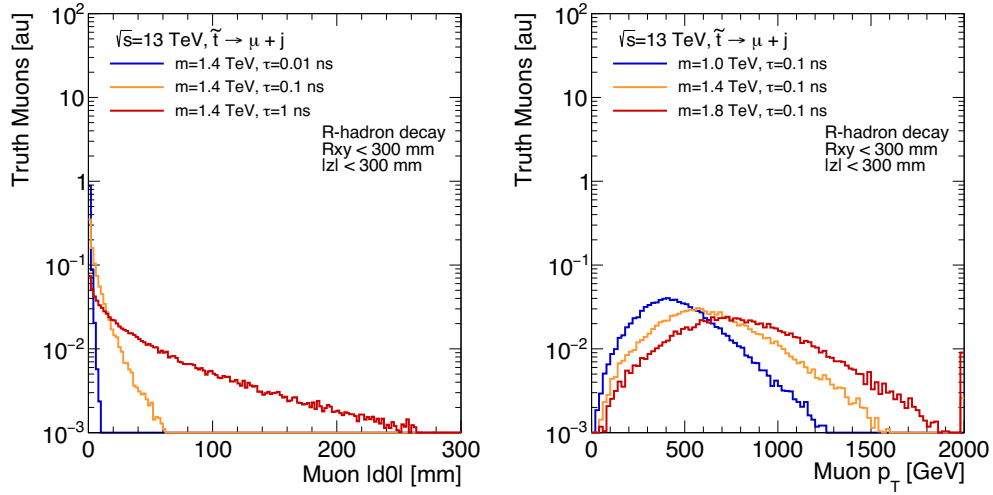
Figure 8.7: Properties of muons produced in the R-hadron decay, referred to as truth muons. Left: Truth muon transverse impact parameter, $|d_0|$, for different $\tilde{t}$ lifetimes. Right: Truth muon transverse momentum, for different $\tilde{t}$ masses.

Figure 8.8 shows the muon η and ϕ distributions for different $\tilde{t}$ masses. The width of the muon η

distribution slightly decreases with increasing stop particle mass. The muons have a flat ϕ distribution,

which does not greatly change as a function of $\tilde{t}$ mass.
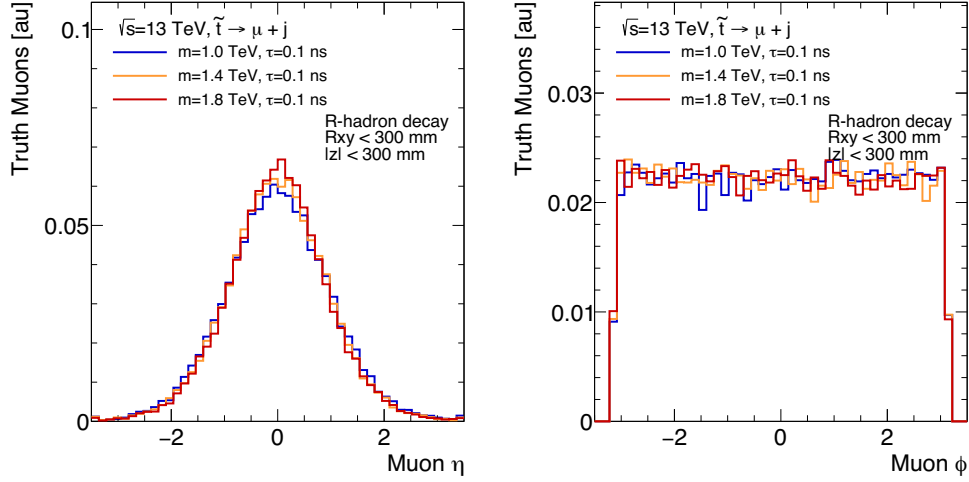
Figure 8.8: Properties of muons produced in the R-hadron decay, referred to as truth muons. Left: Truth muon η for different $\tilde{t}$ masses. Right: Truth muon ϕ for different $\tilde{t}$ masses.

8.2.4 TRACK KINEMATICS

R-hadron daughter particles with electric charge $= \pm1$, transverse momentum $p_T > 1\,\text{GeV}$, which are not muons, are referred to as R-hadron truth tracks. Properties of these R-hadron truth tracks are shown in this section. This selection is designed to study properties of reconstructible particles from the hadronic jet produced in the $\tilde{t}$ decay.

Figure 8.9 shows the R-hadron track $|d_0|$ for different $\tilde{t}$ lifetimes. Stop quarks with longer lifetimes result in daughter particles with larger transverse impact parameters. The R-hadron track transverse momentum is also shown for different $\tilde{t}$ masses. Larger masses result in tracks with larger p_T.

Figure 8.10 shows the R-hadron track η and ϕ distributions for different $\tilde{t}$ masses. These distributions do not greatly change as a function of $\tilde{t}$ mass.
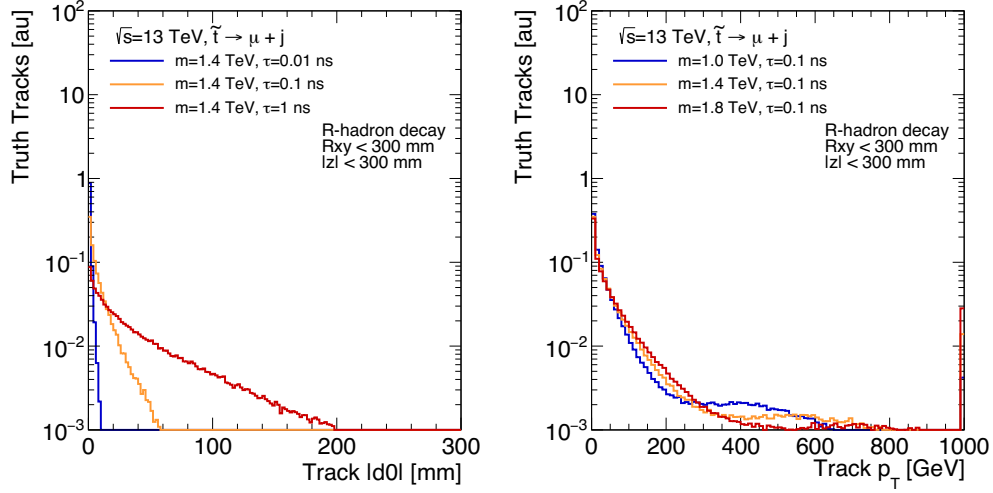
Figure 8.9: Properties of charged particles with $p_T > 1$ GeV produced in the R-hadron decay, referred to as truth tracks. Left: R-hadron track transverse impact parameter, $|d_0|$, for different $\tilde{t}$ lifetimes. Right: R-hadron track transverse momentum, for different $\tilde{t}$ masses.
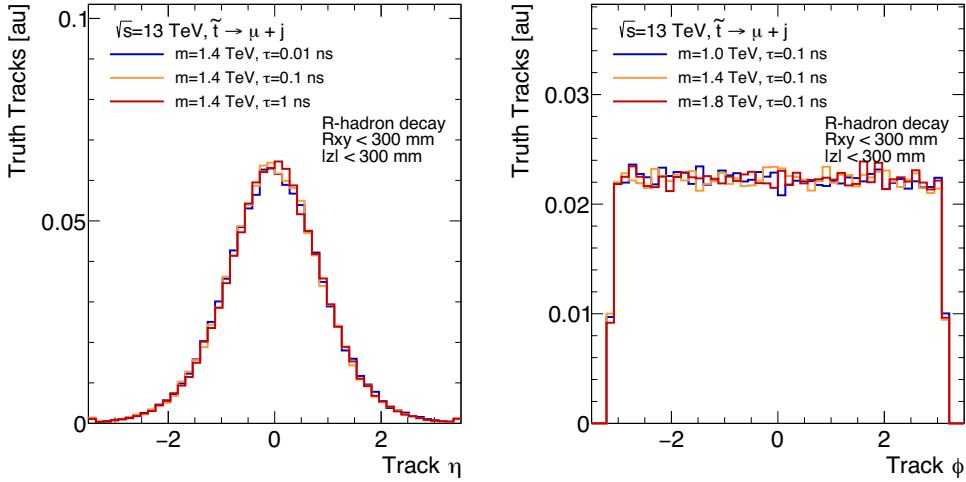
Figure 8.10: Properties of charged hadrons with $p_T > 1$ GeV produced in the R-hadron decay, referred to as truth tracks. Left: R-hadron track transverse impact parameter, η, for different $\tilde{t}$ lifetimes Right: R-hadron track ϕ, for different $\tilde{t}$ masses.

Part IV

Searching for long-lived particles

<div style="text-align: right; font-size: 3em; color: #8B1A2B;">**9**</div>

Event Selection

This chapter describes the criteria used to select events which contain a semi-leptonically decaying long-lived BSM particle. An overview of the selection is provided in Section 9.1, and the rest of the chapter discusses these criteria in detail.

9.1 Overview of Signal Regions

This analysis aims to select events with long-lived stop particles that decay semi-leptonically to a muon and a hadronic jet, which are described by the simplified model presented in Section 3.4. Events are required to pass either a Muon Spectrometer trigger or a missing transverse energy trigger. Though there is no genuine missing transverse energy expected in the simplified model of interest for this analysis, the high momentum muons which only deposit a fraction of their energy in the Calorimeter can

generate a sufficient amount of cluster-based E_T^{miss} to fire a E_T^{miss} trigger.

The analysis selection is designed to be as inclusive as possible to any new long-lived particles predicted in other physics models. Though the stop signal model is used as a benchmark for studying the effects of the selection on displaced muons and displaced vertices, the analysis is not optimized to maximize significance for this particular model. Generally, the event selection is made in stages. A loose *preselection* is made on muons and displaced vertices in order to select a sufficient number of muons and displaced vertices to study backgrounds. A tighter *full selection* is made to reject muons and displaced vertices from these background sources, and achieve an expected background of approximately zero events. Table 9.1 summarizes the complete event selection.

An event preselection is applied by imposing the selections defined by the `DRAW_RPVLL` filters and `DAOD_SUSY15` derivation discussed in Section 8.1.1. Preselected events are also required to have good data quality and at least one primary vertex.

Events are then separated into two selections, or samples, which are defined by the filter and trigger that is used to collect events. The two selections are kept orthogonal by a requirement placed on the cluster-based E_T^{miss}.

- E_T^{miss} Triggered Sample: Events are recorded with the E_T^{miss} trigger, and are required to have cluster-based $E_T^{miss} > 180$ GeV, in order to ensure events are close to the plateau of the trigger turn-on curve. This selection targets events which have a sufficiently boosted muon (or muons) that the event fires an E_T^{miss} trigger.

- Muon Triggered Sample: Events are recorded with the Muon Spectrometer only trigger, and events are required to have at least one reconstructed muon with $p_T > 62$ GeV and $|\eta| < 1.05$ which is matched to the muon that fired the trigger. Events are also required to have cluster-based $E_T^{miss} < 180$ GeV, in order to keep the two samples mutually exclusive.

Events are then required to have at least one preselected, non-prompt muon. Only the leading preselected muon is required to pass the full muon selection in order remain inclusive to other possible signal models. In data, the background processes which result in non-prompt muons include muons reconstructed from an accidental combination of hits (algorithm fakes), cosmic muons, and muons from Standard Model processes such as heavy-flavor decays. Dedicated vetoes are designed to reject muons from each of these processes. Together, these dedicated vetoes make up the full muon selection. Individually, these vetoes can be inverted in order to create control regions which are pure in these background muons.

Events which pass the full muon selection are then required to have at least one displaced vertex. A preselection is also defined to study background vertices from material interactions and random track crossings, and a final selection is applied to reject displaced vertices from those backgrounds.

Table 9.1: Sequential cuts applied to select signal events at analysis level.

	E_T^{miss} selection	Muon selection
Event pre-selection:	Sec 9.2	
Skimming	Sec 8.1.1	
Event cleaning	Rejection of bad/corrupted events (LAr, Tile, Data-taking resynch, ...)	
Good run list	Removal of bad lumi-blocks on data quality assessment	
Primary vertex	≥ 1 good PV, with $N_{PV}^{tracks} \geq 2$ AND $|z_{PV}| < 200$ mm	
Physics Object Selection	Baseline Selections and Overlap Removal Procedure 9.3	
Event selection:	Sec 9.4	
Trigger:		
	2016 Lowest un-prescaled:	
	`HLT_xe100_mht_L1XE50,` `HLT_xe110_mht_L1XE50,` `HLT_xe110_mht_L1XE50_AND_xe70_L1XE50`	`HLT_mu60_0eta105_msonly`
	2017: `HLT_xe110_pufit_L1XE60`	
	2018: `HLT_xe110_pufit_xe70_L1XE50`	
E_T^{miss} cut	cluster-based $E_T^{miss} > 180$ GeV	cluster-based $E_T^{miss} < 180$ GeV
Muon Selection:	Sec 9.5	
Preselection:	Medium, ≥ 2 Pixel or ≥ 1 TRT hits $p_T > 25$ GeV, $|\eta| < 2.5$ $|d_0| < 300$ mm $|d_0| > 2.0$ mm $|z_0| < 500$ mm	
Full Selection: (Leading Presel. μ)	—	trigger matched with $p_T > 62$ GeV, $|\eta| < 1.05$
	Cosmic veto Fake-muon veto Isolation	
DV selection:	Sec 9.6	
Preselection:	$r_{DV} < 300$ mm, $|z_{DV}| < 300$mm PV-DV Radial Distance > 4 mm vertex $\chi^2/N_{DoF} < 5$ Material Map Veto	
Full Selection:	$n_{Tracks}^{DV} \geq 3$ $m_{DV} > 20$ GeV	

9.2 Event Preselection

In order to have access to the low-level hit information needed for Large Radius Tracking and secondary vertexing algorithms, this analysis makes use of the long-lived particle data-flow described in Section 8.1.1. This stream selects a subset of events, which are described by basic trigger and kinematic requirements. Skimming criteria are defined as the selections in the long-lived particle filters.

Several cleaning criteria are also applied to reject events which could be affected by detector problems, or incomplete data. Events are rejected if they are affected by any of the following

- LAr noise bursts and/or data corruption
- corruption of the Tile data
- the recovery procedure for single event upsets in the SCT

Events are also required to pass the `Good Run List`. The `Good Run List` rejects luminosity blocks where any sub-detector of ATLAS is operating below the 90%-level.

Events are required to contain at least one good primary vertex, with at least two tracks and $|z_{\mathrm{PV}}| <$ 200 mm. For events which have multiple primary vertices, the vertex with largest $\Sigma(p_{\mathrm{T}}^{trk})^2$ is selected as the primary vertex, and the rest are identified as pile-up vertices.

These skimming, cleaning, and hard-scatter criteria define the *event preselection*

9.3 Physics Object Selection

Events which pass the event preselection criteria are processed from derivations into analysis specific n-tuples. Physics objects, such as electrons, muons, and jets, are required to pass certain criteria and

an overlap removal procedure in order to be saved in the analysis n-tuples. This section discusses the criteria applied to these physics objects. Even though only muons are required in the analysis selection, electrons and jets are used in the overlap removal procedure.

The overlap removal procedure uses physics objects which satisfy very basic quality criteria, or *baseline* definitions. These baseline definitions are in general looser than the criteria used in the event selection, and are designed to maximize efficiency. Having multiple levels of definitions allows analyzers to tune their analysis event selection to particular signals, while also keeping the overlap removal procedure similar among different analyses.

The object definitions for electrons and jets are summarized below. These definitions are in line with ATLAS combined performance group recommendations, and are nearly identical to ATLAS SUSY group recommendations.

9.3.1   Baseline electrons

Electrons are reconstructed from topological calorimeter clusters which are well matched to an Inner Detector Track. The process of reconstructing electrons is described in Reference [60]. References [111–113] discuss electron calibration, identification criteria, and selection efficiency.

Baseline electron candidates are are required to have $p_\mathrm{T} > 10$ GeV and $|\eta_\mathrm{cluster}| < 2.47$. They are also required to pass the `LooseAndBLayerLLH` quality definition. Electron quality definitions are based on a likelihood algorithm. The likelihood takes into account a number of kinematic variables, including the electromagnetic shower shape and the ratio of electromagnetic to hadronic activity. The likelihood also considers properties of the Inner Detector track associated to the electromagnetic

shower, as well if transition radiation is observed in the TRT. The loose definition is adjusted as a function of pile-up, in order to preserve identification efficiency. A hit in the B-layer of the Pixel detector is required in order to reject photon conversions.

9.3.2 BASELINE MUONS

Baseline muons are required to have $p_\text{T} > 10\,\text{GeV}$, and $|\eta| < 2.7$. Muons must also pass a modified version of the `Medium` quality requirement, which is described more in Section 6.3.4.

9.3.3 BASELINE JETS

In ATLAS jets are defined using the anti-k_t algorithm with a distance parameter $R = 0.4$ [114]. The inputs to the anti-k_t algorithm are the topological calorimeter clusters described in Section 6.4.1. The energy of the topological clusters used in jet reconstruction is measured at the electromagnetic scale, established using electrons in a test beam. Jets are then calibrated to restore the energy of reconstructed jets to that of simulated jets in Monte Carlo [59]. This calibration is based on the detector response observed in Monte Carlo and making comparisons to events in data, using the transverse momentum balance of a jet and a well-measured reference object.

Baseline jets are required to have $p_\text{T} > 20$ GeV, and $|\eta| < 2.8$. Jets with $p_\text{T} < 60$ GeV, and $|\eta| < 2.4$ are also required to pass a Jet Vertex Tagger (JVT) requirement, where the Jet Vertex Tagger is based on a variable called the Jet Vertex Fraction (JVF). The Jet Vertex Fraction is a useful quantity in rejetcting jets which are produced from pile-up interactions. The JVF can be computed as

$$\text{JVF} = \frac{\sum_k p_\text{T}^{\text{trk}_k}(\text{PV,jet})}{\sum_i p_\text{T}^{\text{trk}_i}(\text{jet})}. \tag{9.1}$$

The numerator considers tracks associated to the jet, which are also associated to the event's primary vertex, and takes the sum of the p_T of these tracks. The denominator takes all tracks associated to the jet, and computes the sum of their p_T. The JVF is then the fraction of the jet p_T, which is due to tracks from the primary vertex. Jets with a JVF close to one are likely to be produced at the the primary vertex, while jets with a JVF close to zero are likely to be produced in a pile-up interaction, or be displaced. A more detailed discussion of JVF can be found here [115].

Tracks are associated to jets in a process called *ghost association*. In ghost association, tracks are clustered along with calorimeter clusters according to the anti-k_t algorithm. However, tracks are considered to have $p_\text{T} = 0$ GeV, so that their momentum does not impact the final measurement of the jet. In practice, this means on average tracks within $\Delta R < 0.4$ of the center of a jet are associated to that jet. Only tracks which pass a `Loose` quality requirement are used in the ghost association process. `Loose` quality requirements are summarized in Table 6.1 of Section 6.2.

Tracks which pass a `Tight` vertex association requirement are considered associated to the primary vertex. The `Tight` vertex association requires that a track is used in the primary vertex fit, or that the track's longitudinal impact parameter is consistent with the primary vertex, and has $|z_0| \cdot \sin(\theta) < 3$ mm. The factor $\sin(\theta)$ ensures that the efficiency for tracks passing these selection criteria is not dependent on the track polar angle. Only tracks which pass the `Loose` quality requirements can be associated to a primary vertex.

The JVF decreases with increasing pile-up. In order to maintain similar performance in different pile-up conditions, a correction to the formula is made for the total number of tracks in an event which are not associated to the primary vertex. This correction is applied to the denominator. The JVT is based on this corrected Jet Vertex Fraction, as well as other variables which aim to quantify the fraction of energy of the jet which is due to the primary vertex.

9.3.4 OVERLAP REMOVAL

An overlap removal procedure is used to avoid the duplicate reconstruction of leptons and jets. Generally, the methods to reconstruct different physics objects are run independently of each other. This means that a real muon could be reconstructed as both a muon and an electron, or both a muon and a hadronic jet. The overlap removal procedure is a step-by-step process which aims to remove objects which are nearby in ΔR. The procedure keeps the physics object which is most likely to have caused both signatures, and removes the object which is most likely to be a duplication.

The overlap procedure is performed with baseline electrons, muons, and jets. This procedure can be separated in to three major steps. The first step treats nearby electrons and muons. The second step treats nearby electrons and jets, and the third step treats nearby muons and jets.

In order to quantify the compatibility of two physics objects, the variable $\Delta R = \sqrt{(\Delta\phi)^2 + (\Delta Y)^2}$ is used. The rapidity is used because the pseudorapidity is in general not a good approximation for jets. This definition ensures the distance metric is invariant under a Lorentz boost in the z-direction.

The first step in the overlap removal process is to treat nearby electrons and muons. In this step, electrons are removed if they share an Inner Detector track with a muon. This is because a real muon

can leave a fraction of its energy in the Calorimeter, resulting in a reconstructed electron. If the Inner Detector track is matched to a Muon Spectrometer track, the particle was very likely caused by a muon. If an electron and muon are nearby, but do not share an Inner Detector track, both are kept.

The second step in the overlap removal process is to treat nearby electrons and jets. The primary goal of this step is to remove reconstructed jets that are identical with reconstructed electrons. It is also important to preserve heavy-flavor jets with semi-leptonic decays, as well as light-flavor jets which are incorrectly reconstructed as electrons. Jets are first removed if they are within $\Delta R < 0.2$ of an electron, in order to remove jets which originate from the electron's calorimeter cluster. In these cases, the jet is usually reconstructed from the same cluster as the electron. In a subsequent step, electrons are removed if they are within $\Delta R < 0.4$ of a remaining jet, in order to reject electrons which originate from semi-leptonic heavy-flavor decays. In these cases, the electron is usually clustered separately from the jet.

The third step in the overlap removal process is to treat nearby muons and jets. This step aims to separate prompt and signal muons from muons originating from the decays of hadrons within jets. Muons can be produced inside a jet from the decays of light hadrons such as $\pi^{\pm}$ and $K^{\pm}$ as well as semi-leptonic decays of heavy-flavor jets. In order to reduce the contribution of heavy-flavor muons to the analysis, this analysis aims to identify such objects as jets instead of as muons. An isolation requirement is also applied to muons in order to aid in rejecting muons from heavy-flavor decays. Another goal is to remove jets which are reconstructed from photons produced in muon bremsstrahlung or collinear final state radiation. In these cases, the analysis aims to identify such objects as muons instead of as jets.

The best discriminating variable between muons produced in the decays of jets, and jets produced from bremsstrahlung or final state radiation is the number of tracks associated to the jet. Real hadronic jets tend to have more tracks, while jets reconstructed from bremsstrahlung or final state radiation will usually have only one track. In order to reject jets which are reconstructed from muon bremsstrahlung, jets with fewer than 3 tracks are removed if the muon is ghost associated to a jet. Otherwise the jet is kept. In a subsequent step, muons are removed if they are within $\Delta R < 0.4$ of a remaining jet, in order to reject muons which originate from hadronic decays.

9.4 TRIGGER SELECTION

After event preselection and physics object selection, events are separated into either the Muon or $E_{\mathrm{T}}^{\mathrm{miss}}$ triggered selections, which are defined below.

9.4.1 MUON TRIGGERED SAMPLE

The Muon Filter requires events pass a MS-only trigger, `HLT_mu60_0eta105_msonly`. This trigger requires a high-p_{T} muon candidate in the RPC ($|\eta| < 1.05$), with $p_{\mathrm{T}} > 60$ GeV, and does not require a matching Inner Detector track. Standard ATLAS muon triggers explicitly require a matched Inner Detector track with $|d_0| < 10$ mm, which drastically reduces signal acceptance for muons with large impact parameters. The high p_{T} threshold and strict η requirements of the MS-only trigger are due to bandwidth limitations in the Muon Spectrometer end-caps.

The MS-only trigger is fully turned-on for muons with $p_{\mathrm{T}} > 62$ GeV, and reaches an efficiency between 70% and 75% for muons with transverse impact parameters, $|d_0| < 50$ mm. The trigger

efficiency is reduced near $\eta \approx 0$, where there aren't any muon detectors, and in the feet of the detector, where there is reduced space for trigger chambers. For muons with impact parameters above $|d_0| > 50$ mm the trigger efficiency decreases with increasing impact parameter, largely due to the road requirements at Level 1, which were designed to select muons which originate from the primary vertex.

9.4.2 $E_{\mathrm{T}}^{\mathrm{miss}}$ TRIGGERED SAMPLE

Events with high-p_{T} muons can also fire the $E_{\mathrm{T}}^{\mathrm{miss}}$ trigger. The $E_{\mathrm{T}}^{\mathrm{miss}}$ trigger is based on Calorimeter cells and clusters. Muons, which are minimum ionizing particles, deposit only a fraction of their energy in the Calorimeter. Muons are therefore effectively invisible to the Calorimeter and can fire the $E_{\mathrm{T}}^{\mathrm{miss}}$ trigger. The $E_{\mathrm{T}}^{\mathrm{miss}}$ trigger is nearly fully efficient for events with cluster-based $E_{\mathrm{T}}^{\mathrm{miss}} > 180$ GeV.

Unlike the strict barrel requirement of the MS-only trigger, the $E_{\mathrm{T}}^{\mathrm{miss}}$ trigger's coverage uses $|\eta| < 4.9$. The $E_{\mathrm{T}}^{\mathrm{miss}}$ trigger also does not have efficiency losses in ϕ, or from large muon impact parameters like the muon trigger. When the $E_{\mathrm{T}}^{\mathrm{miss}}$ trigger is fully turned-on, it has an efficiency of approximately 100%.

A requirement on an event's cluster-based $E_{\mathrm{T}}^{\mathrm{miss}}$ is applied to keep the Muon and $E_{\mathrm{T}}^{\mathrm{miss}}$ samples mutually exclusive. A requirement of cluster-based $E_{\mathrm{T}}^{\mathrm{miss}} > 180$ GeV is applied for the $E_{\mathrm{T}}^{\mathrm{miss}}$ selection, which ensures that events are likely to fire the $E_{\mathrm{T}}^{\mathrm{miss}}$ trigger, and also pass the `DRAW_RPVLL` $E_{\mathrm{T}}^{\mathrm{miss}}$ filter. Events with cluster-based $E_{\mathrm{T}}^{\mathrm{miss}} < 180$ GeV enter the Muon triggered sample, which has lower trigger efficiency, but is able to trigger on events which do not make it into the plateau of the $E_{\mathrm{T}}^{\mathrm{miss}}$

trigger.

Figure 9.1 shows the distribution of cluster-based E_T^miss for stop signal samples with different stop masses and lifetimes. For the simplified signal model studied in this analysis, roughly 95% of events enter into the E_T^miss sample, while roughly 5% of signal events enter into the Muon sample.
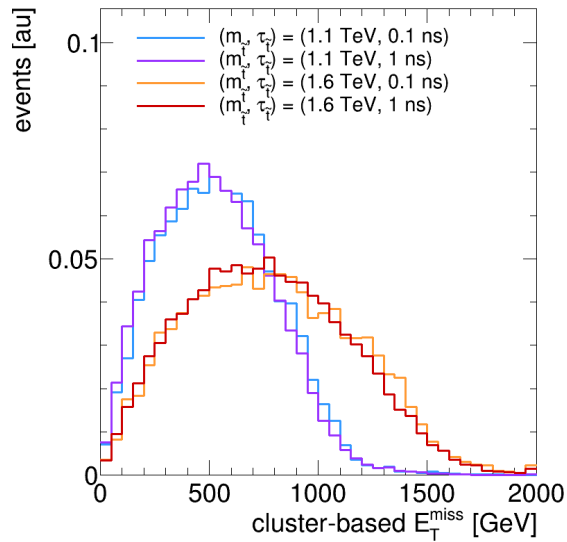
Figure 9.1: Cluster-based E_T^miss distributions for $\tilde{t} \to \mu + j$ signal samples with different stop masses and lifetimes. No event selection is applied.

9.5 Muon Selection

Events are required to contain at least one muon which passes the preselection criteria described below. Muons are required to be combined and pass a slightly modified `Medium` quality requirement. The hit requirements associated to the `Medium` definition are relaxed in order to retain efficiency to displaced muons. The standard `Medium` definitions requires muons have at least one associated Pixel

hit, which would drastically reduce sensitivity to long-lived particle decays that occur outside the last layer of the Pixel detector. This analysis instead requires muons have at least two associated Pixel hits or at least one TRT hit on track. Muons are still required to have at least five associated SCT hits.

Preselected muons are additionally required to satisfy:

- $p_T > 25$ GeV, and $|\eta| < 2.5$.
- $2.0 < |d_0| < 300$ mm
- $|z_0| < 500$ mm

The requirement that muons have pseudorapidity $|\eta| < 2.5$ ensures muons will be reconstructed with an Inner Detector track. Muons are required to have transverse momentum $p_T > 25$ GeV, in order to reduce the contribution from algorithm fakes, which are preferentially produced at low transverse momentum.

Cosmic muons are the dominant background in the Muon triggered sample after muon preselection. Algorithm fakes are the dominant background in the E_T^{miss} triggered sample. Muons from heavy-flavor decays are a sub-dominant background in both the E_T^{miss} and Muon triggered samples. The contribution of muons from heavy-flavor decays is suppressed by the requirement that displaced muons have transverse impact parameter $|d_0| > 2.0$ mm.

The requirements that muons have impact parameters $|d_0| < 300$ mm and $|z_0| < 500$ mm are designed to ensure that the muon is consistent with a long-lived particle decay which occurred inside the fiducial volume of $R_{xy} < 300$ mm and $|z| < 300$ mm. The requirement $|z_0| < 500$ mm has the additional benefit of reducing contributions from fake and cosmic muons with a $< 1\%$ loss in signal efficiency.

In order to keep the search inclusive, no explicit veto is applied on the number of preselected muons. However, the leading preselected muon (with the highest transverse momentum) is required to pass further criteria in order to reject background processes. If the leading muon fails any one of these requirements, the event is rejected. These requirements define the *full muon selection*, which is described below.

- *Trigger Matching:* the leading preselected muon for events collected in the Muon triggered sample is required to be matched to the muon that fired the trigger, within a cone of $\Delta R < 0.1$. The muon must additionally have $p_T > 62$ GeV and $|\eta| < 1.05$ in order to be fully within the plateau of the trigger efficiency. No such requirement is placed on the leading muon for events from the E_T^{miss} triggered sample.

- *Cosmic Veto:* Events in which the leading preselected muon is back-to-back in η and in ϕ with a Muon Spectrometer segment are rejected. Events in which the leading preselected muon is back-to-back with a region of the Muon Spectrometer that lacks detector coverage are also vetoed. The cosmic veto is described in Section 9.5.1.

- *Fake Veto:* The leading preselected muon is required to have a combined muon $\chi^2/N_{DoF} < 8$ and at least three precision layers in order to reject muons which are reconstructed from fake Muon Spectrometer and Inner Detector Tracks. The fake-muon veto is described in Section 9.5.2.

- *Isolation:* The leading preselected muon is additionally required to pass track and calorimeter isolation requirements, in order to reject real muons which are produced inside heavy-flavor jets. The heavy-flavor veto is described in Section 9.5.3

Unlike previous versions of this analysis, muons are not required to be explicitly associated to a displaced vertex.

9.5.1 Cosmic veto

Cosmic muons can pass through the ATLAS detector during collision events, typically from the positive ϕ direction to negative ϕ. Two muons which are reconstructed from the same cosmic muon will be back-to-back in ϕ, and have $|\Delta\phi(\mu_1, \mu_2)| \approx \pi$, and have equal and opposite η, or $|\eta(\mu_1) + \eta(\mu_2)| \approx 0$, as shown in Figure 9.2. The variable $\Delta R_{\mathrm{Cosmic}}$ can be used to easily identify two muons which are reconstructed from the same cosmic muon, where $\Delta R_{\mathrm{Cosmic}}$ is defined as

$$\Delta R_{\mathrm{Cosmic}} = \sqrt{(\Delta\phi - \pi)^2 + (\eta_1 + \eta_2)^2}. \tag{9.2}$$

The variable $\Delta R_{\mathrm{Cosmic}}$ sharply peaks at zero for events with cosmic muons, and takes on larger values for events with collision muons.

The ϕ distribution of events in data dominated by cosmic muons is shown in Figure 9.3. The muon in the bottom half of the detector (-ϕ) is most likely to fire a muon trigger, because its direction of motion is consistent with that of a collision muon, and appears to be produced at the interaction point. In comparison, the muon in the top half of the detector (+ϕ) is reconstructed opposite its true direction of motion, and arrives to the Muon Spectrometer approximately 30 to 70 ns earlier than collision muons.

Due to these timing considerations, a combined muon is only reconstructed in +ϕ for 70% of events with cosmic muons. The remaining 30% of cosmic events are partially reconstructed in positive ϕ, and would survive a veto rejecting two back-to-back combined muons. One cosmic signature that
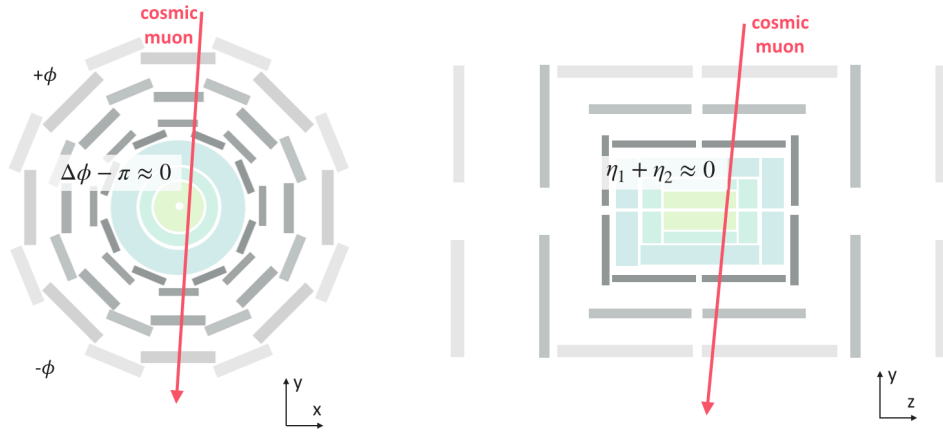
Figure 9.2: Two sketches of a cosmic muon passing through the ATLAS detector. The cosmic muon is drawn in red. The Inner Detector is drawn in green, and the Calorimeters are drawn in shades of blue. The three stations of the Muon Spectrometer are drawn in different shades of gray. The x-y plane is shown on the left, demonstrating that the two legs of the cosmic muon have $\Delta\phi(\mu_1, \mu_2) \approx \pi$, and the y-z plane is shown on the right, demonstrating the the two legs of the cosmic muon also have $\eta(\mu_2) + \eta(\mu_2) \approx 0$.
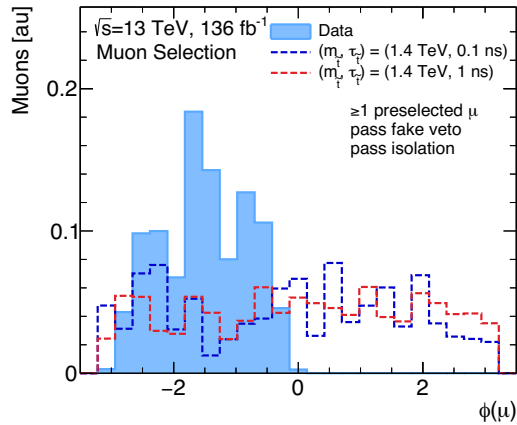
Figure 9.3: Leading preselected muon ϕ, for events in the Muon triggered sample. The fake muon veto and isolation requirements have been applied. Data are expected to be dominated by cosmic muons, as shown in light blue. Muons from two different signal lifetimes and masses are shown in dark blue and red. No displaced vertex selection is applied.

is consistently reconstructed in positive ϕ are Muon Spectrometer segments which are back-to-back

in (η, ϕ) with a displaced muon, as demonstrated in the sketch shown in Figure 9.4.
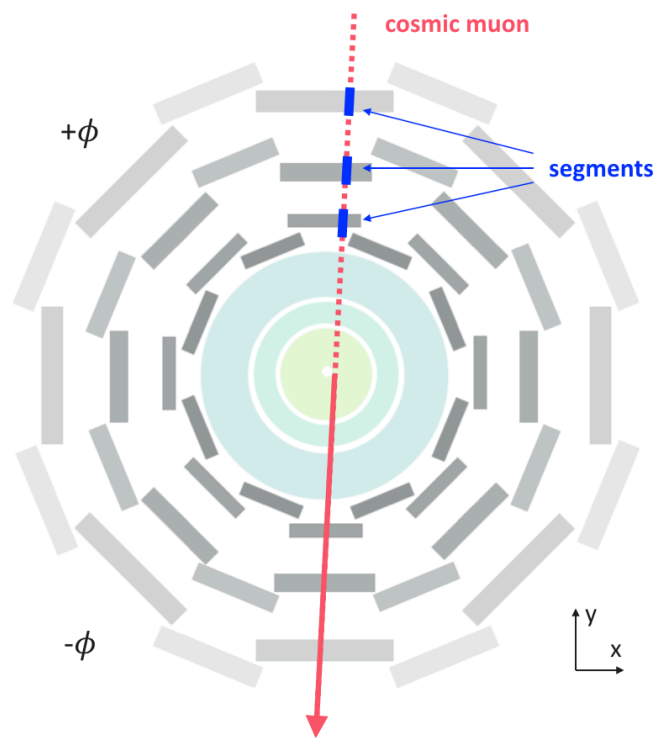
Figure 9.4: A sketch of a cosmic muon passing through the ATLAS detector in the x-y plane. In this sketch, the muon in negative ϕ (red solid line) is in time with collision and fully reconstructed, while the muon in $+\phi$ (red dotted line) is not reconstructed. However, Muon Spectrometer segments (blue) from the positive ϕ muon are reconstructed and back-to-back with the $-\phi$ muon.

The following subsections discuss how Muon Spectrometer segments which are back-to-back with

a displaced muon may be used to veto cosmic muons. Note that no requirements are placed on the

Muon Spectrometer Segments, in order to obtain maximal cosmic rejection.

Properties of back-to-back segments

The first step in designing a new cosmic veto is to look for Muon Spectrometer segments which are back-to-back with a preselected muon in η and ϕ, or have $\Delta R_{\text{Cosmic}} \approx 0$. Figure 9.5 shows ΔR_{Cosmic} for the leading preselected muon in the Muon triggered sample and the Muon Spectrometer segment which results in the smallest ΔR_{Cosmic} with the preselected muon. The fake-muon and heavy-flavor vetoes are applied to events, in order to obtain a data sample which is pure in cosmic muons. In data, the ΔR_{Cosmic} distribution peaks sharply at zero, while for signal muons the distribution is much flatter in ΔR_{Cosmic}.

The long tail of the cosmic distribution is the result of geometric and acceptance effects described below. For these reasons, ΔR_{Cosmic} is not used in this analysis. Instead, a more sophisticated veto in two-dimensions (η, ϕ) is used along with the various corrections described below.

In Figure 9.5, the segment most back-to-back with a cosmic muon, or which has the smallest ΔR_{Cosmic} with the muon, tends to be from the Middle station of the Muon Spectrometer. The Middle station has the most matched segments for two reasons. Segments reconstructed in the Middle station of the barrel benefit from additional ϕ information from RPC hits as well as timing considerations. The efficiency of finding a segment in the Inner, Middle, and Outer stations of the Muon Spectrometer is shown in Table 9.2

There are no RPC detectors in the Inner station of the Muon Spectrometer barrel. Therefore, Inner station segments consist only of MDT hits. If an Inner station segment consists of hits from a single MDT chamber, its ϕ location is set to the center of chamber. The Muon Spectrometer is made up
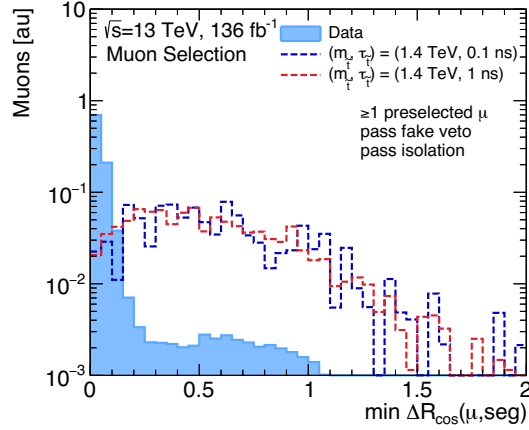
Figure 9.5: For the leading preselected muon in the Muon triggered sample, the $\Delta R_{\mathrm{Cosmic}}$ for the Muon Spectrometer segment most back-to-back in (η, ϕ). The fake muon veto and isolation requirements are applied. Data are expected to be dominated by cosmic muons, as shown in light blue. Muons from two different signal lifetimes and masses are shown in dark blue and red dotted lines. No displaced vertex selection is applied.

Table 9.2: The efficiency of finding a segment in the Inner, Middle, and Outer Muon Spectrometer within $\Delta R_{\mathrm{Cosmic}} < 0.2$ of the leading preselected muon in the Muon triggered sample. The fake-muon veto and isolation requirements are applied.

Station:	Inner	Middle	Outer
Efficiency [%]	93	91	81

of sixteen sectors in ϕ, which results in a ϕ resolution of approximately $\frac{2\pi}{16} \frac{1}{\sqrt{12}} = 0.11$ radians. An Inner station segment composed of hits from multiple MDT chambers, in the case of chamber overlaps, will have better ϕ resolution.

There are RPC detectors in the Middle and Outer barrel of the Muon Spectrometer. The Middle station has two RPC layers (the low-p_T and confirm layer), and the Outer station has one layer (the high-p_T layer). Hits from the RPC have ϕ information, and as a result, Middle and Outer segments have better ϕ resolution than those from the Inner station. However, segments in the Outer station are the most out of time, and are most likely to fail to be reconstructed. Because segments in the Middle station benefit from the best ϕ resolution, and are still likely to be reconstructed, these segments are most likely to be matched in ΔR_Cosmic.

The η resolution of segments is better than that of the ϕ coordinate, and the η resolution differs depending on the segment's station. The muon's η and ϕ used to calculate ΔR_Cosmic is computed with respect to the muon's distance of closest approach to the primary vertex. The segment η and ϕ, however, are purely detector-based definitions. The segment position is computed with respect to the origin of the ATLAS detector and does not account for the muon's displacement. The muon's displacement in z_0, results in a difference in the muon and segment η measurements. Preselected muons can be displaced as far as ± 500 mm in the z-direction.

As a rough approximation of the η resolution, consider a muon with $d_0 = 0$ mm, $z_0 = 500$ mm and $\eta(\mu) = 0$. The matched segment's θ_seg and η_seg can be calculated as

$$\theta_{\text{seg}} = \arctan(\frac{R_{\text{seg}}}{z_0})$$

$$\eta_{\text{seg}} = -\ln(\tan(\frac{\theta_{\text{seg}}}{2}))$$

(9.3)

where R_{seg} is the radial position of the segment, corresponding to the radial position of the Muon Spectrometer station in which it is reconstructed, and z_0 is the longitudinal impact parameter of the muon.

For a segment in the Inner station of the barrel, which is located at $R = 5$ m, $\eta_{\text{seg}} = 0.10$. For segments in the Middle and Outer barrel, $\eta_{\text{seg}} = 0.07$, and 0.05 respectively. The deviation from $\eta = 0$ due to the muon's displacement in z_0 is roughly correlated with the width of the $|\eta(\mu) + \eta_{\text{seg}}|$ distribution for cosmic muons. Figure 9.6 demonstrates how the η and ϕ resolutions change depending on the Muon Spectrometer station in which the segment is reconstructed.
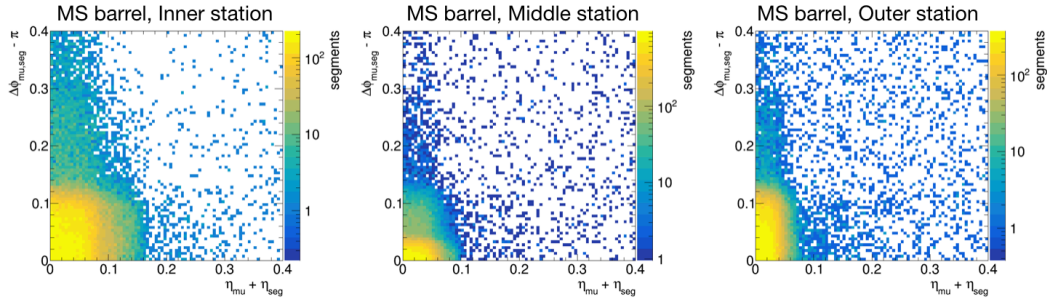
Figure 9.6: From left to right, $|\Delta\phi - \pi|$ and $|\eta_\mu + \eta_{\text{seg}}|$ for the Inner, Middle, and Outer Muon Spectrometer segment most back-to-back in ΔR_{Cosmic} with the leading preselected muon of the Muon triggered sample. The fake-muon veto and isolation requirements are also applied to the muon.

Due to the difference in the (η, ϕ) resolution of the muon-segment pair, rejecting cosmics with a

one-dimensional cut on $\Delta R_{\mathrm{Cosmic}}$ is less optimal than designing a rectangular veto in the $|\Delta\phi - \pi|$ and $|\Sigma\eta|$ plane. However, before optimizing a rectangular cut, it is possible to further improve the η resolution by making a geometric correction for the muon's displacement in z.

Geometric correction

In order to improve the η resolution of the muon-segment pair, such that $|\eta_{\mathrm{Corr}}(\mu) + \eta_{\mathrm{seg}}| = 0$, the muon's η measurement can be geometrically corrected to match that of the segment's η. Figure 9.7 shows a schematic of the geometric correction procedure. Note that this corrected pseudorapidity is only used for the cosmic veto, and not for any other part of the analysis.
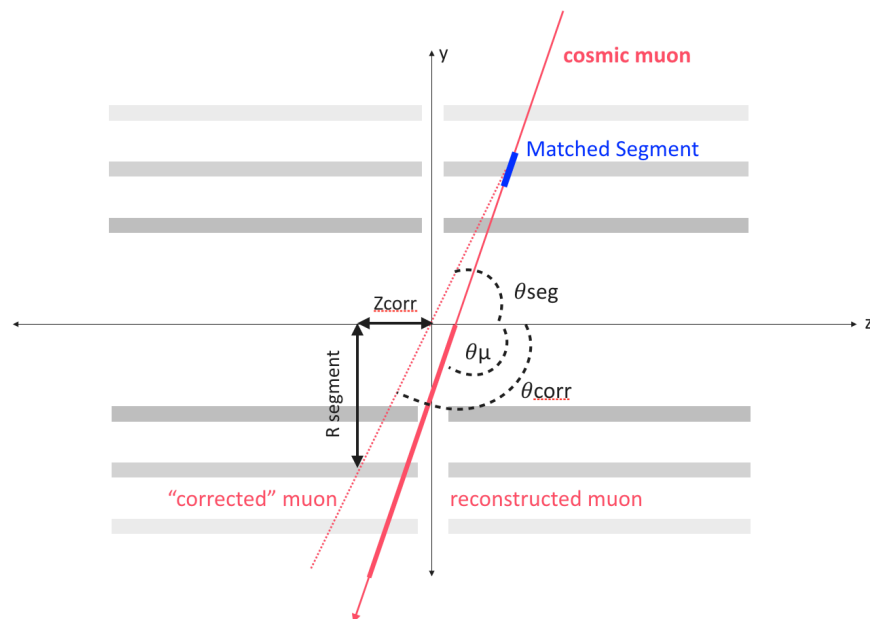
Figure 9.7: A sketch of the cosmic muon geometric correction procedure, shown in the y-z plane. The muon's η is originally measured with respect to the muon's distance of closest approach to the beam spot, while the segment's η is measured using the position in the Muon Spectrometer with respect to the ATLAS origin. The muon's pseudorapidity can be corrected such that $|\eta_{\mathrm{Corr}}(\mu) + \eta_{\mathrm{seg}}| = 0$.

This procedure aims to compute η_{Corr}, defined as

$$\eta_{\text{Corr}} = -\ln(\tan(\frac{\theta_{\text{Corr}}}{2}))\qquad(9.4)$$

where θ_{Corr} can be computed using the following equations

$$\theta_{\text{Corr}} = \arctan(\frac{R_{\text{seg}}}{Z_{\text{Corr}}})$$
$$Z_{\text{Corr}} = \frac{R_{\text{seg}}}{\tan(\theta_\mu)} - z_0\qquad(9.5)$$

Figure 9.8 shows the improvement on the η resolution for the muon-segment pair with smallest ΔR_{Cosmic}, by comparing $\eta_\mu + \eta_{\text{seg}}$ before and after the geometric correction is applied. Once the geometric correction is applied, the width of the $\eta_\mu + \eta_{\text{seg}}$ distribution is greatly reduced.
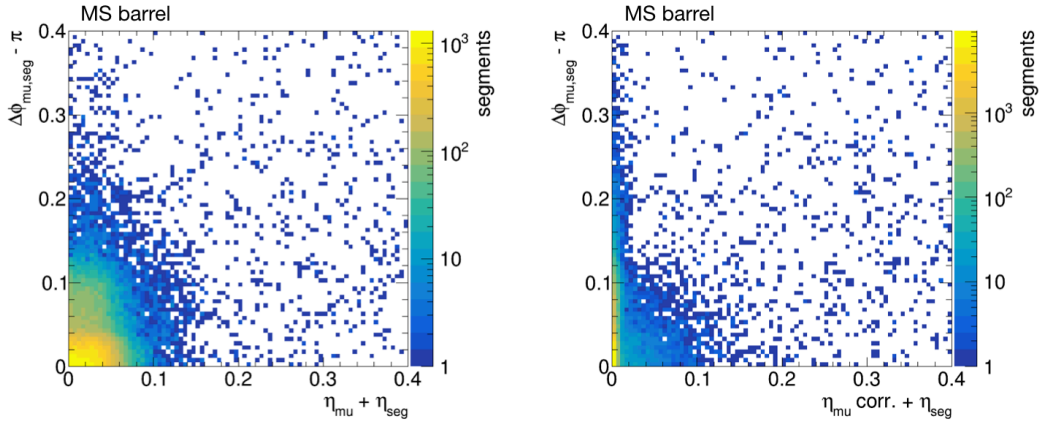
Figure 9.8: $\Delta\phi - \pi$ and $\eta_\mu + \eta_{\text{seg}}$ for the Muon Spectrometer segment most back-to-back in ΔR_{Cosmic} with the leading preselected muon of the Muon triggered sample. The fake-muon veto and isolation requirements are also applied to the muon. Left: before geometeric correction. Right: after geometric correction

Two-dimensional veto

After correcting for the muon displacement, the tail of $|\eta_{\text{Corr}}(\mu) + \eta_{\text{seg}}|$ distribution is much smaller than that of the $|\Delta\phi - \pi|$ distribution. Rejecting muons if they have a segment in $\Delta R_{\text{Cosmic}} < 0.2$ would reject approximately 95% of cosmic muons and 10% of signal muons. However, by looking in a rectangular region in (η, ϕ) back-to-back with a preselected muon instead of a circle, it is possible to achieve the same cosmic rejection power, with improved signal efficiency.

The fraction of of muons rejected by a rectangular cut in $|\eta_{\text{Corr}}(\mu) + \eta_{\text{seg}}|$ and $|\Delta\phi - \pi|$ is shown for signal muons and cosmic muons in Figure 9.9. The rectangular selection was designed to obtain a cosmic rejection factor of 95%, the same rejection obtained by requiring $\Delta R_{\text{Cosmic}} < 0.2$, and maximal signal efficiency. Muons are rejected if they are back to back with a segment in $|\eta_{\text{Corr}}(\mu) + \eta_{\text{seg}}| < 0.05$ and $|\Delta\phi(\mu, \text{seg}) - \pi| < 0.22$.

Acceptance requirement

Cosmic muons that fail to be rejected by looking for a back-to-back segment are most often near $|\eta| \approx 0.1$, and have a ϕ position corresponding to Large MDT chambers. These regions in η are just at the edge of the MDT chamber's acceptance, and point backwards in η and in ϕ to a region where there is no detector coverage, as shown in Figure 9.10. For these muons, it is impossible to reconstruct a Muon Spectrometer segment from the opposite leg of the cosmic muon. In order to prevent these cosmic muons which are outside of acceptance from entering the signal region, an additional requirement that muons are back-to-back with detector coverage is applied. This requirement is only applied
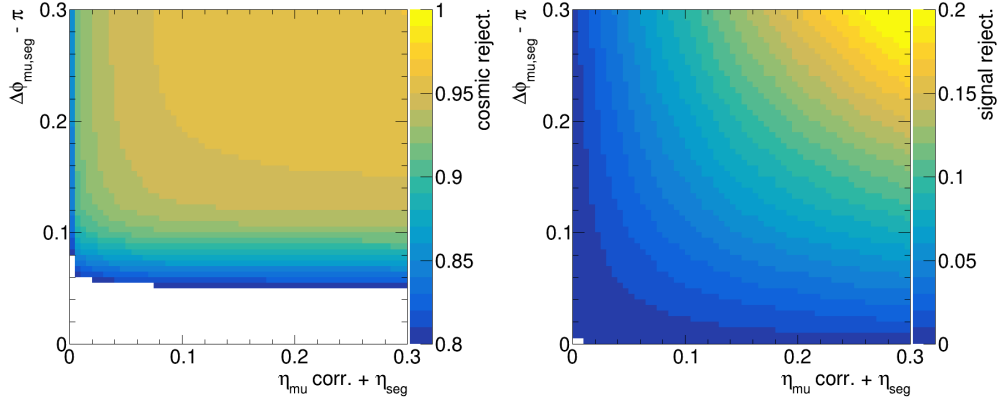
Figure 9.9: Left: The fraction of cosmic muons rejected by applying a rectangular veto in $|\Delta\phi - \pi|$ and $|\eta_{\mathrm{Corr}}(\mu) + \eta_{\mathrm{seg}}|$, shown as a function of $|\Delta\phi - \pi|$ and $|\eta_{\mathrm{Corr}}(\mu) + \eta_{\mathrm{seg}}|$. Distributions are shown for the leading preselected muon in Muon triggered events, which are also required to pass the fake-muon veto and isolation. Right: The fraction of signal muons rejected by by applying a rectangular veto in $\Delta\phi - \pi$ and $|\eta_{\mathrm{Corr}}(\mu) + \eta_{\mathrm{seg}}|$, shown as a function of $|\Delta\phi - \pi|$ and $|\eta_{\mathrm{Corr}}(\mu) + \eta_{\mathrm{seg}}|$. Muons from a variety of signal masses and lifetimes are considered.

to muons reconstructed in the barrel of the Muon Spectrometer ($|\eta| < 1.05$), because the Muon Spectrometer end-cap benefits from nearly 100% detector coverage in η and ϕ.

In order to determine if a cosmic muon would pass through a region with detector coverage, separate maps of detector coverage in (η, ϕ) are constructed using segment positions in the Inner, Middle, and Outer stations of the Muon Spectrometer. The procedure for producing these maps is detailed below, and Figures 9.11 shows the final results of these three maps.

- Produce distributions of muon segments in η versus ϕ, for segments in the Inner, Middle, and Outer Muon Spectrometer stations

- Each histogram is rebinned in ϕ, in order to account for segment resolution. For the Inner and Outer stations, 32 bins are used in ϕ, which corresponds to twice the number of MDT ϕ sectors. For the Middle station, 64 bins are used in ϕ, to account for the improved ϕ resolution from the RPC chambers, and account for regions without coverage near $|\eta| \approx 0.4$ and 0.75.
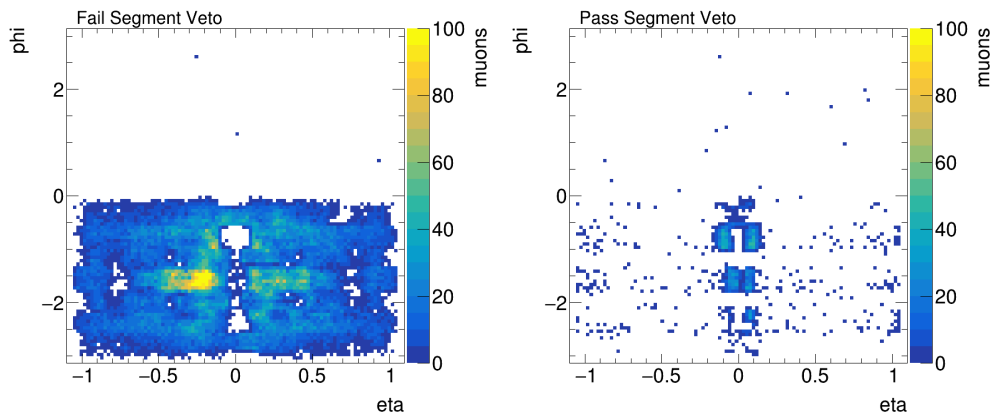
Figure 9.10: Left: muons which are rejected by looking for a segment back-to-back in (η, ϕ). Right: muons which are not rejected by looking for a back-to-back segment. Both plots are taken from the Muon triggered sample, and use the leading preselected muon which passes a fake-muon veto and isolation. No vertex requirements are applied.

- In order to be conservative, any regions within $\phi < 0.04$ or $\eta < 0.03$ of another (η, ϕ) bin without detector coverage, are also marked as not having detector coverage.

In order to determine if a muon passes the acceptance requirement or not, the following selection is applied to each preselected muon. Figure 9.12 shows the distribution of cosmic muons which are rejected by the acceptance requirement, and those muon which survive, in η versus ϕ.

- If the muon is reconstructed in the end-cap, with $|\eta| > 1.05$, the muon passes acceptance

- If the muon is in the barrel, require that the muon's $-\eta$ and $\phi + \pi$ has detector coverage in at least two stations of the Muon Spectrometer.

In order to determine if a cosmic muon would have passed through a region of detector coverage, the muon's pseudorapidity is corrected to the starting radius of the station in question. $R = 4500$, 7000, 9200 mm is used for the Inner, Middle, and Outer stations respectively. Using the radius closest to the interaction point is designed to check if the cosmic muon would be able to pass through entire
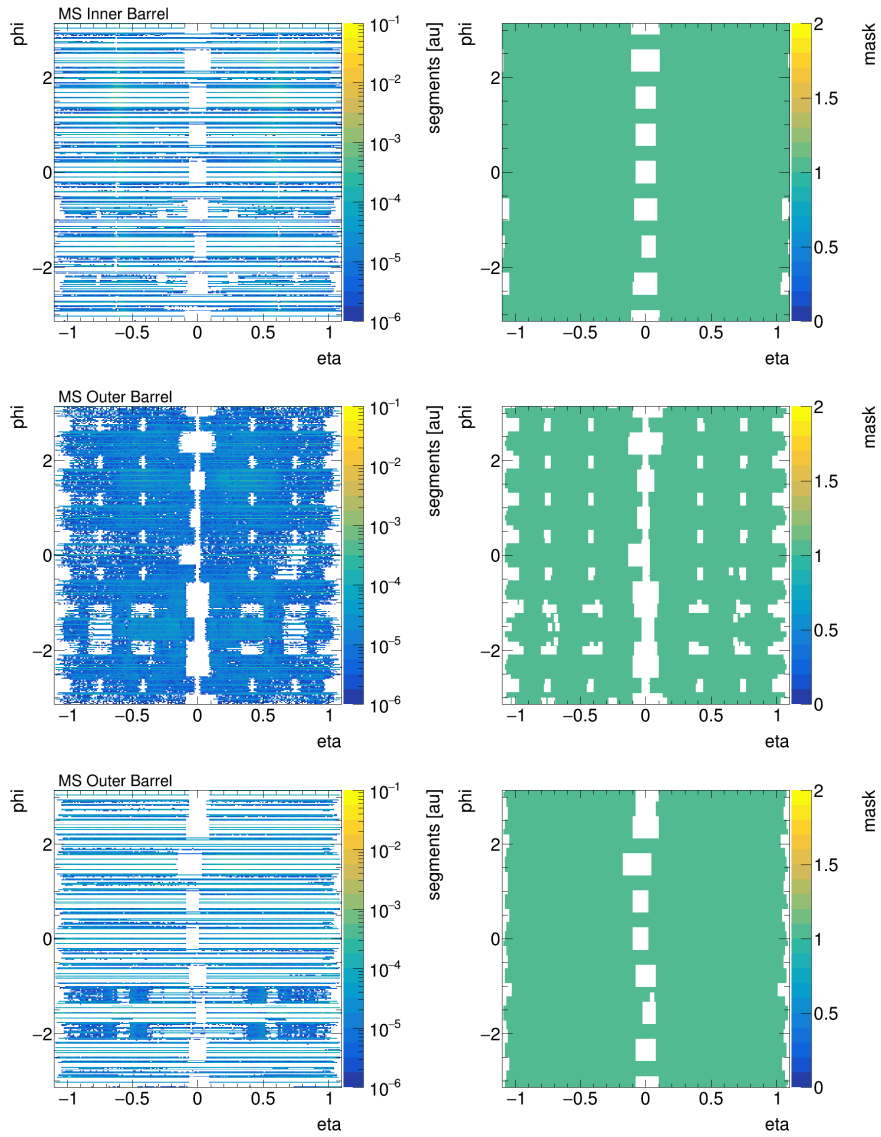
Figure 9.11: Left: position of Muon Spectrometer Segments in η v. ϕ. Right: maps defining regions of detector coverage. From top to bottom Inner, Middle, and Outer stations

chamber, whereas using R of the center of the chamber would correspond to a test if the cosmic could pass through a single multilayer. Note that this geometric correction is not applied to determine if a muon is reconstructed in the end-cap.
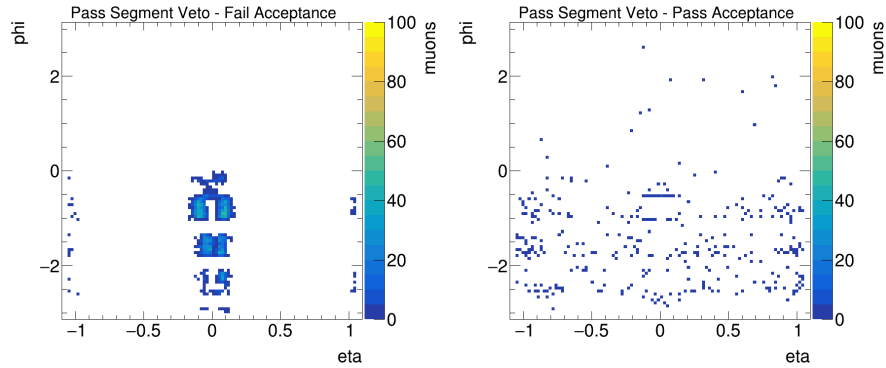
Figure 9.12: Left: Muons which are rejected by an acceptance requirement. Right: Muons which are not rejected by an acceptance requirement. Both plots are taken from the Muon triggered sample, and use the leading preselected muon which passes a fake-muon veto, isolation requirement, and are not back-to-back with a segment. No vertex requirements are applied.

Summary of improvements

Table 9.3 summarizes the effect of each improvement made to the cosmic veto. The efficiency for cosmic and signal muons are shown for three different vetoes which look for back-to-back segments. The first veto looks for a segment back-to-back in a circular region of η and ϕ, and rejects muons with $\Delta R_{\mathrm{Cosmic}}(\mu, \mathrm{seg}) < 0.2$. The second veto makes a geometric correction for the muon's displacement in z_0, and looks for a segment back-to-back in a rectangular region of η and ϕ, and rejects muons with $|\eta_{\mathrm{Corr}}(\mu) + \eta_{\mathrm{seg}}| < 0.05$ and $|\Delta\phi - \pi| < 0.22$. The final veto additionally rejects muons which would pass through regions of the Muon Spectrometer without detector coverage. These improve-

227

ments increase the signal efficiency from 91% to 96%, and reduce the percentage of cosmic muons

surviving the veto from 5% to 0.3%.

Table 9.3: The efficiency of cosmic muons and signal muons passing different cosmic vetoes. The cosmic efficiency corresponds to the percentage of preselected muons in the Muon triggered sample, with the fake-muon veto, and isolation applied, which pass the veto in question. The signal efficiency corresponds to the percentage of muons from a variety of $m(\tilde{t})$ and $\tau(\tilde{t})$. No vertex requirements are applied. Efficiencies for muons in data are determined using 3.2 fb^{-1} of data from 2016 and 2017.

Cosmic Veto:	Cosmic Efficiency [%]	Signal Efficiency [%]
Circular Veto in $\Delta R_{\mathrm{Cosmic}}(\mu, \mathrm{seg}) < 0.2$	4.8	90.7
Rectangular Veto in $|\eta_{\mathrm{Corr}}|$ and $|\Delta\phi - \pi|$	5.0	96.3
Rectangular Veto And Acceptance	0.3	95.9

9.5.2   FAKE-MUON VETO

In $E_{\mathrm{T}}^{\mathrm{miss}}$ triggered events, algorithm fakes are the dominant background after requiring events have

at least one preselected muon. These algorithm fakes consist of muons with both fake Muon Spec-

trometer Track and a fake Inner Detector Track. These algorithm fakes are unique to analyses which

make use of Large Radius Tracking, and most of these algorithm fakes are located in the end-cap of

the Muon Spectrometer.

Figure 9.13 shows the η distribution for the leading preselected muon in the $E_{\mathrm{T}}^{\mathrm{miss}}$ triggered sample,

where the cosmic veto and isolation requirements are already applied. Data, shown in yellow, are

dominated by fake muons, while muons from signal are shown in dark blue and red. The fake Muon

Spectrometer track most likely results from interactions with the end-cap toroid that produce low energy protons. These protons produce muon tracks with segments, or hits on track, in the Middle and Outer stations of the end-cap, both after the end-cap toroid in z. The Inner end-cap, which is before the end-cap toroid in z, usually does not have a segment on track. Figure 9.13 also shows the number of precision layers, $N_{\mathrm{precision\ layers}}$, or muon stations with a segment on track for fake muons in data and muons from signal. Most fake muons in data tend to have two stations with segments, while muons from signal tend to have at least three.

Figure 9.13: Data are taken from the E_T^{miss} trigger selection, and properties of the leading preselected muon are shown. Muons are required to pass the full cosmic veto and heavy-flavor veto. Left: Muon η and Right: Number of precision layers per muon, or the number of Muon Spectrometer stations with a segment on track.

As discussed in Chapter 6, ATLAS combined muon reconstruction proceeds *outside-in*. The algorithm begins by finding a Muon Spectrometer track, and then looks for a matching Inner Detector Track. For analyses which use standard tracking in the Inner Detector, these fake muon tracks produced in the end-cap are usually not matched up to a fake Inner Detector track. However, the Large Radius Tracking algorithm produces many more fake Inner Detector tracks than standard tracking.

These fake tracks tend to have fewer hits in the Pixel, SCT, and TRT, and are available to be matched

up to fake Muon Spectrometer tracks. Figures 9.14-9.15 show the number of Pixel detector hits, SCT

strips, and TRT hits on track for fake muons in data, and muons from signal. Muons from signal tend

to have more hits on track than fake tracks in data. Figure 9.15 also shows the transverse impact param-

eter of fake muons in data and muons from signal. Most fake muons have Inner Detector Tracks from

Large Radius Tracking, and as a result have large impact parameters.

Figure 9.14: Data are taken from the E_T^{miss} trigger selection, and properties of the leading preselected muon are shown. Muons are required to pass the full cosmic veto and heavy-flavor veto. Left: Number of Pixel hits on track and Right: Number of SCT hits on track.

One variable of interest in muon reconstruction is the charge momentum significance, or $\sigma(q/p)$,

which compares charge and momentum as measured in the Muon Spectrometer to that of the In-

ner Detector. This significance is defined in Equation 6.1. For Muon Spectrometer tracks and Inner

Detector tracks which are not produced from the same particle, the combined muon's charge momen-

tum significance is expected to be large. Figure 9.16, shows the charge momentum significance for

fake muons in data, a flat distribution, to muons from signal, which is peaked at zero and falls off by
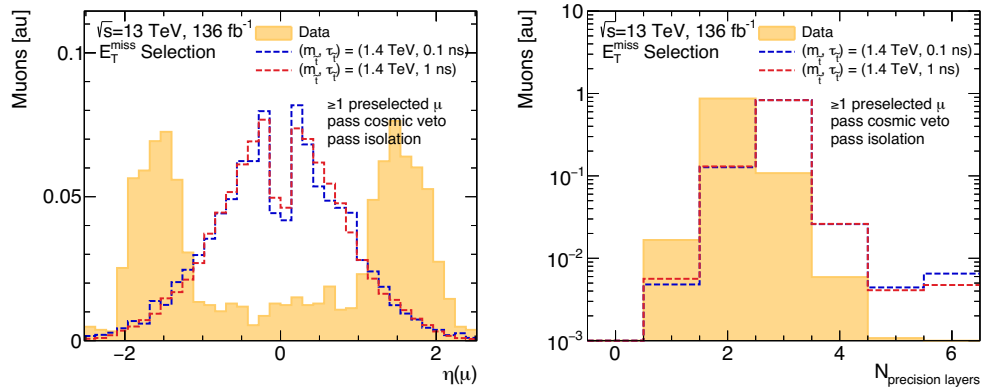
Figure 9.15: Data are taken from the E_T^{miss} trigger selection, and properties of the leading preselected muon are shown. Muons are required to pass the full cosmic veto and heavy-flavor veto. Left: Number of TRT hits on track and Right: Muon transverse impact parameter d_0.

$\sigma(q/p) = 7$. In ATLAS, `Medium` combined muons are required to have $\sigma(q/p) < 7$.

Because the Inner Detector track and Muon Spectrometer track are not produced from the same real muon, fake muons in data tend to have poor fit quality, or a large combined muon χ^2/N_{DoF}, as shown in Figure 9.16. In contrast, the χ^2/N_{DoF} for muons from signal tends to be lower, nearly always $\chi^2/N_{DoF} < 8$. Note that the variable χ^2/N_{DoF} is sensitive to detector alignment. The MC simulation assumes detectors are aligned, whereas the actual detector is not always perfectly aligned. Any requirement placed on χ^2/N_{DoF} should account for the fact that in MC, the χ^2/N_{DoF} variable is nearly always underestimated.

In order to reject fake muons, muons are required to have at least three stations with a segment, $N_{\text{Precision Layers}} \geq 3$ and good quality of fit $\chi^2/N_{DoF} < 8$. These requirements reject more than 99% of fake muons in data, and keep roughly 85% of muons from signal.
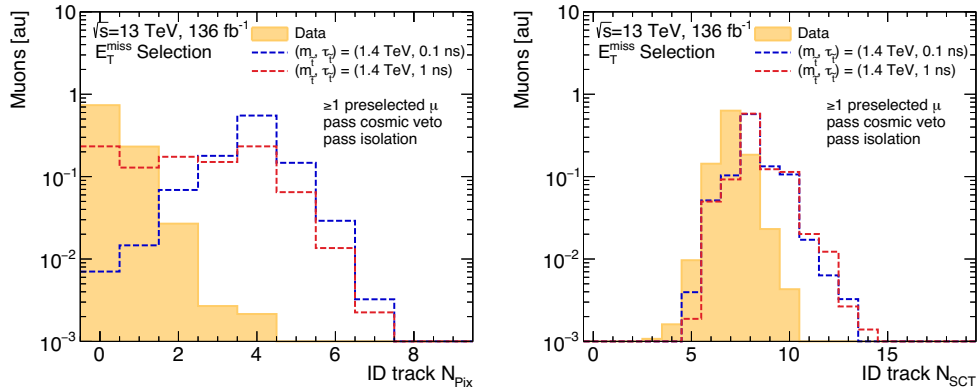
Figure 9.16: Data are taken from the E_T^{miss} trigger selection, and properties of the leading preselected muon are shown. Muons are required to pass the full cosmic veto and heavy-flavor veto. Left: Muon charge momentum significance. Right: Combined muon χ^2/N_{DoF}.

9.5.3 HEAVY-FLAVOR VETO

In E_T^{miss} triggered and Muon triggered events, there is an additional contribution of muons from heavy-flavor decays after muon preselection requirements are applied. These muons are produced from decays of b-hadrons, or other heavy-flavor hadrons inside jets. With a lifetime on the order of picoseconds, b-hadron decays do produce some muons which survive the $|d_0| > 2$ mm preselection requirement. Figure 9.17 shows the transverse and longitudinal impact parameters of muons in data from the E_T^{miss} triggered sample which pass preselection, the fake-muon veto, and cosmic veto in green. These muons are dominated by heavy-flavor decays, and have smaller impact parameters. There is a small contribution of muons with $|d_0| > 5$ mm. These muons at larger d_0 are likely from fake muons which are not rejected by the fake-muon veto.

Muons from heavy-flavor decays tend to be produced inside jets, while muons from signal tend to be produced in isolation. It is possible to reject muons from heavy-flavor decays by requiring muons
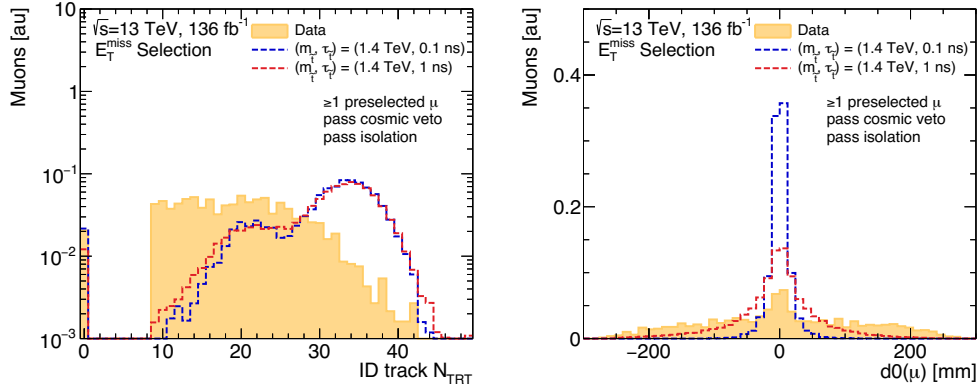
232

Figure 9.17: Data are taken from the E_T^{miss} trigger selection, and properties of the leading preselected muon are shown. Muons are required to pass the full cosmic veto and fake veto. Left: Muon transverse impact parameter d_0. Right: Muon longitudinal impact parameter z_0.

are well isolated from other nearby hadronic activity. There are two ways to quantify the isolation of a muon.

The first method, a track-based definition, uses a variable referred to as ptvarcone30/p_T. This track-based definition looks inside a cone of varying radius around the muon, and computes the total momentum from tracks not associated to the muon. The ratio of this sum is taken with respect to the momentum of the muon. The cone has a maximum size of $\Delta R = 0.3$ for muons with $p_T < 33.3$ GeV, and a cone size of 10 GeV/pT is used for muons with higher p_T. Similarly, the ratio of cluster energy around the muon is taken with respect to the momentum of the muon, in a cone of $\Delta R < 0.2$, in order to compute a calorimeter-based isolation definition, referred to as topoetcone20/p_T.

Figure 9.18 shows track and calorimeter isolation, ptvarcone30/p_T and topoetcone20/p_T, for muons from heavy-flavor decays and muons from signal. In both cases, muons from heavy-flavor decays tend to have larger isolation values than muons from signal.
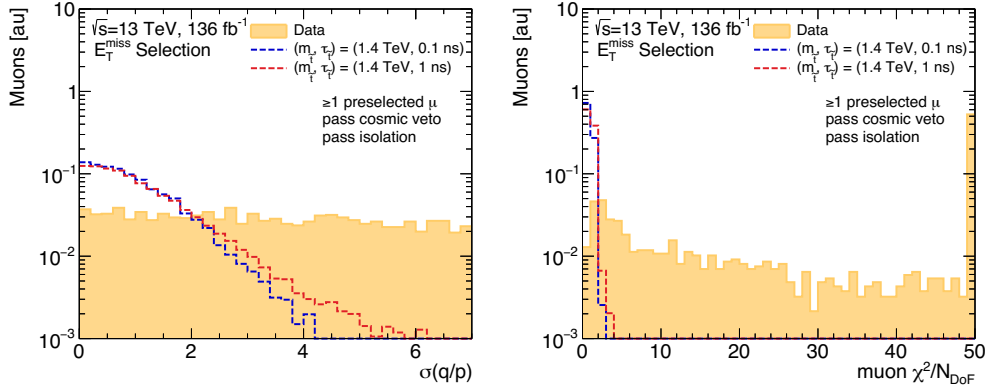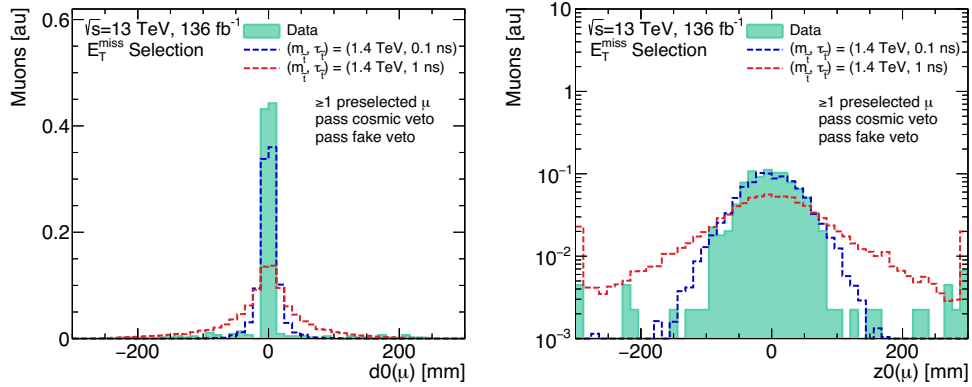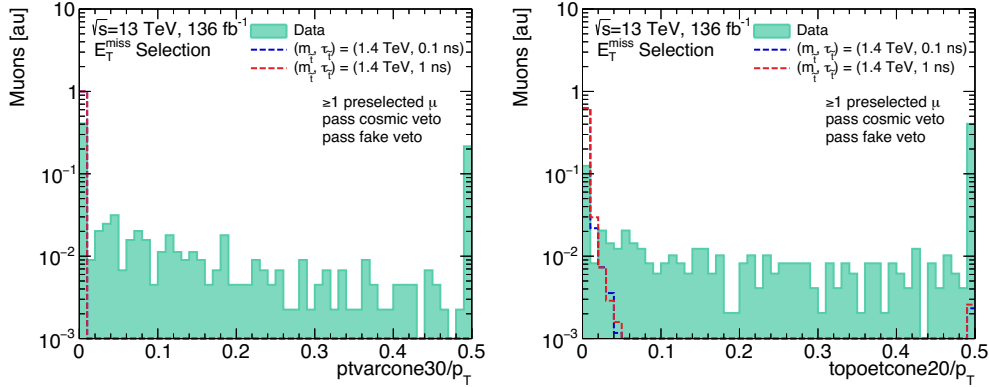
Figure 9.18: Data are taken from the E_T^{miss} trigger selection, and properties of the leading preselected muon are shown. Muons are required to pass the full cosmic veto and fake veto. Left: Muon track isolation, ptvarcone30/p_T. Right: Muon calorimeter isolation, topoetcone20/p_T

In order to reduce the contribution of heavy-flavor muons to the analysis, muons are required to pass a `Fixed Cut Tight` isolation requirement, or ptvarcone30/p_T < 0.06 and topoetcone20/p_T < 0.06

9.6 Displaced Vertex Selection

Events are also required to contain at least one displaced vertex which satisfies the following requirements. The vertex selection is separated into two stages, a *preselection* and *full selection*.

The following requirements define the *displaced vertex preselection*.

- Vertices are required to be reconstructed in the Pixel barrel volume, with $r_{DV} < 300$ mm and $|z_{DV}| < 300$ mm.
- The vertex fit must have $\chi^2/N_{DoF} < 5$.
- The vertex must be at least 4 mm in the x-y plane from all reconstructed primary vertices in the event.

- The vertex must not be in a region of ATLAS detector material. A map of detector material is constructed from studying vertices in data and known regions of material in simulation. More information on how the material map is defined in the following Section 9.6.1.

After vertex preselection, displaced vertices in data are dominated by vertices produced from random track crossings. These displaced vertices tend to have fewer tracks than vertices from signal and lower invariant mass. Signal region displaced vertices, or *fully selected* displaced vertices must also have $n_{\text{Tracks}}^{\text{DV}} \geq 3$ and $m_{\text{DV}} > 20$ GeV.

The $n_{\text{Tracks}}^{\text{DV}}$ and m_{DV} requirements were optimized to maximize signal efficiency and reduce the expected background to approximately zero events in the $E_{\text{T}}^{\text{miss}}$ trigger Signal Region. The requirement $n_{\text{Tracks}}^{\text{DV}} \geq 3$ was loosened from $n_{\text{Tracks}}^{\text{DV}} \geq 5$, which was the requirement used in the Run 1 version of this analysis. Loosening the requirement on the displaced vertex track multiplicity is particularly important for models in which the long-lived particle decays to only one hadronic jet. Requiring vertices have at least three associated tracks is essential to reject displaced vertices from random track crossings. The requirement $m_{\text{DV}} > 20$ GeV helps reject any remaining background vertices.

In addition to providing an overview of the displaced vertex selection criteria, this section also discusses the efficiency for reconstructing a displaced vertex for the benchmark signal model. Improvements to the signal efficiency due to Large Radius Tracks and sources of background vertices are also discussed. Several event displays of secondary vertices in signal and data can also be found in Appendix A. Recall that all figures shown in this section have the track cleaning requirements, described in Section 6.5.2, applied to displaced vertices.

Hadronic interactions with detector material can produce secondary vertices with large track multiplicities. These vertices are difficult to distinguish from long-lived particle decays, and constitute a major background to the analysis. In order to reduce the contribution of hadronic interactions, it is essential to reject vertices found inside regions of detector material.

A simplified map of the detector material in the analysis fiducial volume is used to veto hadronic interactions. The material map is three dimensional, and defined in (R, z, ϕ). The material map covers $R < 300$ mm, $|z| < 300$ mm, and $-\pi < \phi < \pi$, and indicates the presence or absence of material.

Two methods are used to create the map. The first method uses the density of low mass and low-track multiplicity vertices observed in data, in order to extract the position of complex structures such as pixel modules. The second method uses information about material from the ATLAS detector simulation, especially in regions where there are not sufficient statistics to derive a data-driven map. This map is designed to indicate the presence of material in the actual ATLAS detector, over the course of 2016-2018 data taking, as well as the presence of material in simulation.

The material map is separated into an Inner and Outer Section, which are created with different strategies.

- Inner Section: For $R < 150$ mm, there are sufficient vertices to derive a data-driven material map. The positions of the beam pipe and support tubes are hard coded given information from simulation and in observed vertices data.
- Outer Section: In $R > 150$ mm, there are not enough vertices to derive a density-based map. Instead, the position of material is taken from simulation and validated using data. Regions

with material exclusively in Monte Carlo are removed from the map, while regions in data which suggest the presence of material are added to the map.

The material map has the following bin sizes, which are designed to account for the vertex position resolution. Bins are smaller in the transverse plane than in the z-direction. Bins are also larger for the Outer Section, in order to account for a degradation in the vertex position resolution which occurs at increasing radii.

- $R < 150$ mm has $\Delta R_{xy} = 0.2$ mm, $\Delta \phi = \pi/423$, $\Delta z = 1$ mm
- $R > 150$ mm has $\Delta R_{xy} = 0.8$ mm, $\Delta \phi = \pi/217$, $\Delta z = 2$ mm

In order to create the Inner Section of the material map, the following vertices are selected in data. The selection is designed to reduce contributions of vertices from real long-lived particles and random track crossings or fake vertices. Once the selection is applied, the remaining vertices are dominated by hadronic interactions. A high density of vertices indicates the presence of material.

- The first step is to remove vertices from known long-lived particles. Long-lived particles can decay anywhere in the analysis fiducial volume, and produce vertices outside regions of material. Vertices with two associated tracks, and $0.45 < m_{\mathrm{DV}} < 0.55$ GeV are removed in order to exclude vertices from K_S decays.
- Vertices are also required to have $m_{\mathrm{DV}} < 2.5$ GeV, in order to reduce contributions from random track crossings, and to avoid any potential bias from signal vertices.
- In order to reduce the contribution from vertices made up of fake tracks, the number of Pixel hits on track is required to be at least the same number of Pixel layers expected after a displaced vertex.
- The angle between the outgoing momentum of the tracks associated to the displaced vertex, and the vector between the primary vertex and displaced vertex is required to be small, < 0.5 radians. This selection is also designed to reduce the contribution from fake vertices.
- Vertices with at least three associated tracks are rejected if the largest opening angle between outgoing tracks is below 0.15 radians, and are additionally required to have $m_{\mathrm{DV}} > 0.95$ GeV. These requirements are designed to reduce backgrounds from photon conversions.

237

Once vertices in data have been selected, the symmetry of the ATLAS detector is exploited by folding the vertex distribution in ϕ, given the symmetries given by the number of Pixel staves, after accounting for measured overall transverse translations of each of these components. These translations can be as large as a millimeter. The translation sizes in (x, y) are as follows:

- Beam pipe – $(0.29, 0.99)$ mm
- IBL – $(0.19, 0.32)$ mm
- B-Layer – $(0.17, 0.26)$ mm

Folding the map increases the available statistics for determining which regions are likely to have material. This folding is done separately for different Pixel layers, in order to account for the geometry of the detector.

- IBL – folded 7 times
- B-Layer – folded 11 times
- Pixel 1 – folded 19 times
- Pixel 2 – folded 13 times

After folding the detector, the distribution of vertices is smoothed along the z-ϕ plane, which is along the direction of most detector material. Smoothing helps to fill any unpopulated bins inside regions of detector coverage. Then a threshold is applied to the distribution to create a map of booleans. Bins which have more vertices than this threshold are defined as material regions, and bins below threshold are defined to be empty.

Finally, known elements of detector material are added by hand, including the beam pipe and support tubes. It is important to note that the beam pipe is coupled to the LHC ring, while other supports are coupled to the the floor of the experimental cavern. The floor of the ATLAS cavern is rising with

respect to the beam pipe over time. This effect is accounted for when making approximations from simulation, and validated in data. The final map is tested on a large inclusive sample of displaced vertices and the resulting distributions are checked for seemingly missed material contributions across the entire dataset.

Figures 9.19 and 9.20 show distributions of the displaced vertices in data before applying the material veto, and for vertices which fail the material veto. A higher density of vertices indicates the presence of detector material. These distributions are shown for the R-z and x-y planes. Displaced vertices are required to be inside the analysis fiducial volume.

Figures 9.21 shows projections of the material map for $R < 150$ mm in the R-z and R-ϕ planes. Figure 9.22 show projections of the material map for $R > 150$ mm in the R-z and R-ϕ planes. In total the material map vetoes roughly 42% of the total fiducial volume.

9.6.2 DISPLACED VERTEX SIGNAL EFFICIENCY

This section discusses the efficiency for reconstructing a displaced vertex for the R-parity violating stop simplified model. This efficiency is related to the efficiency for reconstructing charged particles as displaced tracks, and the efficiency for reconstructing those tracks as a displaced vertex. In order to disentangle these effects, first the efficiency for reconstructing displaced tracks is investigated, followed by a study of the secondary vertex efficiency given a set of reconstructible tracks.
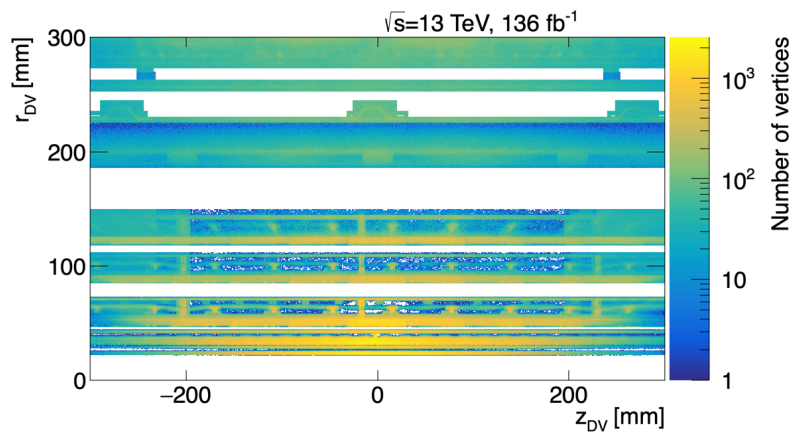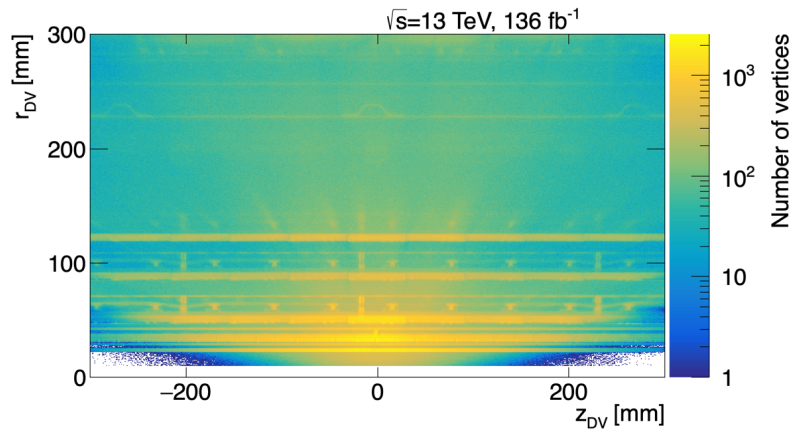
Figure 9.19: Distributions of all displaced vertices in data in the R-z plane. Top: Before applying a material veto. Bottom: displaced vertices which are rejected by the material veto.
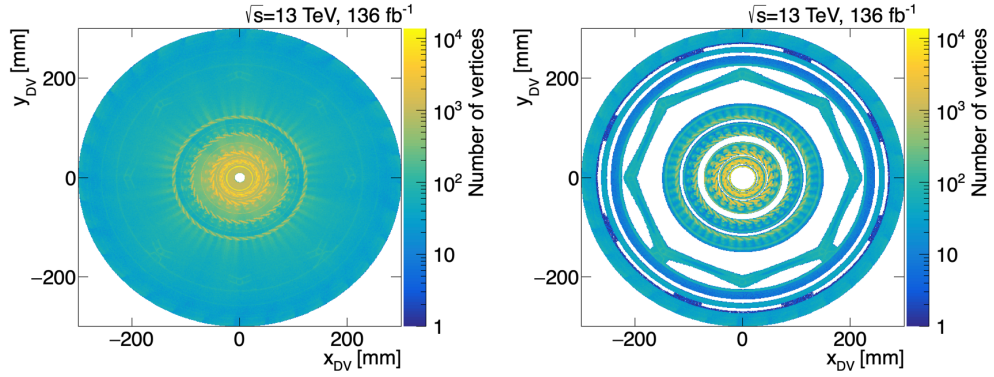
Figure 9.20: Distributions of displaced vertices in data in the x-y plane. Left: Before applying a material veto. Right: displaced vertices which which are rejected by the material veto.
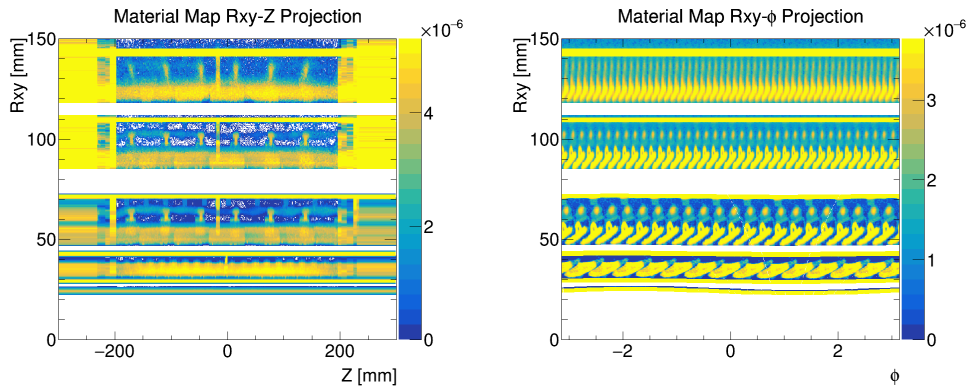
Figure 9.21: Projections of the material map for $R < 150$ mm. Left: Projection in the R-z plane. Right: Projection in the R-ϕ plane.

241
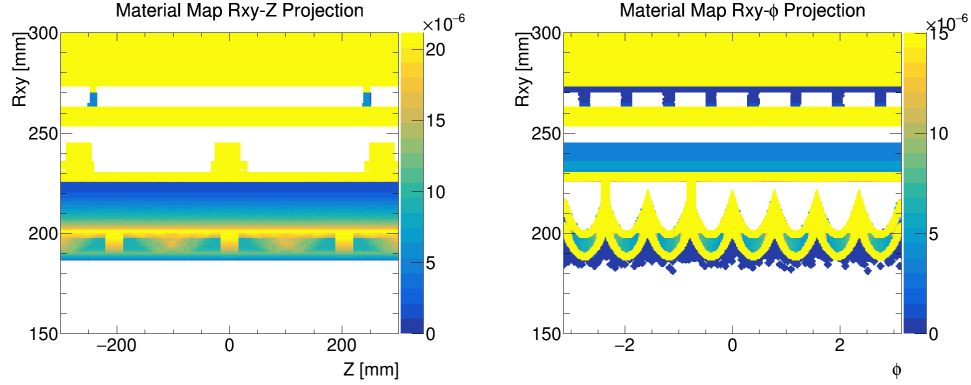
Figure 9.22: Projections of the material map for $R > 150$ mm. Left: Projection in the R-z plane. Right: Projection in the R-ϕ plane.

Tracking Efficiency

As discussed in Section 6.5.1, the efficiency for reconstructing a charged particle as a track degrades as a function of the particle's production radius, as well as the charged particle's impact parameter. These efficiencies are studied in the context of the simplified model of interest for this analysis. In order to study only particles which could be reasonably reconstructed by the ATLAS Inner Detector, the fiducial selections listed in Table 9.4 are applied to truth particles.

Table 9.4: Fiducial selections applied to truth hadrons and muons.

$$p_\mathrm{T} > 1\,\mathrm{GeV}$$
$$|\eta| < 2.5$$
$$\mathrm{Prod}\ R_{xy} < 300\,\mathrm{mm}$$
$$\mathrm{charge} = \pm 1$$
$$\mathrm{From\ stop\ particle\ decay}$$

Figure 9.23, shows the distribution of the production radius, Prod. R_{xy}, for truth muons and truth

hadrons produced in the stop particle decay, as well as their transverse impact parameters $|d_0|$. These distributions are shown for a signal sample with stop mass $m(\tilde{t}) = 1.4$ TeV and lifetime $\tau(\tilde{t}) = 1$ ns.
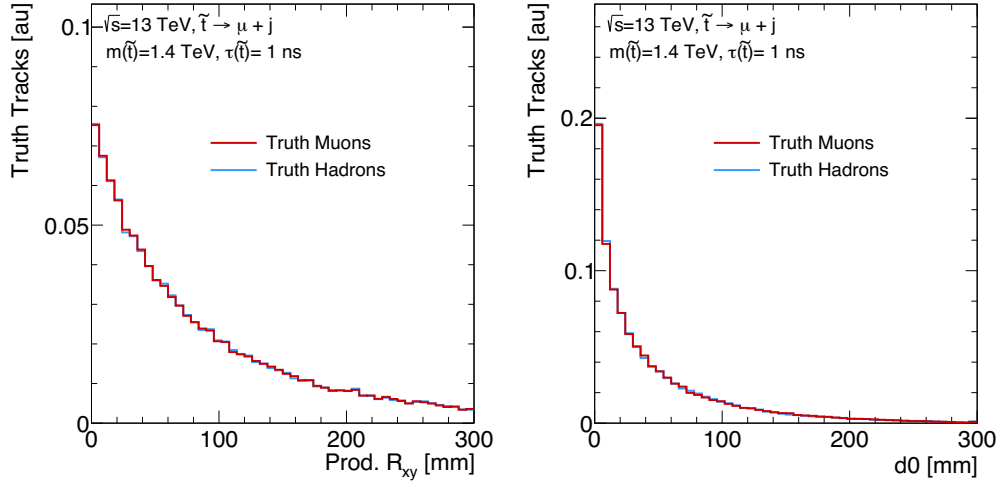
Figure 9.23: For a signal model with stop mass $m(\tilde{t}) = 1.4$ TeV and lifetime $\tau(\tilde{t}) = 1$ ns. Left: The production radius, Prod. R_{xy}, for truth muons and truth hadrons produced in the stop particle decay. Right: The transverse impact parameter $|d_0|$ for truth muons and truth hadrons.

The inclusive tracking efficiency is shown as a function of the track's production radius, Prod R_{xy}, and the track's transverse impact parameter, d_0 in Figure 9.24. The inclusive efficiency is evaluated separately for displaced muons and displaced hadrons. Truth particles may be reconstructed by either the standard ATLAS tracking, or the Large Radius Tracking.

The inclusive efficiency for reconstructing a track decreases as a function of long-lived particle decay radius, Prod R_{xy}, and displaced track impact parameter, d_0. Hadrons have a lower inclusive efficiency for being reconstructed than muons. This effect is due to the fact that hadrons are produced inside jets with large transverse momentum (jet $p_{\mathrm{T}} > 100$ GeV), while muons are produced in isolation.
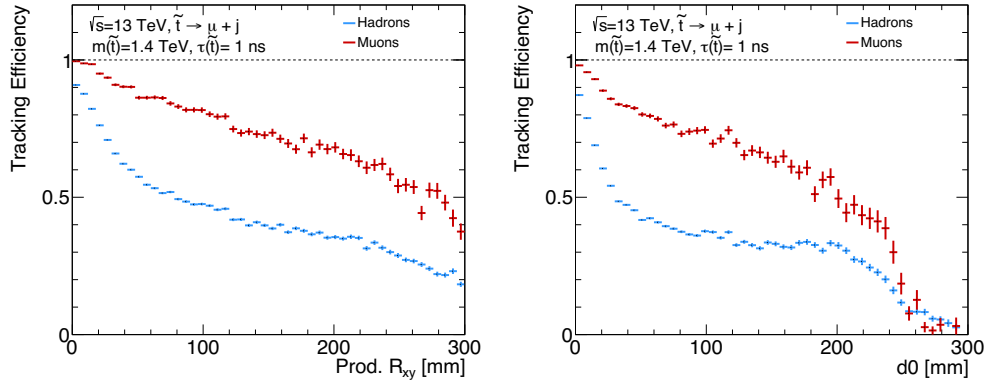
Figure 9.24: Left: Track reconstruction efficiency as a function of the long-lived parent decay radius, Prod. R_{xy}, for both muons and hadrons. Right: Track reconstruction efficiency as a function of charged particle transverse impact parameter $|d_0|$, for both muons and hadrons

Hadrons from these high momentum jets are highly collimated in ΔR. Charged particles which are close by in ΔR are reconstructed with a lower efficiency than particles produced in isolation. This reduction in efficiency is due to the fact that it is difficult to resolve clusters and hits produced from two different particles if they are close by in ΔR.

Figure 9.25 shows the distribution of the angle between the truth hadron considered, and the nearest charged daughter particle from the same R-hadron decay in ΔR, or $\Delta R_{\text{nearest track}}$. Most hadrons have $\Delta R_{\text{nearest track}} < 0.05$. Figure 9.25 also shows the inclusive efficiency for reconstructing a displaced hadron as a function ΔR nearest track. The overall tracking reconstruction efficiency efficiency drops from a maximum of $\approx 75\%$ to under 50% for hadrons which are nearby other daughter particles, and have $\Delta R_{\text{nearest track}} \approx 0$.
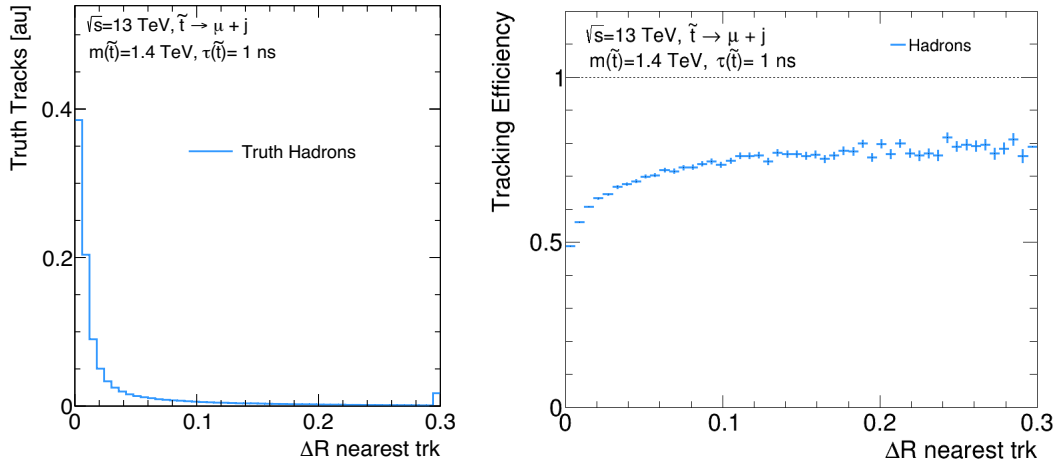
Figure 9.25: Left: the ΔR between the truth track considered, and the nearest truth track from the same R-hadron decay. The Right: Track reconstruction efficiency as a function the ΔR between the truth track considered, and the nearest truth track from the same R-hadron decay.

VERTEX EFFICIENCY

In order to study the efficiency of reconstructing a displaced vertex, stop $\tilde{t}$ decays are matched to reconstructed displaced vertices in Monte Carlo. The procedure for finding a matching reconstructed displaced vertex is as follows.

- The $\tilde{t}$ of interest is identified, and its decay position, R_{xy} and z is recorded.
- A fiducial selection of $p_{\mathrm{T}} > 1$ GeV, $|d_0| > 2$ mm, charge $= \pm 1$, $|\eta| < 2.5$ is applied to the daughter particles from the $\tilde{t}$ decay, in order to identify particles which could reasonably be reconstructed by the secondary vertex algorithm.
- Truth tracks which pass the fiducial selection are then used to compute the $\tilde{t}$ *truth mass* and *truth* $n_{\mathrm{Tracks}}^{\mathrm{DV}}$.
- Stop quarks must have a truth mass greater than 20 GeV and at least three truth tracks in order to be considered in acceptance

245

- An attempt is made to find a reconstructed displaced vertex in a sphere of 3 mm around the stop's decay position in (x, y, z). Displaced vertices are required to pass the following selection. Acceptance criteria are applied in order to ensure the stop decay occurs inside the detector volume of interest. Requirements on the reconstructed vertex number of tracks and invariant mass are applied in order to avoid matching to a vertex produced by random track crossings or hadronic interactions. These requirements are:

  - $R_{xy} < 300$ mm, $|z| < 300$mm
  - the DV must be at least 4 mm away from any PV in the event in (x, y)
  - $\chi^2/N_{DoF} < 5$
  - reconstructed $m_{\mathrm{DV}} > 20$ GeV
  - reconstructed $n_{\mathrm{Tracks}}^{\mathrm{DV}} \geq 3$

- If no displaced vertex is found, the number of vertex tracks, and the vertex mass is recorded as zero.

Figure 9.26 shows how the efficiency for reconstructing and associating tracks to vertices changes as a function of the vertex location in R_{xy}. In the left plot, the number of truth tracks in acceptance is shown in black. This line represents the largest number of tracks that could reasonably be expected to be reconstructed as a part of the vertex, or truth $n_{\mathrm{Tracks}}^{\mathrm{DV}}$. The blue line shows the number of those truth tracks which are matched to reconstructed tracks. The reduction in the number of tracks between the black and blue lines represents a loss in efficiency from the Large Radius Tracking algorithm. The red line shown the number of those truth tracks which are reconstructed as part of a displaced vertex. The reduction in the number of tracks between the blue and red lines represents an efficiency loss due to the secondary vertex algorithm. Figure 9.26 also shows how the reduction in the number of reconstructed tracks, and tracks associated to the vertex, affect the reconstructed vertex mass as a function of vertex displacement in R_{xy}.
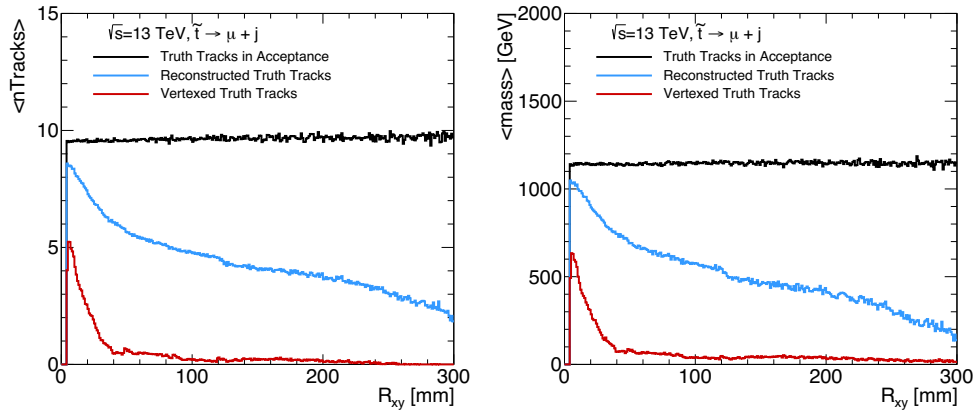
Figure 9.26: Left: The average number of tracks from long-lived $\tilde{t}$ decays as a function of decay position in R_{xy}. The average number of tracks is computed using truth tracks which pass a basic acceptance requirement, shown in in black. In blue, truth tracks which are properly reconstructed, and in red, reconstructed tracks which have been included as part of the vertex. If no reconstructed vertex is found, the reconstructed vertex mass is set to zero. Right: The average mass for long-lived $\tilde{t}$ decays as a function of decay position in R_{xy}. The average mass is computed using truth tracks which pass a basic acceptance requirement in black, truth tracks which are properly reconstructed in blue, and reconstructed tracks which have been included as part of the vertex in red. If no reconstructed vertex is found, the reconstructed vertex mass is set to zero.

Figure 9.27 shows the fraction of all R-hadron decays which pass the acceptance criteria described

above as a function of the R-hadron decay position in R_{xy} and z. The vertex acceptance is reduced

for decays which occur close to the interaction point in R_{xy}, due to the requirement that vertices must

be at least 4 mm away from the pp-interaction point. The acceptance is also reduced for decays which

occur near the end of the fiducial volume in R_{xy} or z. This effect is because decays with large R_{xy} may

be out of acceptance in z, or vice versa.

The tracking efficiency, and efficiency for associating tracks to vertices both decrease as a function

of displacement in R_{xy}. It is important to understand how these losses in efficiency translate to the

efficiency for finding a multi-track displaced vertex with high mass. Figure 9.28 shows the efficiency

Figure 9.27: Left: The acceptance for evaluating the efficiency of reconstructing a displaced vertex with $m_{\mathrm{DV}} > 20\,\mathrm{GeV}$ and $n^{\mathrm{DV}}_{\mathrm{Tracks}} \geq 3$ in the analysis fiducial volume as a function of R_{xy}. Right: The acceptance for evaluating the efficiency of reconstructing a displaced vertex with $m_{\mathrm{DV}} > 20\,\mathrm{GeV}$ and $n^{\mathrm{DV}}_{\mathrm{Tracks}} \geq 3$ in the analysis fiducial volume as a function of z.

for finding a displaced vertex in the analysis fiducial volume ($R_{xy} < 300$ mm and $|z| < 300$ mm),

which is matched to a $\tilde{t}$ decay.

Figure 9.28: Left: The efficiency for reconstructing a displaced vertex with $m_{\mathrm{DV}} > 20\,\mathrm{GeV}$ and $n^{\mathrm{DV}}_{\mathrm{Tracks}} \geq 3$ in the fiducial volume of the analysis as a function of (left) R_{xy} and (right) z.

As expected, the efficiency for finding a vertex decreases as a function of displacement in R_{xy} as

well as in z. The maximal efficiency in R_{xy} is about 60%, in the region closest to the beam pipe. At displacements of $R_{xy} \approx 50$ mm and greater, this efficiency has reduced to about 10%.

Section 6.5.2 also discussed how the efficiency for reconstructing a secondary vertex increases with the number of charged particles produced in the long-lived particle decay. This result is due to the increased probability for reconstructed tracks, and the increased probability for associating those tracks to secondary vertices.

Figure 9.29 shows the fraction of all R-hadron decays in acceptance as a function of the number of truth tracks produced in the R-hadron decay and the resulting truth mass. The acceptance is slightly reduced for R-hadron decays which result in a small multiplicity truth tracks, because they may result in a low truth vertex mass, and vice versa.
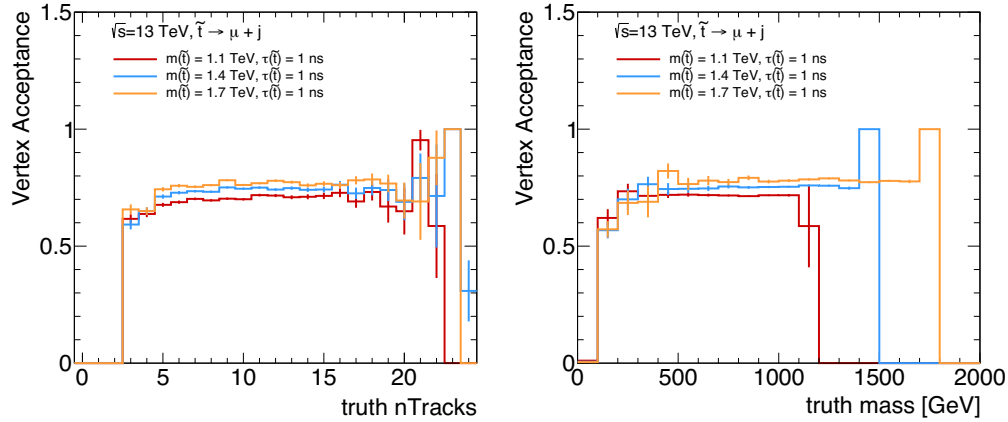
Figure 9.29: Left: The acceptance for evaluating the efficiency of reconstructing a displaced vertex with $m_{\mathrm{DV}} > 20$ GeV and $n_{\mathrm{Tracks}}^{\mathrm{DV}} \geq 3$ in the analysis fiducial volume as a functi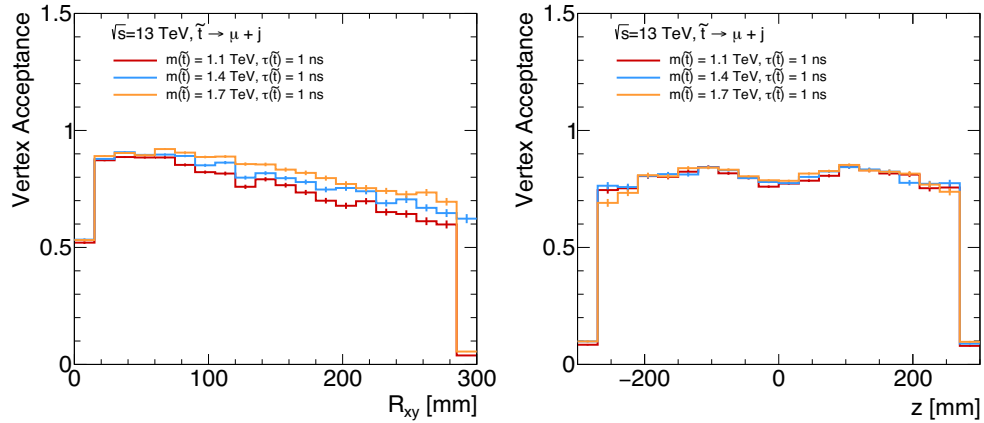on of the number of truth tracks in acceptance. Right: The acceptance for evaluating the efficiency of reconstructing a displaced vertex with $m_{\mathrm{DV}} > 20$ GeV and $n_{\mathrm{Tracks}}^{\mathrm{DV}} \geq 3$ in the analysis fiducial volume as a function of truth mass in acceptance.

Figure 9.30 shows how the efficiency for reconstructing a vertex from a $\tilde{t}$ decay changes as func-

tion of the number of truth tracks produced in the R-hadron decay and resulting truth vertex mass. Within uncertainties the vertex efficiency does not show any dependence on the number of tracks in acceptance or the truth mass.
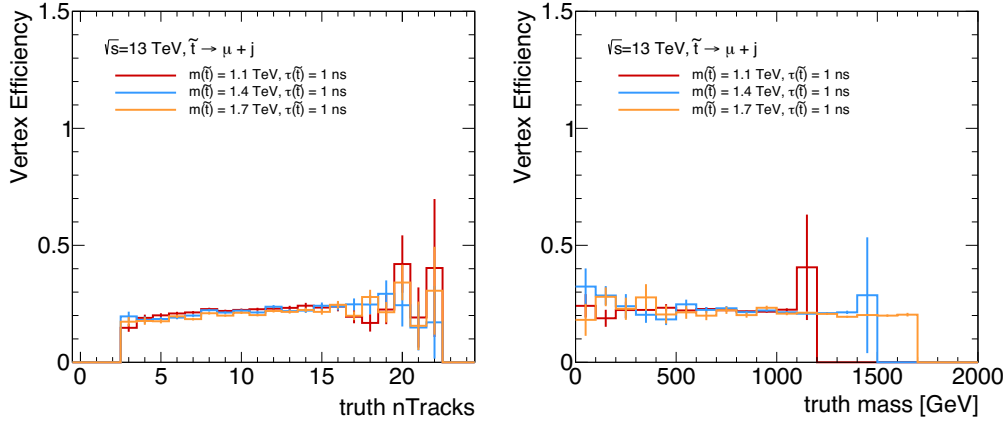
Figure 9.30: Left: The efficiency for reconstructing a displaced vertex with $m_{\mathrm{DV}} > 20$ GeV and $n_{\mathrm{Tracks}}^{\mathrm{DV}} \geq 3$ in the analysis fiducial 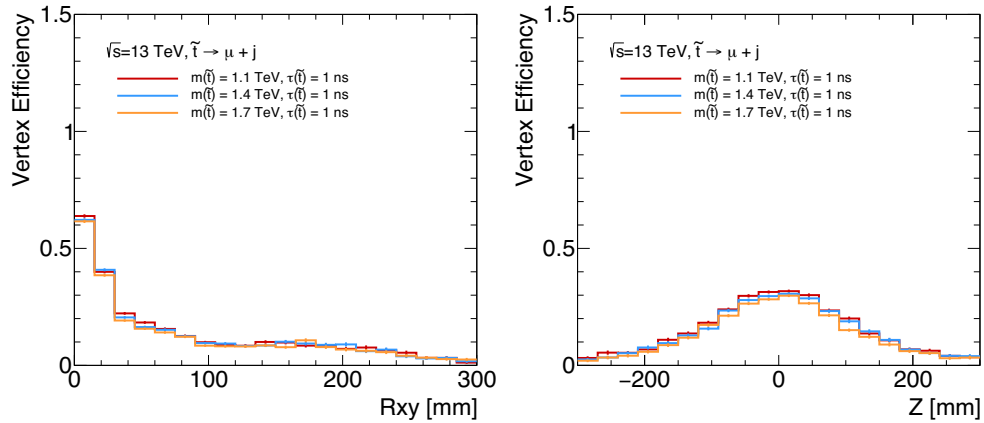volume as a function of the number of truth tracks in acceptance. Right: The efficiency for reconstructing a displaced vertex with $m_{\mathrm{DV}} > 20$ GeV and $n_{\mathrm{Tracks}}^{\mathrm{DV}} \geq 3$ in the analysis fiducial volume as a function of truth mass in acceptance.

IMPROVEMENTS DUE TO LARGE RADIUS TRACKING

For displaced vertices which are successfully reconstructed and matched to signal, it is important to understand how many of the tracks were reconstructed by the Large Radius Tracking algorithm.

Figure 9.31 shows the total number tracks associated to reconstructed vertices which are truth matched to a $\tilde{t}$ decay. Reconstructed vertices are additionally required to have at least three associated tracks, and a mass greater than 20 GeV. When considering $\tilde{t}$ particles with the same mass, fewer tracks are associated to displaced vertices for R-hadron decays with longer lifetimes. This behavior is expected

to the reduced tracking efficiency as a function of radial displacement.

Figure 9.31 also shows the number of vertex associated tracks which are reconstructed from Large Radius Tracking. Stop particles with longer lifetimes produce vertices with a larger number of Large Radius tracks. For stop R-hadrons with $\tau(\tilde{t}) = 0.01$ ns most secondary vertices have zero associated Large Radius tracks, while stop R-hadrons with $\tau(\tilde{t}) = 1$ ns result in secondary vertices which are likely to have at least one Large Radius Track.
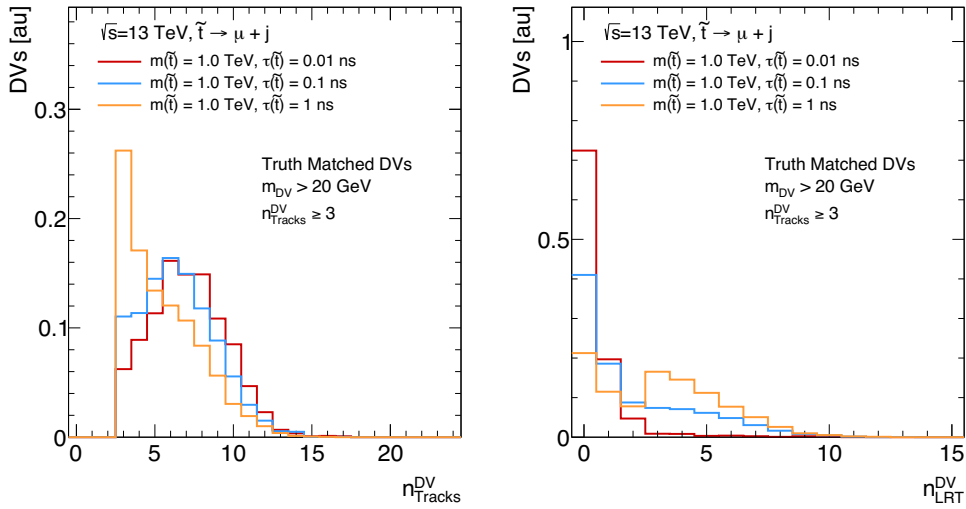
Figure 9.31: Left: The number of tracks associated to reconstructed vertices which are truth matched to a $\tilde{t}$ for three different $\tilde{t}$ lifetimes. Right: The number of tracks reconstructed with Large Radius Tracking, which are associated to reconstructed vertices that have been truth matched to a $\tilde{t}$, for three different $\tilde{t}$ lifetimes.

These results are expected because long-lived particles with longer lifetimes produced secondary vertices with decay positions at larger radii, and tracks which are produced at larger radii are more likely to be reconstructed with Large Radius tracking. Figure 9.32 shows the fraction of reconstructed and vertexed tracks from Large Radius Tracking as a function of the radial decay position of the $\tilde{t}$. For radii

smaller than $R_{xy} \approx 20$ mm, the majority of tracks associated to vertices are from standard ATLAS

tracking algorithms. For radii around $R_{xy} \approx 20$ mm, roughly half of tracks are from standard tracking

and half of tracks in vertices are from Large Radius Tracking. For radii around $R_{xy} \approx 140$, and larger,

nearly all tracks associated to vertices are from Large Radius tracking.
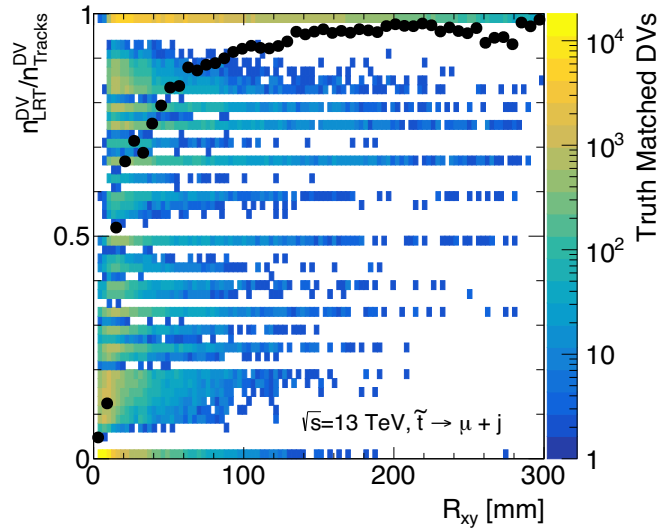
Figure 9.32: The fraction of tracks which are reconstructed with Large Radius Tracking, from reconstructed vertices which are truth matched to $\tilde{t}$ decays, shown as a function of $\tilde{t}$ decay position in R_{xy}. The average fraction of Large Radius Tracks per vertex is overlaid in black for each bin in R_{xy}.

9.6.3 VERTICES RECONSTRUCTED FROM FAKE TRACKS

Roughly 80% of the tracks reconstructed from Large Radius Tracking are algorithm fakes, recon-

structed from an accidental combination of hits. These fake tracks can randomly cross and be recon-

structed as displaced vertices. In order to study this effect, properties of reconstructed vertices which

are not matched to a stop R-hadron decay, *unmatched vertices*, are studied. These unmatched vertices

are compared to vertices which are successfully matched to stop R-hadron decay, or *truth matched vertices*.

Figure 9.33 compares the number of associated tracks and the reconstructed displaced vertex mass for truth matched and unmatched vertices. Unmatched vertices tend to have fewer associated tracks than truth matched vertices, because the probability of randomly crossing multiple tracks is low. Due to the fewer number of associated tracks, unmatched vertices also tend to have lower reconstructed mass than truth matched vertices.
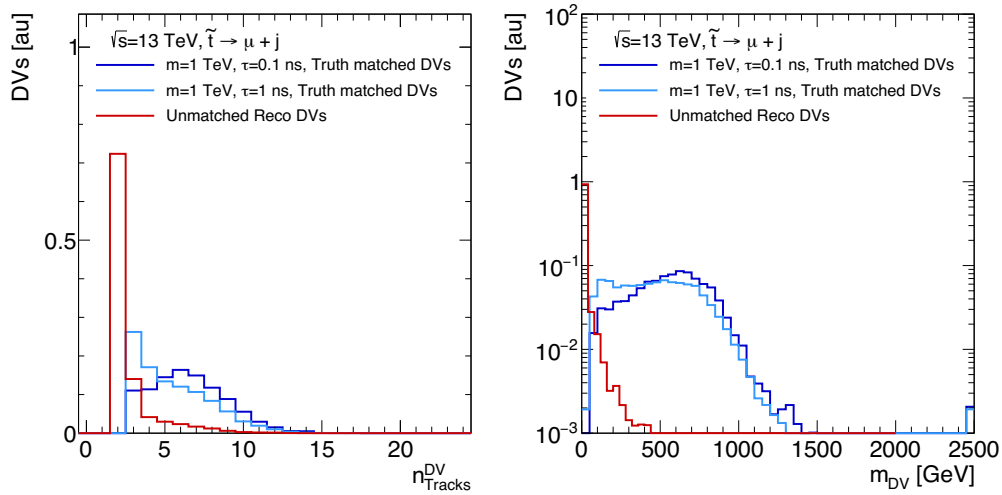
Figure 9.33: Left: Displaced vertex number of tracks. Shown for reconstructed vertices which have been matched to signal, as well as reconstructed vertices unmatched to any $\tilde{t}$ decay. Right: Displaced vertex mass. Shown for reconstructed vertices which have been matched to signal, as well as reconstructed vertices unmatched to any $\tilde{t}$ decay.

Figure 9.34 compares the decay position in R_{xy} and z for truth matched and unmatched displaced vertices. The radial position of truth matched vertices is consistent with that of a long-lived particle decay, and falls exponentially with increasing radii. In contrast, the radial position of unmatched dis-

placed vertices is roughly flat as a function of R_{xy}, with an increase in the number of displaced vertices located after the last layer of the Pixel detector (near $R_{xy} = 120$ mm). The reduced impact parameter resolution of tracks which do not have any associated Pixel hits means that these tracks are slightly more likely to be associated to a displaced vertex. Because the impact parameter resolution also degrades as a function of the longitudinal displacement, unmatched vertices also have a wider distribution in z than vertices which are matched to R-hadron decays.
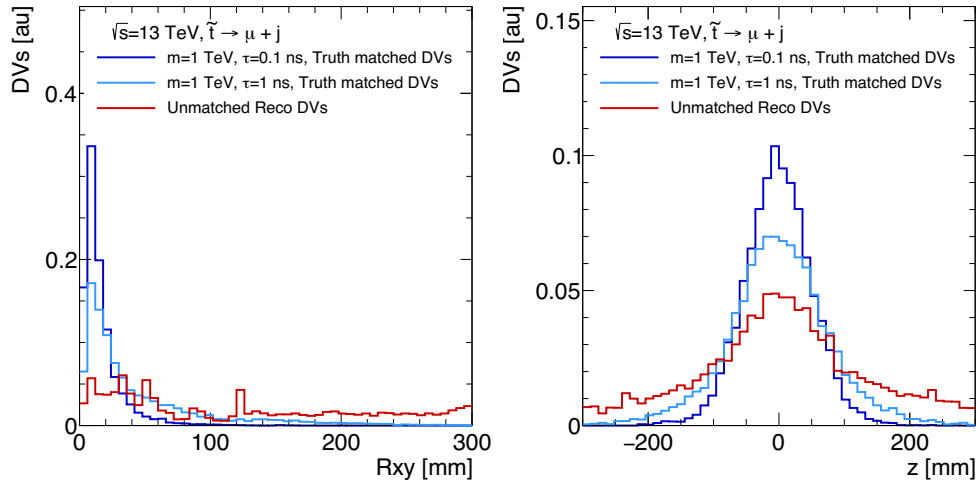
Figure 9.34: Left: Displaced vertex position in R_{xy}. Shown for reconstructed vertices which have been matched to signal, as well as reconstructed vertices unmatched to any $\tilde{t}$ decay. Right: Displaced vertex position in z. Shown for reconstructed vertices which have been matched to signal, as well as reconstructed vertices unmatched to any $\tilde{t}$ decay.

It is also important to understand the properties of tracks which are reconstructed as these unmatched displaced vertices. Figure 9.35 shows the number of Pixel and SCT hits for tracks which are associated to unmatched vertices, and compares these distributions to tracks which are associated to displaced vertices that are matched to a truth R-hadron decay. Tracks from unmatched displaced ver-

254

tices tend to have fewer Pixel and SCT hits, in line with the hypothesis that these tracks are produced

from an accidental combination of hits.
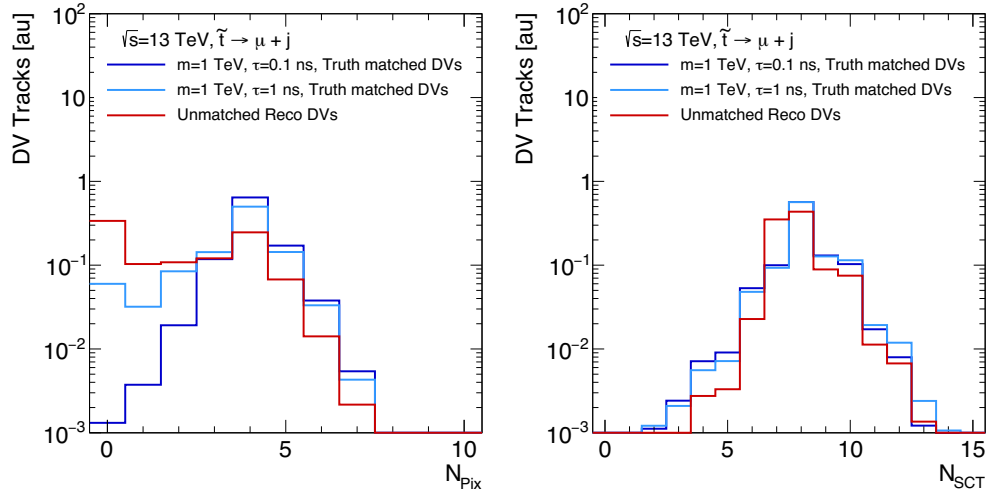
Figure 9.35: Left: The number of Pixel hits on track. Shown for tracks from reconstructed vertices which have been matched to signal, as well as tracks from reconstructed vertices unmatched to any $\tilde{t}$ decay. Right: The number of SCT hits on track. Shown for tracks from reconstructed vertices which have been matched to signal, as well as tracks from reconstructed vertices unmatched to any $\tilde{t}$ decay.

Figure 9.36 compares the number of TRT hits on track, and the track transverse momentum p_T

for tracks from unmatched and truth matched displaced vertices. Tracks from unmatched displaced

vertices tend to have a similar number of TRT hits as tracks from truth matched displaced vertices.

However, there is a jump in the number of TRT hits near 20 associated hits. This jump is due to

the requirement that selected tracks with $p_T < 25$ GeV and $|\eta| < 1.7$ are required to have at least

20 TRT hits on track. This jump in the number of TRT hits appears in unmatched displaced vertex

tracks because these tracks have lower transverse momentum than tracks associated to truth matched

displaced vertices.
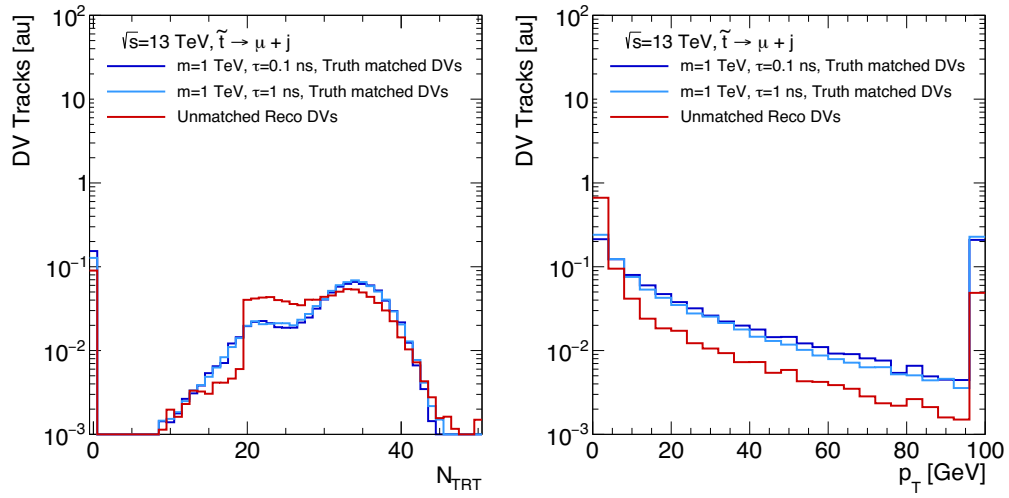
Figure 9.36: Left: The number of TRT hits on track. Shown for tracks from reconstructed vertices which have been matched to signal, as well as tracks from reconstructed vertices unmatched to any $\tilde{t}$ decay. Right: Track transverse momentum, p_T [GeV]. Shown for tracks from reconstructed vertices which have been matched to signal, as well as tracks from reconstructed vertices unmatched to any $\tilde{t}$ decay.

Figure 9.36 compares the transverse and longitudinal impact parameter for tracks from unmatched and truth matched displaced vertices. Unmatched displaced vertices tend to have associated tracks with larger impact parameters than tracks associated to truth matched displaced vertices, in line with previous observations.
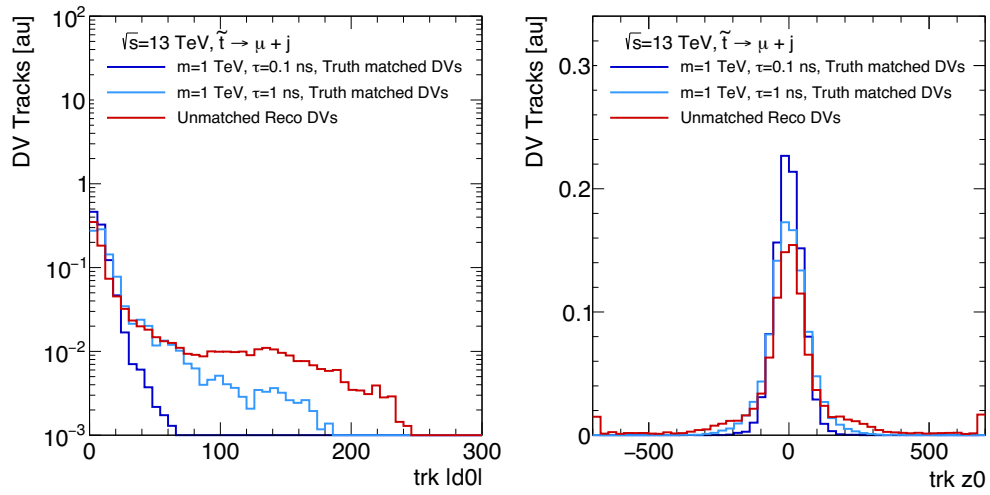
Figure 9.37: Left: Track transverse impact parameter $|d_0|$ [mm]. Shown for tracks from reconstructed vertices which have been matched to signal, as well as tracks from reconstructed vertices unmatched to any $\tilde{t}$ decay. Right: Track longitudinal impact parameter. Shown for tracks from reconstructed vertices which have been matched to signal, as well as tracks from reconstructed vertices unmatched to any $\tilde{t}$ decay.

10

Background Estimation

As discussed in the previous section, there are three major processes which result in reconstructed displaced muons that can contribute to this analysis: cosmic muons, algorithm fakes, and muons from Standard Model processes, such as in-flight decays of pions, kaons, and heavy-flavor hadrons.

Events which have a preselected muon from a cosmic ray event, algorithm fake, or decay in flight may also have a high-mass and high-$n_{\text{Tracks}}^{\text{DV}}$ displaced vertex. The processes which result in a high mass and high $n_{\text{Tracks}}^{\text{DV}}$ displaced vertex are expected to be unrelated to the process which resulted in a displaced muon. The three major sources of multi-track displaced vertices are described below.

- *Hadronic interactions*: Particles which interact with the detector also produce secondary vertices. These secondary vertices can have high invariant mass and have many associated tracks, but most often occur in regions of material. The contribution of hadronic interactions is drastically reduced by the material veto.

- *Randomly crossing tracks*: A random track which crosses a low-mass, low-$n_{\text{Tracks}}^{\text{DV}}$ displaced vertex might be reconstructed as part of the vertex. Reconstructing a vertex with an additional track both promotes the vertex to a higher track multiplicity and increases the mass of the vertex, especially if the randomly crossing track crosses the displaced vertex at a large angle.

- *Merged vertices*: One key step in secondary vertex reconstruction is to merge vertices which are nearby. If two low-mass, and low-$n_{\text{Tracks}}^{\text{DV}}$ vertices from different sources are merged, a single high-mass, high-$n_{\text{Tracks}}^{\text{DV}}$ vertex is formed.

A *transfer factor* inspired method is used to estimate background contributions from cosmic muons, fake muons, and muons from heavy-flavor decays to the final signal regions. This technique hinges on the assumption that the features of the muon used to veto these background muons are uncorrelated with the properties of displaced vertices reconstructed in the event. This assumption is validated by comparing background predictions to observed data in dedicated validation regions.

The following sections begin by providing an overview of the method used to estimate contributions from muon backgrounds. This overview is followed by a detailed description of the estimation for each background, as well as validations performed to ensure the method performs as expected.

10.1 Overview of Control, Validation, and Signal Regions

A schematic which describes the various muon selections and displaced-vertex selections used in the background estimation can be found in Figure 10.1. Two axes are defined, which represent properties of the leading preselected muon (y-axis) and the displaced vertices in the event (x-axis).

The y-axis defines four exclusive categories of events based on the leading preselected muon in the event. These categories include three Control Region (CR)s, and one region where muons satisfy the full muon selection.
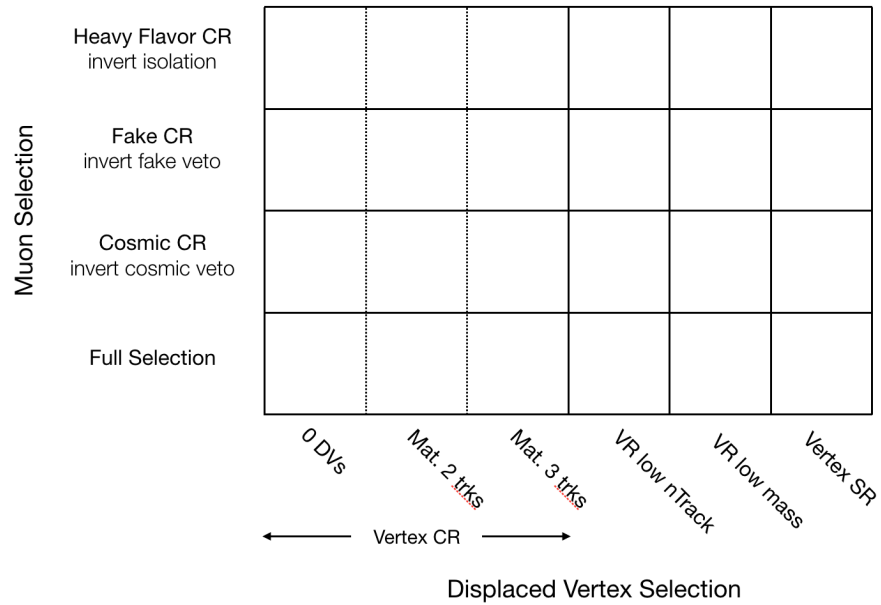
Figure 10.1: Skematic of event selections used to study background processes

- Heavy-Flavor CR: Events in which the leading preselected muon passes all criteria in the full muon selection, except for isolation. The isolation requirement is inverted, and this category is dominated by events with muons from Standard Model processes such as pion, kaon, and heavy-flavor decays.

- Fake-Muon CR: Events in which the leading preselected muon passes all criteria in the full muon selection, except for the veto for fake muons. The fake muon veto is inverted, and this category is dominated by events with algorithm fake muons.

- Cosmic CR: Events in which the leading preselected muon passes the full muon selection, except for the cosmic veto. The cosmic veto is inverted, and this category is dominated by events with cosmic muons.

- Full Selection: Events in which the leading preselected muon passes the full muon selection. This category is most sensitive to signal.

The x-axis defines six exclusive categories of events based on the displaced vertices in an event. Each

subsequent category is increasingly sensitive to displaced vertices from signal. The first three categories are collectively referred to as the Displaced Vertex Control Region (DV CR). The next two categories are regions used to validate the background estimation method, or Validation Region (VR)s, and the final category includes events which have at least one displaced vertex that passes the full selection. The final category also serves as a Signal Region (SR).

- Vertex CR: Events with no preselected displaced vertices. This category is expected to be dominated by background. This control region can be further separated into three subcategories, which will be useful for evaluating systematic uncertainties associated with the transfer factor measurement.

  - 0 DVs: Events with no vertices satisfying $R_{xy} < 300\,\text{mm}$, $|Z| < 300\,\text{mm}$, $\chi^2/N_{DoF} < 5$, and 4 mm from any PV in the event.

  - Mat. 2 trk: Events with at least one displaced vertex located inside material, as indicated by the material map, that has exactly 2 tracks.

  - Mat. 3 trk: Events with at least one displaced vertex located inside material, as indicated by the material map, that has ≥ 3 tracks.

- VR low $n_{\text{Tracks}}^{\text{DV}}$: Events with a displaced vertex that passes preselection, in which the highest track multiplicity vertex has $n_{\text{Tracks}}^{\text{DV}} = 2$.

- VR low m_{DV}: Events with a displaced vertex that passes preselection, and has at least 3 tracks and $m_{\text{DV}} < 20\,\text{GeV}$. No displaced vertices in the event pass the full displaced vertex selection.

- Vertex SR: Events which have at least one displaced vertex passing the full selection. This includes all preselection requirements, $n_{\text{Tracks}}^{\text{DV}} \geq 3$ and $m_{\text{DV}} > 20\,\text{GeV}$

10.2   Overview of Transfer Factor Method

The general idea behind the transfer factor background estimation method is summarized below, using the cosmic background as an example. Four regions are defined, labeled A, B, C, and D. Regions A and B have *signal-like* displaced vertices, while C and D have no preselected displaced vertices. Regions A and C have *signal-like* muons, while B, and D have *cosmic-like* muons. These regions are labeled in Figure 10.2, and described in more detail below.

- A: Events in which the leading preselected muon passes the full muon selection, and at least one displaced vertex passes the full DV selection. This region corresponds to the bottom right square in Figure 10.1.

- B: Events in which the leading preselected muon passes all criteria in the full muon selection, but fails the cosmic veto. The event also has at least one displaced vertex which pases the full DV selection. This region corresponds to events in the Cosmic CR and Vertex SR.

- C: Events in which the leading preselected muon passes the full muon selection, but has no displaced vertices which pass preselection. This region correspond to events in the muon Full Selection category and the Vertex CR.

- D: Events in which the leading preselected muon passes all criteria in the full muon selection, but fails the cosmic veto. Events in this region also have no displaced vertices which pass preselection. Events in this category correspond to the Cosmic CR and Vertex CR.

The first step in this background estimation is to measure a transfer factor. In the case of the cosmic background, this transfer factor, TF, estimates the ratio of cosmic muons which pass the cosmic veto, to that of cosmic muons which which fail the cosmic veto (TF = N_C/N_D). This transfer factor must be measured in a region which is pure in the background of interest, and expected to be free of events from signal. Because events in Regions C and D do not have any displaced vertices which pass preselection, they should be sufficiently free of signal to measure such a transfer factor.
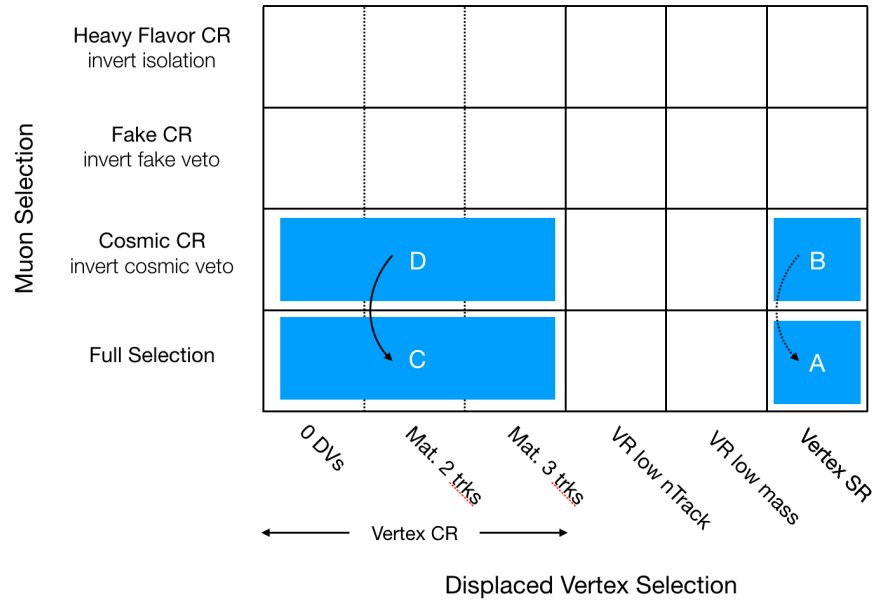
Figure 10.2: Schematic of the transfer factor background estimation for cosmic background. Important regions are indicated in blue and labeled in white. The transfer factor is measured using event counts in Regions C and D (solid black line), and applied to Region B to predict the background contribution to Region A (dotted line).

Once the transfer factor is measured, it can be used to estimate the expected contribution of cosmic events to the final signal region. One key assumption in the this background estimation method is that the ratio of cosmic muons which pass the cosmic veto to those which fail the veto does not change as a function of the displaced vertex properties of the event. This assumption means the ratio N_A/N_B should be equivalent to N_C/N_D for cosmic muons.

If this assumption holds true, the transfer factor can be applied to events which have a cosmic-like muon, but a signal-like displaced vertex (i.e. Region B), in order to estimate the number of cosmic events in Region A. The expected cosmic muon contribution to the final Signal Region is defined as $N_A = N_B \cdot N_C/N_D$.

This method can be validated by applying the same transfer factor to regions with displaced vertices that are consistent with background, and have a cosmic-like muon.

For completeness, the total expected background in the signal region A in sample s is:

$$N_A[s] = \sum_k N_{B_k}[s] \times \frac{N_{C_k}^{k,s'(k)}}{N_{D_k}^{k,s'(k)}} \tag{10.1}$$

where N is the number of events, k is cosmics, fakes, or isolation, s' differs based on the particular background component, and regions are denoted by A, B, C, D.

10.3 Transfer Factors

The first step in the background estimation method is finding regions in which to measure the associated transfer factors. These regions must be dominated by a single background. One natural way to separate backgrounds is to use the E_T^{miss} and the Muon triggered samples as two separate regions. However, there are three transfer factors which must be measured, and only two different samples.

Cosmic muons are the dominant background in the Muon triggered sample, with a sub-dominant contribution of heavy-flavor muons, and a negligible contribution of fake muons. Muons from algorithm fakes and heavy-flavor decays dominate the E_T^{miss} selection, where cosmic muons are a negligible background. Thus far, it is clear that events without any preselected displaced vertices in the Muon triggered sample can be used to measure the cosmic transfer factor, while the E_T^{miss} triggered sample can be used used to measure fake and heavy-flavor transfer factors.

It is possible to use the muon's transverse impact parameter to separate muons from heavy-flavor decays and fakes. Figure 10.3 shows the transverse impact parameter, $|d_0|$, for muons in the Heavy-Flavor CR and Fake-Muon CR of the E_T^{miss} triggered sample. Events are required to have no preselected displaced vertices. Muons from heavy-flavor decays tend to have smaller transverse impact parameters, with a tail that extends to a few millimeters, which is expected given the lifetime of b-hadrons. Muons which are reconstructed from algorithm fakes have a relatively flat transverse impact parameter distribution. This effect is expected because algorithm fakes are combined muons reconstructed with fake Large Radius Tracks, which tend to produce a flat distribution in $|d_0|$.
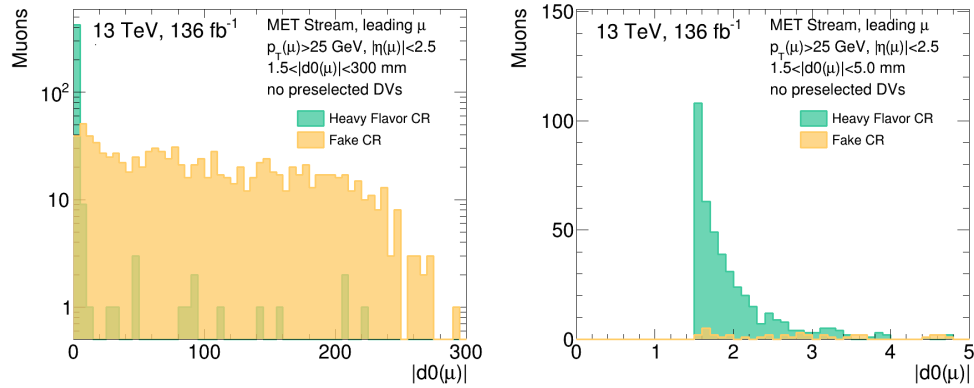
Figure 10.3: Transverse impact parameter for muons in the E_T^{miss} triggered sample Fake-Muon and Heavy-Flavor Control Regions. The minimum impact parameter is relaxed from $|d_0| > 2.0$ mm to $|d_0| > 1.5$ mm in order to increase the statistics available for measuring the Heavy-Flavor Transfer Factor. Events are required to have no preselected displaced vertices.

The following requirements were designed to separate fake-muons and muons from heavy-flavor decays. Heavy-flavor muons selected by requiring muons have $1.5 < |d_0| < 3$ mm. In contrast, fake muons are selected by requiring $|d_0| > 5$ mm. A similar requirement on the muon transverse

impact parameter, of $|d_0| > 5$ mm, is also applied to the muons when measuring the cosmic muon transfer factor. This requirement ensures that muons from heavy-flavor decays do not contribute to the cosmic transfer factor measurement.

10.3.1 Cosmic Transfer Factor

As described above, the cosmic transfer factor is evaluated in the Muon triggered sample, using muons which pass the following selections.

- Selection applied to all muons: leading preselected muon with $p_T > 62$ GeV, $|\eta| < 1.05$, $|d_0| > 5.0$ mm, trigger matched, pass fake-muon veto, pass isolation
- Numerator: muon pass cosmic veto
- Denominator: muons rejected by cosmic veto

Events used to evaluate the nominal cosmic transfer factor must also have zero preselected displaced vertices. The nominal transfer factor is evaluated using events in the displaced vertex CR. In order to evaluate a systematic uncertainty, the transfer factor is separately evaluated using the 0 DV and the Mat. 2 trk displaced vertex categories and compared to the nominal estimate. From these two separate measurements, the largest variation from the nominal transfer factor is taken as a systematic designed to account for possible correlations of the transfer factor with displaced vertex properties. The Mat. 3 trk region is not considered for evaluating a systematic uncertainty, because the heavy-flavor background is predicted to dominate this region by orthogonal background estimates.

An additional source of uncertainty is evaluated to account for the assumption that a transfer factor evaluated with muons that have $|d_0| > 5.0$ mm, can be extrapolated to muons with smaller $|d_0|$. This

uncertainty is estimated by evaluating the transfer factor separately for muons with $5 < |d_0| < 100$ mm and $100 < |d_0| < 300$ mm. Events with zero preselected displaced vertices are used to evaluate these two transfer factors. The binning used to evaluate these two transfer factors was optimized to minimize the statistical uncertainty on each measurement. From these two separate measurements, the largest variation from the nominal transfer factor is taken as a systematic.

The two separate sources of systematic uncertainty (variations of DV requirements and variations of muon requirements) are assumed to be uncorrelated, and added in quadrature to estimate the total systematic uncertainty.

10.3.2 Fake Transfer Factor

The fake transfer factor is evaluated in the $E_\mathrm{T}^\mathrm{miss}$ triggered sample, using muons which pass the following selections.

- Selection applied to all muons: leading preselected muon with $p_\mathrm{T} > 25$ GeV, $|\eta| < 2.5$, $|d_0| > 5.0$ mm, pass cosmic veto, pass isolation

- Numerator: muons pass fake-muon veto

- Denominator: muons rejected by fake-muon veto

Events used to evaluate the nominal fake-muon transfer factor must also have zero preselected displaced vertices. The nominal transfer factor is evaluated using events in the displaced vertex CR. In order to evaluate a systematic uncertainty, the transfer factor is separately evaluated using the three displaced vertex CR sub-regions, and compared to the nominal estimate. From these separate measurements, the largest variation from the nominal transfer factor is taken as the systematic uncertainty.

This uncertainty is designed to account for any possible correlation of the fake-muon transfer factor with properties of vertices in the event. Events with more collision activity could result in more fake muons and more displaced vertices from random crossings or hadronic interactions.

An additional source of uncertainty is evaluated to account for the assumption that a transfer factor evaluated with muons that have $|d_0| > 5.0$ mm can be extrapolated to muons with smaller $|d_0|$. This uncertainty is estimated by evaluating the transfer factor separately for muons with $5 < |d_0| < 100$ mm and $100 < |d_0| < 300$ mm. Events with zero preselected displaced vertices are used to evaluate these two transfer factors. The binning used to evaluate these two transfer factors was optimized to minimize the statistical uncertainty on each measurement. From these two separate measurements, the largest variation from the nominal transfer factor is taken as a systematic.

The two separate sources of systematic uncertainty (variations of DV requirements and variations of muon requirements) are assumed to be uncorrelated, and added in quadrature to estimate the total systematic uncertainty.

10.3.3 Heavy Flavor Transfer Factor

The heavy-flavor transfer factor is evaluated in the E_T^{miss} triggered sample, using muons which pass the following selections.

- Selection applied to all muons: leading preselected muon with $p_T > 25$ GeV, $|\eta| < 2.5$, $1.5 < |d_0| < 3.0$ mm, pass fake-muon veto, pass cosmic veto

- Numerator: muons pass isolation criteria

- Denominator: muons rejected by isolation criteria

Events used to evaluate the nominal heavy-flavor transfer factor must also have zero preselected displaced vertices. The nominal transfer factor is evaluated using events in displaced vertex CR. In order to evaluate a systematic uncertainty, the transfer factor is separately evaluated using the three different displaced vertex CR sub-regions, and compared to the nominal estimate. This uncertainty is designed to account for any possible correlation of the heavy-flavor transfer factor with properties of vertices in the event. From these separate measurements, the largest variation from the nominal transfer factor is taken as the systematic uncertainty.

A second source of uncertainty is evaluated to account for the assumption that a transfer factor evaluated with muons that have $1.5 < |d_0| < 3.0$ mm can be extrapolated to muons with larger $|d_0|$. This uncertainty is estimated by evaluating the transfer factor separately for muons with $1.5 < |d_0| < 1.7$ mm and $1.7 < |d_0| < 3.0$ mm. Events without any preselected displaced vertices are used to evaluate these two transfer factors. As was done in the fake and cosmic transfer factor measurements, the binning used to evaluate these two transfer factors was optimized to minimize the statistical uncertainty on each measurement. From these two separate measurements, the largest variation from the nominal transfer factor is taken as a systematic.

The two separate sources of systematic uncertainty (variations of DV requirements and variations of muon requirements) are assumed to be uncorrelated, and added in quadrature to estimate the total systematic uncertainty.

10.3.4 Transfer factor results

Table 10.1 shows the measured transfer factors for the cosmic, fake-muon, and heavy-flavor backgrounds. The nominal transfer factor is shown for each background, along with the statistical and systematic uncertainty of each measurement.

Cosmic muons have the smallest transfer factor, followed by fake muons, and muons from heavy-flavor decays. The cosmic veto and fake-muon veto do an excellent job of rejecting each background to less than 1% of their original values. In contrast, nearly 10% of heavy-flavor muons pass the isolation requirement.

Because cosmic muons are the largest background for this analysis, the cosmic transfer factor has the smallest statistical uncertainty. The cosmic transfer factor has a total systematic uncertainty of 12%. In contrast, the fake-muon transfer factor has a statistical uncertainty of approximately 30% and a systematic uncertainty of approximately 50%. The heavy-flavor transfer factor has a statistical uncertainty of roughly 20%, and a systematic uncertainty of approximately 35%.

10.4 Validation of Background Estimation

These transfer factors are then used to estimate the number of expected events from each background to the Signal Region. In order to validate the performance of this method, background predictions are made for all six displaced vertex categories, and these predictions are compared to the observed number of events in data.

Table 10.1: Measured transfer factors

Cosmic Transfer Factor Measurement Muon Trigger, cluster-based $E_T^{miss} < 180$ GeV Zero preselected DVs, $|d_0(\mu)| > 5.0$ mm	
Variation	Transfer Factor ($\times 10^{-3}$)
Nominal	4.0 ± 0.2 (stat.)
Zero DVs	3.9 ± 0.2 (stat.)
Material, two tracks	3.9 ± 0.6 (stat.)
Low d_0	3.5 ± 0.3 (stat.)
High d_0	4.5 ± 0.3 (stat.)
TF =	4.0 ± 0.2 (stat.) ± 0.5 (sys.)
Fake Transfer Factor Measurement E_T^{miss} Trigger, cluster-based $E_T^{miss} > 180$ GeV Zero preselected DVs, $|d_0(\mu)| > 5.0$ mm	
Variation	Transfer Factor ($\times 10^{-2}$)
Nominal	1.0 ± 0.3 (stat.)
Zero DVs	0.7 ± 0.4 (stat.)
Material, two tracks	1.4 ± 0.6 (stat.)
Material, three tracks	1.2 ± 1.2 (stat.)
Low d_0	1.2 ± 0.5 (stat.)
High d_0	0.8 ± 0.4 (stat.)
TF =	1.0 ± 0.3 (stat.) ± 0.5 (sys.)
Heavy Flavor Transfer Factor Measurement E_T^{miss} Trigger, cluster-based $E_T^{miss} > 180$ GeV Zero preselected DVs, $1.5 < |d_0(\mu)| < 3.0$ mm	
Variation	Transfer Factor ($\times 10^{-2}$)
Nominal	9.1 ± 1.6 (stat.)
Zero DVs	10.0 ± 2.2 (stat.)
Material, two tracks	6.6 ± 2.3 (stat.)
Material, three tracks	12.5 ± 5.9 (stat.)
Low d_0	7.0 ± 2.1 (stat.)
High d_0	10.7 ± 2.3 (stat.)
TF =	9.1 ± 1.6 (stat.) ± 4.0 (sys.)

10.4.1 E_T^{miss} selection Results

Table 10.2 shows the number of events observed in each muon event category and the six displaced vertex categories for the E_T^{miss} triggered sample.

Table 10.2: E_T^{miss} triggered sample Control Regions yields

DV Selection	Cosmic CR	Fake CR	HeavyFlavor CR	Nominal
No DVs	83	437	92	19
Mat. 2 Track	14	268	71	10
Mat. 3 Track	0	61	18	3
VR low nTrack	8	849	169	22
VR low mass	1	172	34	4
DV SR	0	16	3	0

The number of observed events in the three muon Control Regions are then scaled by the relevant transfer factor. Table 10.3 shows the predicted contribution of each muon background to the six displaced vertex categories. The total predicted background is compared to the observed number of events in data.

In the E_T^{miss} triggered sample, the total background is expected to be less than one event. The dominant background is due to muons from heavy-flavor decays, followed by a subdominant contribution of fake muons. The contribution of cosmic muons to the E_T^{miss} sample is expected to be negligible. The total statistical uncertainty on the background is 37%, while the systematic uncertainty is 37%. The total background prediction for the E_T^{miss} triggered Signal Region is $0.43 \pm 0.16 \pm 0.16$ events.

Figure 10.4 shows the number of predicted events in the E_T^{miss} Triggered sample, separated by Validation Region. Good agreement between the predicted and observed number of events is observed

Table 10.3: Background Estimation for E_T^{miss} Triggered Sample

DV Selection	Background	Predicted Events $\pm$ stat. $\pm$ sys.	Observed Events
No DVs	Total Pred.	$13.11 \pm 0.90 \pm 4.64$	19
	Cosmic	$0.33 \pm 0.04 \pm 0.05$	
	Fake	$4.41 \pm 0.21 \pm 2.45$	
	Heavy Flavor	$8.36 \pm 0.87 \pm 3.95$	
Mat. 2 Track	Total Pred.	$9.22 \pm 0.78 \pm 3.40$	10
	Cosmic	$0.06 \pm 0.01 \pm 0.01$	
	Fake	$2.71 \pm 0.17 \pm 1.50$	
	Heavy Flavor	$6.45 \pm 0.77 \pm 3.05$	
Mat. 3 Track	Total Pred.	$2.25 \pm 0.39 \pm 0.84$	3
	Cosmic	$0.00 \pm 0.00 \pm 0.00$	
	Fake	$0.62 \pm 0.08 \pm 0.34$	
	Heavy Flavor	$1.64 \pm 0.39 \pm 0.77$	
VR low nTrack	Total Pred.	$23.97 \pm 1.22 \pm 8.67$	22
	Cosmic	$0.03 \pm 0.01 \pm 0.00$	
	Fake	$8.57 \pm 0.29 \pm 4.75$	
	Heavy Flavor	$15.36 \pm 1.18 \pm 7.25$	
VR low mass	Total Pred.	$4.83 \pm 0.55 \pm 1.75$	4
	Cosmic	$0.00 \pm 0.00 \pm 0.00$	
	Fake	$1.74 \pm 0.13 \pm 0.96$	
	Heavy Flavor	$3.09 \pm 0.53 \pm 1.46$	
DV SR	Total Pred.	$0.43 \pm 0.16 \pm 0.16$	0
	Cosmic	$0.00 \pm 0.00 \pm 0.00$	
	Fake	$0.16 \pm 0.04 \pm 0.09$	
	Heavy Flavor	$0.27 \pm 0.16 \pm 0.13$	

within uncertainties.

10.4.2 MUON TRIGGERED SAMPLE RESULTS

Table 10.4 shows the number of events observed in each muon event category and the six displaced vertex categories for the Muon selection.

Figure 10.4: Background predicted and observed events in E_T^{miss} triggered sample Validation Regions are shown in the top panel. The bottom panel shows the ratio of observed events to the total background prediction. The error band shows the total uncertainty of the background prediction, which includes the statistical and systematic uncertainties added in quadrature [1].

Table 10.4: Muon triggered sample Control Regions yields

DV Selection	Cosmic CR	Fake CR	HeavyFlavor CR	Nominal
No DVs	78230	144	92	291
Mat. 2 Track	10629	49	45	46
Mat. 3 Track	992	8	29	11
VR low nTrack	16143	103	135	92
VR low mass	1325	11	35	11
DV SR	376	1	4	1

The number of observed events in each control region is then scaled by the relevant transfer factor.

Table 10.5 shows the predicted contribution of each muon background, to the six displaced vertex

categories. The total predicted background is compared to the observed number of events in data.

The total background prediction for the Muon selection Signal Region is $1.88 \pm 0.20 \pm 0.28$ events.

Table 10.5: Background Estimation for Muon Triggered Sample

DV Selection	Background	Predicted Events $\pm$ stat. $\pm$ sys.	Observed Events
No DVs	Total Pred.	$322.74 \pm 1.42 \pm 47.11$	291
	Cosmic	$312.92 \pm 1.12 \pm 46.94$	
	Fake	$1.45 \pm 0.12 \pm 0.81$	
	Heavy Flavor	$8.36 \pm 0.87 \pm 3.95$	
Mat. 2 Track	Total Pred.	$47.10 \pm 0.74 \pm 6.67$	46
	Cosmic	$42.52 \pm 0.41 \pm 6.38$	
	Fake	$0.49 \pm 0.07 \pm 0.27$	
	Heavy Flavor	$4.09 \pm 0.61 \pm 1.93$	
Mat. 3 Track	Total Pred.	$6.68 \pm 0.51 \pm 1.38$	11
	Cosmic	$3.97 \pm 0.13 \pm 0.60$	
	Fake	$0.08 \pm 0.03 \pm 0.04$	
	Heavy Flavor	$2.64 \pm 0.49 \pm 1.24$	
VR low nTrack	Total Pred.	$77.88 \pm 1.18 \pm 11.30$	92
	Cosmic	$64.57 \pm 0.51 \pm 9.69$	
	Fake	$1.04 \pm 0.10 \pm 0.58$	
	Heavy Flavor	$12.27 \pm 1.06 \pm 5.79$	
VR low mass	Total Pred.	$8.59 \pm 0.56 \pm 1.70$	11
	Cosmic	$5.30 \pm 0.15 \pm 0.79$	
	Fake	$0.11 \pm 0.03 \pm 0.06$	
	Heavy Flavor	$3.18 \pm 0.54 \pm 1.50$	
DV SR	Total Pred.	$1.88 \pm 0.20 \pm 0.28$	1
	Cosmic	$1.50 \pm 0.08 \pm 0.23$	
	Fake	$0.01 \pm 0.01 \pm 0.01$	
	Heavy Flavor	$0.36 \pm 0.18 \pm 0.17$	

Figure 10.5 also shows the number of predicted events in the Muon triggered sample, separated by displaced vertex category. Good agreement between the predicted and observed number of events is observed within statistical uncertainties.
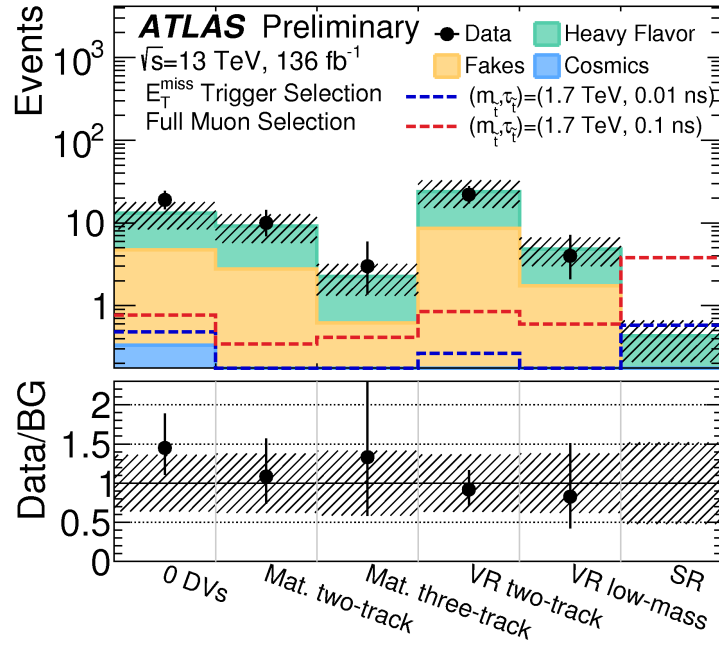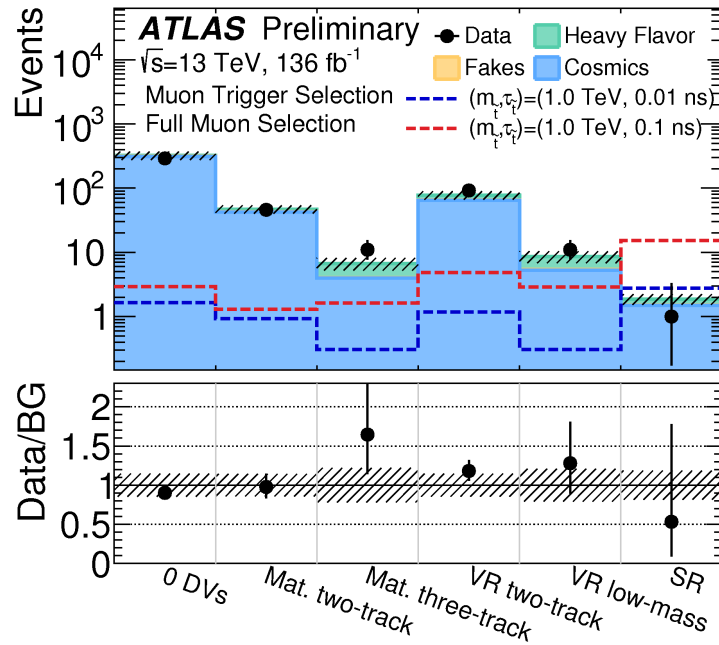
Figure 10.5: Background predictions and observed events in Muon triggered sample Validation Regions are shown in the top panel. The bottom panel shows the ratio of observed events to the total background prediction. The error band shows the total uncertainty of the background prediction, which includes the statistical and systematic uncertainties added in quadrature [1].

In the Muon triggered sample Signal Region, the total background is expected to be nearly two events. The dominant background is from cosmic muons, followed by a sub-dominant contribution of heavy-flavor muons. The contribution of fake muons to the Muon triggered sample is negligible in comparison. The statistical uncertainty on the total predicted background is 10% while the systematic uncertainty is 14%.

11

Signal Systematics

This section discusses some of the corrections and systematic uncertainties that are applied to the signal samples used in this analysis. Corrections to Monte Carlo simulated signals are made to ensure that the pile-up profile in MC matches that of the data, and that the muon trigger and reconstruction efficiency in MC also matches that of the data. In addition to these corrections, uncertainties are applied in order account how possible mis-modeling in Monte Carlo could affect the predicted signal efficiency. These uncertainties are evaluated for the non-standard reconstruction used in tracking and vertex reconstruction, the use of the $E_\mathrm{T}^\mathrm{miss}$ trigger to collect events with high momentum muons and cluster-based $E_\mathrm{T}^\mathrm{miss}$, how the muon trigger and reconstruction efficiency might change as a function of the muon's transverse impact parameter, and how the modeling of initial state and final state radiation could affect the event's cluster-based $E_\mathrm{T}^\mathrm{miss}$ distribution.

Standard ATLAS uncertainties are also evaluated but not discussed in detail in this thesis. These uncertainties are applied to muons and jets, the pile-up correction procedure, and the luminosity measurement. A detailed discussion of these uncertainties can be found in Reference [2].

A summary of systematic uncertainties on the overall signal selection efficiency can be found in Table 11.1. When a single value is given for an uncertainty, that uncertainty is applied to all stop signal masses and lifetimes. When a range is shown, different values for the uncertainty are applied to different stop masses and lifetimes, and the range indicates the smallest and largest values for that uncertainty. The largest source of systematic uncertainty on the signal selection efficiency is due to the Large Radius Tracking efficiency.

Table 11.1: Summary of signal systematic uncertainties for long-lived top squark model.

Systematic Uncertainty Source	Selection Efficiency Uncertainty [%]
Tracking and vertexing	$14.5 - 15.4$
Muon displacement	$10 - 11.8$
Muon reconstruction	$(0.01 - 0.7) \oplus (0.9 - 4.0)$
Radiation model	3
Pile-up distribution	$0.37 - 2.2$
Jet measurement	2.1
Integrated luminosity of dataset	1.7
$E_{\mathrm{T}}^{\mathrm{miss}}$ trigger efficiency	< 0.2

11.1 Large Radius Tracking and Vertexing

The effect of track reconstruction efficiency on vertex yields is estimated with a method used by several previous ATLAS searches for events with multi-track displaced vertices [116, 117]. A search

which selected events with a displaced vertex and large missing transverse energy describes has also used this method and describes the results in an ATLAS Internal Note [78]. More recently, this technique has been used by analyses which search for events with di-lepton displaced vertices [118] and displaced Heavy Neutral Leptons [119].

These searches used a sample of reconstructed K_s^0 vertices to compare the tracking efficiency in data and MC. K_s^0 vertices are selected by requiring a displaced vertex have exactly two tracks, with opposite-sign charge, and a mass consistent with $m(K_s^0)$. The distribution of vertex radii is compared between data and MC. For short decay lengths, the reconstruction efficiency and its uncertainty are assumed to be given by standard tracking prescriptions. The distributions of vertex radii in data and MC are normalized to each other for vertices with small radii, $R < 10 \, \text{mm}$, and the deviation between MC and data is studied at larger radii. The largest deviation is taken as an uncertainty on the tracking and vertex efficiency of K_s^0 vertices. The analyses listed above find track reconstruction efficiency uncertainties of 10% at most.

To be conservative, this analysis takes the uncertainty on the track reconstruction efficiency to be 10% for all tracks. This 10% uncertainty is applied to all tracks despite the fact that Standard track reconstruction efficiency is associated with uncertainties of at most a few percent.

Once the uncertainty on the track reconstruction efficiency is evaluated, this uncertainty is propagated through vertex reconstruction using a *track-killing* method. Reconstructed tracks from secondary vertices are randomly killed with a 10% probability per track. Each vertex is considered and each track is assigned a probability for being killed. Given these probabilities, toys are thrown with different possible views of the vertex. For each possible altered vertex, the vertex mass and associated

number of tracks are recomputed.

An additional requirement that there be at least two tracks which satisfy the selected track requirements (from Table 6.6) is also included in this method. After tracks are killed, if a vertex does not have at least two selected tracks, displaced vertex reconstruction would not be seeded, and the vertex would not be reconstructed.

Figure 11.1 shows an example of this track-killing method used on a stop signal sample with $m(\tilde{t}) = 1.5$ TeV and $\tau(\tilde{t}) = 1$ ns. The nominal number of reconstructed displaced vertices in the analysis fiducial volume satisfying $m_{\mathrm{DV}} > 20$ GeV and $n^{\mathrm{DV}}_{\mathrm{Tracks}} \geq 3$ is shown in black. For the distribution shown in red, reconstructed tracks from vertices are randomly killed as discussed above. The number of displaced vertices satisfying $m_{\mathrm{DV}} > 20$ GeV and $n^{\mathrm{DV}}_{\mathrm{Tracks}} \geq 3$ is then shown in red, normalized by the number of toys thrown for each vertex.

The fraction of events with at least one displaced vertex that satisfies $m_{\mathrm{DV}} > 20$ GeV and $n^{\mathrm{DV}}_{\mathrm{Tracks}} \geq 3$ is used as a proxy for the event selection efficiency. This fraction of events is compared between the black and red distributions. For the $m(\tilde{t}) = 1.5$ TeV, $\tau(\tilde{t}) = 1$ ns signal sample, this method results in an overall 15.4% systematic uncertainty on the signal efficiency. This procedure is repeated across the available signal sample grid, and a lifetime-dependent systematic is estimated.

In addition to studying uncertainty in the tracking efficiency, the uncertainty associated with track momentum resolution is evaluated by lowering the p_{T} of all tracks by 10% and reevaluating the mass of the vertex. This effect is found to be at most 1.7% when measured across all available signal samples, negligible in comparison to the effect described above.

The following systematic uncertainties are applied to signal samples in order to account for tracking
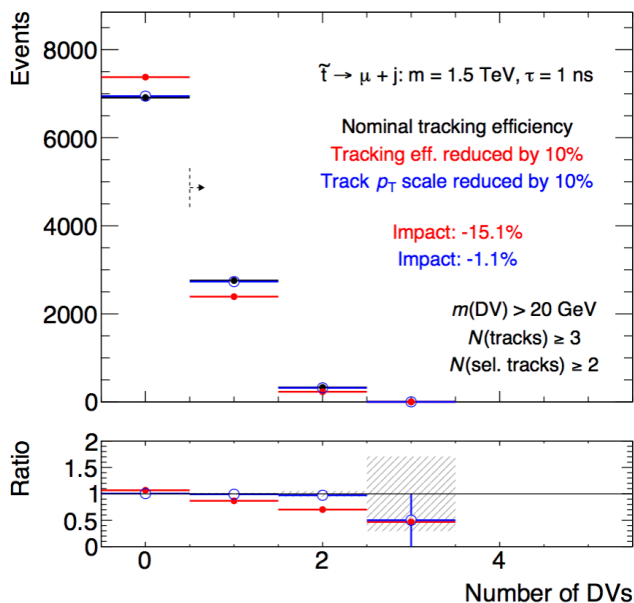
Figure 11.1: The number of vertices with $m_{\mathrm{DV}} > 20$ GeV and $n_{\mathrm{Tracks}}^{\mathrm{DV}} \geq 3$ for a stop signal sample with $m(\tilde{t}) = 1.5$ TeV and $\tau(\tilde{t}) = 1$ ns. The number of vertices is shown in black for events with the nominal tracking reconstruction efficiency. The selection in red shows the number of vertices for events in which the tracking reconstruction efficiency has been reduced by 10%. An arrow drawn indicates events with at least one displaced vertex that satisfies $m_{\mathrm{DV}} > 20$ GeV and $n_{\mathrm{Tracks}}^{\mathrm{DV}} \geq 3$.

and vertex reconstruction efficiency:

- $\tau(\tilde{t}) = 10$ ps $\rightarrow 14.5\%$

- $\tau(\tilde{t}) = 100$ ps $\rightarrow 15.1\%$

- $\tau(\tilde{t}) = 1$ ns $\rightarrow 15.4\%$

11.2 MUONS

The efficiency for triggering on, reconstructing, identifying, and selecting a muon is an important input to the signal selection efficiency. In order to avoid overestimating, or underestimating, the ex-

pected number of selected signal events in simulation, it important that these efficiencies in simulation are the same as in data. Muons in Monte Carlo signal are weighted by a scale factor, in order to correct the efficiency observed in simulation to that observed in data.

Scale factors are designed to account for the differences in muon reconstruction, identification, and trigger efficiency between data and MC, and are applied to the leading preselected signal muon. These scale factors are evaluated using muons from $Z \rightarrow \mu\mu$ decays in a tag-and-probe analysis. These scale factors are applied to displaced, signal muons, as if these muons were prompt. An additional uncertainty is applied to the muon in order to account for any potential mis-modeling of trigger or reconstruction efficiency as a function of the muon's displacement.

Standard ATLAS uncertainties for the muon momentum scale and resolution are also applied to simulated signal samples, though these results are not discussed in detail in this thesis.

11.2.1 Muon Scale Factors

This section discusses how scale factors are derived to correct muon related efficiencies in Monte Carlo to the efficiencies observed in 2016-2018 data. A scale factor can be defined as

$$SF = \frac{\text{Efficiency Data}}{\text{Efficiency MC}}. \qquad (11.1)$$

Scale factors designed to correct for `Medium` muon reconstruction efficiency modeling in Monte Carlo to that observed in data are taken from the ATLAS Muon Combined performance group. Two

additional sets of scale factors are evaluated which are specific to this analysis. These additional scale factors are designed to account for the analysis specific identification criteria required in the full muon selection and muon trigger efficiency. These scale factors are evaluated by performing a dedicated tag-and-probe analysis in $Z \rightarrow \mu\mu$ events.

The first set of dedicated scale factors is used to account for identification criteria used in the full muon selection. These scale factors are applied to the leading preselected muon in the $E_{\mathrm{T}}^{\mathrm{miss}}$ triggered sample. The other set of scale factors are designed to account for the modeling of the efficiency for a muon passing both identification criteria and muon trigger matching are also evaluated using $Z \rightarrow \mu\mu$ events. These identification and trigger scale factors are applied to the leading preselected muon in the Muon triggered sample.

In the $E_{\mathrm{T}}^{\mathrm{miss}}$ triggered sample, the total scale factor applied to the leading preselected muon is the product of the muon reconstruction scale factor and the muon identification scale factor.

$$SF = \text{reconstruction SF} \cdot \text{identification SF} \tag{11.2}$$

In the Muon triggered sample, the total scale factor applied to the leading preselected muon is the product of the muon reconstruction scale factor, and the scale factor for both identification and trigger efficiency.

$$SF = \text{reconstruction SF} \cdot \text{identification and trigger SF} \tag{11.3}$$

283

The subsequent sections discuss the three different muon scale factors used in this analysis, and how those scale factors are obtained.

Muon Reconstruction Scale Factors

This section discusses the efficiency for reconstructing a baseline muon. The baseline muon definition is very similar to that of the standard ATLAS `Medium` working point. Because of the similarity in selections, scale factors evaluated for the reconstruction of `Medium` muons are used to correct the reconstruction efficiency in Monte Carlo to that observed in data. These scale factors are derived using a tag-and-probe analysis with $Z \to \mu\mu$ events. Scale factors are evaluated for each data taking run, and applied to events in Monte Carlo which have a similar pile-up profile as the run in question.

For easy reference, Figure 11.2 shows the average reconstruction scale factor applied to Monte Carlo as a function of muon η and ϕ. Most scale factors are small, indicating $< 2\%$ difference between the reconstruction efficiency in data and MC.

Analysis specific scale factor measurement

Events with a Z boson decaying to two muons are used to study the efficiency of prompt muons passing the full muon selection, as well as the efficiency for firing the Muon Spectrometer only trigger. The `HLT_mu60_0eta105_msonly` trigger is used to select events for the tag-and-probe analysis. N-tuples are skimmed to require exactly two baseline muons. In order to select events with a Z boson, events are required to have two baseline muons, which have opposite sign charge, and an invariant mass consistent with the Z, or $81 < m(\mu^+\mu^-) < 101$ GeV.
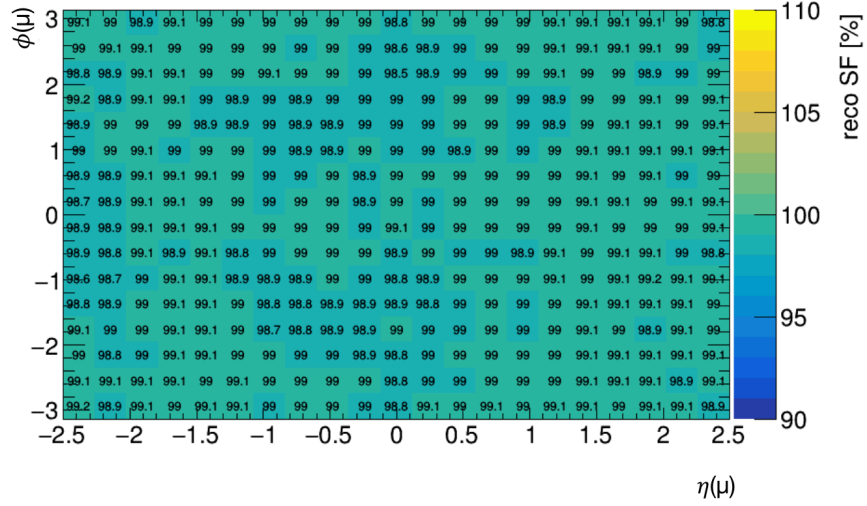
Figure 11.2: Muon reconstruction scale factors as a function of muon η and ϕ. The average scale factor applied to muons in a given (η, ϕ) bin is shown.

In a tag-and-probe analysis, one muon must pass a tight identification, the *tag*, and the second muon is required to pass a looser identification, the *probe*. Probe muons are used to measure an efficiency. *Passing probes* are defined according to whatever is the efficiency being measured. The efficiency is then defined as follows.

$$\epsilon = \frac{\text{Number probes passing selection}}{\text{Number of probes}} \tag{11.4}$$

For this analysis, the tag muon is required to have fired the trigger. Table 11.2 summarizes the selection applied to tag muons.

Figure 11.3 and Figure 11.4 show properties of tag muons in Monte Carlo and in data. The number of muons in MC are normalized to the number of muons in data. Note that the distributions in data

Table 11.2: Tag muon requirements

Baseline Muon
$p_{\mathrm{T}} > 62\,\mathrm{GeV}$
$|\eta| < 1.05$
$|d_0| < 0.5\,\mathrm{mm}$
$|z_0| < 200\,\mathrm{mm}$
`Fixed Cut Tight` isolation
Trigger match `HLT_mu60_0eta105_msonly`

and Monte Carlo do not need to agree exactly for tag muons. In particular, differences in η and ϕ distributions are to be expected due to the trigger matching requirement placed on tags muons. In MC the trigger efficiency is known to be higher than in data for certain regions of the detector. This effect is discussed below, and measured using probe muons.
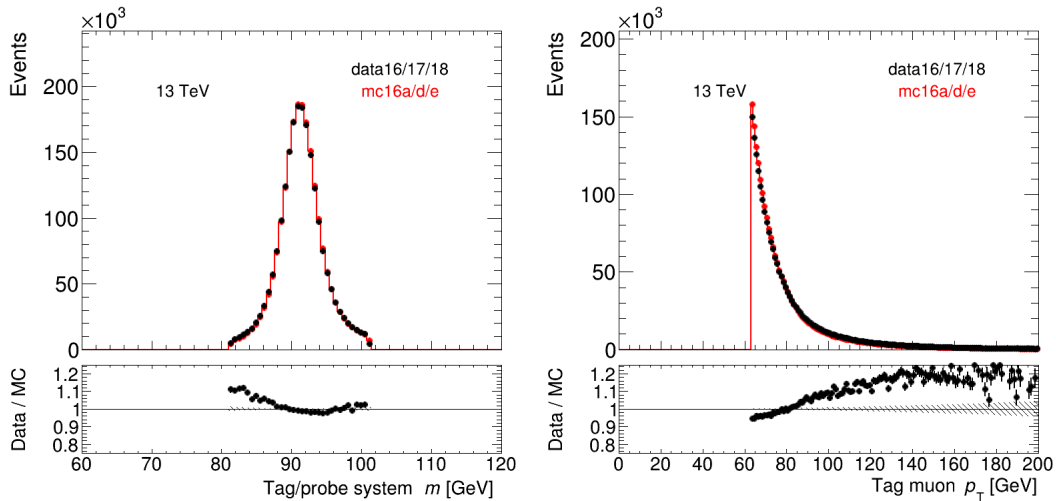

Figure 11.3: Left: tag-and-probe system di-lepton mass in data and Monte Carlo. Right: tag muon p_{T} in data and Monte Carlo. In both plots, MC is normalized to data in the top panel, and the bottom panel shows the ratio between the two.

Different probes are used to measure the scale factors needed for the $E_{\mathrm{T}}^{\mathrm{miss}}$ triggered sample and the
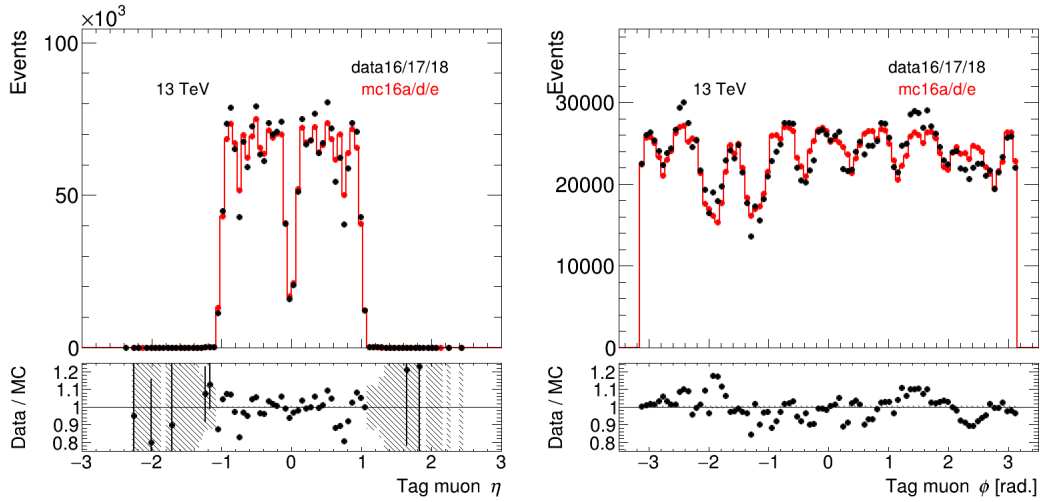
Figure 11.4: Tag muon η and ϕ in data and Monte Carlo. MC is normalized to data in the top panel, and the bottom panel shows the ratio between the two.

Muon triggered sample.

$E_{\mathrm{T}}^{\mathrm{miss}}$ Sample Identification Scale Factors

The scale factors for muon identification criteria in the full muon selection are evaluated in $Z \to \mu\mu$ events. These scale factors are used to correct the leading preselected muon of the $E_{\mathrm{T}}^{\mathrm{miss}}$ sample. The requirements applied to probe muons are summarized in Table 11.3.

Figure 11.5 shows the efficiency for a baseline muon to pass the full muon selection in data and in Monte Carlo as a function of η and ϕ. Figure 11.6 shows the efficiency for a baseline muon to pass the full muon selection in data and in Monte Carlo as a function of muon p_{T} and the average number of interactions per event.

The full muon selection efficiency shows the greatest dependence on muon η and ϕ. This result

Table 11.3: Probe muon requirements for identification scale factors

Probe Muon Selection
Baseline Muon
$p_{\mathrm{T}} > 25\,\mathrm{GeV}$
$|\eta| < 2.5$
Passing Probe selection
$\geq 2\,\mathrm{Pix\ hits\ or} \geq 0\,\mathrm{TRT\ hits}$
`Fixed Cut Tight` isolation
Combined muon $\chi^2/N_{DoF} < 8$
N precision layers ≥ 3
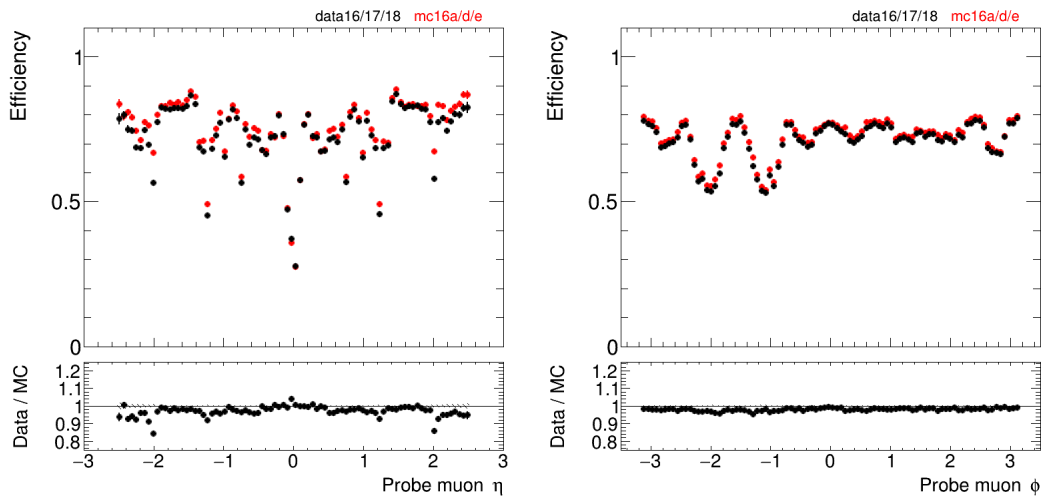
Figure 11.5: Probe muon efficiency as a function of muon η and ϕ in data and Monte Carlo. The bottom panel shows the ratio of efficiencies.

is expected due to the requirement that muons have a segment in at least three precision layers. The efficiency for passing this requirement is highly dependent on features of Muon Spectrometer geometry, as well as data quality issues which may arise during data taking. There is a slight efficiency loss for muons with lower transverse momentum, and the efficiency is also slightly reduced with increasing
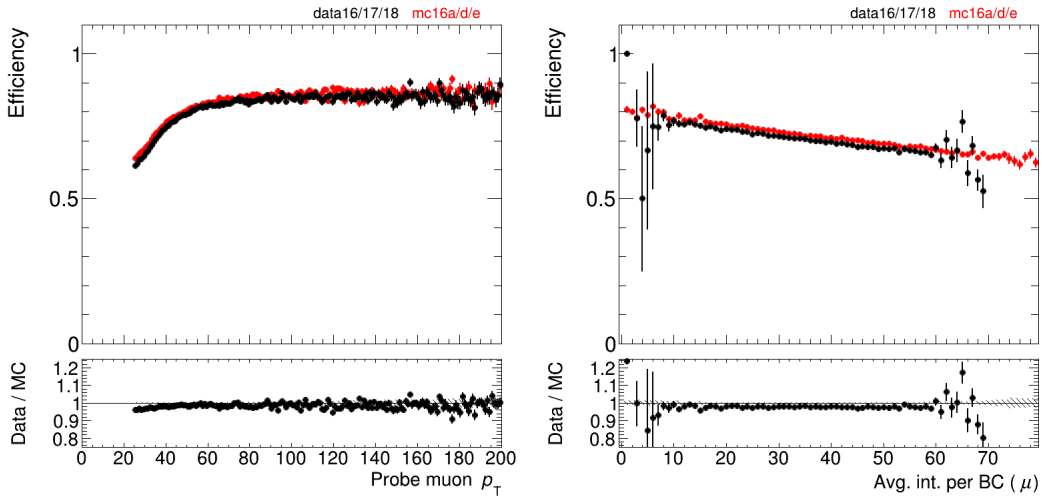
Figure 11.6: Probe muon efficiency as a function of muon p_T and average number of interactions per crossing in data and Monte Carlo. The bottom panel shows the ratio of efficiencies.

pile-up interactions. However, both of these effects are well modeled in MC.

Scale factors for muons are therefore evaluated as a function of muon η and ϕ, in order to account for data quality issues that can arise during data taking, which aren't modeled in Monte Carlo. Most differences in efficiency between data and MC are due to muon chambers which become inoperable or inefficient during data taking. These chambers reduce the efficiency for a baseline muon to have at least three precision layers.

Figure 11.7 shows the efficiency for a baseline muon to pass the full muon selection in data and in Monte Carlo as a function of muon η and ϕ. Figure 11.8 shows the ratio of the efficiency in data to that of Monte Carlo. The histogram with larger bins is used to derive the scale factors which are applied to the leading preselected muon.

The vast majority of scale factors for muon identification, evaluated as a function of muon (η, ϕ)

289
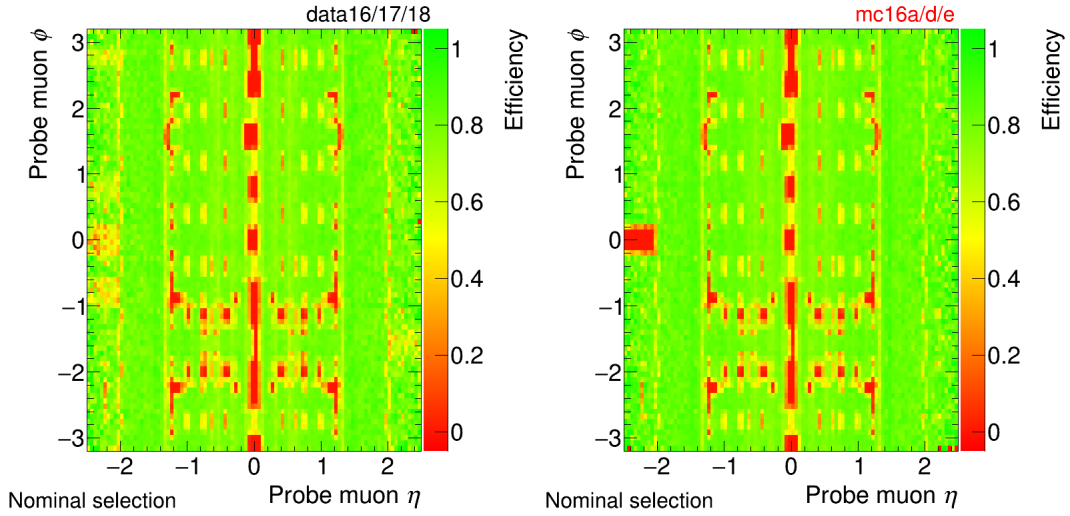
Figure 11.7: Probe muon efficiency as a function of muon (η, ϕ) in data (left) and MC (right).
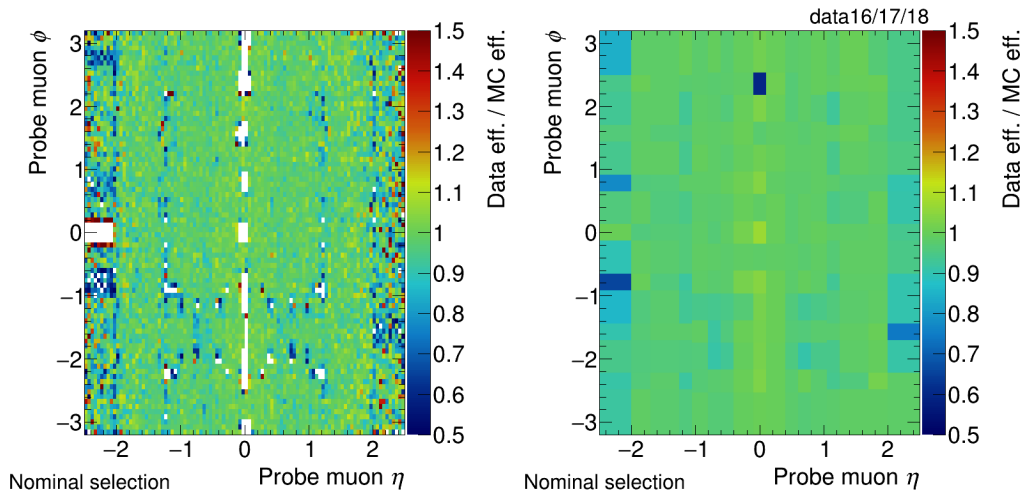

Figure 11.8: Ratio of identification efficiency in data to MC. On the left, small bins are used to help discern features. The right shows the ratio, with the binning used to determine scale factors.

are close to unity. A few regions at $|\eta| > 2.0$ have scale factors much lower than one, due to a variety of CSC related challenges during data taking.

One region is treated specially when deriving scale factors. This region corresponds to $\eta \approx -2.5$ and $\phi \approx 0$. This area corresponds to a region in Monte Carlo where a CSC chamber is marked as having two dead layers (out of a total of four layers). Note that a CSC chamber needs a cluster in three of four layers to form a segment. This chamber did actually have two dead layers for part of 2016 data taking, but the chamber was recovered in time for 2017 data taking. Because the denominator (MC efficiency) for this region in η-ϕ is close to zero it is impossible to compute a reasonable scale factor. For this region only, the scale factor is set to one by hand, and given a 100% systematic uncertainty.

The effect of applying these scale factors on the overall signal efficiency in the $E_{\mathrm{T}}^{\mathrm{miss}}$ triggered sample is on the order of a few percent or less.

Muon Stream Identification and Trigger Scale Factors

This section describes the procedure used to evaluate muon identification and trigger scale factors for the Muon Stream. These scale factors are also evaluated in $Z \to \mu\mu$ events. They use the same tag as was used to compute the $E_{\mathrm{T}}^{\mathrm{miss}}$ triggered sample scale factors, with a modified probe selection. The requirements applied to probe muons are summarized in Table 11.4.

Figure 11.9 shows the probe muon efficiency as a function of η and ϕ in data and in Monte Carlo. Figure 11.10 shows the ratio of efficiency in data to that of MC. Scale factors for muons are again evaluated as a function of muon η and ϕ, in order to account for data quality issues that can arise during data taking and are not modeled in Monte Carlo.

The trigger efficiency in Monte Carlo is much better than that observed in data. This result is expected, because the Monte Carlo assumes a nearly perfect efficiency for RPC chambers. During

Table 11.4: Probe muon requirements for identification+trigger scale factors

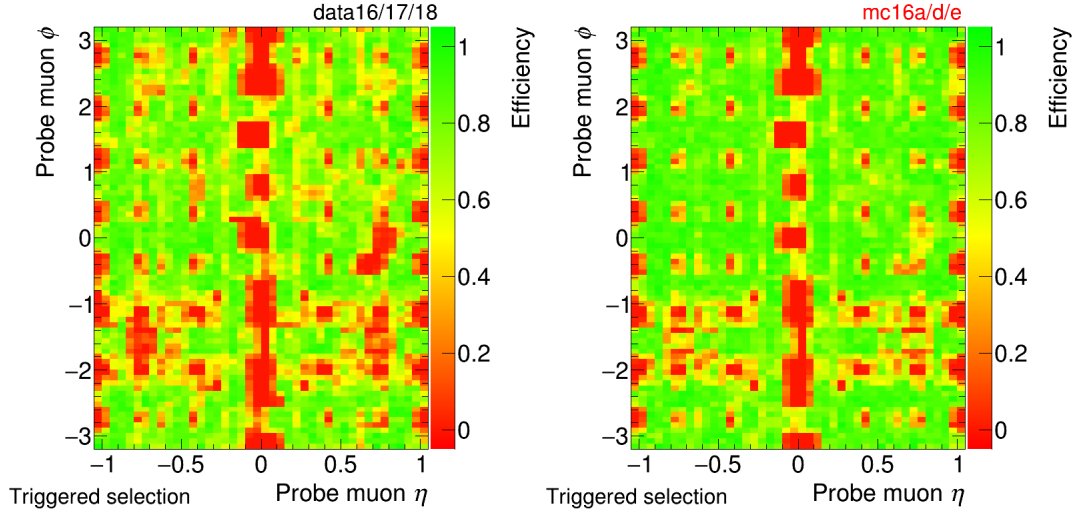| Probe Muon Selection |
| --- |
| Baseline Muon |
| $p_{\mathrm{T}} > 62\,\mathrm{GeV}$ |
| $|\eta| < 1.05$ |
| Passing Probe Selection |
| $\geq 2\,\mathrm{Pix\ hits\ or} \geq 0\,\mathrm{TRT\ hits}$ |
| `Fixed Cut Tight` isolation |
| Combined muon $\chi^2/N_{DoF} < 8$ |
| N precision layers ≥ 3 |
| Trigger match `HLT_mu60_0eta105_msonly` |

Figure 11.9: Probe muon efficiency as a function of muon (η, ϕ) in data (left) and MC (right)

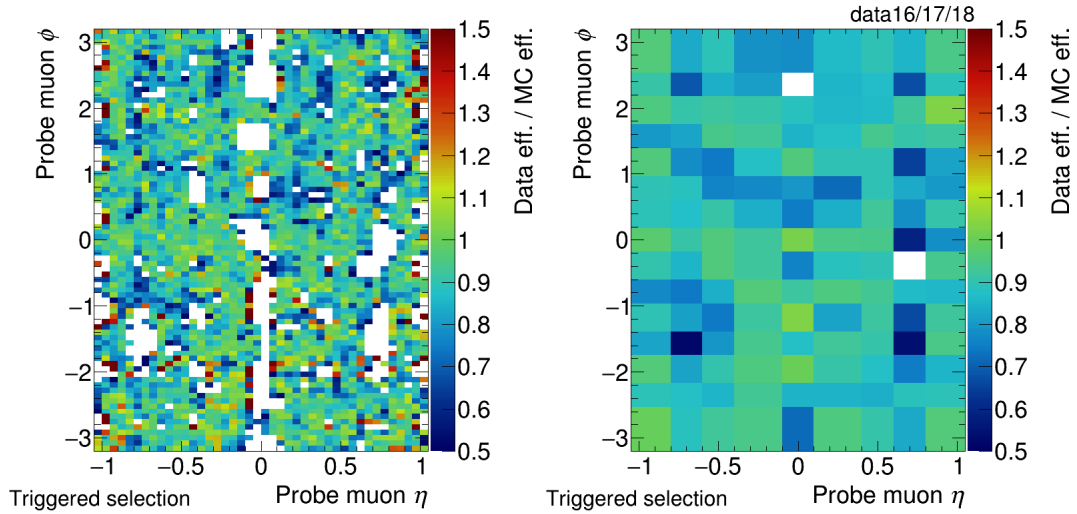data taking, a handful of RPC chambers may be masked at any given time.

Figure 11.10: Ratio of identification efficiency in data to MC. On the right small bins are used to help discern features. The right shows the ratio, with the binning used to determine scale factors.

Closure Test

A cross check is performed in order to ensure that when the scale factors are applied to muons in Monte Carlo, the resulting efficiency matches that observed in data, or that *closure* is observed. In the following histograms, the probe efficiency is evaluated as described above. However, muons in Monte Carlo have scale factors applied. If scale factors close well, the ratio of the efficiency in data to that of MC should be equal to one.

Figure 11.11 shows the closure of the $E_\mathrm{T}^\mathrm{miss}$ triggered sample scale factors, while Figure 11.12 shows a test of closure for the Muon triggered sample scale factors. Both sets of scale factors show good closure. There are a few bins where the closure is not exactly one, but these bins occur in regions where statistics for evaluating scale factors are limited. Any deviation from unity is covered by statistical uncertainties.

Figure 11.11: Left: the ratio of E_T^{miss} sample probe efficiency in data and in MC, with scale factors applied, as a function of muon η and ϕ. Right: The statistical uncertainties on the E_T^{miss} sample closure test as a function of muon η and ϕ.
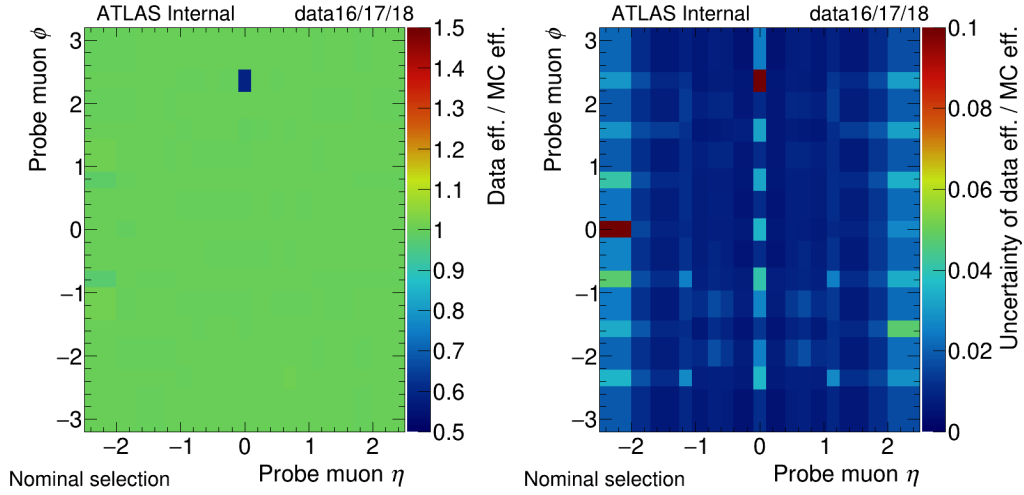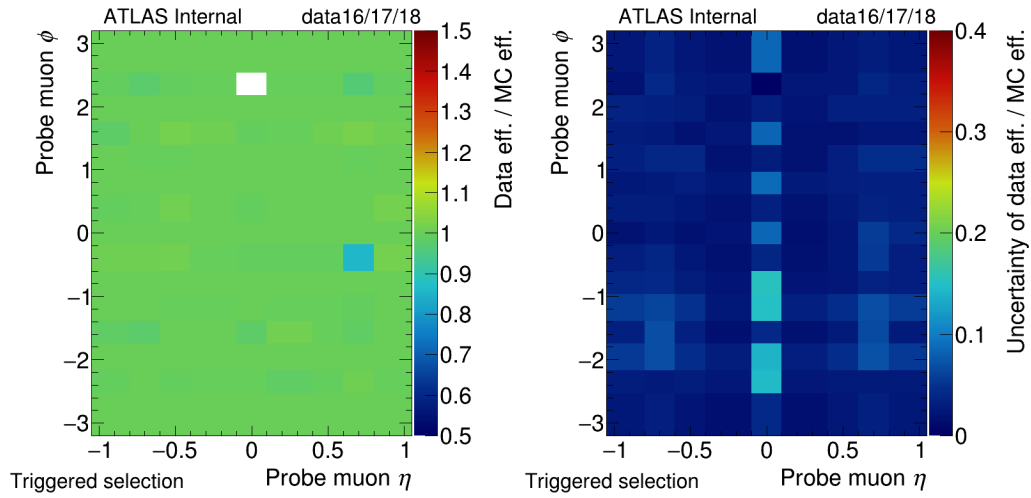

Figure 11.12: Left: the ratio of Muon sample probe efficiency in data and in MC, with scale factors applied, as a function of muon η and ϕ. Right: The statistical uncertainties on the Muon sample closure test as a function of muon η and ϕ.

Additionally, closure for E_T^{miss} sample scale factors was tested in a few key variables. Figure 11.13 shows a test for closure as a function of muon p_T and pile-up. For all variables closure is observed.
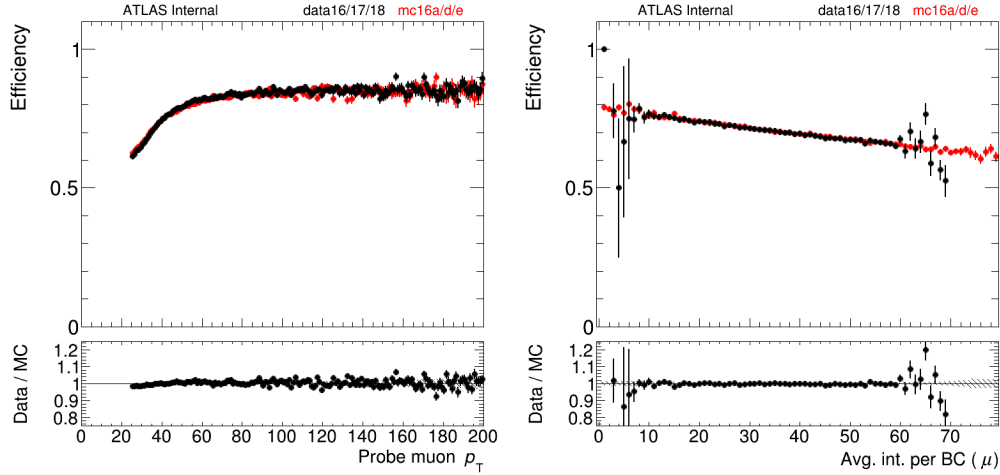
Figure 11.13: Closure test for E_T^{miss} triggered sample scale factors as a function of muon p_T (left) and the mean number of pile-up interactions per bunch crossing (right).

RESULTING SYSTEMATIC UNCERTAINTY

The statistical uncertainty on the scale factor measurement is taken as a systematic on muon efficiency. The size of the uncertainty on the event selection efficiency is evaluated by pulling down the muon scale factors by their statistical errors, and comparing the reduced efficiency to the nominal efficiency when running with nominal scale factors.

In the E_T^{miss} triggered sample the percent change in signal efficiency ranges from $0.7 - 0.9\%$, while in the Muon sample it ranges from $1.7 - 4.0\%$. The change in efficiency shows no dependence on long-lived particle lifetime or mass. For each stream, the largest percent change is taken as the total

systematic uncertainty due to the scale factor measurement. The larger statistical uncertainty in the Muon sample is due to the fact that the scale factors are evaluated with smaller sample of muons. The Muon sample scale factor calculation requires higher momentum muons in a smaller range of pseudorapidity and also requires a trigger match.

11.2.2 DISPLACED MUON EFFICIENCY

Scale factors measured using muons from $Z \to \mu\mu$ events ensure that for muons with small impact parameters, $|d_0| < 0.5$ mm, the reconstruction, identification, and trigger efficiency in Monte Carlo match those of the data. However, these scale factors do not account for any mis-modeling in the reduction of efficiency as a function of the muon's transverse impact parameter. Because there is no source of Standard Model muons with impact parameters as large as expected for signal muons, most uncertainties related to muon efficiency are derived from Monte Carlo.

Uncertainties as a function of muon displacement are evaluated for the MS-only trigger efficiency, Inner Detector tracking efficiency, baseline muon reconstruction, and full muon selection efficiency as a function of the muon's transverse impact parameter, $|d_0|$. The trigger, baseline muon, and full muon selection uncertainties are evaluated using Monte Carlo. Signal samples with a stop lifetime $\tau(\tilde{t}) = 1$ ns are used to evaluate the size of these systematic uncertainties. The uncertainty on the efficiency for reconstructing an Inner Detector track is taken to be a flat 10%, based on the same K_s^0 studies used to evaluate the vertex reconstruction efficiency. All four uncertainties are assumed to be uncorrelated.

The general strategy for evaluating these uncertainties is to study how the efficiency in Monte Carlo

changes as a function of the muon transverse impact parameter with respect to the efficiency for a prompt muon.

Reconstruction Efficiencies

Reconstruction efficiencies are measured by evaluating the fraction of truth muons which are reconstructed and pass various analysis selections. In order to evaluate these reconstruction efficiencies, the following truth matching procedure has been defined.

1. Truth muons from the stop R-hadron decay are required to pass the following acceptance requirements.

   - The muon must have $|\eta| < 2.5$ and $p_T > 25\,\text{GeV}$
   - The muon must also have $2 < |d_0| < 300\,\text{mm}$ and $|z_0| < 500\,\text{mm}$

2. In order to evaluate any efficiency, only the leading muon in p_T passing the above acceptance criteria is considered.

3. Truth muons are matched to the nearest reconstructed baseline muon in $\Delta R < 0.05$. If no reconstructed muon is found in $\Delta R < 0.05$, the truth muon is considered unmatched

Figure 11.14 shows that a cone size of $\Delta R = 0.05$ is more than sufficient for matching to truth muons to the correct reconstructed muon, and minimizing the rate of truth matching to the wrong reconstructed muon. Figure 11.15 shows a comparison of truth and reconstructed muon properties. The truth muon and reconstructed muon have correlated transverse momentum and transverse impact parameter, indicating that the truth matching procedure is working correctly.
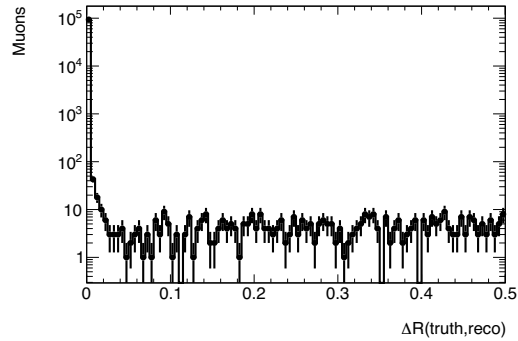
Figure 11.14: ΔR between the truth muon and nearest reconstructed baseline muon in signal, no overflow bin is shown.
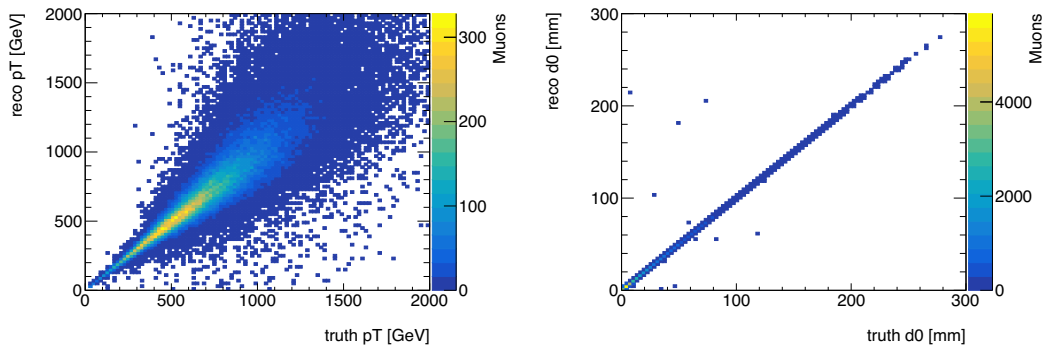
Figure 11.15: A comparison of the truth and reconstructed muon transverse momentum p_T (left) and transverse impact parameter $|d_0|$ (right) in stop signal samples.

Inner Detector Tracking

The efficiency for reconstructing an Inner Detector track from a truth muon is shown in Figure 11.16.

The efficiency degrades from 95% for nearly prompt muons to 15% for muons with transverse impact parameters larger than 200 mm. This efficiency is evaluated using the following numerator and denominator.

- Numerator: The number of truth muons in acceptance which are truth matched to an Inner

Detector Track based on a hit matching procedure.

- Denominator: The number of truth muons in acceptance, as defined above.

Baseline Muon Reconstruction

The efficiency for reconstructing a baseline muon, for muons which have a reconstructed Inner Detector track is shown in Figure 11.16. This efficiency does not appreciably degrade as a function of muon displacement. This efficiency is evaluated using the following numerator and denominator.

- Numerator: The number of truth muons in acceptance, which are matched to a reconstructed baseline muon, using the truth matching procedure defined above.

- Denominator: The number of truth muons in acceptance which have a reconstructed Inner Detector Track.
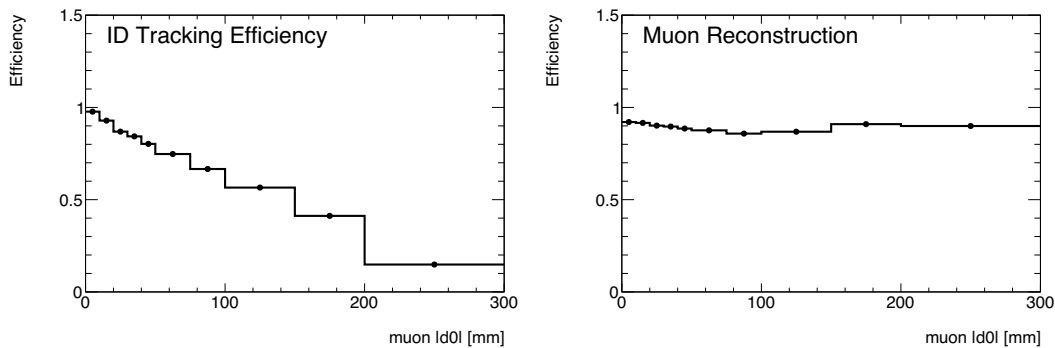

Figure 11.16: Measured large radius tracking (left) and muon reconstruction efficiencies (right) versus the muon transverse impact parameter.

Full Muon Selection

The efficiency for a baseline muon to pass the full muon selection is shown in Figure II.17. This efficiency does not appreciably degrade as a function of muon displacement. This efficiency is evaluated using the following numerator and denominator.

- Numerator: The number of truth muons in acceptance, which are matched to a reconstructed muon passing the full selection

- Denominator: The number of truth muons in acceptance which are matched to a reconstructed muon which passes the baseline muon selection

Muon Spectrometer only trigger

The Muon Spectrometer trigger efficiency is evaluated by measuring the fraction of signal muons with $p_T > 62$ GeV and $|\eta| < 1.05$ that also fire a MS-only trigger. Muons with $p_T > 62$ GeV and $|\eta| < 1.05$ have been determined to be within the plateau of the MS-only trigger efficiency by other long-lived particle analyses which target displaced muon signatures [92]. Figure II.17 shows the trigger efficiency as a function of muon transverse impact parameter. The efficiency is around 75% for prompt muons, but degrades to below 50% for muons with impact parameters $|d_0| > 200$ mm.

Uncertainties versus impact parameter

The general strategy for evaluating these uncertainties is summarized below.

- For each bin in $|d_0|$, compute the difference in efficiency with respect to prompt muons, and take the absolute value of this difference.
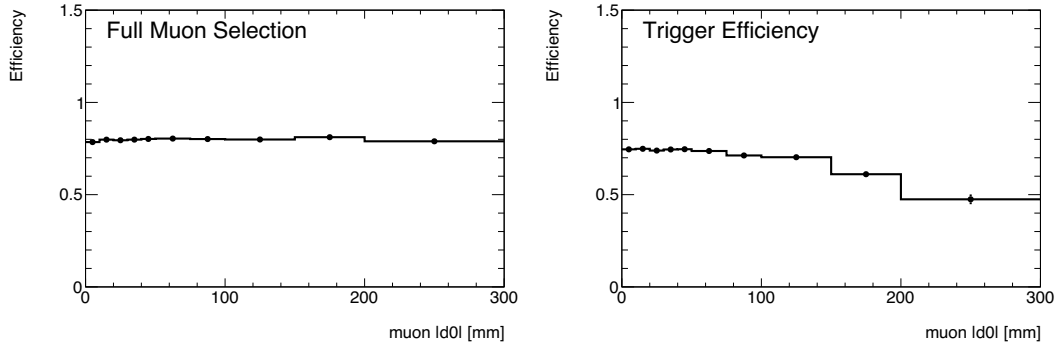
Figure II.17: Measured efficiencies for the full muon selection (left) and muon trigger (right) versus the muon transverse impact parameter.

- A correction is performed in order to ensure the uncertainty cannot decrease with $|d_0|$ even if the efficiency measured in Monte Carlo does decrease with muon displacement. Moving from the smallest bin in $|d_0|$ to the largest bin in $|d_0|$, if the uncertainty in a given $|d_0|$ bin is smaller than the previous $|d_0|$ bin, the uncertainty is taken to be that of the previous bin.

For the Inner Detector tracking efficiency, a flat uncertainty of 10% is taken as a function of the muon transverse impact parameter $|d_0|$. This number is derived from the same studies of K_s^0 decays in data and Monte Carlo to evaluate the Large Radius Tracking uncertainty, as discussed in Section II.1.

The total systematic uncertainty on the $E_\mathrm{T}^\mathrm{miss}$ triggered sample adds the reconstruction and identification uncertainties in quadrature. The total systematic uncertainty in the Muon triggered sample adds all four uncertainties in quadrature. Figure II.18 shows the resulting uncertainties as a function of muon transverse impact parameter $|d_0|$. In the $E_\mathrm{T}^\mathrm{miss}$ triggered sample the uncertainty increases from 10% to 12%, while in the Muon triggered sample the uncertainty increases from 10% to 30%.
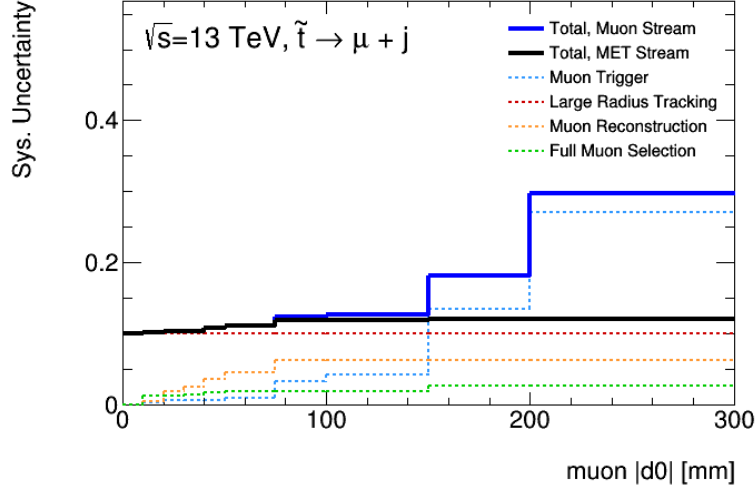
Figure 11.18: Measured systematic uncertainties related to muon trigger, reconstruction, and identification as a function of muon transverse impact parameter $|d_0|$.

Systematic Uncertainties versus lifetime

This section estimates the effect of these uncertainties on the number of expected events in signal. The uncertainties shown in Figure 11.18, which are evaluated per muon, as a function of muon impact parameter, were applied on an event level basis in to signal. The leading preselected muon's transverse impact parameter was used to determine the reduction in efficiency per event. Events with cluster-based $E_T^{miss} > 180$ GeV were weighted down by the E_T^{miss} triggered sample uncertainties, and events with cluster-based $E_T^{miss} < 180$ GeV were weighted down by the Muon Stream uncertainties.

For the E_T^{miss} triggered sample, the percent change in signal expectation due to potential muon reconstruction and identification efficiency mis-modeling as function of $|d_0(\mu)|$ is summarized below.

- $\tau(\tilde{t}) = 0.01$ ns : 10.0%
- $\tau(\tilde{t}) = 0.1$ ns : 10.1%

302

- $\tau(\tilde{t}) = 1 \, \mathrm{ns} : 10.4\%$

For the Muon triggered sample, the percent change in signal expectation due to potential muon trigger and reconstruction mis-modeling as function of $d_0(\mu)$ is summarized below.

- $\tau(\tilde{t}) = 0.01 \, \mathrm{ns} : 10.0\%$

- $\tau(\tilde{t}) = 0.1 \, \mathrm{ns} : 10.1\%$

- $\tau(\tilde{t}) = 1 \, \mathrm{ns} : 11.8\%$

For both the $E_\mathrm{T}^\mathrm{miss}$ and Muon triggered samples, the largest source of uncertainty is due to the 10% uncertainty on Inner Detector track reconstruction efficiency.

11.2.3 Muon momentum scale and resolution

In order to account for muon momentum scale and resolution uncertainties, standard variations as provided by the ATLAS Muon Combined Performance group are used. These uncertainties are obtained from measurements of the width of the di-muon mass distribution in $Z \to \mu^+\mu^-$ events. Across the different signal masses and lifetimes considered in this search, the largest effect on the signal efficiency is due to the uncertainty on the muon sagitta resolution bias. This uncertainty results in at most a 0.7% effect on the signal region yield for small lifetimes (0.01 ns), and at the per-mille level or below at larger lifetimes.

11.3 Radiation Model

Another uncertainty which affects the expected signal yields stems from the modeling of initial and final state QCD radiation. Initial and final state radiation affect the kinematics of the di-stop system,

which in turn affects the cluster-based $E_{\mathrm{T}}^{\mathrm{miss}}$ and muon transverse momentum distribution.

In order to estimate the effect of initial state radiation modeling on the signal efficiency, the p_{T} distribution of the di-stop system in MadGraph is reweighted to match that of Pythia 6.427. The weights used to correct the di-stop p_{T} distribution were obtained from an ATLAS search for stable massive particles [120]. These weights were obtained from a simplified model inspired by Split Super-symmetry, with gluino R-hadrons. The weights applied to the di-stop system in this simplified model of interest for this thesis can be seen in Figure 11.19.

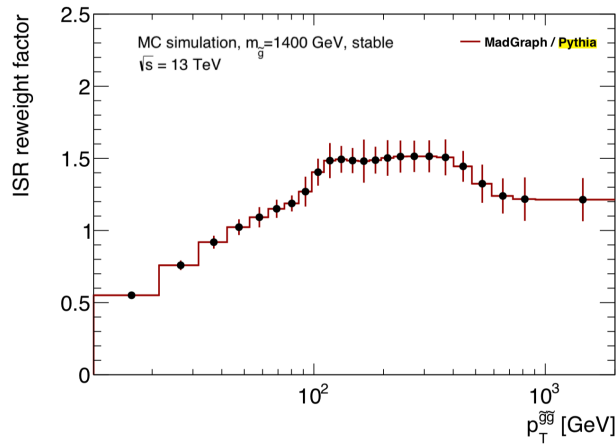Figure 11.19: Ratio of Gluino-gluino system p_{T} in Pythia 6.427 to that of MadGraph [120].

After applying these weights to the di-stop p_{T} distribution, the size of the effect on the overall signal efficiency is less than 3% for a range of stop masses and lifetimes. A conservative 3% uncertainty is applied to all stop masses and lifetimes in order to account for this effect.

11.4 Jet Measurement Uncertainties

While no direct requirements are placed on jets in this search, jets which are incorrectly measured can result in systematic effects on the signal selection efficiency via various indirect means. These effects include the muon isolation requirements and the requirement on cluster-based E_T^{miss}. The recommended set of jet energy scale and resolution variations are used to define signal efficiency variations. The effect of these variations on the signal region yield is seen to be at most 1.5%.

The effect of jet measurement uncertainties on the efficiency of passing the cluster-based E_T^{miss} requirement is not directly measurable because the cluster-based E_T^{miss} is not calculated from analysis-level jets. Another variable which is calculated from standard ATLAS jets must be used as a proxy variable. The variable *missing* H_T, is defined as the magnitude of the vector sum of all jet transverse momenta, and measures the momentum imbalance in the jet system.

An event's missing H_T is highly correlated with an event's cluster-based E_T^{miss}. Figure 11.20 shows the correlation between missing H_T and cluster-based E_T^{miss} for a single stop sample with $m(\tilde{t}) = 1$ TeV, and $\tau(\tilde{t}) = 0.01$ ns, which also demonstrates that the intrinsic values for both of these quantities in the signals of interest is well above the requirement that cluster-based $E_T^{miss} > 180$ GeV used in the analysis.

Figure 11.20 shows that signal events with cluster-based $E_T^{miss} = 180$ GeV have values of missing H_T which vary between approximately 100 and 300 GeV. In order to test the effect of the jet measurement uncertainty on the efficiency for passing a cluster-based $E_T^{miss} > 180$ GeV, the efficiency for signal events to pass requirements that missing $H_T > 100, > 200,$ and > 300 GeV is used
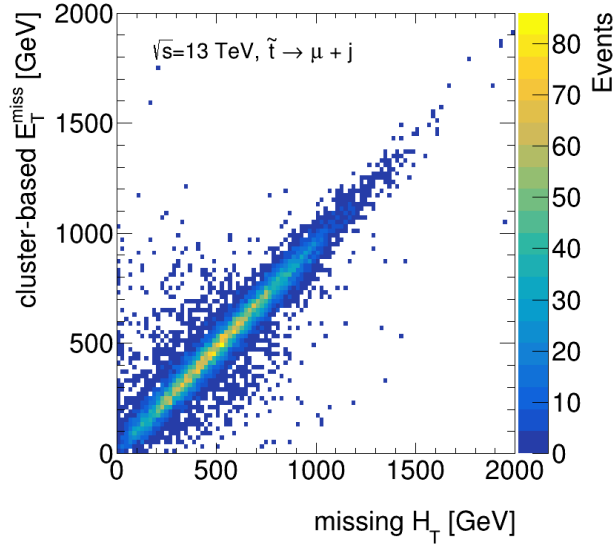
Figure 11.20: Cluster-based E_T^miss versus missing H_T for a stop signal sample with $m(\tilde{t}) = 1.0$ TeV.

as a conservative proxy.

Because of the high momentum scale of the muons in the signal models considered, the largest variation due to jet measurement uncertainties seen across these missing H_T requirements is at most 1.5%. Overall, combining the effects of the standard jet measurement uncertainty, and the uncertainties derived from the missing H_T studies, a conservative systematic uncertainty of 2.1% is taken for all signal efficiencies due to jet momentum measurement uncertainties.

11.5 E_T^MISS TRIGGER EFFICIENCY

In stop signal samples, the E_T^miss trigger is 100% efficient for events with cluster-based $E_\text{T}^\text{miss} > 180$ GeV. However, in data, the E_T^miss trigger is not fully turned-on for events with cluster-based $E_\text{T}^\text{miss} > 180$ GeV. Events with a Z boson decaying to two muons are used to study the E_T^miss trigger efficiency in data.

Figure 11.21 shows the E_T^{miss} trigger efficiency as a function of the transverse momentum of the $Z \to \mu^+\mu^-$ system, and as a function of the cluster-based E_T^{miss} of the event. The dotted line indicates events with cluster-based $E_T^{miss} = 180$ GeV, which is the requirement used to separate the E_T^{miss} and Muon triggered samples.
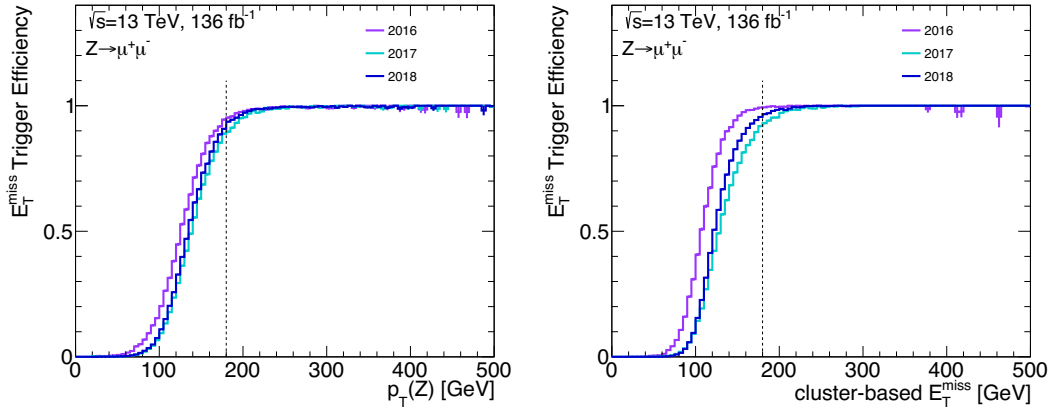
Figure 11.21: E_T^{miss} Trigger efficiency as a function of the transverse momentum of the $Z \to \mu\mu$ system (left) cluster-based E_T^{miss} (right). The E_T^{miss} trigger efficiency is evaluated separately for each year of data taking.

In order to account for the difference in E_T^{miss} trigger efficiency between data and Monte Carlo, the cluster-based E_T^{miss} distribution for signal events with a fully selected muon and displaced vertex was reweighted by the E_T^{miss} trigger efficiency turn-on curve observed in data. The change in signal efficiency between the nominal and reweighted distributions was taken as a systematic uncertainty. However, because signal events are predicted to have large values of cluster-based E_T^{miss}, a negligible change in efficiency ($< 0.2\%$) was observed.

12

Results

12.1 FINAL YIELDS

The event yields in data are shown as a function of the various selections of the analysis. Table 12.1 shows the event cutflows in the E_T^{miss} triggered sample, while Table 12.2 shows the event cutflow for the Muon triggered sample.

The first selection shown is the total number of events in the `DAOD_SUSY15` derivations. The next selection shown is the number of events surviving n-tuple skimming. N-tuples were skimmed to require that each event have at least one baseline muon with $|d_0(\mu)| > 1.0$ mm. For subsequent selections the relative and total efficiency is given with respect to the number of events surviving the n-tuple skimming.

Event level requirement requirements are applied first, followed by the muon selection and displaced vertex selections. The $E_{\mathrm{T}}^{\mathrm{miss}}$ trigger sample primarily consists of events with a fake muon, and the muon preselection and full selection requirements are effective in rejecting these events. Only 58 events pass the event selection and full muon selection in the $E_{\mathrm{T}}^{\mathrm{miss}}$ trigger sample. In contrast, the Muon triggered sample primarily consists of events with a cosmic muon. There are 108147 events which survive the event selection and all muon selection criteria except for the cosmic veto, highlighting the size of the cosmic muon background and importance of the cosmic veto. After the cosmic veto is applied, there only 452 events in the Muon triggered sample.

In the $E_{\mathrm{T}}^{\mathrm{miss}}$ triggered sample, most events which pass the muon selection also have a displaced vertex, while in the Muon triggered sample, fewer than half of the events also have a displaced vertex. First, fiducial and quality requirements are applied to displaced vertices, followed by the Material Veto. The Material Veto is the last DV preselection requirement applied, in order to understand the contribution of hadronic interactions. In both the Muon and $E_{\mathrm{T}}^{\mathrm{miss}}$ triggered samples, roughly 35% of displaced vertices in the fiducial volume are rejected by the Material Veto.

In both the $E_{\mathrm{T}}^{\mathrm{miss}}$ and Muon triggered samples, the full displaced vertex requirements are effective in reducing the final yields to only a handful of events. After the Material Veto is applied, displaced vertices are dominated by randomly crossing tracks. The requirement that displaced vertices have at least three tracks rejects between 85% and 90% of displaced vertices which survive a Material Veto. In the $E_{\mathrm{T}}^{\mathrm{miss}}$ triggered sample, no events survive the full selection. In the Muon triggered sample, only one event survives the full event selection.

Table 12.1: $E_{\mathrm{T}}^{\mathrm{miss}}$ triggered sample cutflows in data. The first selection shown is the total number of events in the SUSY derivations. The next selection shown is the number of events surviving n-tuple skimming. N-tuples were skimmed to require that each event have at least one baseline muon with $|d_0(\mu)| > 1.0$ mm. For subsequent selections the relative and total efficiency is given with respect to the number of events surviving the n-tuple skimming.

Cut	Events	Rel. Efficiency [%]	Total Efficiency [%]
Derivation	564932150		
N-tuple skimming	2703349	100.0	100.0
$E_{\mathrm{T}}^{\mathrm{miss}}$ Trigger	506730	18.7	18.7
cluster-based $E_{\mathrm{T}}^{\mathrm{miss}} > 180$ GeV	173892	34.3	6.4
At least one Muon	173892	100.0	6.4
$p_{\mathrm{T}}(\mu) > 25$ GeV	64591	37.1	2.4
$|\eta(\mu)| < 2.5$	49531	76.7	1.8
Min. Pixel/TRT hits	28297	57.1	1.0
$2 < |d_0(\mu)| < 300$ mm	4740	16.8	$1.8 \cdot 10^{-1}$
$|z_0(\mu)| < 500$ mm	3527	74.4	$1.3 \cdot 10^{-1}$
Pass fake-muon veto	625	17.7	$2.3 \cdot 10^{-2}$
Pass isolation	164	26.2	$6.1 \cdot 10^{-3}$
Pass cosmic-muon veto	58	35.4	$2.1 \cdot 10^{-3}$
At least one DV	46	79.3	$1.7 \cdot 10^{-3}$
DV Fiducial Volume	41	89.1	$1.5 \cdot 10^{-3}$
$\chi^2/N_{DoF} < 5$	40	97.6	$1.5 \cdot 10^{-3}$
4 mm $< R_{\mathrm{PV-DV}}$	39	97.5	$1.4 \cdot 10^{-3}$
Material Veto	26	66.7	$9.6 \cdot 10^{-4}$
$n_{\mathrm{Tracks}}^{\mathrm{DV}} \geq 3$	4	15.4	$1.5 \cdot 10^{-4}$
$m_{\mathrm{DV}} > 20$ GeV	0	0.0	0.0

Table 12.2: Muon triggered sample cutflows in data. The first selection shown is the total number of events in the SUSY derivations. The next selection shown is the number of events surviving n-tuple skimming. N-tuples were skimmed to require that each event have at least one baseline muon with $|d_0(\mu)| > 1.0$ mm. For subsequent selections the relative and total efficiency is given with respect to the number of events surviving the n-tuple skimming.

Cut	Events	Rel. Efficiency [%]	Total Efficiency [%]
Derivation	564932150		
N-tuple skimming	2703349	100.0	100.0
Muon Trigger	434907	16.1	16.1
cluster-based $E_T^{miss} < 180$ GeV	426709	98.1	15.8
At least one Muon	426709	100.0	15.8
Trigger Match	301145	70.6	11.1
$p_T(\mu) > 62$ GeV	244679	81.2	9.1
$|\eta(\mu)| < 1.05$	244623	100.0	9.0
Min. Pixel/TRT hits	226792	92.7	8.4
$2 < |d_0(\mu)| < 300$ mm	148983	65.7	5.5
$|z_0(\mu)| < 500$ mm	138737	93.1	5.1
Pass fake-muon veto	111797	80.6	4.1
Pass isolation	108147	96.7	4.0
Pass cosmic-muon veto	452	0.4	$1.7 \cdot 10^{-2}$
At least one DV	194	42.9	$7.2 \cdot 10^{-3}$
DV Fiducial Volume	168	86.6	$6.2 \cdot 10^{-3}$
$\chi^2/N_{DoF} < 5$	165	98.2	$6.1 \cdot 10^{-3}$
4 mm $< R_{PV-DV}$	161	97.6	$6.0 \cdot 10^{-3}$
Material Veto	104	64.6	$3.8 \cdot 10^{-3}$
$n_{Tracks}^{DV} \geq 3$	12	11.5	$4.4 \cdot 10^{-4}$
$m_{DV} > 20$ GeV	1	8.3	$3.7 \cdot 10^{-5}$

12.2   Signal Acceptance and Efficiency

Results are interpreted in the context of R-parity violating Supersymmetry model discussed in Section 3.4. In this simplified model, long-lived stop particles are pair produced in pp-collisions. In this model, the stop is the lightest SUSY particle, and decays via a non-zero but small λ'_{23k} coupling to a muon and quark.

The number of events selected, and total selection efficiency for the $E_{\mathrm{T}}^{\mathrm{miss}}$ triggered sample are shown in Table 12.3 for stops with $m(\tilde{t}) = 1.4$ TeV, and three lifetimes. Figure 12.1 also shows the expected number of stop events expected to pass the full selection as well as the total signal acceptance times efficiency in the $E_{\mathrm{T}}^{\mathrm{miss}}$ triggered sample, as a function of $m(\tilde{t})$ and $\tau(\tilde{t})$, for 136 fb^{-1} of integrated luminosity.

The total acceptance times efficiency for this signal model ranges from 33% to 35% for stops with lifetime $\tau(\tilde{t}) = 0.1$ ns, with little dependence on stop mass. For stops with lifetime $\tau(\tilde{t}) = 1$ ns, the total acceptance times efficiency ranges from 15% to 16%, while for stops with lifetime $\tau(\tilde{t}) = 0.01$ ns the total acceptance times efficiency ranges from 4% to 6%.

The Muon triggered signal selection efficiency and expected number of events for stops with $m(\tilde{t}) = 1.4$ TeV, and three lifetimes are shown in Table 12.4. Figure 12.2 also shows the total number of stop events expected to pass the full Muon triggered selection, as well as the total signal acceptance times efficiency in the Muon triggered sample as a function of stop mass and lifetime. Most signal events produce very high-p_{T} muons, which are not back-to-back in ϕ. The resulting large cluster-based $E_{\mathrm{T}}^{\mathrm{miss}}$ means that most signal events entering the $E_{\mathrm{T}}^{\mathrm{miss}}$ triggered sample. Though the Muon triggered sam-

Table 12.3: E_T^{miss} triggered sample cutflows for signal samples with $m(\tilde{t}) = 1.4$ TeV, and $\tau(\tilde{t}) = 0.01, 0.1,$ and 1 ns.

Selection	$m(\tilde{t}) = 1.4$ TeV, $\tau(\tilde{t}) = 0.01$ ns		$m(\tilde{t}) = 1.4$ TeV, $\tau(\tilde{t}) = 0.1$ ns		$m(\tilde{t}) = 1.4$ TeV, $\tau(\tilde{t}) = 1$ ns	
	Events	Overall Efficiency [%]	Events	Overall Efficiency [%]	Events	Overall Efficiency [%]
All	64.2	100.0	64.2	100.0	64.2	100.0
PV	64.2	100.0	64.2	100.0	64.2	100.0
E_T^{miss} Trigger	63.0	98.1	63.0	98.1	62.7	97.6
cluster-based $E_T^{\text{miss}} > 180$ GeV	60.9	94.8	61.0	95.0	60.6	94.3
At least one Muon	57.9	90.1	58.8	91.6	52.8	82.3
$p_T(\mu) > 25$ GeV	57.9	90.1	58.8	91.5	52.5	81.8
$|\eta(\mu)| < 2.5$	57.8	90.1	58.7	91.5	52.5	81.7
Min. Pixel/TRT hits	57.8	90.1	58.7	91.4	51.8	80.6
$2 < |d_0(\mu)| < 300$ mm	11.3	17.6	49.1	76.5	49.5	77.1
$|z_0(\mu)| < 500$ mm	11.3	17.6	49.1	76.5	49.3	76.8
Pass fake-muon veto	9.7	15.2	42.2	65.7	42.1	65.6
Pass isolation	9.4	14.7	41.6	64.8	41.4	64.5
Pass cosmic-muon veto	9.1	14.2	40.0	62.3	39.4	61.4
At least one DV	8.5	13.3	37.6	58.5	32.6	50.8
DV Fiducial Volume	8.4	13.1	37.1	57.8	31.2	48.6
$\chi^2/N_{DoF} < 5$	8.3	12.9	36.9	57.5	30.7	47.7
4 mm $< R_{\text{PV}-\text{DV}}$	6.6	10.3	35.4	55.1	30.3	47.1
Material Veto	5.3	8.2	31.0	48.3	22.2	34.6
$n_{\text{Tracks}}^{\text{DV}} \geq 3$	3.8	5.9	26.0	40.4	13.7	21.3
$m_{\text{DV}} > 20$ GeV	3.4	5.2	22.7	35.3	10.3	16.0

ple has very low efficiency for the $\tilde{t} \to \mu + j$ signals, it is used to retain sensitivity to other potential signals which might produce lower p_T, or fewer, muons.

For $\tilde{t} \to \mu + j$ signals, the analysis sensitivity depends largely on the stop particle lifetime. For particles with shorter lifetimes, for example $\tau = 0.01$ ns, most long-lived particles decay too close to the interaction point to pass the requirement that secondary vertices be displaced from any primary vertex in the event by more than 4 mm in the transverse plane. As seen in Figure 12.3, only 10% of
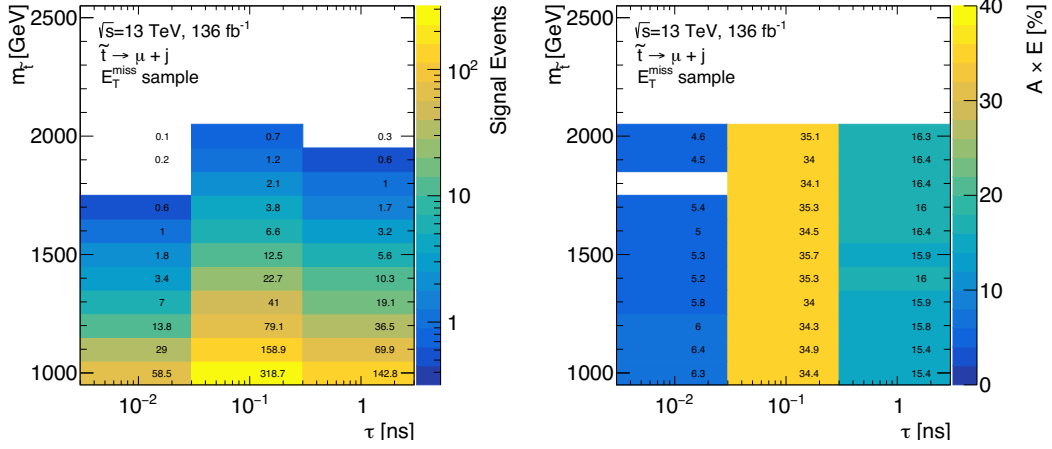
Figure 12.1: E_T^{miss} triggered sample expected signal yields, for three lifetimes and stop masses between 1 and 2 TeV. Left: The number of stop events expected to pass the full selection as a function of $m(\tilde{t})$ and $\tau(\tilde{t})$ Right: The total signal efficiency for selecting stop events as a function of $m(\tilde{t})$ vs. $\tau(\tilde{t})$.
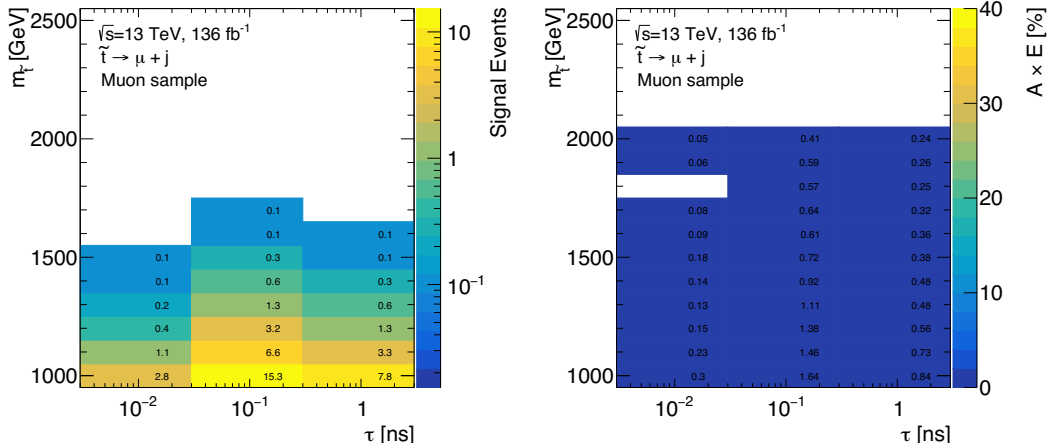

Figure 12.2: Muon triggered sample expected signal yields, for three lifetimes and stop masses between 1 and 2 TeV. Left: The number of stop events expected to pass the full selection as a function of $m(\tilde{t})$ and $\tau(\tilde{t})$ Right: The total signal efficiency for selecting stop events as a function of $m(\tilde{t})$ vs. $\tau(\tilde{t})$

stop particles with $\tau(\tilde{t}) = 0.01$ ns and $m(\tilde{t}) = 1$ TeV would decay inside the fiducial volume of

$4 < R_{xy} < 300$ mm and $|z| < 300$ mm.

Table 12.4: Muon triggered sample cutflows for signal samples with $m(\tilde{t}) = 1.4$ TeV, and $\tau(\tilde{t}) = 0.1$ and 1 ns.

Selection	$m(\tilde{t}) = 1.4$ TeV, $\tau(\tilde{t}) = 0.01$ ns		$m(\tilde{t}) = 1.4$ TeV, $\tau(\tilde{t}) = 0.1$ ns		$m(\tilde{t}) = 1.4$ TeV, $\tau(\tilde{t}) = 1$ ns	
	Events	Overall Efficiency [%]	Events	Overall Efficiency [%]	Events	Overall Efficiency [%]
All	64.2	100.0	64.2	100.0	64.2	100.0
PV	64.2	100.0	64.2	100.0	64.2	100.0
Muon Trigger	50.2	78.2	50.6	78.8	46.4	72.3
cluster-based $E_{\mathrm{T}}^{\mathrm{miss}} < 180$ GeV	2.5	3.9	2.6	4.0	2.5	3.9
At least one Muon	2.2	3.5	2.0	3.2	1.8	2.8
Trigger Match	2.1	3.3	1.9	3.0	1.7	2.6
$p_{\mathrm{T}}(\mu) > 62$ GeV	2.1	3.3	1.9	3.0	1.7	2.6
$|\eta(\mu)| < 1.05$	2.1	3.3	1.9	3.0	1.7	2.6
Min. Pixel/TRT hits	2.1	3.3	1.9	3.0	1.6	2.6
$2 < |d_0(\mu)| < 300$ mm	0.3	0.4	1.4	2.2	1.5	2.4
$|z_0(\mu)| < 500$ mm	0.3	0.4	1.4	2.2	1.5	2.4
Pass fake-muon veto	0.2	0.4	1.2	1.8	1.3	2.0
Pass isolation	0.2	0.3	1.1	1.8	1.3	2.0
Pass cosmic-muon veto	0.2	0.3	1.0	1.6	1.2	1.8
At least one DV	0.2	0.3	1.0	1.5	1.0	1.5
DV Fiducial Volume	0.2	0.3	1.0	1.5	0.9	1.4
$\chi^2/N_{DoF} < 5$	0.2	0.3	1.0	1.5	0.9	1.4
4 mm $< R_{\mathrm{PV-DV}}$	0.1	0.2	0.9	1.4	0.9	1.4
Material Veto	0.1	0.2	0.8	1.3	0.7	1.0
$n_{\mathrm{Tracks}}^{\mathrm{DV}} \geq 3$	0.1	0.2	0.7	1.1	0.4	0.6
$m_{\mathrm{DV}} > 20$ GeV	0.1	0.1	0.6	0.9	0.3	0.5

In contrast, signals with longer lifetimes produce more decays past $R_{xy} > 4$ mm. For example 71% of decays from stops with $\tau(\tilde{t}) = 0.1$ ns and $m(\tilde{t}) = 1$ TeV, and 70% of decays from stops with $\tau(\tilde{t}) = 1$ ns and $m(\tilde{t}) = 1$ TeV occur in the same fiducial fiducial volume of $4 < R_{xy} < 300$ mm and $|z| < 300$ mm.

Despite having similar acceptance, the analysis is more sensitive to stop particles with lifetime $\tau(\tilde{t}) = 0.1$ ns than $\tau(\tilde{t}) = 1$ ns. This difference in sensitivity is due to reduced reconstruction efficiency for
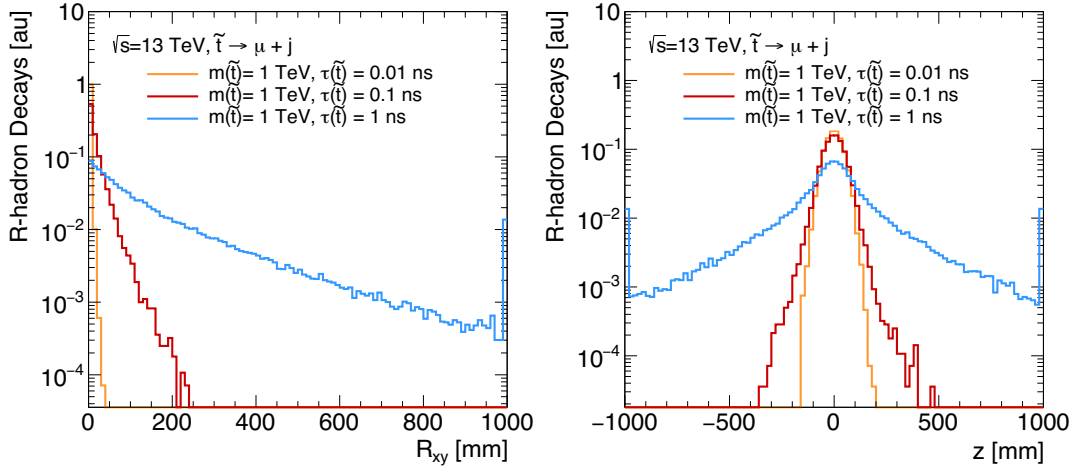
Figure 12.3: Left: The R-hadron decay position in R_{xy} for stop particles with $m(\tilde{t}) = 1$ TeV, and different lifetimes. Right: The R-hadron decay position decay position in z for stop particles with $m(\tilde{t}) = 1$ TeV, and different lifetimes.

decays with larger radial displacement. Because tracking efficiency degrades as a function of radial displacement, fewer muons are likely to be reconstructed if $\tau(\tilde{t}) = 1$ ns, and there are also fewer tracks available to form vertices at large radii. Secondary vertex reconstruction efficiency also degrades as a function of displacement, even after accounting for reduced tracking efficiency. The effect of the Material Veto on signal efficiency is also different for different lifetimes. For stop particles with $\tau(\tilde{t}) = 0.1$ ns, most decays occur at radii before beam-pipe and first Pixel layer. In contrast, stop particles with $\tau(\tilde{t}) = 1$ ns do decay at radii past the first Pixel layer, and 25% of vertices are rejected by the Material Veto.

The analysis sensitivity does not greatly change as a function of stop particle mass. The reason for this effect is that decay kinematics do not significantly change as a result of the stop mass. For

Table 12.5: Vertex Level Acceptance and Efficiencies for $m(\tilde{t}) = 1$ TeV, and $\tau(\tilde{t}) = 0.1$ and 1 ns

	$m(\tilde{t}) = 1.4$ TeV, $\tau(\tilde{t}) = 0.01$ ns	$m(\tilde{t}) = 1.4$ TeV, $\tau(\tilde{t}) = 0.1$ ns	$m(\tilde{t}) = 1.4$ TeV, $\tau(\tilde{t}) = 1$ ns
Acceptance			
DV Fiducial Volume	0.11	0.71	0.70
DV-PV Distance			
Efficiency			
Reco Matched			
$\chi^2/N_{dof} < 5$	0.64	0.63	0.28
$n^{\mathrm{DV}}_{\mathrm{Tracks}} \geq 3$			
$m_{\mathrm{DV}} > 20$ GeV			
Material Veto	1.00	0.90	0.75
Total Vertex Efficiency	0.07	0.40	0.15

the masses considered by this analysis, the stop will always be a heavy object undergoing a two-body decay. There are two minor competing effects in terms of signal acceptance and efficiency as the stop mass increases. Stop particles with larger mass tend to result in higher momentum muons and tracks. The higher momentum muons produce events with larger cluster-based $E_{\mathrm{T}}^{\mathrm{miss}}$, increasing the analysis sensitivity. However, higher momentum tracks, which are separated at a large angle result in slightly poorer vertex reconstruction efficiency. For the signal considered here, these two effects are small (order 1%) compared to the more substantial changes in sensitivity to lifetime.

12.3 DISTRIBUTIONS

Figure 12.4 shows the track multiplicity for displaced vertices in events which have at least one fully selected muon and at least one displaced vertex passing preselection. In events which have multiple

317

displaced vertices passing selection, all vertices are shown. The background predictions for events with

cosmic, fake, and heavy-flavor muons are shown as filled histograms. Vertices observed in data are

shown with black markers. Signal predictions are overlaid with dashed lines. There is good agreement

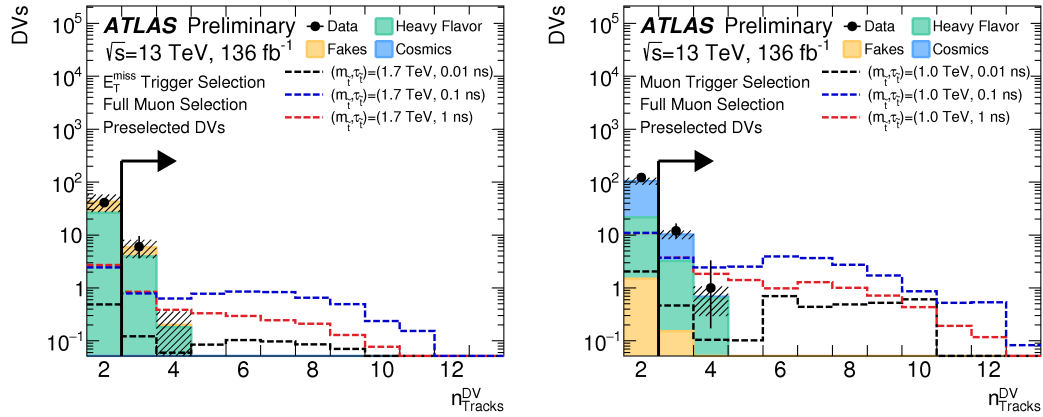between vertices observed in data, and the background prediction.

Figure 12.4: Displaced vertex track multiplicity. Events are required to have at least one fully selected muon, and at least one displaced vertex which passes preselection. Vertices observed in data are shown with black points. The heavy-flavor, fake, and cosmic muon backgrounds are shown as filled histograms. The statistical and systematic uncertainty on the total predicted background is shown with hashed lines. Signal predictions are overlaid with dashed lines. The requirement that $n_{\mathrm{Tracks}}^{\mathrm{DV}} \geq 3$ is visualized with a black arrow. Left: $E_{\mathrm{T}}^{\mathrm{miss}}$ triggered sample. Right: Muon triggered sample [1].

Figure 12.5 shows the displaced vertex mass for events which have at least one fully selected muon

and at least one displaced vertex with at least three tracks which passes preselection. In events which

have multiple displaced vertices passing selection, only the highest mass displaced vertex is shown.

The background predictions for events with cosmic, fake, and heavy-flavor muons are shown as filled

histograms. Vertices observed in data are shown with black markers. Signal predictions are overlaid

with dashed lines. There is good agreement between vertices observed in data, and the background
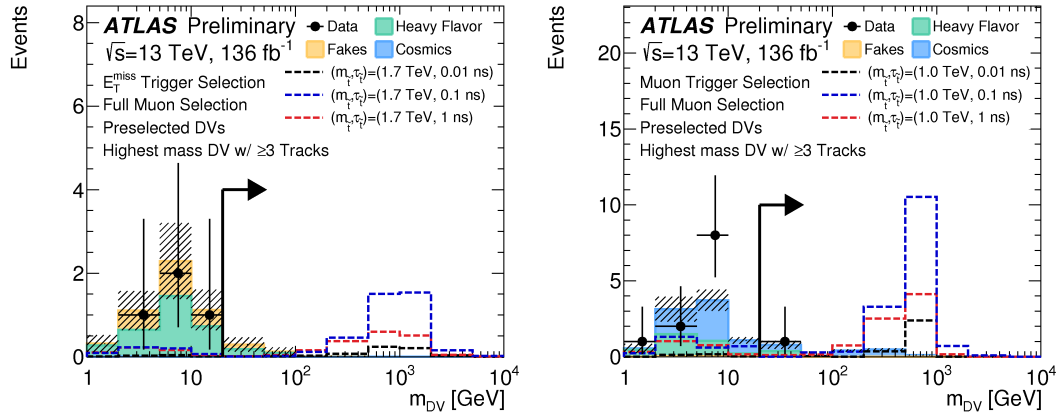
318

prediction.

Figure 12.5: Displaced vertex mass. Events are required to have at least one fully selected muon, and at least one displaced vertex which passes preselection with three or more associated tracks. Only the displaced vertex with the largest invariant mass is shown per event. Vertices observed in data are shown with black points. The heavy-flavor, fake, and cosmic muon backgrounds are shown as filled histograms. The statistical and systematic uncertainty on the total predicted background is shown with hashed lines. Signal predictions are overlaid with dashed lines. The requirement that $m_{\mathrm{DV}} > 20$ GeV is visualized with a black arrow. Left: $E_{\mathrm{T}}^{\mathrm{miss}}$ triggered sample. Right Muon triggered sample [1].

Cutflows for the $E_{\mathrm{T}}^{\mathrm{miss}}$ triggered sample and Muon triggered sample are visualized in Figure 12.6.

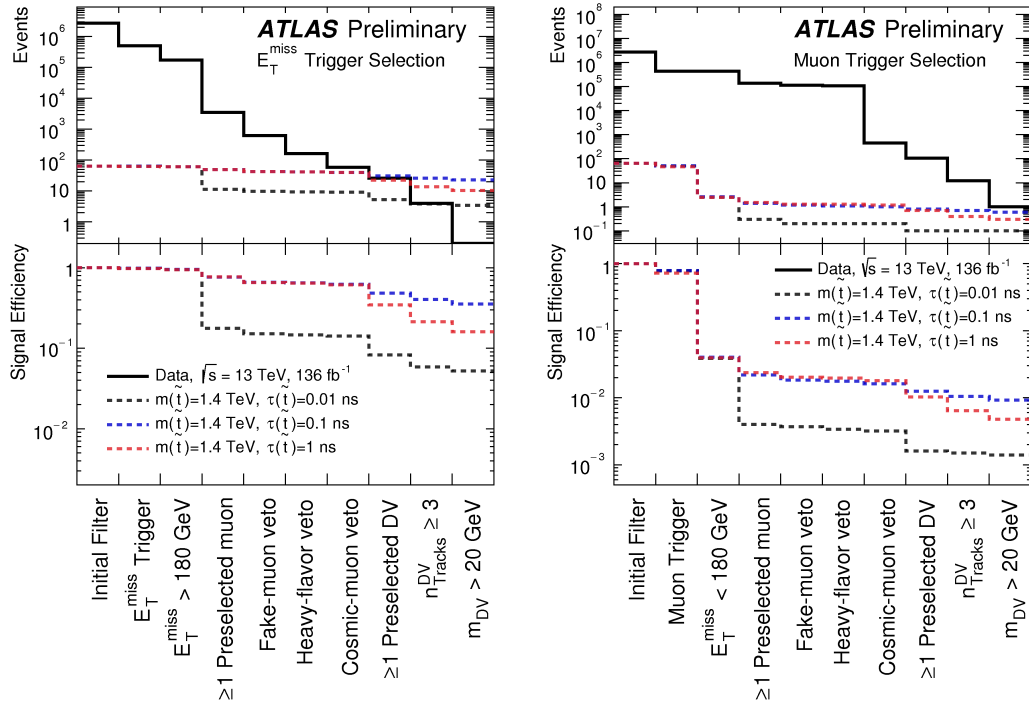Cutflows are shown for event yields in data and for three example signal points.

Figure 12.6: The cutflow is visualized for the E_T^{miss} triggered sample (left) and the Muon triggered sample (right) in data and for three example signal points. The first selection shown, referred to as the Initial Filter, is the total number of events events surviving n-tuple skimming. N-tuples were skimmed to require that each event have at least one baseline muon with $|d_0(\mu)| > 1.0$ mm. For subsequent selections the relative and total efficiency is given with respect to the number of events surviving the n-tuple skimming. Muon and displaced vertex preselection criteria are combined into a single point.

12.4.1   Simplified Model Interpretation

The expected and observed 95% CL exclusion limits on the mass $m(\tilde{t})$ of a long-lived stop squark as a function of its mean proper lifetime $\tau(\tilde{t})$ are shown in Figure 12.7. For the stop masses and lifetimes considered, the E_T^{miss} trigger Signal Region provides the best sensitivity. Contours of constant values of $\lambda'_{32k} \cos\theta_t$ are also shown where θ_t is the mixing angle between the right- and left-handed stop squarks.
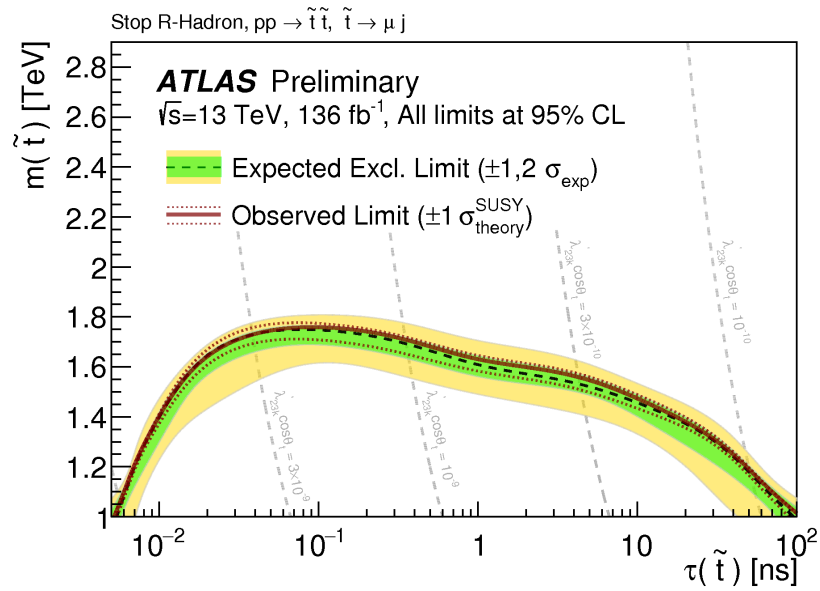
Figure 12.7: Observed and expected exclusion limits at 95% CL on $m(\tilde{t})$ as a function of $\tau(\tilde{t})$ are shown along with contours showing fixed values of $\lambda'_{23k} \cos\theta_t$. Results are interpreted in terms of di-stop production, where the stop decays via a λ'_{23k} R-parity violating coupling. Experimental and theoretical uncertainties are shown. [1].

For a mean proper lifetime of $\tau(\tilde{t}) = 0.1$ ns, masses below roughly $m(\tilde{t}) = 1.7$ TeV are excluded. For the range of mean proper lifetimes between $\tau(\tilde{t}) = 0.01$ ns and $\tau(\tilde{t}) = 30$ ns, masses below 1.3 TeV are excluded. For $m(\tilde{t}) = 1$ TeV, values of $\lambda'_{23k} \cos \theta_t$ between roughly 10^{-8} and 10^{-10} are excluded at 95% CL.

Figure 12.8 shows the 95% CL upper limits on the production cross section of these signals as a function of $m(\tilde{t})$ for various values of $\tau(\tilde{t})$. For a mean proper lifetime of $\tau(\tilde{t}) = 0.1$ ns, cross section upper limits are set below 100 ab. For mean proper lifetimes between $\tau(\tilde{t}) = 0.01$ ns and $\tau(\tilde{t}) = 100$ ns, these limits are the strictest to date on models with a metastable stop squark decaying via a λ'_{ijk} R-parity violating coupling.
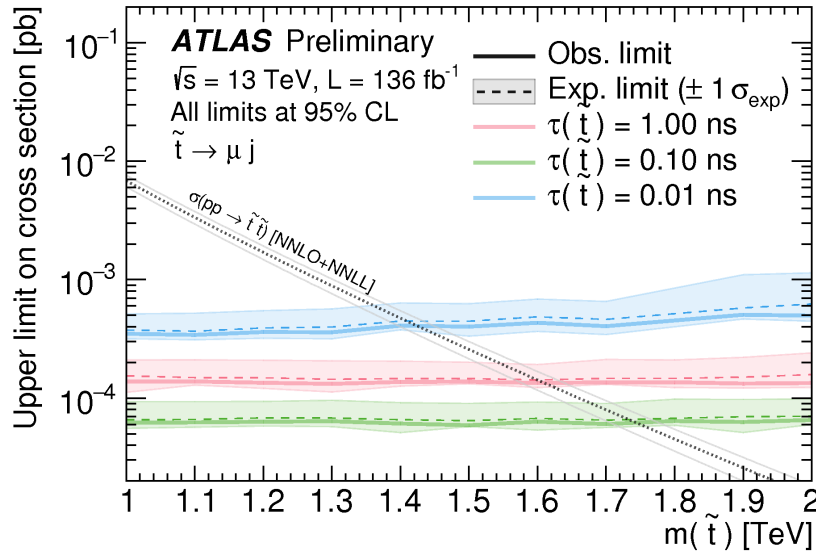

Figure 12.8: Cross section upper limits are shown as a function of $m(\tilde{t})$ for several values of $\tau(\tilde{t})$. Results are interpreted in terms of di-stop production, where the stop decays via a λ'_{23k} R-parity violating coupling. The nominal signal production cross section and its theoretical uncertainty are also indicated [1]

Signal Region	$\langle\epsilon\sigma\rangle^{95}_{\text{obs}}[\text{fb}]$	S^{95}_{obs}	S^{95}_{exp}	CL_B	$p(s=0)$
$E^{\text{miss}}_{\text{T}}$ triggered SR	0.02	3.1	$3.1^{+1.1}_{-0.1}$	0.12	0.50
Muon triggered SR	0.03	3.7	$4.2^{+1.6}_{-1.0}$	0.28	0.50

Table 12.6: Left to right: 95% CL upper limits on the visible cross section ($\langle\epsilon\sigma\rangle^{95}_{\text{obs}}$) and on the number of signal events (S^{95}_{obs}). The third column (S^{95}_{exp}) shows the 95% CL upper limit on the number of signal events, given the expected number (and $\pm1\sigma$ excursions on the expectation) of background events. The last two columns indicate the CL_B value, i.e. the confidence level observed for the background-only hypothesis, and the discovery p-value ($p(s=0)$).

12.4.2 MODEL-INDEPENDENT LIMITS

Model-independent 95% CL cross section limits are also obtained. At 95% CL, the $E^{\text{miss}}_{\text{T}}$ triggered signal region excludes visible BSM cross sections above 0.02 fb while the Muon triggered signal excludes visible BSM cross sections above 0.03 fb. The results of these model-independent fits can be found in Table 12.6.

Part V

Conclusions

13

Conclusions and Outlook

This thesis describes a search for long-lived particles decaying to a muon and a hadronic jet, as predicted in Supersymmetry models where R-parity is violated. Data used correspond to 136 fb^{-1} of $\sqrt{s} = 13$ TeV pp-collisions, collected by the ATLAS experiment in 2016-2018. Events containing a displaced vertex and a displaced muon are selected. Two orthogonal signal regions are employed, using $E_\mathrm{T}^\mathrm{miss}$- and muon-based triggers. For these signal regions, the predicted Standard Model backgrounds are $0.43 \pm 0.16 \pm 0.16$ events and $1.88 \pm 0.20 \pm 0.28$ events, respectively. The observed yields are 0 and 1 events, respectively, in agreement with the predicted background yields.

Limits are placed on a simplified Supersymmetry signal model of pair-produced, long-lived stop squarks that decay via an R-parity violating coupling to a hadronic jet and a muon. For a proper lifetime of 100 ps, stop squark masses are excluded at the 95% CL up to roughly 1.75 TeV. Weakened

limits are obtained at smaller and larger proper lifetimes.

This search benefits from many improvements with respect to the previous versions of this analysis, performed with Run 1 LHC data. In particular, the addition of a $E_\mathrm{T}^\mathrm{miss}$ trigger to the analysis improved the total signal efficiency by over 40% for all stop masses and lifetimes considered by the analysis. This analysis also benefits from improved cosmic muon rejection, and a modified displaced vertex selection. The Run 1 version of this analysis required displaced vertices have at least five associated tracks, one of which was a muon, and $m_\mathrm{DV} > 10$ GeV. This analysis only requires displaced vertices have at least three associated tracks, $m_\mathrm{DV} > 20$ GeV, and does not require the muon be a part of the displaced vertex. These modified requirements improve the overall signal efficiency by ten to twenty percent, depending on the stop lifetime.

ATLAS is not scheduled to take more data until 2021, and it will take several years to double the size of the Run 2 ATLAS dataset. In the meantime, there are several improvements which can be made to this analysis using the currently available Run 2 dataset.

Perhaps the most important update to consider is to the track extrapolation method used to reconstruct secondary vertices. Switching to a more detailed track extrapolation method should reduce the rate of displaced vertices reconstructed from randomly crossing fake tracks. With a reduced background, it would be possible to loosen one or more requirements in the event selection. For example, the requirement on the displaced vertex mass could be reduced in order to improve sensitivity to lower mass long-lived particles.

There are also several possible extensions of this search which should be considered. For example, an additional signal region could be designed to improve sensitivity to long-lived particles with shorter

lifetimes ($10^{-3} < \tau < 10^{-1}$ ns). The first step in designing such a signal region would be to reduce the transverse impact parameter requirements on displaced muons, as well as the displaced tracks used in secondary vertex reconstruction. It would be particularly interesting to reduce these requirements from $|d_0| < 2.0$ mm to $|d_0| < 0.5$ mm. Such a change would require adjustments to the secondary vertex reconstruction algorithm, and result in an increase in background. However, additional requirements on the event could be made in order to compensate for the increase in background. For example, one could require two displaced vertices, or two displaced muons, per event.

Another possible improvement that should be considered is to use a standard single muon trigger, designed for prompt leptons, to collect events. This sample could be used to create a signal region for events with muons that have transverse impact parameters $|d_0| < 10$ mm and transverse momenta $p_{\mathrm{T}} > 25$ GeV. This strategy would help improve sensitivity to signal models with lower momentum muons. This strategy would still retain sensitivity to a wide range of lifetimes, because long-lived particle decay positions are described by an exponential distribution. This strategy would eliminate the need to run Large Radius Tracking on events, and could open up the possibility of reconstructing secondary vertices in the full ATLAS dataset.

There are also improvements to this analysis which can be made with future ATLAS data. In Run 3, ATLAS will replace parts of the Inner station of the Muon Spectrometer end-cap with detectors that provide improved triggering capabilities. This upgrade is specifically designed to reduce the rate of fake muon triggers in the end-cap. With this upgrade, ATLAS will be able to trigger on displaced muon signatures in the end-cap, improving the acceptance of the Muon triggered sample.

A

Displaced Vertex Event Displays

The following distributions are simplified event displays representing reconstructed displaced vertices. Events from signal Monte Carlo are shown, as events from data.

The displaced vertex position is shown in the x-y plane. Displaced vertices are required to be inside the analysis fiducial volume of $R_{xy} < 300$ mm and $|z| < 300$ mm. Displaced vertices must also be more than 4 mm away in the transverse plane from any primary or pile-up vertex in the event, and have a vertex quality of fit $\chi^2/N_{DoF} < 5$. No material veto is applied. However, guidelines for Pixel layers are draw in gray, in order to show which vertices are likely to be material interactions.

Only tracks associated to displaced vertices are shown. Tracks which are also associated to combined muons are shown in red, and tracks which are not associated to muons are shown in blue. The length of the track is proportional to its p_{T}.

A.1 Displaced Vertices in Signal Monte Carlo

The following event displays are from a Monte Carlo stop signal sample with $m(\tilde{t}) = 1.7$ TeV and $\tau(\tilde{t}) = 0.1$ ns.

In many events, the stop decay to a muon and a jet is correctly reconstructed as a single displaced vertex. The muon has large transverse momentum, and it is easy to discern the daughter particles from the hadronic jet. Some events even have two well reconstructed displaced vertices.

However, in other events, none of the daughter particles from the displaced vertex are identified as a combined muon. In some cases, this is clearly a case of failed muon identification. In other scenarios, the muon is not associated to the displaced vertex at all. The displaced vertex appears to be formed of particles from the jet only.

Most well reconstructed displaced vertices, which have high track multiplicity and large reconstructed mass, are located within the first layer of the Pixel detector. Displaced vertices which are poorly reconstructed tend to be located inside the various layers of the Pixel, or past the Pixel detector altogether. These poorly reconstructed vertices appear to either be split vertices from stop particle decays, hadronic interactions, or random track crossings.
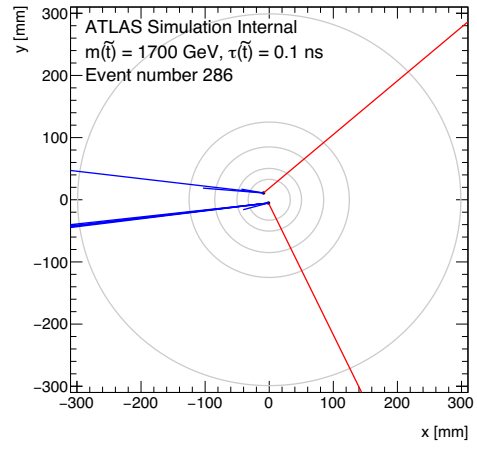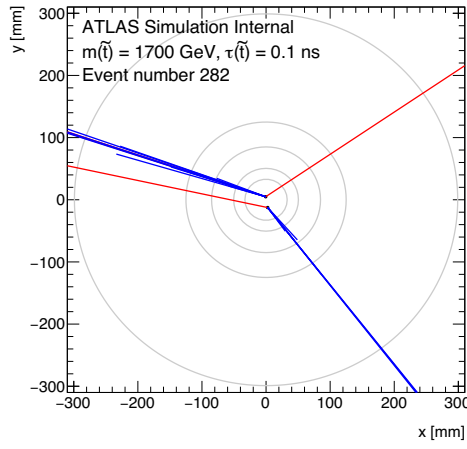
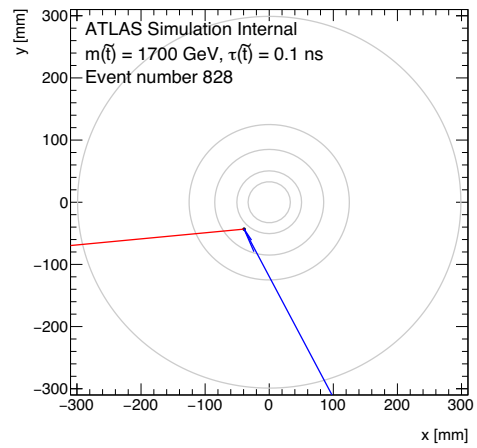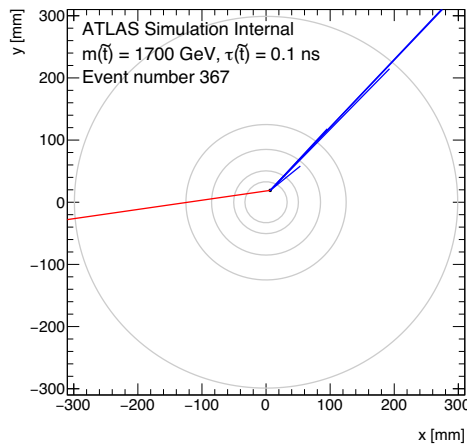Figure A.1: $\tilde{t} \rightarrow \mu + $ jet Vertex Event Displays

Figure A.2: $\tilde{t} \rightarrow \mu + $ jet Vertex Event Displays

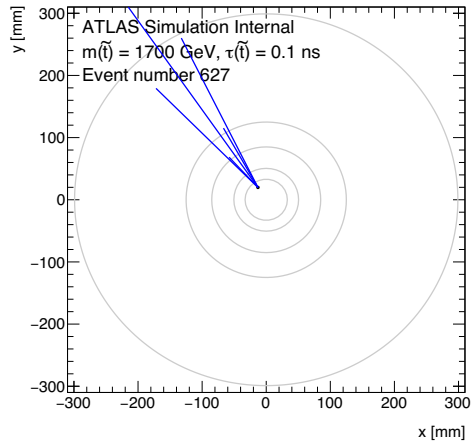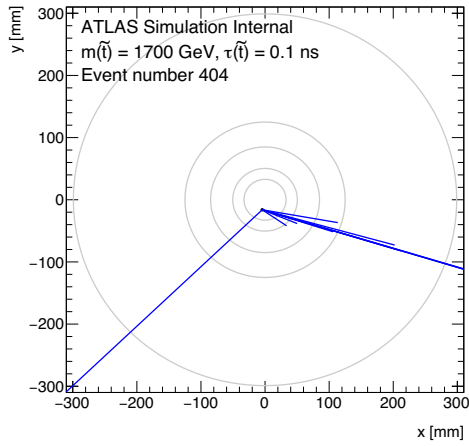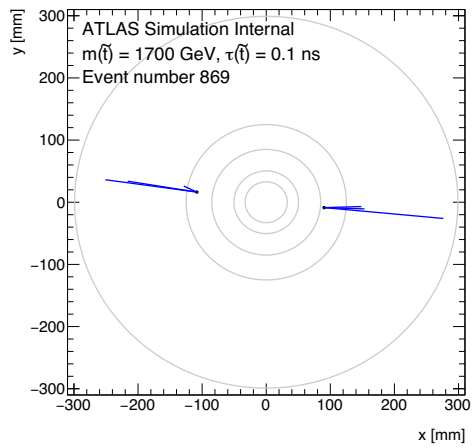Figure A.3: $\tilde{t} \rightarrow \mu + $ jet Vertex Event Displays

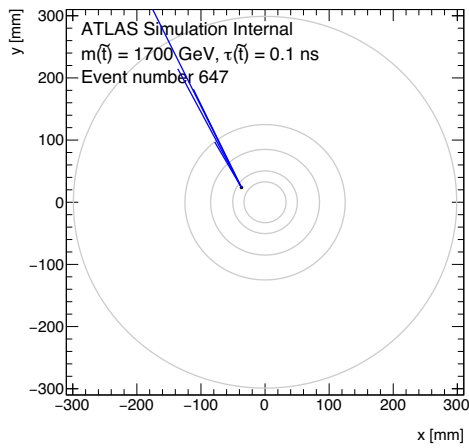Figure A.4: $\tilde{t} \rightarrow \mu + $ jet Vertex Event Displays

331

A.2 Displaced Vertices in Muon Control Regions
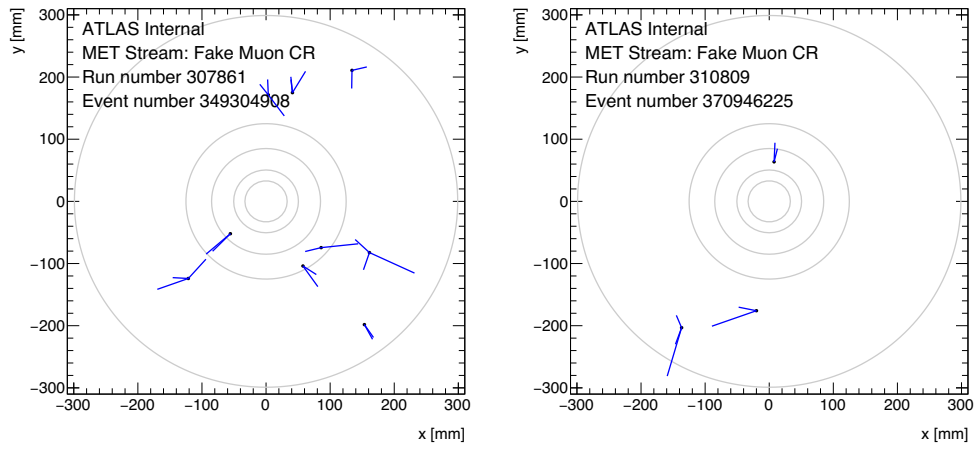
A.2.1 Fake Control Region
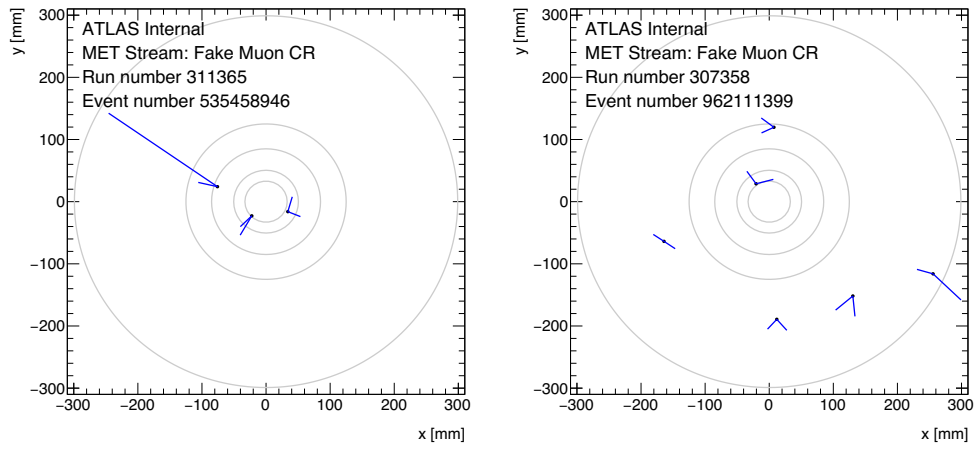

Figure A.5: Fake CR Vertex Event Displays

Figure A.6: Fake CR Vertex Event Displays
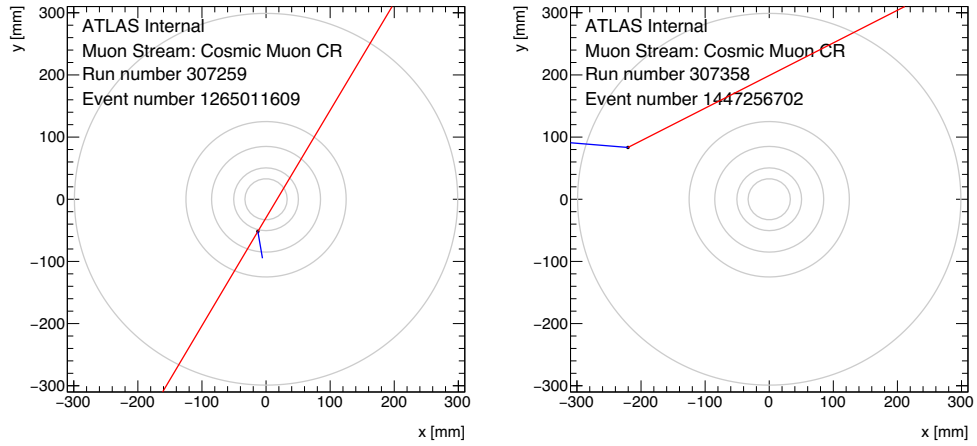
A.2.2 Cosmic Control Region

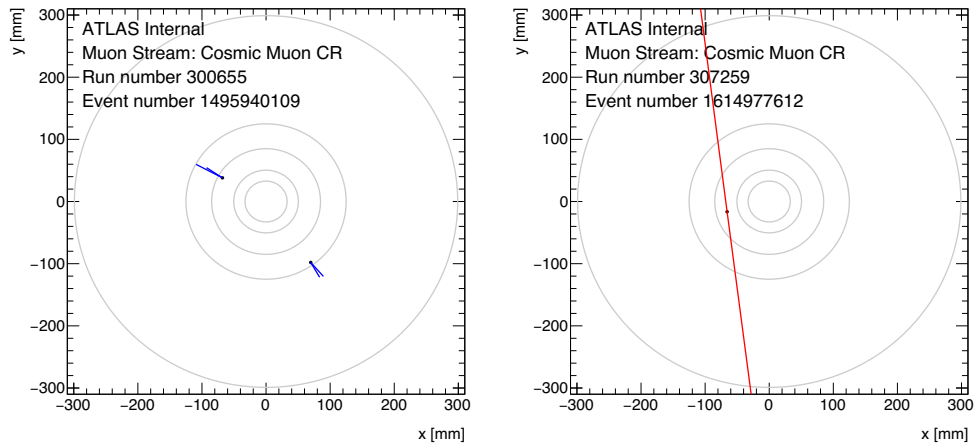Figure A.7: Cosmic CR Vertex Event Displays

Figure A.8: Cosmic CR Vertex Event Displays
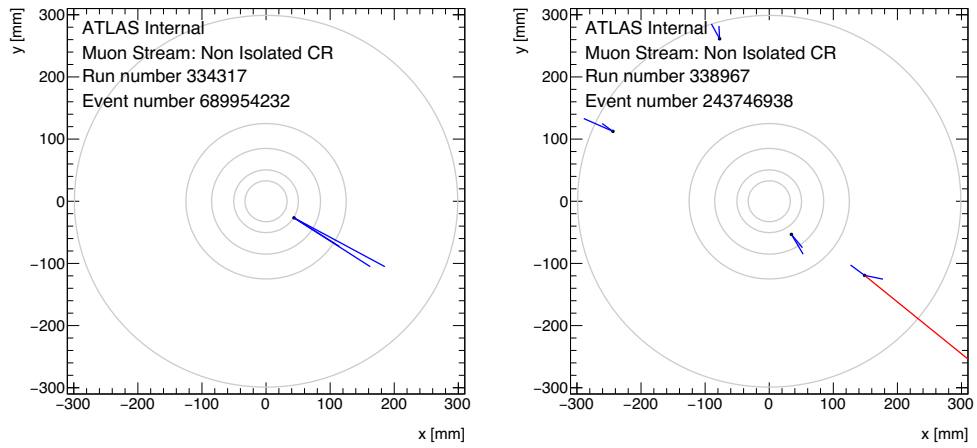
A.2.3 Heavy Flavor Control Region

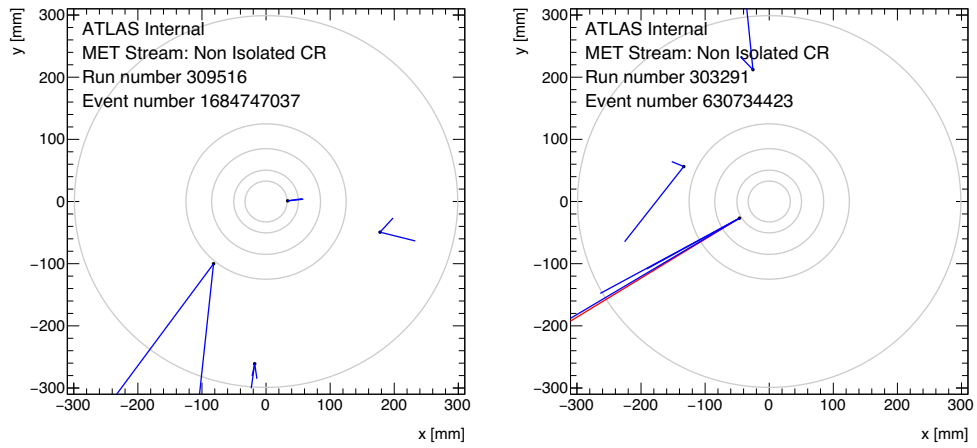Figure A.9: Heavy Flavor CR Vertex Event Displays

Figure A.10: Heavy Flavor CR Vertex Event Displays

References

[1] ATLAS Collaboration. Search for long-lived, massive particles in events with a displaced vertex and muon in pp collisions at $\sqrt{s} = 13$ TeV with the ATLAS detector. ATLAS-CONF-2019-006, 2019. URL https://cds.cern.ch/record/2668377.

[2] ATLAS Collaboration. Search for long-lived, massive particles in events with a displaced vertex and muon in pp collisions at $\sqrt{s} = 13$ TeV with the ATLAS detector. 2018. URL https://cds.cern.ch/record/2633973.

[3] Lawrence Lee, Christian Ohm, Abner Soffer, and Tien-Tien Yu. Collider searches for long-lived particles beyond the standard model. *Progress in Particle and Nuclear Physics*, 2019. ISSN 0146-6410. doi: https://doi.org/10.1016/j.ppnp.2019.02.006. URL http://www.sciencedirect.com/science/article/pii/S0146641019300109.

[4] Stephen P. Martin. A Supersymmetry primer. *Adv. Ser. Direct. High Energy Phys.*, 18:1, 1998. doi: 10.1142/9789812839657_0001,10.1142/9789814307505_0001.

[5] Matic Lubej. Standard model. 2015. URL https://www.physik.uzh.ch/groups/serra/StandardModel.html.

[6] Mary K. Gaillard, Paul D. Grannis, and Frank J. Sciulli. The standard model of particle physics. *Rev. Mod. Phys.*, 71:S96–S111, Mar 1999. doi: 10.1103/RevModPhys.71.S96. URL https://link.aps.org/doi/10.1103/RevModPhys.71.S96.

[7] S. F. Novaes. Standard model: An introduction, 2000.

[8] ATLAS Collaboration. Measurement of the Higgs boson mass in the $H \to ZZ^* \to 4\ell$ and $H \to \gamma\gamma$ channels with $\sqrt{s} = 13$ TeV pp collisions using the ATLAS detector. *Phys. Lett. B*, 784:345, 2018. doi: 10.1016/j.physletb.2018.07.050.

[9] et al. Tanabashi, M. Review of particle physics. *Phys. Rev. D*, 98:030001, Aug 2018. doi: 10.1103/PhysRevD.98.030001. URL https://link.aps.org/doi/10.1103/PhysRevD.98.030001.

[10] Gerard 't Hooft. Computation of the Quantum Effects Due to a Four-Dimensional Pseudoparticle. *Phys. Rev.*, D14:3432–3450, 1976. doi: 10.1103/PhysRevD.18.2199.3,10.1103/PhysRevD.14.3432.

[11] V. A. Kuzmin, V. A. Rubakov, and M. E. Shaposhnikov. On the Anomalous Electroweak Baryon Number Nonconservation in the Early Universe. *Phys. Lett.*, 155B:36, 1985. doi: 10. 1016/0370-2693(85)91028-7.

[12] Christoph Borschensky, Michael Krämer, Anna Kulesza, Michelangelo Mangano, Sanjay Padhi, Tilman Plehn, and Xavier Portell. Squark and gluino production cross sections in pp collisions at $\sqrt{s}$ = 13, 14, 33 and 100 TeV. *Eur. Phys. J.*, C74(12):3174, 2014. doi: 10.1140/epjc/s10052-014-3174-y.

[13] Gian F Giudice, Riccardo Rattazzi, Markus A Luty, and Hitoshi Murayama. Gaugino mass without singlets. *Journal of High Energy Physics*, 1998(12):027–027, dec 1998. doi: 10.1088/1126-6708/1998/12/027. URL https://doi.org/10.1088%2F1126-6708% 2F1998%2F12%2F027.

[14] Clifford Cheung, Gilly Elor, Lawrence J. Hall, and Piyush Kumar. Origins of hidden sector dark matter ii: collider physics. *Journal of High Energy Physics*, 2011(3):85, Mar 2011. ISSN 1029-8479. doi: 10.1007/JHEP03(2011)085. URL https://doi.org/10.1007/JHEP03(2011) 085.

[15] Nima Arkani-Hamed and Savas Dimopoulos. Supersymmetric unification without low energy supersymmetry and signatures for fine-tuning at the LHC. *Journal of High Energy Physics*, 2005(06):073–073, jun 2005. doi: 10.1088/1126-6708/2005/06/073. URL https: //doi.org/10.1088%2F1126-6708%2F2005%2F06%2F073.

[16] G.F. Giudice and A. Romanino. Split supersymmetry. *Nuclear Physics B*, 699(1):65 – 89, 2004. ISSN 0550-3213. doi: https://doi.org/10.1016/j.nuclphysb.2004.08.001. URL http: //www.sciencedirect.com/science/article/pii/S0550321304005759.

[17] Herbert K. Dreiner. An Introduction to explicit R-parity violation. 1997. doi: 10.1142/ 9789814307505_0017. [Adv. Ser. Direct. High Energy Phys.21,565(2010)].

[18] R. Barbier et al. R-parity violating supersymmetry. *Phys. Rept.*, 420:1–202, 2005. doi: 10.1016/ j.physrep.2005.08.006.

[19] Tadashi Kon, Tetsuro Kobayashi, and Shoichi Kitamura. Signatures of scalar top with R-parity breaking coupling at HERA. *Phys. Lett.*, B333:263–270, 1994. doi: 10.1016/0370-2693(94) 91042-1.

[20] C. Friberg, E. Norrbin, and T. Sjostrand. QCD aspects of leptoquark production at HERA. *Phys. Lett. B*, 403:329–334, 1997. doi: 10.1016/S0370-2693(97)00543-1.

[21] Matthew J. Strassler and Kathryn M. Zurek. Discovering the Higgs through highly-displaced vertices. *Phys. Lett. B*, 661:263–267, 2008. doi: 10.1016/j.physletb.2008.02.008.

[22] Yanou Cui and Brian Shuve. Probing Baryogenesis with Displaced Vertices at the LHC. *JHEP*, 02:049, 2015. doi: 10.1007/JHEP02(2015)049.

[23] Takehiko Asaka and Mikhail Shaposhnikov. The nuMSM, dark matter and baryon asymmetry of the universe. *Phys. Lett. B*, 620:17–26, 2005. doi: 10.1016/j.physletb.2005.06.020.

[24] B. C. Allanach, M. A. Bernhardt, H. K. Dreiner, C. H. Kom, and P. Richardson. Mass Spectrum in R-Parity Violating mSUGRA and Benchmark Points. *Phys. Rev. D*, 75:035002, 2007. doi: 10.1103/PhysRevD.75.035002.

[25] Borut Bajc, Junji Hisano, Takumi Kuwahara, and Yuji Omura. Threshold corrections to dimension-six proton decay operators in non-minimal susy su(5) guts. *Nuclear Physics B*, 910: 1 – 22, 2016. ISSN 0550-3213. doi: https://doi.org/10.1016/j.nuclphysb.2016.06.017. URL http://www.sciencedirect.com/science/article/pii/S0550321316301596.

[26] Alexei Yu. Smirnov and Francesco Vissani. Upper bound on all products of R-parity violating couplings lambda-prime and lambda-prime-prime from proton decay. *Phys. Lett.*, B380:317–323, 1996. doi: 10.1016/0370-2693(96)00495-9.

[27] ATLAS Collaboration. Search for B-L R-parity-violating top squarks in $\sqrt{s}$=13 TeV pp collisions with the ATLAS experiment. *Phys. Rev. D*, 97(3):032003, 2018. doi: 10.1103/PhysRevD.97.032003.

[28] CMS Collaboration. Search for pair production of second-generation leptoquarks at $\sqrt{s} = 13$ TeV. *Phys. Rev. D*, 99(032014), 2019. doi: 10.1103/PhysRevD.99.032014.

[29] CMS Collaboration. Search for new long-lived particles at $\sqrt{s} = 13$ TeV. *Phys. Lett. B*, 780: 432–454, 2018. doi: 10.1016/j.physletb.2018.03.019.

[30] CMS Collaboration. Search for Displaced Supersymmetry in events with an electron and a muon with large impact parameters. *Phys. Rev. Lett.*, 114(6):061801, 2015. doi: 10.1103/PhysRevLett.114.061801.

[31] CMS Collaboration. Search for long-lived particles decaying into displaced jets in proton-proton collisions at $\sqrt{s} = 13$ TeV. *Phys. Rev. D*, 99(3):032011, 2019. doi: 10.1103/PhysRevD.99.032011.

[32] ATLAS Collaboration. Search for displaced vertices arising from decays of new heavy particles in 7 TeV pp collisions at ATLAS. *Phys. Lett. B*, 707:478–496, 2012. doi: 10.1016/j.physletb.2011.12.057.

[33] ATLAS Collaboration. Search for long-lived, heavy particles in final states with a muon and multi-track displaced vertex in proton-proton collisions at $\sqrt{s} = 7$ TeV with the ATLAS detector. *Phys. Lett. B*, 719:280–298, 2013. doi: 10.1016/j.physletb.2013.01.042.

[34] CMS Collaboration. Search for decays of stopped exotic long-lived particles produced in proton-proton collisions at $\sqrt{s} = 13$ TeV. *JHEP*, 05:127, 2018. doi: 10.1007/JHEP05(2018)127.

[35] ATLAS Collaboration. Search for long-lived stopped R-hadrons decaying out-of-time with pp collisions using the ATLAS detector. *Phys. Rev.*, D88(11):112003, 2013. doi: 10.1103/PhysRevD.88.112003.

[36] ATLAS Collaboration. Search for heavy charged long-lived particles in proton-proton collisions at $\sqrt{s} = 13$ TeV using an ionisation measurement with the ATLAS detector. *Phys. Lett.*, B788:96–116, 2019. doi: 10.1016/j.physletb.2018.10.055.

[37] ATLAS Collaboration. Search for heavy charged long-lived particles in the ATLAS detector in 31.6 fb^{-1} of proton-proton collision data at $\sqrt{s} = 13$ TeV. 2019.

[38] B.J. Holzer. Introduction to Particle Accelerators and their Limitations. (arXiv:1705.09601): 29–50. 22 p, May 2017. URL https://cds.cern.ch/record/2203629. 22 pages, contribution to the CAS - CERN Accelerator School: Plasma Wake Acceleration, CERN, Geneva, Switzerland, 23 - 29 Nov 2014, pp.29-50.

[39] Lyndon Evans and Philip Bryant. LHC Machine. *JINST*, 3:S08001, 2008. doi: 10.1088/1748-0221/3/08/S08001.

[40] Oliver Sim Brüning, Paul Collier, P Lebrun, Stephen Myers, Ranko Ostojic, John Poole, and Paul Proudlock. *LHC Design Report*. CERN Yellow Reports: Monographs. CERN, Geneva, 2004. URL http://cds.cern.ch/record/782076.

[41] Radiofrequency cavities. Sep 2012. URL http://cds.cern.ch/record/1997424.

[42] TOTEM Collaboration. First measurement of elastic, inelastic and total cross-section at sqrt(s)= 13 TeV by TOTEM and overview of cross-section data at LHC energies. First measurement of elastic, inelastic and total cross-section at $\sqrt{s} = 13$ TeV by TOTEM and overview of cross-section data at LHC energies. *Eur. Phys. J. C*, 79(CERN-EP-2017-321. 2):103. 16 p, Dec 2017. URL http://cds.cern.ch/record/2296409. 16 pages, 7 figures, 5 tables. Three figures, the references and the author list was updated, presentation is improved. Submitted for a publication to Phys. Rev. D.

[43] AC Team. Diagram of an LHC dipole magnet. Schéma d'un aimant dipôle du LHC. Jun 1999. URL https://cds.cern.ch/record/40524.

[44] B. Salvachua. Overview of proton runs during run 2. 2019. URL https://indico.cern.ch/event/751857/contributions/3259373/attachments/1783143/2910577/belen-Evian2019.pdf.

[45] ATLAS Collaboration. Luminosity public results. 2019. URL https://twiki.cern.ch/twiki/bin/view/AtlasPublic/LuminosityPublicResultsRun2.

[46] ATLAS Collaboration. Luminosity determination in *pp* collisions at $\sqrt{s} = 8$ TeV using the ATLAS detector at the LHC. *Eur. Phys. J. C*, 76:653, 2016. doi: 10.1140/epjc/s10052-016-4466-1.

[47] S van der Meer. Calibration of the effective beam height in the ISR. Technical Report CERN-ISR-PO-68-31. ISR-PO-68-31, CERN, Geneva, 1968. URL https://cds.cern.ch/record/296752.

[48] V Cindro, D Dobos, I Dolenc, H Frais-Kölbl, S Gorisek, E Griesmayer, H Kagan, G Kramberger, B Macek, I Mandic, M Mikuz, M Niegl, H Pernegger, D Tardif, W Trischuk, P Weilhammer, and M Zavrtanik. The ATLAS beam conditions monitor. *JINST*, 3:P02004, 2008. doi: 10.1088/1748-0221/3/02/P02004. URL http://cds.cern.ch/record/1094819.

[49] G Avoni, M Bruschi, G Cabras, D Caforio, N Dehghanian, A Floderus, B Giacobbe, F Giannuzzi, F Giorgi, P Grafström, V Hedberg, F Lasagni Manghi, S Meneghini, J Pinfold, E Richards, C Sbarra, N Semprini Cesari, A Sbrizzi, R Soluk, G Ucchielli, S Valentinetti, O Viazlo, M Villa, C Vittori, R Vuillermet, and A Zoccoli. The new LUCID-2 detector for luminosity measurement and monitoring in ATLAS. *JINST*, 13(07):P07017. 33 p, 2018. doi: 10.1088/1748-0221/13/07/P07017. URL http://cds.cern.ch/record/2633501.

[50] ATLAS Collaboration. The ATLAS Experiment at the CERN Large Hadron Collider. *JINST*, 3:S08003, 2008. doi: 10.1088/1748-0221/3/08/S08003.

[51] Dan Green. *At the leading edge*. World Scientific, Batavia, Illinois, Dec 2019.

[52] Maurice Garcia-Sciveres and Norbert Wermes. A review of advances in pixel detectors for experiments with high rate and radiation. *Reports on Progress in Physics*, 81(6):066101, may 2018. doi: 10.1088/1361-6633/aab064. URL https://doi.org/10.1088%2F1361-6633%2Faab064.

[53] ATLAS Collaboration. Study of the material of the ATLAS inner detector for Run 2 of the LHC. *JINST*, 12:P12009, 2017. doi: 10.1088/1748-0221/12/12/P12009.

[54] ATLAS Collaboration. ATLAS pixel detector electronics and sensors. *Journal of Instrumentation*, 3(07):P07007–P07007, jul 2008. doi: 10.1088/1748-0221/3/07/p07007. URL https://doi.org/10.1088%2F1748-0221%2F3%2F07%2Fp07007.

[55] ATLAS Collaboration. ATLAS Insertable B-Layer Technical Design Report. Technical Report CERN-LHCC-2010-013. ATLAS-TDR-19, Sep 2010. URL https://cds.cern.ch/record/1291633.

[56] T. Kondo. Selected photos of ATLAS SCT: Design. 2007. URL http://atlas.kek.jp/sub/photos/SCTJ/SCTJDesign/SCTJDesign.html.

[57] Dai Kobayashi. Performance of the ATLAS muon trigger in run 1 and upgrades for run 2. *Journal of Physics: Conference Series*, 664(9):092016, dec 2015. doi: 10.1088/1742-6596/664/9/092016. URL https://doi.org/10.1088%2F1742-6596%2F664%2F9%2F092016.

[58] ATLAS Collaboration. Muonrecpedia. 2010. URL https://twiki.cern.ch/twiki/bin/viewauth/AtlasProtected/MuonRecoPedia.

[59] ATLAS Collaboration. Jet energy scale measurements and their systematic uncertainties in proton–proton collisions at $\sqrt{s} = 13$ TeV with the ATLAS detector. *Phys. Rev. D*, 96:072002, 2017. doi: 10.1103/PhysRevD.96.072002.

[60] ATLAS Collaboration. Electron and photon reconstruction and performance in ATLAS using a dynamical, topological cell clustering-based approach. ATL-PHYS-PUB-2017-022, 2017. URL https://cds.cern.ch/record/2298955.

[61] ATLAS Collaboration. Reconstruction of hadronic decay products of tau leptons with the ATLAS experiment. *Eur. Phys. J. C*, 76:295, 2016. doi: 10.1140/epjc/s10052-016-4110-0.

[62] ATLAS Collaboration. Performance of *b*-jet identification in the ATLAS experiment. *JINST*, 11:P04008, 2016. doi: 10.1088/1748-0221/11/04/P04008.

[63] ATLAS Collaboration. ATLAS event at 13 TeV - First stable beam, 3 June 2015 - run: 266904, evt: 25884805. General Photo, Jun 2015. URL https://cds.cern.ch/record/2022202.

[64] R. Fruhwirth. Application of Kalman filtering to track and vertex fitting. *Nucl. Instrum. Meth.*, A262:444–450, 1987. doi: 10.1016/0168-9002(87)90887-4.

[65] ATLAS Collaboration. Track Reconstruction Performance of the ATLAS Inner Detector at $\sqrt{s} = 13$ TeV. ATL-PHYS-PUB-2015-018, 2015. URL https://cds.cern.ch/record/2037683.

[66] ATLAS Collaboration. Inner detector tracking public results. 2019. URL https://twiki.cern.ch/twiki/bin/view/AtlasPublic/InDetTrackingPerformanceApprovedPlots.

[67] ATLAS Collaboration. Reconstruction of primary vertices at the ATLAS experiment in Run 1 proton–proton collisions at the LHC. *Eur. Phys. J. C*, 77:332, 2017. doi: 10.1140/epjc/s10052-017-4887-5.

[68] ATLAS Collaboration. Muon reconstruction performance of the ATLAS detector in proton–proton collision data at $\sqrt{s} = 13$ TeV. *Eur. Phys. J. C*, 76:292, 2016. doi: 10.1140/epjc/s10052-016-4120-y.

[69] ATLAS Collaboration. Muon public results. 2019. URL https://twiki.cern.ch/twiki/bin/view/AtlasPublic/MuonPublicResults.

[70] J. Illingworth and J. Kittler. A survey of the hough transform. *Computer Vision, Graphics, and Image Processing*, 44:87–116, 1988. doi: 10.1016/S0734-189X(88)80033-1. URL https://www.sciencedirect.com/science/article/pii/S0734189X88800331.

[71] *ATLAS muon spectrometer: Technical Design Report*. Technical Design Report ATLAS. CERN, Geneva, 1997. URL https://cds.cern.ch/record/331068.

[72] ATLAS Collaboration. Studies of the performance of the atlas detector using cosmic-ray muons. *The European Physical Journal C*, 71(3):1593, Mar 2011. ISSN 1434-6052. doi: 10.1140/epjc/s10052-011-1593-6. URL https://doi.org/10.1140/epjc/s10052-011-1593-6.

[73] ATLAS Collaboration. Topological cell clustering in the ATLAS calorimeters and its performance in LHC Run 1. *Eur. Phys. J. C*, 77:490, 2017. doi: 10.1140/epjc/s10052-017-5004-5.

[74] et al. J. Pinfold. Performance of the atlas liquid argon endcap calorimeter in the pseudorapidity region 2.5<|η|<4.0 in beam tests. *Nuclear Instruments and Methods in Physics Research Section A: Accelerators, Spectrometers, Detectors and Associated Equipment*, 593(3): 324 – 342, 2008. ISSN 0168-9002. doi: https://doi.org/10.1016/j.nima.2008.05.033. URL http://www.sciencedirect.com/science/article/pii/S0168900208007456.

[75] et al. P. Adragna. Measurement of pion and proton response and longitudinal shower profiles up to 20 nuclear interaction lengths with the ATLAS tile calorimeter. *Nucl. Instrum. Meth.*, A615:158–181, 2010. doi: 10.1016/j.nima.2010.01.037.

[76] et al. P. Adragna. Testbeam Studies of Production Modules of the ATLAS Tile Calorimeter. *Nucl. Instrum. Methods Phys. Res., A*, 606(ATL-TILECAL-PUB-2009-002. ATL-COM-TILECAL-2009-004. 3):362–394. 73 p, Feb 2009. URL http://cds.cern.ch/record/1161354. revised version, includes new author lists.

[77] ATLAS Collaboration. Single hadron response measurement and calorimeter jet energy scale uncertainty with the ATLAS detector at the LHC. *Eur. Phys. J. C*, 73:2305, 2013. doi: 10.1140/epjc/s10052-013-2305-1.

[78] ATLAS Collaboration. Search for long-lived, massive particles in events with displaced vertices and missing transverse momentum in $\sqrt{s} = 13$ TeV pp collisions with the ATLAS detector. 2016. URL https://cds.cern.ch/record/2152010.

[79] ATLAS Collaboration. Performance of the reconstruction of large impact parameter tracks in the inner detector of ATLAS. ATL-PHYS-PUB-2017-014, 2017. URL https://cds.cern.ch/record/2275635.

[80] ATLAS Collaboration. VrtSecInclusive: an inclusive displaced vertex reconstruction package in release 21. 2018. URL https://cds.cern.ch/record/2303549.

[81] Performance of vertex reconstruction algorithms for detection of new long-lived particle decays within the ATLAS inner detector. Technical Report ATL-PHYS-PUB-2019-013, CERN, Geneva, Mar 2019. URL http://cds.cern.ch/record/2669425.

[82] M. Gignac. Attached tracks in vsi. 2019. URL https://indico.cern.ch/event/801430/contributions/3334832/attachments/1804057/2943510/2019_02_28_VSI_phiasymmetry.pdf.

[83] ATLAS Collaboration. Performance of the ATLAS trigger system in 2015. *Eur. Phys. J. C*, 77: 317, 2017. doi: 10.1140/epjc/s10052-017-4852-3.

[84] Aranzazu Ruiz-Martinez and ATLAS Collaboration. The Run-2 ATLAS Trigger System. Technical Report ATL-DAQ-PROC-2016-003, CERN, Geneva, Feb 2016. URL https://cds.cern.ch/record/2133909.

[85] ATLAS Collaboration. Trigger public results. 2019. URL https://twiki.cern.ch/twiki/bin/view/AtlasPublic/TriggerPublicResults.

[86] A Aloisio, G Carlino, F Conventi, R De Asmundis, V Izzo, A Migliaccio, G Ciapetti, A Di Mattia, C Luci, L Luminari, A Nisati, F Pastore, E Petrolo, R Vari, Stefano Veneziano, and A Salamon. The Muon Spectrometer Barrel Level-1 Trigger of the ATLAS Experiment at LHC. Technical Report ATL-DAQ-CONF-2006-014. ATL-COM-DAQ-2006-022, CERN, Geneva, May 2006. URL https://cds.cern.ch/record/947275.

[87] Philipp Lösel and Ralph Müller. Design and Construction of Large Size Micromegas Chambers for the Upgrade of the ATLAS Muon Spectrometer. Technical Report arXiv:1508.02541, Aug 2015. URL https://cds.cern.ch/record/2042404.

[88] ATLAS Collaboration. L1muon trigger public results. 2019. URL https://twiki.cern.ch/twiki/bin/view/AtlasPublic/L1MuonTriggerPublicResults.

[89] ATLAS Collaboration. Muon trigger public results. 2019. URL https://twiki.cern.ch/twiki/bin/view/AtlasPublic/MuonTriggerPublicResults.

[90] ATLAS Collaboration. L1calo trigger public results. 2019. URL https://twiki.cern.ch/twiki/bin/view/AtlasPublic/L1CaloTriggerPublicResults.

[91] ATLAS Collaboration. Met trigger public results. 2019. URL https://twiki.cern.ch/twiki/bin/view/AtlasPublic/MissingEtTriggerPublicResults.

[92] ATLAS Collaboration. Search for long-lived, massive particles decaying into leptons in *pp* collisions at 13 TeV centre-of-mass energy, with the ATLAS detector at the LHC. 2017. URL https://cds.cern.ch/record/2275055.

[93] Richard D. Ball et al. Parton distributions with LHC data. *Nucl. Phys. B*, 867:244, 2013. doi: 10.1016/j.nuclphysb.2012.10.003.

[94] J. Alwall, R. Frederix, S. Frixione, V. Hirschi, F. Maltoni, et al. The automated computation of tree-level and next-to-leading order differential cross sections, and their matching to parton shower simulations. *JHEP*, 07:079, 2014. doi: 10.1007/JHEP07(2014)079.

[95] J. Alwall, R. Frederix, S. Frixione, V. Hirschi, F. Maltoni, O. Mattelaer, H.-S. Shao, T. Stelzer, P. Torrielli, M. Zaro. The automated computation of tree-level and next-to-leading order differential cross sections, and their matching to parton shower simulations. *JHEP*, 079, 2014. doi: 10.1007/JHEP07(2014)079.

[96] Torbjorn Sjostrand, Stephen Mrenna, and Peter Z. Skands. A brief introduction to PYTHIA 8.1. *Comput. Phys. Commun.*, 178:852, 2008. doi: 10.1016/j.cpc.2008.01.036.

[97] ATLAS Collaboration. ATLAS Pythia 8 tunes to 7 TeV data. ATL-PHYS-PUB-2014-021, 2014. URL https://cds.cern.ch/record/1966419.

[98] M. Fairbairn, A. C. Kraan, D. A. Milstead, T. Sjostrand, P. Z. Skands and T. Sloan. Stable massive particles at colliders. *Phys. Rept.*, 438, 2007. doi: 10.1016/j.physrep.2006.10.002.

[99] ATLAS Collaboration. Summary of ATLAS Pythia 8 tunes. ATL-PHYS-PUB-2012-003, 2012. URL https://cds.cern.ch/record/1474107.

[100] A. D. Martin, W.J. Stirling, R. S. Thorne, and G. Watt. Parton distributions for the LHC. *Eur. Phys. J. C*, 63:189, 2009.

[101] S. Agostinelli et al. GEANT4: A Simulation toolkit. *Nucl. Instrum. Meth. A*, 506:250, 2003. doi: 10.1016/S0168-9002(03)01368-8.

[102] Aafke Christine Kraan. Interactions of heavy stable hadronizing particles. *Eur. Phys. J. C*, 37: 91–104, 2004. doi: 10.1140/epjc/s2004-01946-6.

[103] Rasmus Mackeprang and Andrea Rizzi. Interactions of Coloured Heavy Stable Particles in Matter. *Eur. Phys. J. C*, 50:353–362, 2007. doi: 10.1140/epjc/s10052-007-0252-4.

[104] Rasmus Mackeprang and David Milstead. An Updated Description of Heavy-Hadron Interactions in GEANT-4. *Eur. Phys. J. C*, 66:493–501, 2010. doi: 10.1140/epjc/s10052-010-1262-1.

[105] W. Beenakker, M. Kramer, T. Plehn, M. Spira, and P. M. Zerwas. Stop production at hadron colliders. *Nucl. Phys. B*, 515:3, 1998.

[106] Wim Beenakker, Silja Brensing, Michael Kramer, Anna Kulesza, Eric Laenen, and Irene Niessen. Supersymmetric top and bottom squark production at hadron colliders. *JHEP*, 08: 098, 2010. doi: 10.1007/JHEP08(2010)098.

[107] Wim Beenakker, Christoph Borschensky, Raphael Heger, Michael Krämer, Anna Kulesza, and Eric Laenen. NNLL resummation for stop pair-production at the LHC. *JHEP*, 05:153, 2016. doi: 10.1007/JHEP05(2016)153.

[108] Jon Butterworth et al. PDF4LHC recommendations for LHC Run II. *J. Phys. G*, 43:023001, 2016. doi: 10.1088/0954-3899/43/2/023001.

[109] Paolo Nason. A new method for combining NLO QCD with shower Monte Carlo algorithms. *JHEP*, 11:040, 2004. doi: 10.1088/1126-6708/2004/11/040.

[110] Torbjörn Sjöstrand, Stefan Ask, Jesper R. Christiansen, Richard Corke, Nishita Desai, Philip Ilten, Stephen Mrenna, Stefan Prestel, Christine O. Rasmussen, and Peter Z. Skands. An Introduction to PYTHIA 8.2. *Comput. Phys. Commun.*, 191:159, 2015. doi: 10.1016/j.cpc.2015.01.024.

[111] ATLAS Collaboration. Electron and photon energy calibration with the ATLAS detector using data collected in 2015 at $\sqrt{s} = 13$ TeV. ATL-PHYS-PUB-2016-015, 2016. URL https://cds.cern.ch/record/2203514.

[112] ATLAS Collaboration. Electron identification measurements in ATLAS using $\sqrt{s} = 13$ TeV data with 50 ns bunch spacing. ATL-PHYS-PUB-2015-041, 2015. URL https://cds.cern.ch/record/2048202.

[113] ATLAS Collaboration. Electron efficiency measurements with the ATLAS detector using the 2015 LHC proton–proton collision data. ATLAS-CONF-2016-024, 2016. URL https://cds.cern.ch/record/2157687.

[114] Matteo Cacciari, Gavin P. Salam, and Gregory Soyez. The anti-k_t jet clustering algorithm. *JHEP*, 04:063, 2008. doi: 10.1088/1126-6708/2008/04/063.

[115] ATLAS Collaboration. Pile-up subtraction and suppression for jets in ATLAS . 2013. URL https://cds.cern.ch/record/1522015.

[116] ATLAS Collaboration. Search for long-lived, massive particles in events with displaced vertices and missing transverse momentum in $\sqrt{s} = 13$ TeV pp collisions with the ATLAS detector. *Phys. Rev. D*, 97:052012, 2018. doi: 10.1103/PhysRevD.97.052012.

[117] ATLAS Collaboration. Search for massive, long-lived particles using multitrack displaced vertices or displaced lepton pairs in pp collisions at $\sqrt{s} = 8$ TeV with the ATLAS detector. *Phys. Rev. D*, 92:072004, 2015. doi: 10.1103/PhysRevD.92.072004.

[118] Dominik Krauss, Siinn Che, Christopher Blake Martin, and K.K. Gan. Search for long-lived, massive particles decaying into leptons in pp collisions at 13 TeV centre-of-mass energy, with the ATLAS detector at the LHC. Technical Report ATL-COM-PHYS-2017-1060, CERN, Geneva, Jul 2017. URL https://cds.cern.ch/record/2275055.

[119] Philippe Mermod, Arnaud Dubreuil, Shohei Shirabe, Mario Campanelli, Filips Fedotovs, Heiko Lacker, Jyoti Prakash Biswal, Michele Michetti, Abner Soffer, Sergio Grancagnolo, Craig Sawyer, and Monika Wielers. Search for heavy neutral leptons produced in W boson decays using a displaced-vertex signature with the ATLAS detector. Technical Report ATL-COM-PHYS-2017-701, CERN, Geneva, Jun 2017. URL https://cds.cern.ch/record/2267569.

[120] Sascha Mehlhase, Michael Adersberger, Jochen Jens Heinrich, Troels Petersen, Shlomit Tarem, and Massimiliano Bellomo. Search for heavy long-lived charged particles with the ATLAS detector in 36.1/fb of proton–proton collision data at $\sqrt{s} = 13$ TeV. Technical Report ATL-COM-PHYS-2016-1722, CERN, Geneva, Nov 2016. URL https://cds.cern.ch/record/2235433.